Alma Mater Studiorum - Università di Bologna

DOTTORATO DI RICERCA IN

MECCANICA E SCIENZE AVANZATE DELL'INGEGNERIA

Ciclo 34

Settore Concorsuale: 09/A1 - INGEGNERIA AERONAUTICA, AEROSPAZIALE E NAVALE

Settore Scientifico Disciplinare: ING-IND/03 - MECCANICA DEL VOLO

MODELLING, SIMULATION AND CONTROL OF ROTARY-WING AIRCRAFT IN MULTI-AGENT SCENARIO

Presentata da: Giulia Bertolani

Coordinatore Dottorato

Marco Carricato

Supervisore

Fabrizio Giulietti

Co-supervisore

Paolo Tortora

Esame finale anno 2022

All that is now
All that is gone
All that's to come
and everything under the sun is in tune
but the sun is eclipsed by the moon.
"There is no dark side of the moon really. Matter of fact it's all dark.".

Pink Floyd, *Eclipse*, The Dark Side of the Moon, 1973.

Shakyamuni insegnó che il superficiale é facile, ma il profondo é difficile. Il cuore di un coraggioso lascia il superficiale e cerca il profondo.

Nichiren Daishonin, *Sulla profezia del budda*, RSND, Vol.1, Pag.352-357.

Acknowledgments

This thesis is submitted in partial fulfillment of the requirements for the Doctor of Philosophy in "Mechanics and Advanced Sciences of Engineering". The work has been carried out during the period from November 2018 to January 2022 under the supervision of Professor Fabrizio Giulietti.

I would like to thank Prof. Fabrizio Giulietti for his guidance and fundamental support during the research work.

I also acknowledge Emanuele Luigi de Angelis, Gianluca Rossetti e Matteo Turci for their precious help.

I would also like to thank Professor Marilena Pavel of the Delft University for her valuable advice and to thank professor Pollini of the University of Pisa and his research team for their support in ur collaboration.

Finally, thanks to my dear family and to all people who encouraged me in these years.

Giulia Bertolani,
Forlí, January 2022

Summary

The topic of this thesis is the design and the implementation of mathematical models and control system algorithms for rotary-wing unmanned aerial vehicles to be used in cooperative scenarios.

The use of rotorcrafts has many attractive advantages, since these vehicles have the capability to take-off and land vertically, to hover and to move backward and laterally. Rotary-wing aircraft missions require precise control characteristics due to their unstable and heavy coupling aspects. As a matter of fact, flight test is the most accurate way to evaluate flying qualities and to test control systems. However, it may be very expensive and/or not feasible in case of early stage design and prototyping. A good compromise is made by a preliminary assessment performed by means of simulations and a reduced flight testing campaign. Consequently, having an analytical framework represents an important stage for simulations and control algorithm design.

In this work mathematical models for various helicopter configurations are implemented. Different flight control techniques for helicopters are presented with theoretical background and tested via simulations and experimental flight tests on a small-scale unmanned helicopter. The same platform is used also in a cooperative scenario with a rover. Control strategies, algorithms and their implementation to perform missions are presented for two main scenarios.

One of the main contributions of this thesis is to propose a suitable control system made by a classical PID baseline controller augmented with $\mathcal{L}_1$ adaptive contribution. In addition a complete analytical framework and the study of the dynamics and the stability of a synch-rotor are provided. At last, the implementation of cooperative control strategies for two main scenarios that include a small-scale unmanned helicopter and a rover.

Contents

List of Figures **xi**

List of Tables **xv**

1 Introduction **1**

1.1 State of the art . . . 2
1.2 Contributions . . . 5
1.3 Outline . . . 6

2 Mathematical modelling **9**

2.1 Helicopter model . . . 9
2.1.1 Equations of motion . . . 12
2.1.2 Forces and moments . . . 12
2.1.3 Main rotor Forces and moments . . . 13
2.1.4 Tail rotor forces and moments . . . 33
2.1.5 Fuselage . . . 33
2.2 Synch-rotor model . . . 34
2.2.1 Synch-rotor non-linear model . . . 34
2.2.2 Linearized synch-rotor equations of motion . . . 41
2.2.3 Synch-rotor stability derivatives . . . 43
2.2.4 Synch-rotor stability analysis . . . 56
2.3 Rover model . . . 67

3 Control systems algorithms **71**
3.1 Classical flight controllers . . . 73
3.1.1 Attitude controller . . . 73
3.1.2 Heading hold controller . . . 75
3.1.3 Altitude hold controller . . . 76
3.1.4 Velocity controller . . . 76
3.2 $\mathcal{L}_1$ adaptive controller . . . 78
3.3 Cooperative control . . . 85
3.3.1 Cooperative control scenario and strategies problem definition . . . 85
3.3.2 Cooperative control navigation architecture . . . 92

4 Simulation **95**
4.1 Classical flight controllers simulation results . . . 95
4.1.1 Helicopter PID controllers simulation results . . . 96
4.1.2 Synchrotor PID controllers simulation results . . . 102
4.2 $\mathcal{L}_1$ adaptive controllers simulation results . . . 105
4.2.1 $\mathcal{L}_1$ adaptive controller for attitude stabilization . . . 106
4.2.2 $\mathcal{L}_1$ adaptive controller for speed hold . . . 113
4.3 Cooperative control . . . 115
4.3.1 Simulations for leader-wingman scenario . . . 116
4.3.2 Simulations for behavioural approach scenario . . . 117

5 Experimental validation **125**
5.1 Experimental setup . . . 125
5.1.1 Helicopter airframe . . . 125
5.1.2 Hardware . . . 126
5.1.3 Flight software . . . 127
5.1.4 Ground station . . . 128
5.2 Flight test . . . 128
5.2.1 ArduCopter flight test . . . 128
5.2.2 Helicopter PIDs flight test . . . 129
5.2.3 $\mathcal{L}_1$ flight test . . . 132

6 Conclusions **143**

A Tip path plane equations **145**

B Relevant helicopter data **147**

C Relevant synch-rotor data 149

D State and Control matrices 153

Bibliography 155

List of Figures

2.1 Helicopter XY view 10
2.2 Helicopter XZ view 10
2.3 Helicopter YZ view 11
2.4 U_p and U_T velocity components on blade element 16
2.5 Synch-rotor XY view 35
2.6 Synch-rotor XZ view 36
2.7 Synch-rotor YZ view 36
2.8 Synch-rotor geometry 38
2.9 Trend of d vs Γ 39
2.10 Overlapping area geometry 40
2.11 Interference actor k vs tilt angle 40
2.12 Stability derivatives - $Z_w Z_u$ 45
2.13 Stability derivatives - $X_u Y_v$ 46
2.14 Stability derivatives - $X_v Y_u$ 47
2.15 Stability derivatives - $M_u M_w$ 48
2.16 Stability derivatives - $L_v N_v$ 49
2.17 Stability derivatives - $N_u N_w$ 50
2.18 Stability derivatives - $X_q Y_p$ 52
2.19 Stability derivatives - $M_q L_p$ 53
2.20 Stability derivatives - $M_p L_q$ 54
2.21 Stability derivatives - $L_r N_r$ 55
2.22 Loci of synch coupled eigenvalues as a function of different dihedral angle Γ in hovering 56

2.23 Loci of synch longitudinal eigenvalues as a function of different dihedral angle Γ in hovering . . . 57
2.24 Loci of synch lateral eigenvalues as a function of different dihedral angle Γ in hovering . . . 58
2.25 Loci of synch coupled eigenvalues as a function of different dihedral angle Γ in hovering without the horizontal stabilizer . . . 59
2.26 Loci of synch longitudinal eigenvalues as a function of different dihedral angle Γ in hovering without the horizontal stabilizer . . . 60
2.27 Loci of synch lateral eigenvalues as a function of different dihedral angle Γ in hovering without the horizontal stabilizer . . . 61
2.28 Loci of synch coupled eigenvalues as a function of different dihedral angle Γ at 140 km/h . . . 62
2.29 Loci of synch longitudinal eigenvalues as a function of different dihedral angle Γ at 140 km/h . . . 63
2.30 Loci of synch lateral eigenvalues as a function of different dihedral angle Γ at 140 km/h . . . 64
2.31 Rover independent steering model . . . 69

3.1 Flight control software overview . . . 72
3.2 Helicopter roll controller architecture . . . 74
3.3 Helicopter pitch controller architecture . . . 74
3.4 Helicopter yaw rate controller architecture . . . 75
3.5 Helicopter altitude hold controller scheme . . . 76
3.6 Helicopter speed hold controllers . . . 77
3.7 $\mathcal{L}_1$ adaptive control scheme . . . 78
3.8 $\mathcal{L}_1$ adaptive control scheme for attitude stabilization . . . 79
3.9 $\mathcal{L}_1$ adaptive control scheme for velocity . . . 80
3.10 $\mathcal{L}_1$ augmentation of baseline PID . . . 84
3.11 Wind velocity components . . . 87
3.12 Cooperative control strategy global architecture . . . 88
3.13 Cooperative control problem definition . . . 89
3.14 Cooperative control plane problem definition . . . 90
3.15 Cooperative control guidance logic diagram . . . 91
3.16 Cooperative control architecture . . . 93

4.1 SAB® Goblin700 Thunder helicopter . . . 96
4.2 FlightGear flight simulator . . . 96

4.3 North velocity profile tracking - NED velocities . . . 98
4.4 North velocity profile tracking - roll, pitch angles and yawrate . . . 99
4.5 Trajectory tracking - NED velocities . . . 100
4.6 Trajectory tracking - roll, pitch angles and yawrate . . . 101
4.7 Simulation with human pilot - NED velocities . . . 103
4.8 Simulation with human pilot and wind - NED velocities . . . 104
4.9 Reference vs actual attitude angles - synchrotor PID controller . . . 105
4.10 Reference vs actual north velocity - synchrotor PID controller . . . 105
4.11 Reference tracking baseline PID vs augmented PID . . . 107
4.12 Multiple Reference tracking baseline PID vs augmented PID. . . . 108
4.13 Attitude and yawrate in simulation . . . 109
4.14 Helicopter normalized inputs . . . 110
4.15 Adaptation terms over time . . . 111
4.16 Switch effect on attitude and yawrate . . . 112
4.17 Combined model wind rejection . . . 113
4.18 V_N reference tracking, adaptive vs PID . . . 114
4.19 V_E reference tracking, adaptive vs PID . . . 114
4.20 V_N reference tracking, adaptive vs PID in case of wind disturbances . . . 115
4.21 V_E reference tracking, adaptive vs PID in case of wind disturbances . . . 116
4.22 Cooperative control simulation - First test . . . 118
4.23 Rover and helicopter trajectories - First test . . . 119
4.24 Cooperative control simulation - Second test . . . 120
4.25 Distance errors in case of helicopter adaptive speed hold controller . . . 121
4.26 Reference vs actual values for rover in cooperative control - behavioural approach . . . 122
4.27 Reference vs actual values for helicopter in cooperative control - behavioural approach . . . 123

5.1 Goblin 700 helicopter electronic scheme . . . 126
5.2 Goblin 700 Flight control architecture . . . 127
5.3 Helicopter actual velocities in hovering . . . 130
5.4 Helicopter percentage error on roll angle in hovering . . . 131
5.5 Helicopter percentage error on pitch angle in hovering . . . 131
5.6 Helicopter percentage error on yaw-rate in hovering . . . 132
5.7 Helicopter percentage error on roll angle . . . 133
5.8 Helicopter percentage error on pitch angle . . . 133
5.9 Helicopter percentage error on yaw-rate . . . 134

5.10 Helicopter actual velocities 134
5.11 Helicopter flight test results: reference and actual roll angle, baseline vs augmented controller 136
5.12 Helicopter flight test results: error of roll angle, baseline vs augmented controller 137
5.13 Helicopter flight test results: reference and actual pitch angle, baseline vs augmented controller 138
5.14 Helicopter flight test results: error of pitch angle, baseline vs augmented controller 139
5.15 Helicopter flight test results: reference and actual yawrate, baseline vs augmented controller 141

List of Tables

2.1 Analytical vs numerical values for Z_w 44
2.2 Comparison of exact and approximated values of phugoid frequency and damping 65
2.3 Comparison of exact and approximated values of lateral/directional modes 66

5.1 Comparison of simulated and experimental values of trim attitude angles in hovering 129

A.1 Tip path plane equation 146

B.1 Relevant helicopter data 147

C.1 Relevant synch-rotor data 149

Nomenclature

List of Symbols

a	Lift curve slope	
a_0	Rotor coning angle	rad
a_1	Longitudinal TPP deflection angle in rotor-hub system	rad
A_{1c}	Lateral cyclic angle in wind-hub axes	rad
A_{1s}	Lateral cyclic angle in hub-body axes	rad
A_b	Blade area	m^2
b_1	Lateral TPP deflection angle in rotor-hub system	rad
B_{1c}	Longitudinal cyclic angle in wind-hub axes	rad
B_{1s}	Longitudinal cyclic angle in hub-body axes	rad
c	Blade chord	m
C_D	Drag coefficient	
C_Y	Lateral force coefficient	
C_L	Lift coefficient	
C_T	Thrust coefficient	
$\tilde{D}$	Damping matrix	
e	Flapping hinge offset	m
$\tilde{f}$	Forcing function	
$\boldsymbol{F} = [X\ Y\ Z]^T$	Force vector	N
i_s	Rotor tilt angle	rad
$\boldsymbol{I}$	Inertia tensor	kg/m^2
I_β	Blade inertia moment with respect to flapping hinge	kgm^2
$\tilde{K}$	Stiffness matrix	
K_1	Pitch-flap coupling ratio	

K_β	Stiffness of the flapping hinge	
m	Mass	kg
$\boldsymbol{M} = [L\ M\ N]^T$	Moment vector	Nm
M_β	Blade weight moment about the flapping hinge	kg/m^2
N	Number of blades	
R	Rotor radius	m
s	Rotor solidity	
$\boldsymbol{V} = [u\ v\ w]^T$	Velocity vector	m/s

Greek symbols

α	Angle of attack	rad
β	Side-slip angle	rad
β	Blade flapping	rad
β_{1c}	Lateral blade flapping	rad
β_{1s}	Longitudinal blade flapping	rad
ϵ	Hinge offset ratio	
γ	Lock number	
μ	Advance ratio	
ϕ, θ, ψ	Roll, pitch, yaw euler angles	rad
ρ	Density	kg/m^3
θ_t	Blade twist	rad
λ	Inflow ratio	
Γ	Synch-rotor tilt angle	rad
Θ	Blade collective	rad
$\boldsymbol{\Omega} = [p\ q\ r]^T$	Angular velocity vector	rad/s
Ω	Rotor angular velocity	rad/s

Subscripts and superscripts

^{a}	Aerodynamical
a	Actual
cl	Clockwise
ccl	Counter-clockwise
des	Desired
e	Equilibrium condition
^{e}	External
fus	Fuselage
^{g}	Gravitational
hs	Horizontal stabilizer
mr	Main rotor
tr	Tail rotor
vs	Vertical stabilizer

Acronyms

BL	Buttline
FCS	Flight Control System
FGC	Formation Control Geometry
FMU	Flight Management Unit
NED	North East Down
PID	Proportional Integal Derivative
PSP	Pilot Support Package
$RUAV$	Rotorcraft Unamnned Aerial Vehicle
$RUAV$	Rotorcraft Unamnned Aerial Vehicle
STA	Stationline
$TPPV$	Tip Path Plane
UAS	Unamnned Aerial System
UAV	Unamnned Aerial Vehicle
WL	Waterline

CHAPTER 1

Introduction

The topic of this work is the design and the implementation of mathematical models and control system algorithms for rotary-wing unmanned aerial vehicles. The use of these vehicles in a wide range of applications is expanding. With the goal of increasing operability and expanding mission tasks, cooperative control is becoming more discussed by the scientific and industrial communities. The aim of the thesis is to extend the knowledge within the framework of control systems for autonomous rotorcrafts in cooperative scenarios. The goal is to propose a general scheme that gives the opportunity to easily pilot the formation as desired among different strategies. Thus, vehicles own autopilot remains independent from the formation controller. Accordingly, it is possible to implement and test many possible configurations including also innovative algorithms. The purpose is to investigate many control algorithms by means of numerical simulations and flight tests on small-scale UAVs. Considering this, the use of simulations is relevant for performing tests prior to execute a flight campaign, so that the implementation of suitable mathematical models is another main point of this work. The author intends to propose complete mathematical frameworks for different unamnned rotorcraft configurations, including also unconventional ones.

The chapter is organized as follows: firstly a general overview of the state of the art in the field of rotary-wing aircraft, control system design and multi-agent scenario is given. Then the original contributions of this thesis are presented. Finally the outline of the entire work is described.

1.1 State of the art

Unmanned Aerial Vehicles (UAVs) have become extensively used in a wide range of applications, getting a large interest in the scientific and industrial community and playing increasingly prominent roles in disparate programs around the world. An Unmanned Aerial System (UAS) is composed by the aircraft itself, by a control station, by the communication system and by the support equipment, including sensors, software and microcontrollers [1], [2]. These platforms are suitable for numerous applications both in civilian and military fields, such as aerial photography and video shooting, agriculture, conservation, search and rescue, surveillance and coastguard, tracking and so on. Control functions of the aircraft may be either on-board or off-board. An UAV may have different levels of automation: zero, partly or completely provided of automatic intelligence. Partially or fully automatic UAVs help operators to realize complex missions and offer advantages if compared to manned aircraft. As an example, unmanned vehicles are safer than manned ones in both civilian and military applications as in environmental monitoring or surveillance. Moreover, the cost of a mission performed with an UAS is cheaper than operating with manned vehicles. Firstly, the aircraft results to be smaller than the manned one used for the same role and typically its price is lower. Then, also operating and maintenance costs are reduced [1].

The use of UAVs for the operations mentioned above has been generally accepted and the benefits have been recognized [3]. With the aim to increase the operability of UAVs and to widen the missions tasks, cooperative behaviour have been implemented with autonomy and automation [4]. Accuracy, flexibility, efficiency, robustness and reliability are expected to be enhanced, even if it is exposed to additional possibility of failure and error propagation. In particular, a system of unmanned vehicles is a group of agents interacting each other and with the ambient around [5]. Nowadays cooperative algorithms and their applications are largely discussed by the scientific community. There are numerous reviews of the late contributions on the topic. Ren et al. [6] and Wang [7] give an overview of information consensus in multi-vehicle cooperative control, while Anderson et al. [8] set out the rudiments of the theory for analysing and creating architectures appropriate to the control of formations of autonomous vehicles based on ideas of rigid graph theory. Oh et al. [9] present a survey of multi-agent formation control by categorizing the existing results into the position-based, displacement-based and distance-based control, whereas Zhu [10] and Senanayake [11] present a survey on new progresses on control and optimization approaches for swarm systems.

Among various topics related to multi-vehicle systems, formation control has been studied for many years. Formation control concerns vehicle swarming considering constraints

in relative positions.

Many applications and formation control problems depend on the sensing capability and on the interaction topology of agents. In literature there are examples based on the behavioural approach [12], [13], [14], virtual structures [15], [16], [17], and the leader-follower configurations [18], [19], [20], [21], [22]. Rezaee et al [23] report that the leader-follower configuration is the most popular one due to its facility of implementation and use. As suggested by the name itself, there is an agent moving along a trajectory that is called "leader" and another one, called the "follower", that has to maintain a requested distance and/or orientation or relative positions from the leader by adopting a control strategy [19]. As stated by Dehghani and Menhaj [24], there are three main methods to set up desired relative kinematics between the vehicles. The first one is the so-called "communication based approach": state information are exchanged via radio communication. The second one is the "vision aided strategy": the follower through the use of a visual sensor measures relative information and via global position measurements knows self position. The third one is the "vision based strategy" in which the follower is only provided with a relative measurement sensor. Despite vision aided and vision based strategies are of particular interest for researchers due to practical issues, communication based approach does not need additional sensors and cameras with respect to those normally present on the UAV autopilot.

Even if reference [23] suggests that the leader-follower configuration is the most popular, a comparative study [25] between three different formation structures shows the advantages of the behavioural approach for formation keeping and trajectory tracking. The formation structures analysed by the authors are the leader-wingman, the virtual leader and the behavioural approaches.

There are many different UAVs configurations that can be employed in cooperative scenarios: fixed-wing and rotary-wing aircraft, Vertical Take Off and Landing (VTOL) vehicles and Short-Take Off and Landing vehicles (STOL). Rotary-wing aircraft have many evident advantages compared to fixed-wing ones [26], [27], [28]. A fixed-wing aircraft requires a run-way to take-off and land or other launching mechanisms [29]. Differently, a rotorcraft has the capability to take-off and land vertically, to hover, to move backwards and sideways, to fly also at very low altitudes and to perform both aggressive or non-aggressive maneuvers. There are various types of rotary-wing aircraft: helicopters, autogyros, gyrodyne, rotor-kites and multirotors. Multirotors seem to have more advantages than helicopters, as their mechanic is more simple if compared to conventional helicopters and straightforwards stabilization loops for compensating their inherent instability are available. In addition, these vehicles are also low-cost, since their great demand and supply on the market. However, these platforms have a reduced maximum cruise speed if

compared to helicopters and their efficiency is lower for equal total thrust.

Concerning helicopters, these may have different configurations: the conventional and the most common one with a single main rotor and a tail rotor; the tandem rotor configuration; the coaxial rotor configuration and the intermeshing or synchropter rotor configuration [30]. In this last configuration the total thrust is provided by two counter-rotating intermeshing main rotors that at the same time allow for the yaw-axis torque balance. There are some advantages in the use of the synchropter configuration that helped it to become more popular in the recent years. With respect to a conventional single main rotor helicopter, the synchropter has a greater payload capacity due to the presence of two main rotors, whose total power can be used to provide useful lift [30]. It also results in a lower noise pitch level due to the lack of the tail rotor [31]. Moreover, the lifting capability is increased if compared to a coaxial rotor configuration due to the larger "free" disc area of the synchrotor, bringing to a 10-15 percent larger available payload [31], [32], [33]. The main disadvantage, like coaxial design, is that the induced power is higher than that of two isolated rotors, with a loss of efficiency. This is due to the fact that one rotor may operate in the slipstream of the other one, resulting in the need of an higher induced power for the same thrust [30]. Furthermore, the intermeshing configuration presents a lack of maneuverability on the yaw-axis which, however, may be recovered by a proper control system design. Performance, vibratory loads analysis, servo-flap design, identification and control system design of such configuration have been discussed in the existing literature [34], [35], [36], [37], that is mainly related to the Kaman K-MAX® aircraft or to others small-scale platforms projects [38], [31].

Helicopters in all their configurations and more in general Rotorcraft Unmanned Aerial Vehicles (RUAVs) may operate in potentially obstructed and constrained environments or may be asked to complete complex missions, demanding high capability of the pilots or of the autopilots. Consequently, robust control systems are required. The design of controllers for RUAVs has been reported by a considerable number of researchers. The approaches developed up to present days for the control of helicopters are based on classical, modern and intelligent control techniques. Mettler [39] and Raptis and Valavanis [40] give an overview of the linear and non-linear control techniques for small scale helicopters in their books. PID-based feedback techniques are used in the present helicopter Flight Control System (FCS) design due to their easiness of realization and application [41]. In reference [42] a multi-loop single-input single-output (SISO) control based on proportional feedback is presented. However, these techniques present limited achieved performance. Other classical control methods have been investigated and are currently employed, as model following approach or gain scheduling, but still proving lack of robustness in case of unmodeled non-linearities. Considering the high-level of fidelity required for piloting

RUAVs, there is the necessity to design baseline controllers with a considerable high level of robustness against the uncertainties and possible disturbances. Concerning intelligent control approaches, the two dominant ones are fuzzy logic and Artificial Neural Network (ANN). The former have been mainly studied starting from 1990 [43], as well as the latter with application on unmanned small-scale helicopters [44]. An evolutionary design method for fuzzy logic controller has been presented in reference [45]. It is based on self-organizing process that learns relations between input and output and it is used as regulation layer of a flight management unit for an unmanned helicopter. Among the modern control methodologies, the use of LQR and eigenstructure assignment control is demonstrated by [46] and [47]. In the 1990s, McFarlane and Glover introduced the H_∞ optimal control [48] that started to be used from 1997 [49] on helicopters and is currently research topic also on small-scale platforms [50]. in reference [51], the authors implemented a special scheme based on H_2 and H_∞. Linear Parameter Varying (LPV) approach is widely used for fixed-wing aircraft [52], but there are few examples of its application to helicopters [53]. There are other nonlinear methodologies that have been implemented to rotorcrafts, but these have been slightly researched: sliding mode [54], backstepping [55] and Model Predictive Control (MPC) [56]. In the class of modern controllers, there are also adaptive control methods, that are currently experiencing a revived interest, as presented by Anavatti et al. [57]. These techniques can face with nonlinear uncertainties for both linear and nonlinear systems. In the past decades their application have been extended also to helicopter control [58], [59], [60], [61]. In the current literature there are few examples of this adaptive controller applied to helicopters. From 2009, Guerriero et al. applied this adaptive control technique to provide attitude and velocity stabilization of an autonomous helicopter [62], while Michini et al. used $\mathcal{L}_1$ on indoor autonomous helicopter [63]. Bichlmeier et al. tested this technique on helicopter attitude rate control loop [64]. Gaoyuan et al. tested $\mathcal{L}_1$ on tandem-rotor helicopters [65], whereas Tian et al. implemented the $\mathcal{L}_1$ controller for the vertical flight control of helicopter [66] with piece-wise constant adaptation law.

1.2 Contributions

Main contributions of this work with respect to the state of the art are:

- The mathematical modelling and the dynamics of the synch-rotor configuration. Whereas current studies are focused on the topics mentioned above, an overall theoretical framework to address preliminary design, optimal sizing and control system design is still missing in literature. The scope is to provide an analytical framework to describe aircraft performance, dynamics behaviour and stability issues in virtue

of relevant parameters associated to the configuration itself. As part of this thesis, a non-linear mathematical model of the intermeshing rotors configuration is provided considering the aerodynamic effects due to the intermeshing rotors interaction. In addition, both coupled and decoupled systems and some approximate closed-form solutions for relevant dynamic modes are given with the stability analysis.

- The development of a control framework made by a PID baseline controller augmented with an adaptive contribution for the conventional single main rotor helicopter. In this thesis the $\mathcal{L}_1$ adaptive control technique has been applied to a small-scale remotely piloted helicopter with the aim to improve the PID baseline controller performance. The principal advantage of this adaptive control technique is to decouple robustness from fast adaptation [67]. The present work extends the use of $\mathcal{L}_1$ adaptive control technique to small-scale helicopters through the original architecture that allows the adaptive contribution to be switched-on and off, giving the possibility to safely test the augmented controller. The controller architecture is the Lyapunov-based adaptive control law for nonlinear systems in the hypothesis of matched uncertainties. This architecture is reported in chapter 2.4 of reference [67]. To the author's knowledge,the unique feature of this architecture is that it has never been used to helicopters before.

- The design of a cooperative control strategy for unmanned vehicles in a multi-agent system. The original contribution lies in the implementation of a general scheme whose main peculiarity is the possibility to easily switch among different formation control strategies. Moreover, this design allows to keep unchanged each vehicle autopilot, providing the opportunity to test many algorithms letting the choice independent for each agent.

1.3 Outline

This thesis presents first the analytical frameworks of different helicopter configurations. Then classical and modern control techniques are studied. Finally, these frameworks are used in a multi-agent scenario to test cooperative control strategies. The overall process is covered, from mathematical modelling, control design and validation through simulations and experimental tests.

The work is divided into four main parts: mathematical modelling, control system algorithms design, simulations and experimental validation. The thesis is organized as follows: in Chapter 2 the linear and non-linear mathematical models for the conventional single

main rotor helicopter, for the synch-rotor and for the rover are derived. In particular, the focus of the synch-rotor analysis is on the dynamic issues related to the proper configuration parameters. The simulation models are implemented in Matlab/Simulink® environment.
Chapter 3 explains the controllers architecture. First, classical flight controllers are given. Then, adaptive controllers design is explained. Finally an overview of the cooperative algorithm is showed.
In Chapter 4 simulation results are illustrated with the same structure of the previous chapter. The simulation campaign related to the classical control strategies intends to show the performance of these controllers. Results for the adaptive controllers are also reported and a comparison with classical control systems results is discussed. Ultimately, simulations for the cooperative strategies test the efficiency of these algorithms.
Chapter 5 presents the results of the experimental campaign carried out. In this part the experimental setups are firstly described, then results are given and discussed.
A Chapter 6 of concluding remarks ends this thesis.

CHAPTER 2

Mathematical modelling

In this chapter, the non-linear mathematical models of the vehicles are derived starting from general expressions for kinematics and dynamics of a rigid body. First, the helicopter six degrees of freedom model is presented. Secondly, the synch-rotor non-linear model is given. Then this model is linearized and the dynamic issues are discussed considering the proper configuration parameters. A section presenting the rover model ends this chapter.

2.1 Helicopter model

In this section the classical single main rotor with tail rotor helicopter configuration model is presented. The following assumptions are made:

1. The earth is flat and fixed;

2. Mass, inertia and center of gravity position are constant, accordingly fuel consumption is neglected and the vehicle presents a longitudinal plane of symmetry;

3. Gravity acceleration is considered independent of height and hence constant.

The following reference frames are introduced, as depicted in Fig. 2.1, Fig. 2.2 and Fig. 2.3: Hub-Wind, Hub-Body, Body, Local Wind and NED. In particular, the term "Hub" means that the origin of the coordinate system is at the hub centre. The terms "Wind" and "Body" indicate where the three axes point.

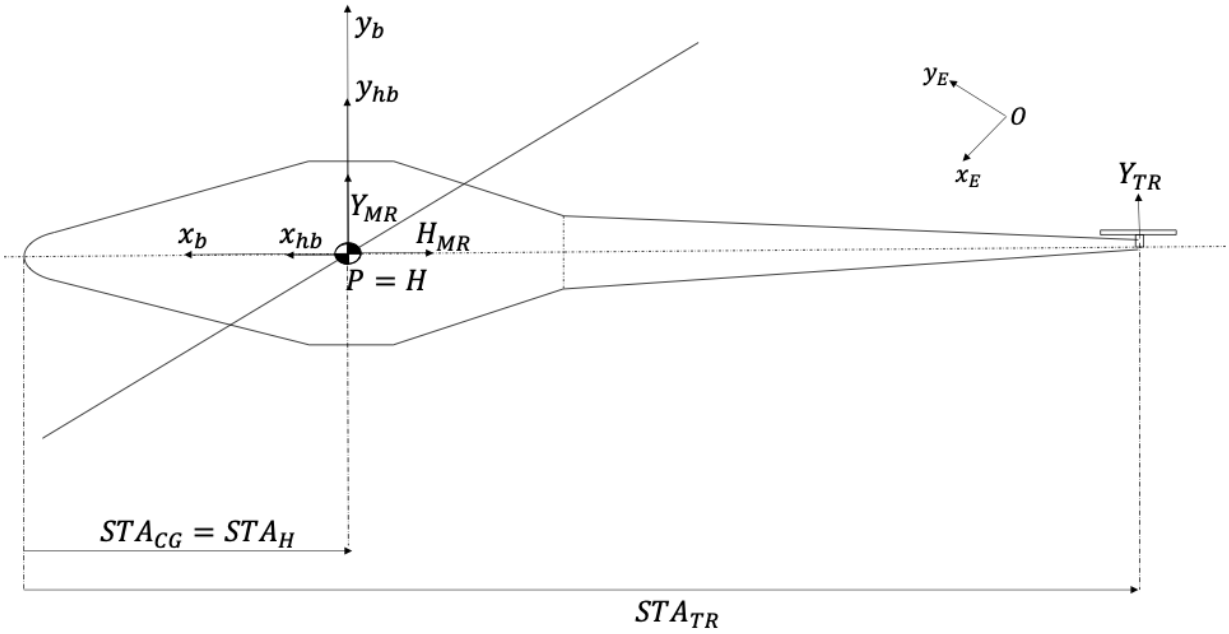

Figure 2.1: Helicopter XY view

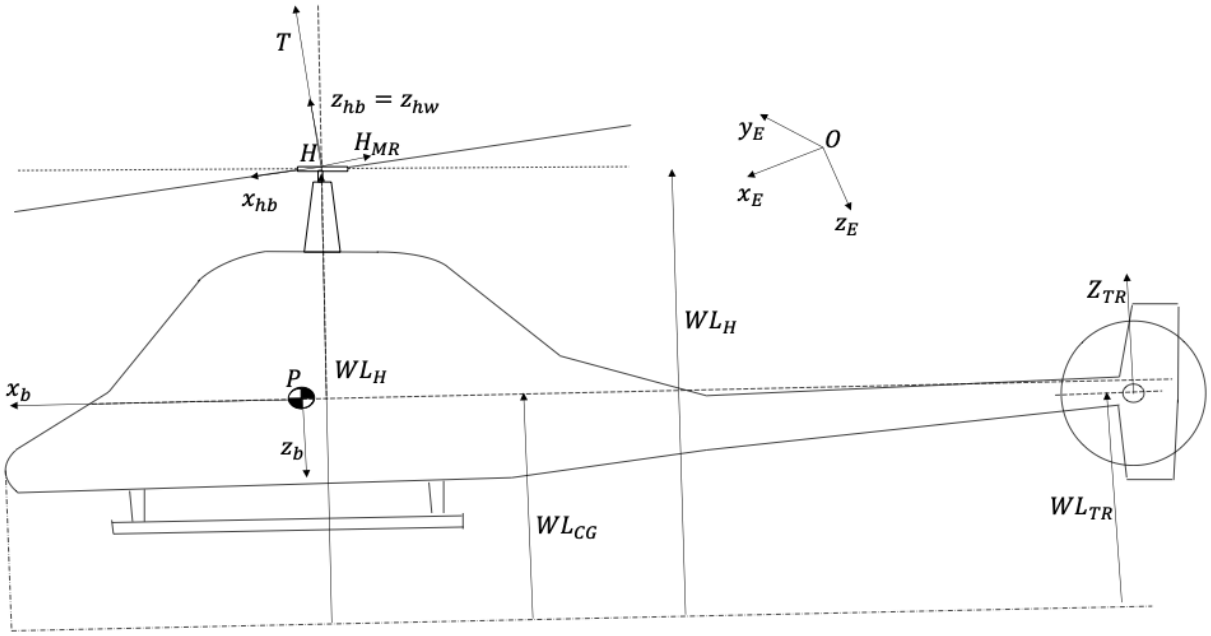

Figure 2.2: Helicopter XZ view

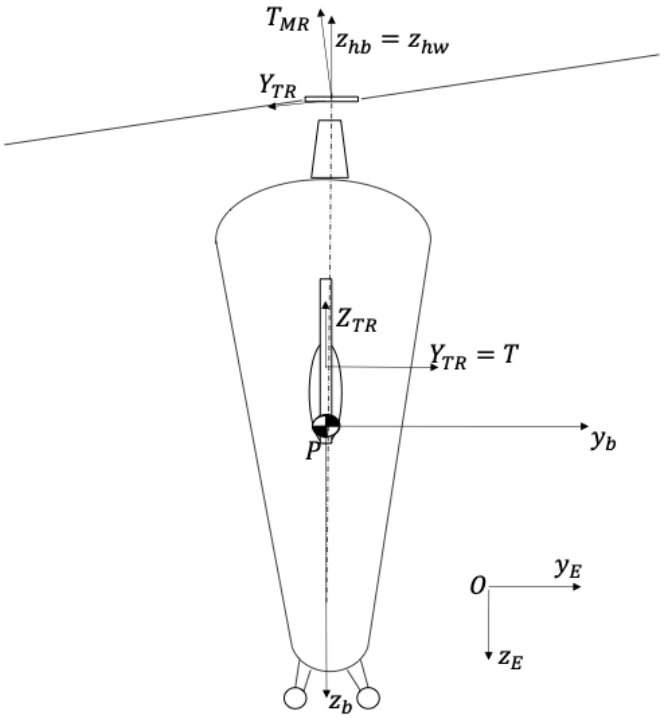

Figure 2.3: Helicopter YZ view

1. Earth-fixed North-east-down (NED) frame, $\mathbb{F}_E = \{O; \boldsymbol{x}_E, \boldsymbol{y}_E, \boldsymbol{z}_E\}$. This frame is inertial under the assumption of flat and non-rotating Earth.

2. Hub-Wind frame $\mathbb{F}_{hw} = \{H; \boldsymbol{x}_{hw}, \boldsymbol{y}_{hw}, \boldsymbol{z}_{hw}\}$. This frame is used in calculation of rotor forces and moments. Its origin is the intersection of the rotor disk plane at zero flap angle and the rotor shaft axis. $\boldsymbol{z}_{hw}$ axis is aligned with the rotor shaft, pointing upward. $\boldsymbol{x}_{hw}$ axis, orthogonal to $\boldsymbol{z}_{hw}$, is aligned with the component of relative wind normal to the shaft axis. $\boldsymbol{y}_{hw}$ axis completes the right-handed orthogonal set.

3. Hub-Body frame $\mathbb{F}_{hb} = \{H; \boldsymbol{x}_{hb}, \boldsymbol{y}_{hb}, \boldsymbol{z}_{hb}\}$. $\boldsymbol{z}_{hb}$ axis is aligned with rotor shaft, pointing upward. This system coincides with the hub-wind system when the sideslip β_w is zero. Its origin H is the same of the Hub-Wind frame.

4. Body-Fixed frame $\mathbb{F}_b = \{P; \boldsymbol{x}_b, \boldsymbol{y}_b, \boldsymbol{z}_b\}$. Origin is located at the centre of gravity of the rotorcraft. $\boldsymbol{x}_b$ axis points in forward direction, it's aligned with the longitudinal axis of the vehicle; $\boldsymbol{z}_b$ axis points downward and $\boldsymbol{y}_b$ axis completes the right-hand system. All forces and moments used in the body equations of motion are expressed relative to this system.

5. Local Vertical frame $\mathbb{F}_{LV} = \{P; \boldsymbol{x}_{LV}, \boldsymbol{y}_{LV}, \boldsymbol{z}_{LV}\}$. Origin is at the centre of gravity and axes are parallel to the inertial frame

The proposed mathematical framework consists of the complete non-linear equations of motions and includes the modelling of forces and moments acting on the vehicle. It is based on the work of references [72], [70].

2.1.1 Equations of motion

Helicopter dynamics is described by Newton-Euler equations of motion projected in the body system of reference $\mathbb{F}_b$. Namely:

$$\dot{\boldsymbol{V}} = -\boldsymbol{\Omega} \times \boldsymbol{V} + \boldsymbol{F}^{(e)}/m \tag{2.1}$$

$$\dot{\boldsymbol{\Omega}} = \boldsymbol{I}^{-1}[-\boldsymbol{\Omega} \times (\boldsymbol{I}\boldsymbol{\Omega}) + \boldsymbol{M}^{(e)}] \tag{2.2}$$

where mass and mass distribution are assumed to be constant. Helicopter attitude kinematics is given by:

$$\begin{bmatrix} \dot{\phi} \\ \dot{\theta} \\ \dot{\psi} \end{bmatrix} = \begin{bmatrix} 1 & \sin\phi\tan\theta & \cos\phi\tan\theta \\ 0 & \cos\phi & -\sin\phi \\ 0 & \sin\phi/\cos\theta & \cos\phi/\cos\theta \end{bmatrix} \boldsymbol{\Omega} \tag{2.3}$$

$$\frac{d}{dt}\begin{bmatrix} x \\ y \\ z \end{bmatrix} = \Pi_b^{hb} \begin{bmatrix} u \\ v \\ w \end{bmatrix} \tag{2.4}$$

provided

$$\Pi_b^{hb} = \begin{bmatrix} c\theta c\psi & s\phi s\theta c\psi - c\phi s\psi & c\phi s\theta c\psi + s\phi s\psi \\ c\theta s\psi & s\phi s\theta s\psi + c\phi c\psi & c\phi s\theta s\psi - s\phi c\psi \\ -s\theta & s\phi c\theta & c\phi c\theta \end{bmatrix} \tag{2.5}$$

where c stays for cos and s for sin.

2.1.2 Forces and moments

The external forces are made of aerodynamic forces $\boldsymbol{F}^{(a)}$ and gravity forces $\boldsymbol{F}^{(g)}$ contributions, whereas total moments include aerodynamic moments $\boldsymbol{M}^{(a)}$. Gravity forces are expressed in the following way:

$$\boldsymbol{F}^{(g)} = \Pi_{be} \begin{bmatrix} 0 \\ 0 \\ mg \end{bmatrix} = \begin{bmatrix} -mg\sin\theta \\ mg\sin\phi\cos\theta \\ mg\cos\phi\cos\psi \end{bmatrix} \tag{2.6}$$

Aerodynamic effects are introduced for all rotorcraft components and summed:

$$\boldsymbol{F}^{(a)} = \boldsymbol{F}^{(\mathrm{mr})} + \boldsymbol{F}^{(\mathrm{fus})} + \boldsymbol{F}^{(\mathrm{tr})} \tag{2.7}$$

$$\boldsymbol{M}^{(a)} = \boldsymbol{M}^{(\mathrm{mr})} + \boldsymbol{M}^{(\mathrm{fus})} + \boldsymbol{M}^{(\mathrm{tr})} \tag{2.8}$$

2.1.3 Main rotor Forces and moments

Main rotor is the primary source of lift, propulsion and control, thus it dominates the helicopter dynamics behaviour. Thus, aerodynamically, momentum theory and uniform inflow were used together; simple strip theory was utilized and the blade forces were analytically integrated over the radius. To obtain the total rotor forces and moments the contributions to each blade, that were analytical functions of the azimuth, were analytically summed. The reversed flow region and the stall and compressibility effects were ignored. This model has been shown in [68] to be suitable for stability and control investigations up to an advance ratio of about 0.3. Rotor forces and moments were first obtained in the wind-hub coordinate system and then transformed into the hub-body reference system. The rotational matrix from hub-body to wind-hub coordinate system is:

$$\begin{bmatrix} (\quad)_x \\ (\quad)_y \\ (\quad)_z \end{bmatrix}_{wh} = \begin{bmatrix} \cos\beta_w & \sin\beta_w & 0 \\ -\sin\beta_w & \cos\beta_w & 0 \\ 0 & 0 & 1 \end{bmatrix} \begin{bmatrix} (\quad)_x \\ (\quad)_y \\ (\quad)_z \end{bmatrix}_{hb} \tag{2.9}$$

where

$$\beta_w = \sin^{-1} \frac{v_h}{(u_h^2 + v_h^2)^{1/2}} \tag{2.10}$$

is the sideslip angle. β_w is definedaz zero as $v_h = u_H = 0$.

The transformation from body-fixed frame to hub-body frame is:

$$\Pi_{hb} = \begin{bmatrix} \cos i_s & 0 & \sin i_s \\ 0 & 1 & 0 \\ -\sin i_s & 0 & \cos i_s \end{bmatrix} \tag{2.11}$$

considering the rotor shaft tilted in the XZ plane with an angle i_s.

In such a way, equations contain periodic terms: the highest harmonic term correspond directly to the number of rotor blades. For example, for a three-bladed rotor, the force and moment equations contain only 3/revolution harmonic terms and for a four-bladed rotor 4/revolution harmonic terms. Before introducing the procedure to derive main rotor forces and moments, it's necessary to give the rotor flapping dynamics equations.

Rotor flapping dynamics

Description of the blade-flapping dynamics is essential to the rotor mathematical model. The flapping of the rotor is a dynamic response to the combined effects of aerodynamic, centrifugal, inertial and gravitational forces. The aerodynamic force results from many different sources of airflow: relative wind velocity, the vehicle's angular velocity, the rotor's rotational speed and the rotor inflow passing through it. A tip-path plane representation is used to approximate the flapping dynamic.

Flapping equation of motion The flapping equation of motion is derived with four parameters of interest:

1. e: the effective hinge offset
2. K_β: the stiffness of the flapping hinge
3. K_1: the pitch-flap coupling
4. γ: the Lock number, defined as $\frac{\rho a c R^4}{I_\beta}$

Many assumptions need to be considered to develop analytical expressions:

- Rotor blade is rigid in bending and torsion;
- Blade twist is linear;
- Flapping and inflow angles are assumed small, the analysis is based on a simple strip theory;
- Only effects due to angular acceleration $\dot{p}$ and $\dot{q}$, angular velocity p, q and the normal acceleration of the aircraft motion are considered to calculate blade flapping;
- Compressibility and stall effects are not considered;
- The reverse flow region is ignored;
- The inflow is assumed to be uniform and inflow dynamic is described by Pitt-Peters [69] model;
- The tip loss factor is assumed to be 1.

The results of the analysis with these assumptions are valid up to an advance ratio of approximately 0.3 [68]. For non-teetering rotor systems the flapping equation of motion for a single blade is derived by summing the moments at the flapping hinge:

$$M_A + M_{CF} + M_I + M_{Cor} + M_R + M_{BA} + M_{BL} + M_W = 0 \tag{2.12}$$

where:

M_A	moment due to aerodynamic force acting on the blade,
M_{CF}	moment due to centrifugal force, $M_{CF} = -\Omega^2[I_\beta \cos\beta + eM_\beta]\sin\beta$,
M_I	moment due to blade inertia, $M_I = -I_\beta \ddot{\beta}$,
M_{Cor}	moment due to Coriolis acceleration, $M_{Cor} = 2[I_\beta + eM_\beta](p\Omega\cos\psi' - q\Omega\sin\psi')$,
M_R	flapping hinge restraint moment, $M_R = -K_\beta\beta$,
M_{BA}	moment due to body angular acceleration, $M_B A = I_\beta(\dot{p}\sin\psi' + \dot{q}\cos\psi')$,
M_{BL}	moment due to body acceleration, $M_{BL} = M_\beta(\dot{w} - uq + pv)$,
M_W	weight moment of the blade about the flapping hinge.

The first term derived is the aerodynamic moment M_A. At an azimuth station ψ, it is given by $M_A = \int_0^{R-e} dF_a r'$, where:

$$dF_A = \frac{\rho}{2}(\Omega R)^2 ac[\bar{U}_T^2\theta + \bar{U}_T\bar{U}_P]dr' \tag{2.13}$$

and

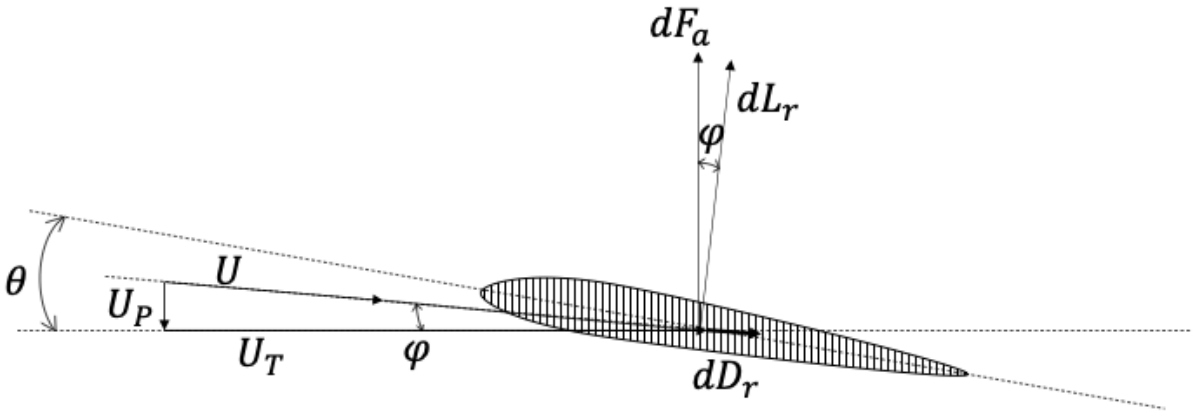

Figure 2.4: U_p and U_T velocity components on blade element

$$
\begin{aligned}
\bar{U}_T \triangleq \frac{U_T}{\Omega R} =& \epsilon(1-\cos\beta) + \mu\sin\psi + x\cos\beta \\
\bar{U}_P \triangleq \frac{U_P}{\Omega R} =& \lambda\cos\beta - \mu\sin\beta\cos\psi - \bar{\beta}(x-\epsilon) + x[(\frac{p}{\Omega}\cos\beta_w + \frac{q}{\Omega}\sin\beta_w)\sin\psi - \\
& (\frac{p}{\Omega}\sin\beta_w - \frac{q}{\Omega}\cos\beta_w)\cos\psi] \\
\mu \triangleq& \frac{V\cos\alpha}{\Omega R} \\
\lambda \triangleq& \frac{V\sin\alpha - v_i}{\Omega R} \\
x \triangleq& \frac{e+r'}{R} \\
\epsilon \triangleq& \frac{e}{R} \\
\bar{\beta} \triangleq& \frac{1}{\Omega}\dot{\beta} \\
\theta =& \theta_0 - A_{1c}\cos\psi - \beta_{1c}\sin\psi + x\theta_t - K_1\beta
\end{aligned}
$$

For small β:

$$
\begin{aligned}
\bar{U_T} =& x + \mu\sin\psi \\
\bar{U}_p =& \lambda - \mu\beta\cos\psi - \bar{\beta}(x-\epsilon) + x[\frac{p}{\Omega}\cos\beta_w + \frac{q}{\Omega}\sin\beta_w)\sin\psi - (\frac{p}{\Omega}\sin\beta_w - \frac{q}{\Omega}\cos\beta_w)\cos\psi]
\end{aligned}
$$

Figure 2.4 shows the perpendicular and the tangential velocity components.

M_A is found to be:

$$\begin{aligned}\frac{M_A}{\frac{\rho}{2}ac(\Omega R)^2R^2} =&[\frac{1}{4}(1-\epsilon^4)+\frac{1}{3}(1-\epsilon^3)(2\mu\sin\psi-\epsilon)+\frac{1}{2}(1-\epsilon^2)(\mu^2\sin^2\psi-2\mu\epsilon\sin\psi)-\\&(1-\epsilon)\mu^2\epsilon\sin^2\psi](\theta_0-A_{1c}\cos\psi-B_{1c}\sin\psi)+\\&[\frac{1}{5}(1-\epsilon^5)+\frac{1}{4}(1-\epsilon^4)(2\mu\sin\psi-\epsilon)+\frac{1}{3}(1-\epsilon^3)(\mu^2\sin^2\psi-2\mu\epsilon\sin\psi)-\\&\frac{1}{2}(1-\epsilon^2)\mu^2\epsilon\sin^2\psi]\theta_t+\\&[\frac{1}{3}(1-\epsilon^3)+\frac{1}{2}(1-\epsilon^2)(\mu\sin\psi-\epsilon)-(1-\epsilon)\epsilon\mu\sin\psi]\lambda-\\&\{[\frac{1}{4}(1-\epsilon^4)+\frac{1}{3}(1-\epsilon^3)(2\mu\sin\psi-\epsilon)+\frac{1}{2}(1-\epsilon^2)(\mu^2\sin^2\psi-2\mu\epsilon\sin\psi)-\\&(1-\epsilon)\mu^2\epsilon\sin^2\psi]K_1+[\frac{1}{3}(1-\epsilon^3)+\frac{1}{2}(1-\epsilon^2)(\mu\sin\psi-\epsilon)-(1-\epsilon)\mu\epsilon\sin\psi]\mu\cos\psi\}\beta\\&-[\frac{1}{4}(1-\epsilon^4)+\frac{1}{3}(1-\epsilon^3)(\mu\sin\psi-2\epsilon)-\frac{1}{2}(1-\epsilon^2)(2\mu\epsilon\sin\psi-\epsilon^2)+\\&(1-\epsilon)\mu\epsilon^2\sin\psi]\bar{\beta}+\\&[\frac{1}{4}(1-\epsilon^4)+\frac{1}{3}(1-\epsilon^3)(\mu\sin\psi-\epsilon)-\frac{\mu\epsilon}{2}(1-\epsilon^2)\sin\psi]\\&[(\frac{p}{\Omega}\cos\beta_w+\frac{q}{\Omega}\sin\beta_w)\sin\psi-(\frac{p}{\Omega}\sin\beta_w-\frac{q}{\Omega}\cos\beta_w)\cos\psi]\end{aligned} \tag{2.14}$$

Since $e << R$ and $\epsilon = \frac{e}{R}$, the terms containing $\epsilon^3, \epsilon^4, \ldots$ are neglected. The result is:

$$\begin{aligned}\frac{M_A}{\frac{\rho}{2}ac(\Omega R)^2R^2} =&[\frac{1}{4}-\frac{\epsilon}{3}+\mu\sin\psi(\frac{2}{3}-\epsilon+\frac{1}{2}\mu\sin\psi-\epsilon\mu\sin\psi+\\&\frac{1}{2}\mu\epsilon^2\sin\psi)](\theta_0-A_{1c}\cos\psi-B_{1c}\sin\psi)+\\&[\frac{1}{5}-\frac{\epsilon}{4}+\mu\sin\psi(\frac{1}{2}-\frac{2}{3}\epsilon+\frac{1}{3}\mu\sin\psi-\frac{1}{2}\mu\epsilon\sin\psi)]\theta_t+\\&[\frac{1}{3}-\frac{\epsilon}{2}+\mu\sin\psi(\frac{1}{2}-\epsilon+\frac{\epsilon^2}{2})]\lambda-\\&\{[\frac{1}{4}-\frac{\epsilon}{3}+\mu\sin\psi(\frac{2}{3}-\epsilon+\frac{\mu}{2}\sin\psi-\epsilon\mu\sin\psi+\frac{\epsilon^2}{2}\mu\sin\psi)]K_1+\\&[\frac{1}{3}-\frac{\epsilon}{2}+\mu\sin\psi(\frac{1}{2}-\epsilon+\frac{\epsilon^2}{2})]\mu\cos\psi\}\beta-\\&[\frac{1}{4}-\frac{2\epsilon}{3}+\frac{\epsilon^2}{2}+\mu\sin\psi(\frac{1}{3}-\epsilon+\epsilon^2)]\bar{\beta}+\\&[(\frac{1}{4}-\frac{\epsilon}{3})+\mu\sin\psi(\frac{1}{3}-\frac{\epsilon}{2})]\\&[(\frac{p}{\Omega}\cos\beta_w+\frac{q}{\Omega}\sin\beta_w)\sin\psi-(\frac{p}{\Omega}\sin\beta_w-\frac{q}{\Omega}\cos\beta_w)\cos\psi]\end{aligned} \tag{2.15}$$

Substituting all the moments in equation (2.12), the flapping equation is obtained:

$$\begin{aligned}
&\ddot{\beta}+\frac{\Omega\gamma}{2}[\frac{1}{4}-\frac{2}{3}\epsilon+\frac{\epsilon^2}{2}+\mu(\frac{1}{3}-\epsilon+\epsilon^2)\sin\psi]\dot{\beta}+([\frac{K_\beta}{I_\beta}+(1+\frac{eM_\beta}{I_\beta})\Omega^2]+\\
&\frac{\Omega^2\gamma}{2}\{[\frac{1}{4}-\frac{\epsilon}{3}+\mu(\frac{2}{3}-\epsilon+\frac{\mu}{2}\sin\psi-\epsilon\mu\sin\psi+\\
&\frac{\epsilon^2}{2}\mu\sin\psi)\sin\psi]K_1+[\frac{1}{3}-\frac{\epsilon}{2}+\mu(\frac{1}{2}-\epsilon+\frac{\epsilon^2}{2})\sin\psi]\mu\cos\psi\})\beta=\\
&2(1+\frac{eM_\beta}{I_\beta})(p\Omega\cos\psi'-q\Omega\sin\psi')+(\dot{p}\sin\psi'+\dot{q}\cos\psi')+\frac{M_\beta}{I_\beta}(\dot{w}-uq+pv)-\frac{M_w}{I_\beta}+\\
&\frac{\Omega^2\gamma}{2}\{[\frac{1}{4}-\frac{\epsilon}{3}+\mu\sin\psi(\frac{2}{3}-\epsilon+\frac{1}{2}\mu\sin\psi-\epsilon\mu\sin\psi+\frac{1}{2}\mu\epsilon^2\sin\psi)](\theta_0-A_{1c}\cos\psi-B_{1c}\sin\psi)+\\
&[\frac{1}{5}-\frac{\epsilon}{4}+\mu(\frac{1}{2}-\frac{2}{3}\epsilon+\frac{1}{3}\mu\sin\psi-\frac{1}{2}\mu\epsilon\sin\psi)\sin\psi]\theta_t+[\frac{1}{3}-\frac{1}{2}\epsilon+\mu(\frac{1}{2}-\epsilon+\frac{1}{2}\epsilon^2)\sin\psi]\lambda\}+\\
&\frac{\gamma}{2}(\frac{1}{4}-\frac{\epsilon}{3})[(p\Omega\cos\beta_w+q\Omega\sin\beta_w)\sin\psi-(p\Omega\sin\beta_w-q\Omega\cos\beta_w)\cos\psi]+\\
&\frac{\gamma}{8}\mu(\frac{2}{3}-\epsilon)[(p\Omega\cos\beta_w+q\Omega\sin\beta_w)(1-\cos2\psi)-(p\Omega\sin\beta_w-q\Omega\cos\beta_w)\sin2\psi]
\end{aligned} \tag{2.16}$$

By defining $\bar{\beta}\triangleq\frac{1}{\Omega}\dot{\beta}=\frac{d\beta}{d\psi}$; $\bar{\bar{\beta}}\triangleq\frac{1}{\Omega^2}\ddot{\beta}=\frac{d^2\beta}{d\psi^2}$, it's possible to rewrite equation (2.16). In addition, let's consider a two-bladed teetering rotor with the following constraints: $\epsilon=0$; $\beta_2=-\beta_1$; $\psi_2=\psi_1+\pi$; $\dot{\beta}_2=-\dot{\beta}_1$ and $\ddot{\beta}_2=-\ddot{\beta}_1$. The result is:

$$\begin{aligned}
&\ddot{\beta}+\frac{\Omega\gamma}{8}\dot{\beta}+\Omega^2[P^2+\frac{\gamma\mu^2}{8}\sin2\psi+\frac{\gamma K_1\mu^2}{8}(1-\cos2\psi)]\beta=\\
&\Omega^2\{(\frac{\gamma}{8}\frac{p_w}{\Omega}-2\frac{q_w}{\Omega}+\frac{\dot{p_w}}{\Omega^2})\sin\psi+(\frac{\gamma}{8}\frac{q_w}{\Omega}+2\frac{p_w}{\Omega}+\frac{\dot{q_w}}{\Omega^2})\cos\psi+\\
&\qquad(\frac{\gamma\mu}{3}\sin\psi)\theta_0-\frac{\gamma}{8}[(1+\frac{\mu^2}{2})\cos\psi-\frac{\mu^2}{2}\cos3\psi]A_{1c}-\\
&\qquad\frac{\gamma}{8}[(1+\frac{3\mu^2}{2})\sin\psi-\frac{\mu^2}{2}\sin3\psi]B_{1c}+\frac{\gamma\mu}{4}[\theta_t+\lambda]\sin\psi\}
\end{aligned} \tag{2.17}$$

where $P^2=1+\frac{K_\beta}{I_\beta\Omega^2}+\frac{K_1\gamma}{8}$ and $p_w=p\cos\beta_w+q\sin\beta_w$, $q_w=-p\sin\beta_w+q\cos\beta_w$.

Equation (2.16) is transformed into a non-rotating coordinate system using the multi-bladed coordinate transformation with the aim to gain a better insight into the dynamics of the flapping motion:

$$\beta_i = \beta_0 + \beta_d(-1)^i + \sum_{n=1}^{k} \beta_{nc}\cos n\psi_i + \beta_{ns}\sin n\psi_i \qquad i = 1, 2, 3, ..., N \tag{2.18}$$

where

$$k = \frac{1}{2}(N-1) \quad Nodd$$
$$= \frac{1}{2}(N-2) \quad Neven$$

$$\beta_0 = \frac{1}{N}\sum_{i=1}^{N}\beta_i$$

$$\beta_d = \frac{1}{N}\sum_{i=1}^{N}\beta_i(-1)^i \quad (\beta_d = 0, if Nodd)$$

$$\beta_{nc} = \frac{2}{N}\sum_{i=1}^{N}\beta_i\cos n\psi_i$$

$$\beta_{ns} = \frac{2}{N}\sum_{i=1}^{N}\beta_i\sin n\psi_i$$

$$\psi_i = \psi + \frac{2\pi}{N}(i-1)$$

Let $\bar{\beta_R}$ and $\bar{\beta}$ be:

$$\begin{aligned}
\bar{\beta_R} &\triangleq (\beta_1, \beta_2, \ldots, \beta_N)^T \\
\bar{\beta} &\triangleq (\beta_0, \beta_{1c}, \beta_{1s}, \beta_{2c}, \beta_{2s}, \ldots, \beta_{\frac{1}{2}(N-1)c}, \beta_{\frac{1}{2}(N-1)s})^T \qquad for \quad N \quad odd \\
&\triangleq (\beta_0, \beta_{1c}, \beta_{1s}, \ldots, \beta_{\frac{1}{2}(N-1)c}, \beta_{\frac{1}{2}(N-1)s}, \beta_d)^T \qquad for \quad N \quad even
\end{aligned}$$

The transformation equation (2.18) may be written:

$$\bar{\beta_R} = T\bar{\beta} \tag{2.19}$$

where T, for N odd, is equal to:

$$T = \begin{bmatrix} 1 & \cos\psi_1 & \sin\psi_1 & \dots & \cos\frac{1}{2}(N-1)\psi_1 & \sin\frac{1}{2}(N-1)\psi_1 \\ 1 & \cos\psi_2 & \sin\psi_2 & \dots & \cos\frac{1}{2}(N-1)\psi_2 & \sin\frac{1}{2}(N-1)\psi_2 \\ . & . & . & \dots & . & . \\ . & . & . & \dots & . & . \\ 1 & \cos\psi_i & \sin\psi_i & \dots & \cos\frac{1}{2}(N-1)\psi_i & \sin\frac{1}{2}(N-1)\psi_i \\ . & . & . & \dots & . & . \\ . & . & . & \dots & . & . \\ 1 & \cos\psi_N & \sin\psi_N & \dots & \cos\frac{1}{2}(N-1)\psi_N & \sin\frac{1}{2}(N-1)\psi_N \end{bmatrix}$$

and for N even is:

$$T = \begin{bmatrix} 1 & \cos\psi_1 & \sin\psi_1 & \dots & \cos\frac{1}{2}(N-2)\psi_1 & \sin\frac{1}{2}(N-2)\psi_1 & (-1)^1 \\ 1 & \cos\psi_2 & \sin\psi_2 & \dots & \cos\frac{1}{2}(N-1)\psi_2 & \sin\frac{1}{2}(N-1)\psi_2 & (-1)^2 \\ . & . & . & \dots & . & . & . \\ . & . & . & \dots & . & . & . \\ 1 & \cos\psi_i & \sin\psi_i & \dots & \cos\frac{1}{2}(N-1)\psi_i & \sin\frac{1}{2}(N-1)\psi_i & (-1)^i \\ . & . & . & \dots & . & . & . \\ . & . & . & \dots & . & . & . \\ 1 & \cos\psi_N & \sin\psi_N & \dots & \cos\frac{1}{2}(N-1)\psi_N & \sin\frac{1}{2}(N-1)\psi_N & (-1)^N \end{bmatrix}$$

where $\psi_i = \psi + \frac{2\Pi}{N}(i-1), \quad i = 1, 2, 3, \dots, N.$

Now, a matrix-vector format can be used to rewrite the flapping equation (2.12):

$$\ddot{\bar{\beta}}_R + A(\psi)\dot{\bar{\beta}}_R = \bar{f}_R \tag{2.20}$$

where $A(\psi) = \begin{bmatrix} A_{11} & & & \\ & . & & 0 \\ & & A_{ii} & \\ & 0 & & . \\ & & & A_{NN} \end{bmatrix}$, $B(\psi) = \begin{bmatrix} B_{11} & & & \\ & . & & 0 \\ & & B_{ii} & \\ & 0 & & . \\ & & & B_{NN} \end{bmatrix}$,

$\bar{f}_R \triangleq (f_1, f_2, \dots, f_i, \dots, f_N)^T$, $A_{ii} \triangleq \frac{\gamma\Omega}{2}[(\frac{1}{4} - \frac{2}{3}\epsilon + \frac{\epsilon^2}{2}) + \mu(\frac{1}{3} - \epsilon + \epsilon^2)\sin\psi_i]$ and
$B_{ii} \triangleq \Omega^2(P^2 + \frac{\gamma}{2}[\mu(\frac{1}{3} - \frac{\epsilon}{2})\cos\psi_i + \frac{\mu^2}{2}(\frac{1}{2} - \epsilon + \frac{\epsilon^2}{2})\sin 2\psi_i] + \frac{\gamma K_1}{2}[\mu(\frac{2}{3} - \epsilon)\sin\psi_i + \frac{\mu^2}{2}(\frac{1}{2} - \epsilon + \frac{\epsilon^2}{2})(1 - \cos 2\psi_i)])$, where $f_i \triangleq$ *right-hand side of equation (2.16).*
The flapping equation (2.20) using the transformation (2.19) may be written with respect to the non-rotating coordinate system:

$$\ddot{\bar{\beta}} + \dot{\bar{\beta}} + K\bar{\beta} = \bar{f} \tag{2.21}$$

where

$$\bar{f} = T^{-1}\bar{f}_R$$
$$D = T^{-1}(2\dot{T} + AT)$$
$$K = T^{-1}(\ddot{T} + A\dot{T} + BT)$$

In order to simplify the calculation of the inverse of T, a proper scaling of variable $\bar{\beta}$ may be made so that:

$$\bar{\beta} = T_S\bar{\beta}_I \tag{2.22}$$

where

$$T_S = \begin{cases} \begin{bmatrix} \frac{1}{\sqrt{N}} & \dots & & 0 \\ 0 & \sqrt{\frac{2}{N}} & \dots & 0 \\ 0 & 0 & . & 0 \\ 0 & 0 & \dots & \sqrt{\frac{2}{N}} \end{bmatrix} & for N odd \\ \begin{bmatrix} \frac{1}{\sqrt{N}} & \dots & \dots & & 0 & \\ 0 & \sqrt{\frac{2}{N}} & \dots & & 0 & \\ 0 & 0 & \dots & . & 0 & 0 \\ 0 & 0 & \dots & \sqrt{\frac{2}{N}} & 0 & \\ 0 & 0 & \dots & 0 & \frac{1}{\sqrt{N}} & \end{bmatrix} & for N even \end{cases}$$

The resulting transformation is orthogonal: $T_I = TT_S$.
Since $T^{-1} = T_S I_I^{-1} = T_S^2 T'$, the desired simplification is achieved.
The flapping equation in the non-rotating coordinate system for three-bladed and four-bladed rotor systems are shown respectively in tables 1 and 2 at pages $34 - 37$ of Chen report [70]. The following observation may be made:

1. Periodic coefficients in forward flight are contained in the flapping equations considering non-rotating coordinates. The basic frequency of the periodicity is directly related to the number of blades of the rotor. For the four-bladed rotor it is 2 and for the three-bladed one it is 3. The basic frequency for odd-bladed rotors is the number of blades itself, for even-bladed rotors it is the half of the number of blades. It can be shown as in [71]. The highest frequency in the periodic terms is N per rev for an N-bladed rotor.

2. The amplitudes of the periodic terms are function of γ, μ and ϵ, that are independent of K_β and K_1. At given advance ratio, the lower the Lock number γ and the larger

the hinge offset ϵ, the smaller the amplitudes of the periodic terms in the damping matrix.

3. The maximum magnitude of the periodic coefficients in the stiffness matrix are functions of γ, ϵ and K_1. The hinge restraint has no direct impact on the periodic terms. At a given advance ratio, a decrease in γ will decrease the amplitude of the periodic terms, however the combined effect of ϵ and K_1 is more complicated. The effect of periodic terms is reduced by an increase in ϵ for $K_1 = 0$.

4. The parametric effect on the periodic terms in the forcing functions is similar to that on the damping terms for a given set of control positions and for the twist of the blade.

These observations may contribute to better understand the the quality of approximation when the time varying equations are simplified to time invariant system of equations by dropping the periodic terms in forward flight. At $\mu = 0$ there is no periodic terms. Dropping the periodic terms, the first three equations in Table 2 of reference [70] (pag.36 − 37) for $N = 4$ collapse to those for $N = 3$. The differential equation for coning (the fourth one) becomes uncoupled and with the forcing function equal to zero. The set of the first three equations is identical to the first-harmonic approximation also known as the "tip-path-plane" equation.

Tip-path plane dynamics The procedure discussed in the previous section is identical to the classical method of approximating the flapping by the first-harmonic terms with time varying coefficients, that is:

$$\beta(t) = a_0(t) - a_1(t)\cos\psi - b_1(t)\sin\psi \tag{2.23}$$

The tip-path plane dynamic equation is achieved relating the constant term and the terms with $\sin\psi$ and $\cos\psi$ in the equation (2.12) using (2.23):

$$\ddot{\bar{a}} + \tilde{D}\dot{\bar{a}} + \tilde{K}\bar{a} = \tilde{\bar{f}} \tag{2.24}$$

Respectively, $\tilde{D}$ is the damping matrix, $\tilde{K}$ is the stiffness matrix and $\tilde{\bar{f}}$ is the forcing function, whose expressions are reported in Appendix A in chapterA. Note that: $a_0 = \beta_0$, $a_1 = -\beta_{1c}$ and $b_1 = -\beta_{1s}$. It's possible to approximate the flapping equation for the teetering rotor with the "tip-path plane" procedure; so equation (2.17) becomes:

$$\begin{bmatrix}\ddot{a}_1\\ \ddot{b}_1\end{bmatrix}+\Omega\begin{bmatrix}\frac{\gamma}{8} & 2\\ -2 & \frac{\gamma}{8}\end{bmatrix}\begin{bmatrix}\dot{a}_1\\ \dot{b}_1\end{bmatrix}+\Omega^2\begin{bmatrix}P^2-1+\frac{\gamma K_1\mu^2}{16} & \frac{\gamma}{8}(1+\frac{\mu^2}{2})\\ -\frac{\gamma}{8}(1-\frac{\mu^2}{2}) & P^2-1+\frac{3\gamma K_1\mu^2}{16}\end{bmatrix}\begin{bmatrix}a_1\\ b_1\end{bmatrix}=$$
$$\Omega^2\begin{bmatrix}0 & 0 & \frac{\gamma}{8}(1+\frac{\mu^2}{2}) & 0\\ -\frac{\gamma\mu}{3} & -\frac{\gamma\mu}{4} & 0 & \frac{\gamma}{8}(1+\frac{3\mu^2}{2})\end{bmatrix}\begin{bmatrix}\theta_0\\ \theta_t\\ A_{1c}\\ B_{1c}\end{bmatrix}+\Omega^2\begin{bmatrix}0\\ -\frac{\gamma\mu}{4}\end{bmatrix}\lambda+$$
$$\Omega\begin{bmatrix}-2 & -\frac{\gamma}{8} & 0 & -\frac{1}{\Omega}\\ -\frac{\gamma}{8} & 2 & -\frac{1}{\Omega} & 0\end{bmatrix}\begin{bmatrix}p_w\\ q_w\\ \dot{p_w}\\ \dot{q_w}\end{bmatrix} \tag{2.25}$$

where $P^2=1+\frac{K_\beta}{I_\beta\Omega^2}+\frac{\gamma K_1}{8}$ and

$$\beta(t)=a_0-a_1(t)\cos\psi-b_1(t)\sin\psi \tag{2.26}$$

For a two-bladed rotor, the tip-path plane approximation is mostly valid for only low frequency excitation ($\dot{p}$ and $\dot{q}$ may be neglected). In the flapping equation (2.23) the coning is constant and it is referred as precone angle. In the tip-path plane dynamics there are three natural modes: coning, advancing ad regressing. Regressing mode is the most important with regards to the effect of rotor dynamics on handling characteristics. It is the mode with the lowest frequency; it usually couples with fuselage modes. The others have higher undamped natural frequencies: on the order of rotating frequency for the coning mode and twice the rotating frequency for the advancing one. These are usually less significant on handling quality influence. Let's analyze the effects of the parametric variations in general rotor system on the modal characteristics, starting from the hovering. Coning equation is decoupled as in table A.1. This mode presents an undamped natural frequency ω_{nc} , here illustrated with the damping ratio ζ_c:

$$\begin{cases}\frac{\omega_{nc}}{\Omega}=P\triangleq[1+\frac{K_\beta}{I_\beta\Omega^2}+\frac{eM_\beta}{I_\beta}+\frac{\gamma K_1}{8}(1-\frac{4}{3}\epsilon)]^{\frac{1}{2}}\\ \zeta_c=\zeta\triangleq\frac{\gamma}{16P}(1-\frac{8}{3}\epsilon+2\epsilon^2)\end{cases} \tag{2.27}$$

For the advancing and regressing modes the undamped natural frequencies and the damping ratio are given by:

$$\begin{cases}\frac{\omega_{nA}}{\Omega}=(1+P^2+2P\sqrt{1-\zeta^2})^{\frac{1}{2}}\\ \zeta_A=\frac{\zeta}{\frac{\omega_{nA}}{\Omega}}\end{cases} \tag{2.28}$$

$$\begin{cases} \frac{\omega_{nR}}{\Omega} = (1 + P^2 - 2P\sqrt{1-\zeta^2})^{\frac{1}{2}} \\ \zeta_R = \frac{\zeta}{\frac{\omega_{nR}}{\Omega}} \end{cases} \tag{2.29}$$

In forward flight the modal characteristics of the tip-path plane dynamics are much more complicated the coning equation is no longer decoupled. Flapping frequency is generally different from rotational one of the rotor system, clear from equation (2.24). The maximum flapping response to a cyclic-control will no longer exhibit 90 deg lag in phase. It's necessary to have a proper control phasing or mixing to achieve the desired flapping decoupling: a longitudinal control input that produces only a steady-state longitudinal flapping and a lateral control input that produces only lateral flapping response. Consider first the steady-state solution of tip-path plane variables at hover in order to link the required control phasing/mixing to the rotor system parameters. From equation (2.24), these responses may be obtained using:

$$\bar{a}_{s.s.} = \tilde{K}^{-1}\bar{\bar{f}} \tag{2.30}$$

Expanding the previous equation at hover, dropping terms containing fuselage angular acceleration $\dot{p}$ and $\dot{q}$:

$$a_{0_{s.s.}} = \frac{1}{P^2}[\frac{-gM_\beta}{I_\beta\Omega^2} + \frac{\gamma}{2}[(\frac{1}{4} - \frac{\epsilon}{3})\theta_0 + (\frac{1}{5} - \frac{\epsilon}{4})\theta_t + (\frac{1}{3} - \frac{\epsilon}{2})\lambda]] \tag{2.31}$$

$$\begin{aligned} a_{1_{s.s.}} =& \frac{1}{\Delta}[\gamma(\frac{1}{8} - \frac{\epsilon}{6})[(P^2-1)(A_{1c} - \frac{q_w}{\Omega}) - \gamma(\frac{1}{8} - \frac{\epsilon}{3} + \frac{\epsilon^2}{4})(B_{1c} - \frac{p_w}{\Omega})] - \\ & 2(1 + \frac{eM_\beta}{I_\beta})[(P^2-1)\frac{p_w}{\Omega} + \gamma(\frac{1}{8} - \frac{\epsilon}{3} + \frac{\epsilon^2}{4})\frac{q_w}{\Omega}]] \end{aligned} \tag{2.32}$$

$$\begin{aligned} b_{1_{s.s.}} =& \frac{1}{\Delta}[\gamma(\frac{1}{8} - \frac{\epsilon}{6})[(A_{1c} - \frac{q_w}{\Omega})\gamma(\frac{1}{8} - \frac{\epsilon}{3} + \frac{\epsilon^2}{4}) + (P^2-1)(B_{1c} - \frac{p_w}{\Omega})] - \\ & 2(1 + \frac{eM_\beta}{I_\beta})[-(P^2-1)\frac{q_w}{\Omega} + \gamma(\frac{1}{8} - \frac{\epsilon}{3} + \frac{\epsilon^2}{4})\frac{p_w}{\Omega}]] \end{aligned} \tag{2.33}$$

where $\Delta = (P^2-1)^2 + \gamma^2(\frac{1}{8} - \frac{\epsilon}{3} + \frac{\epsilon^2}{4})^2$ and $P^2 = 1 + \frac{K_\beta}{I_\beta\Omega^2} + \frac{eM_\beta}{I_\beta} + \frac{\gamma K_1}{8}(1 - \frac{4}{3}\epsilon)$.
For the case $P^2 = 1, \epsilon = 0$, the steady-state response of longitudinal and lateral flapping to the cyclic-control inputs become:
$a_{1_{s.s.}} = -B_{1c}$
$b_{1_{s.s.}} = A_{1c}$

Main rotor thrust

The procedure to obtain the thrust equation is given. The same procedure will be applied for the others main rotor forces and moments, thus only for the thrust case the complete procedure is illustrated. The hub-wind system is used, then it is transformed into the hub-body system. The shear force for a single i^{th} blade at azimuth ψ_i is given by:

$$\begin{aligned} S(\psi_i) =& F_a - \ddot{\beta} M_\beta - mq + m(\dot{w} - uq + pv) \\ &+ [2p\Omega(\frac{M_\beta}{g} + em) + \frac{M_\beta}{g}\dot{q}] \cos\psi_i' \\ &+ [-2q\Omega(\frac{M_\beta}{g} + em) + \frac{M_\beta}{g}\dot{p}] \sin\psi_i' \end{aligned} \tag{2.34}$$

where F_a, the aerodynamic force, is given by:

$$F_a = \int_0^{R-e} \frac{\rho}{2}(\Omega R)^2 ac(\bar{U}_T^2\theta + \bar{U}_T\bar{U}_P)\, dr' \tag{2.35}$$

Let's substitute the following equations in equation 2.35:

$$\bar{U}_T = \frac{U_T}{\Omega R} = \epsilon(1 - \cos\beta) + \mu\sin\psi + x\cos\beta \tag{2.36}$$

$$\begin{aligned} \bar{U}_P = \frac{U_P}{\Omega R} =& \lambda\cos\beta - \mu\sin\beta\cos\psi - \frac{\dot{\beta}}{\Omega}(x - \epsilon) \\ &+ x[(\frac{p}{\Omega}\cos\beta_w + \frac{q}{\Omega}\sin\beta_w)\sin\psi + (-\frac{p}{\Omega}\sin\beta_w + \frac{q}{\Omega}\cos\beta_w)\cos\psi] \end{aligned} \tag{2.37}$$

$$\theta = \theta_0 - A_{1c}\cos\psi - B_{1c}\sin\psi + x\theta_t - K_1\beta \tag{2.38}$$

So F_a results:

$$\begin{aligned} F_a =& \frac{\rho}{2}(\Omega R)^2 acR\{[\frac{1}{3} + (1-\epsilon)(1+\epsilon+\mu\sin\psi)\mu\sin\psi](\theta_0 - A_{1c}\cos\psi - B_{1c}\sin\psi) \\ &+ [\frac{1}{4} + (\frac{2}{3} + \frac{1}{2}1 - \epsilon^2\mu\sin\psi)\mu\sin\psi]\theta_t + [\frac{1}{2}(1-\epsilon^2) + (1-\epsilon)\mu\sin\psi]\lambda \\ &- \{[\frac{1}{3} + (1-\epsilon)(1+\epsilon+\mu\sin\psi)\mu\sin\psi]K_1 \\ &+ [\frac{1}{2}(1-\epsilon^2) + (1-\epsilon)\mu\sin\psi]\mu\cos\psi\}\beta - \frac{1}{\Omega}[\frac{1}{3} - \frac{\epsilon}{2} + \frac{\mu}{2}(1-\epsilon)^2\sin\psi]\dot{\beta} \\ &+ [\frac{1}{3} + \frac{\mu}{2}(1-\epsilon^2)\sin\psi][(\frac{p}{\Omega}\cos\beta_w + \frac{q}{\Omega}\sin\beta_w)\sin\psi + (-\frac{p}{\Omega}\sin\beta_w + \frac{q}{\Omega}\cos\beta_w)\cos\psi]\} \end{aligned} \tag{2.39}$$

The flapping is approximated by equation (2.23), so:

$$\dot{\beta} = \dot{a}_0 - (\dot{a}_1 + b_1\Omega)\cos\psi - (\dot{b}_1 - a_1\Omega)\sin\psi \tag{2.40}$$

$$\ddot{\beta} = \ddot{a}_1 - (\ddot{a}_1 + 2\dot{b}_1\Omega - a_1\Omega^2)\cos\psi - (\ddot{b}_1 - 2\dot{a}_1\Omega - b_1\Omega)\sin\psi \tag{2.41}$$

Noting that:

$$\sum_{i=1}^{N}\sin\psi_i = \sum_{i=1}^{N}\sin\psi_i' = 0$$

$$\sum_{i=1}^{N}\cos\psi_i = \sum_{i=1}^{N}\cos\psi_i' = 0$$

the thrust becomes:

$$T = \sum_{i=1}^{N} F_a(\psi_i) - N[\ddot{a}_0 M_\beta + mg - m(\dot{w} - uq + pv)] \tag{2.42}$$

Let's note that the first term of the right-hand side of equation (2.42) is a function of N, number of blades. For $N = 3$ and 4, T assumes the following expression:

$$\begin{aligned}\frac{1}{0.5\rho acR(\Omega R)^2}\sum_{i=1}^{N} F_a(\psi_i) =& N[\frac{\theta_0}{3} + \frac{\theta_t}{4} + \frac{1}{2}(1-\epsilon^2)\lambda - \frac{K_1 a_0}{3} - \frac{\dot{a}_0}{\Omega}(\frac{1}{3} - \frac{\epsilon}{2})] \\ &+ \frac{N}{2}\{\mu^2(1-\epsilon)\theta_0 + \frac{\mu^2}{2}(1-\epsilon^2)\theta_t - \mu(1-\epsilon^2)B_{1c} \\ &- [a_0\mu^2(1-\epsilon) - b_1\mu(1-\epsilon^2)]K_1 + \frac{a_1}{2}\mu(1-\epsilon^2) \\ &+ \frac{1}{\Omega}(\dot{b}_1 - a_1\Omega)\frac{\mu}{2}(1-\epsilon)^2 \\ &+ \frac{\mu}{2}(1-\epsilon^2)(\frac{p}{\Omega}\cos\beta_w + \frac{q}{\Omega}\sin\beta_w)\} + O(N)\end{aligned} \tag{2.43}$$

where:

$$\begin{aligned}O(4) &= 0 \quad \text{(for four-bladded rotor)} \\ O(3) &= \frac{3}{4}[\mu^2(1-\epsilon)B_{1c} - b_1\mu^2(1-\epsilon)K_1 + a_1\mu^2(1-\epsilon)]\sin 3\psi \\ &\quad + \frac{3}{4}[\mu^2(1-\epsilon)A_{1c} - (a_1K_1 + b_1)\mu^2(1-\epsilon)]\cos 3\psi \quad \text{(for three-bladed rotor)}\end{aligned}$$

In this way, the thrust equation becomes:

$$\begin{aligned}T =&\frac{N}{2}\rho acR(\Omega R)^2\{\frac{1}{2}(1-\epsilon^2)\lambda+[\frac{1}{3}+\frac{\mu^2}{2}(1-\epsilon)]\theta_0+[\frac{1}{4}+\frac{\mu^2}{4}(1-\epsilon^2)]\theta_t\\&-\frac{\mu}{2}(1-\epsilon^2)B_{1c}-a_0[\frac{1}{3}+\frac{\mu^2}{2}(1-\epsilon)]K_1+a_1[\frac{\mu}{2}\epsilon(1-\epsilon)]\\&+b_1[\frac{\mu}{2}(1-\epsilon^2)K_1]-\frac{\dot{a}_0}{\Omega}(\frac{1}{3}-\frac{\epsilon}{2})+\frac{\dot{b}_1}{\Omega}[\frac{\mu}{4}(1-\epsilon)^2]\\&+\frac{\mu}{4}(1-\epsilon^2)(\frac{p}{\Omega}\cos\beta_w+\frac{q}{\Omega}\sin\beta_w)+\frac{O(N)}{N}\}-N[\ddot{a}_0M_\beta+mg-m(\dot{w}-uq+pv)]\end{aligned} \tag{2.44}$$

where

$$\begin{cases}O(4)=0 \qquad \text{for N=4}\\ O(3)=\frac{3}{4}[\mu^2(1-\epsilon)B_{1c}-b_1\mu^2(1-\epsilon)K_1+a_1\mu^2(1-\epsilon)]\sin\psi\\ \qquad\quad+\frac{3}{4}[\mu^2(1-\epsilon)A_{1c}-\mu^2(1-\epsilon)(a_1K_1+b_1)]\cos 3\psi\\ \qquad\qquad \text{for N=3}\end{cases} \tag{2.45}$$

By dropping the high harmonic contributions, the thrust can now be expressed as:

$$\begin{aligned}T =&\frac{N}{2}\rho acR(\Omega R)^2\{\frac{1}{2}(1-\epsilon^2)\lambda+[\frac{1}{3}+\frac{\mu^2}{2}(1-\epsilon)]\theta_0+[\frac{1}{4}+\frac{\mu^2}{4}(1-\epsilon^2)]\theta_t\\&-\frac{\mu}{2}(1-\epsilon^2)(B_{1c}-K_1b_1)-a_0[\frac{1}{3}+\frac{\mu^2}{2}(1-\epsilon)]K_1+a_1[\frac{\mu}{2}\epsilon(1-\epsilon)]\\&-\frac{\dot{a}_0}{\Omega}(\frac{1}{3}-\frac{\epsilon}{2})+\frac{\dot{b}_1}{\Omega}[\frac{\mu}{4}(1-\epsilon)^2]+\frac{\mu}{4}(1-\epsilon^2)(\frac{p}{\Omega}\cos\beta_w+\frac{q}{\Omega}\sin\beta_w)\}\\&-N[\ddot{a}_0M_\beta+mg-m(\dot{w}-uq+pv)]\end{aligned} \tag{2.46}$$

Usually the last two terms, $mg-m(\dot{w}-uq+pv)$, are small compared to the others, so they are dropped and T finally results:

$$\begin{aligned}T =&\frac{N}{2}\rho acR(\Omega R)^2\{\frac{1}{2}(1-\epsilon^2)\lambda+[\frac{1}{3}+\frac{\mu^2}{2}(1-\epsilon)]\theta_0+[\frac{1}{4}+\frac{\mu^2}{4}(1-\epsilon^2)]\theta_t\\&-\frac{\mu}{2}(1-\epsilon^2)(B_{1c}-K_1b_1)-a_=[\frac{1}{3}+\frac{\mu^2}{2}(1-\epsilon)]K_1+a_1[\frac{\mu}{2}\epsilon(1-\epsilon)]\\&-\frac{\dot{a}_0}{\Omega}(\frac{1}{3}-\frac{\epsilon}{2})+\frac{\dot{b}_1}{\Omega}[\frac{\mu}{4}(1-\epsilon)^2]+\frac{\mu}{4}(1-\epsilon^2)(\frac{p}{\Omega}\cos\beta_w+\frac{q}{\Omega}\sin\beta_w)\}\\&-N\ddot{a}_0M_\beta\end{aligned} \tag{2.47}$$

In the computation of thrust the rotor inflow is required. There are two main categories of inflow models: static and dynamic. The Pitt-Peters dynamic inflow model [69] has been

used, only considering a uniform inflow. The induced uniform inflow model implemented is assumed to be, in the wind-hub reference frame:

$$\frac{d}{dt} = \begin{pmatrix} \lambda_0 \\ \lambda_s \\ \lambda_c \end{pmatrix} = \Omega \mathbb{M}^{-1} (-(\mathbb{L}_1 \mathbb{L}_2)^{-1} \begin{pmatrix} \lambda_0 \\ \lambda_s \\ \lambda_c \end{pmatrix} + \boldsymbol{C}_{aero}) \tag{2.48}$$

with $\lambda_s = \lambda_c = 0$ to account only for the uniform inflow (λ_0). $\boldsymbol{C}_{aero}$, $\mathbb{M}$, $\mathbb{L}_1, \mathbb{L}_2$ expressions are fully reported in [69]. The total inflow through the rotor λ, is given by:

$$\lambda = \frac{w_H}{\Omega R} - \lambda_0 \tag{2.49}$$

The expression of rotor-induced velocity at the disk, required in the calculation, is:

$$v_i = (\frac{w_H}{\Omega R} - \lambda)\Omega R \tag{2.50}$$

Main rotor horizontal and lateral forces The expressions for rotor H and Y forces in the hub-body system are:

$$H_w = \frac{N}{2} \rho a c R (\Omega R)^2 \frac{a C_H}{a\sigma} \tag{2.51}$$

$$Y_w = \frac{N}{2} \rho a c R (\Omega R)^2 \frac{2 C_Y}{a\sigma} \tag{2.52}$$

where

$$\frac{2C_H}{a\sigma} = (\frac{2C_H}{a\sigma})_w \cos\beta_w + (\frac{2C_Y}{a\sigma})_w \sin\beta_w \tag{2.53}$$

$$\frac{2C_Y}{a\sigma} = -(\frac{2C_H}{a\sigma})_w \sin\beta_w + (\frac{2C_Y}{a\sigma})_w \cos\beta_w \tag{2.54}$$

where $(\frac{2C_H}{a\sigma})_w$ and $(\frac{2C_Y}{a\sigma})_w$ in the wind-hub system are:

$$
\begin{aligned}
(\frac{2C_H}{a\sigma})_w =& \frac{\delta\mu}{a\sigma}(1-\epsilon^2) - \frac{1}{4}(\theta_0 - K_1 a_0)[2\lambda\mu(1-\epsilon) - \mu(1-\epsilon)^2\frac{\dot{a}_0}{\Omega} \\
& - (\epsilon - \frac{2}{3})(\frac{\dot{b}_1}{\Omega} - a_1) - \frac{2}{3}a_1 + \frac{2}{3}(\frac{p}{\Omega}\cos\beta_w + \frac{q}{\Omega}\sin\beta_w)] \\
& - \frac{\theta_t}{4}[\mu\lambda(1-\epsilon^2) + \frac{\dot{a}_0}{\Omega}\mu(\epsilon - \frac{2}{3}) - 2(\frac{\epsilon}{3} - \frac{1}{4})(\frac{\dot{b}_1}{\Omega} - a_1) - \frac{a_1}{2} \\
& + \frac{1}{2}(\frac{p}{\Omega}\cos\beta_w + \frac{q}{\Omega}\sin\beta_w)] + \frac{1}{4}(A_{1c} - K_1 a_1)[-\frac{b_1\mu}{4}(1-\epsilon^2) \\
& + \frac{1}{4}\mu(1-\epsilon)^2(\frac{\dot{a}_1}{\Omega} + b_1) + \frac{2}{3}a_0 + \frac{\mu}{4}(1-\epsilon^2)(-\frac{p}{\Omega}\sin\beta_w + \frac{q}{\Omega}\cos\beta_w)] \\
& + \frac{1}{4}(B_{1c} - K_1 b_1)[\frac{3}{4}\mu(1-\epsilon)^2(\frac{\dot{b}_1}{\Omega} - a_1) + (1-\epsilon^2)(\lambda - \frac{a_1\mu}{4}) + (\epsilon - \frac{2}{3})\frac{\dot{a}_0}{\Omega} \\
& + \frac{3\mu}{4}(1-\epsilon^2)(\frac{p}{\Omega}\cos\beta_w + \frac{q}{\Omega}\sin\beta_w)] + \frac{1}{4}\{\epsilon(1-\epsilon)(\frac{\dot{b}_1}{\Omega} - a_1)4\lambda \\
& - (1-\epsilon^2)[2\lambda(\frac{\dot{b}_1}{\Omega} - a_1) - a_1\lambda] - (\frac{2}{3} - \epsilon)[a_1\frac{\dot{a}_0}{\Omega} + a_0(\frac{\dot{a}_1}{\Omega} + b_1)] \\
& - \frac{2a_0}{3}(-\frac{p}{\Omega}\sin\beta_w + \frac{q}{\Omega}\cos\beta_w) - [2(1-\epsilon^2)\lambda - 4(\frac{1}{3} - \frac{\epsilon}{2})\frac{\dot{a}_0}{\Omega}](\frac{p}{\Omega}\cos\beta_w + \frac{q}{\Omega}\sin\beta_w) \\
& + 4\frac{a_0}{\Omega}(\frac{\dot{b}_1}{\Omega} - a_1)(\frac{1}{3} - \epsilon + \epsilon^2)\} + \frac{\mu}{4}\{\epsilon(1-\epsilon)[a_1(\frac{\dot{b}_1}{\Omega} - a_1) \\
& + b_1(\frac{\dot{a}_1}{\Omega} + b_1)] + \frac{1}{4}(1-\epsilon)^2[b_1(\frac{\dot{a}_1}{\Omega} + b_1) + a_1(\frac{\dot{b}_1}{\Omega} - a_1)] \\
& - \frac{1}{2}(1-\epsilon^2)[a_1(\frac{\dot{b}_1}{\Omega} - a_1) + b_1(\frac{\dot{a}_1}{\Omega} + b_1) - 2a_0^2 - \frac{b_1^2}{2} - \frac{3}{2}a_1^2] \\
& - \frac{a_1}{4}(1-\epsilon^2)(\frac{p}{\Omega}\cos\beta_w + \frac{q}{\Omega}\sin\beta_w) - \frac{b_1}{4}(1-\epsilon^2)(-\frac{p}{\Omega}\sin\beta_w + \frac{q}{\Omega}\cos\beta_w)\}
\end{aligned}
\tag{2.55}
$$

and

$$
\begin{aligned}
(\frac{2C_Y}{a\sigma})_w = &-\frac{1}{4}(\theta_0 - K_1 a_0)\{[(\epsilon - \frac{2}{3})(\frac{\dot{a}_1}{\Omega} + b_1) - \frac{2}{3}b_1] + 3a_0(1-\epsilon^2)\mu - 2b_1(1-\epsilon)\mu^2 \\
&- \frac{2}{3}(-\frac{p}{\Omega}\sin\beta_w + \frac{q}{\Omega}\cos\beta_w)\} - \frac{\theta_t}{4}\{[(\frac{2\epsilon}{3} - \frac{1}{2})(\frac{\dot{a}_1}{\Omega} + b_1) - \frac{b_1}{2}] \\
&+ 2a_0\mu - b_1(1-\epsilon^2)\mu^2 - \frac{1}{2}(-\frac{p}{\Omega}\sin\beta_w + \frac{q}{\Omega}\cos\beta_w)\} \\
&- \frac{1}{4}(A_{1c} - K_1 a_1)\{[(\epsilon - \frac{2}{3})\frac{\dot{a}_0}{\Omega} + \lambda(1-\epsilon^2)] + \mu[\frac{5a_1}{4}(1-\epsilon^2) \\
&+ \frac{1}{4}(1-\epsilon)^2(\frac{\dot{b}_1}{\Omega} - a_1)] + \frac{\mu}{4}(1-\epsilon^2)(\frac{p}{\Omega}\cos\beta_w + \frac{q}{\Omega}\sin\beta_w)\} \\
&- \frac{1}{4}(B_{1c} - K_1 b_1)\{-\frac{2}{3}a_0 + \mu[\frac{7}{4}b_1(1-\epsilon^2) + \frac{1}{4}(1-\epsilon)^2(\frac{\dot{a}_1}{\Omega} + b_1) \\
&+ \frac{1}{4}(-\frac{p}{\Omega}\sin\beta_w + \frac{q}{\Omega}\cos\beta_w)] - \mu^2[2a_0(1-\epsilon)]\} \\
&- \frac{1}{4}\{4(\frac{1}{3} - \epsilon + \epsilon^2)\frac{\dot{a}_0}{\Omega}(\frac{\dot{a}_1}{\Omega} + b_1) - 2\lambda(1-\epsilon)^2(\frac{\dot{a}_1}{\Omega} + b_1) \\
&+ \frac{2a_0}{3}(\frac{p}{\Omega}\cos\beta_w + \frac{q}{\Omega}\sin\beta_w) + 2a_0(\frac{1}{3} - \frac{\epsilon}{2})(\frac{\dot{b}_1}{\Omega} - a_1) - 2b_1[\frac{\lambda}{2}(1-\epsilon^2) \\
&- \frac{\dot{a}_0}{\Omega}(\frac{1}{3} - \frac{\epsilon}{2})] + [4(\frac{1}{3} - \frac{\epsilon}{2})\frac{\dot{a}_0}{\Omega} - 2(1-\epsilon^2)\lambda](-\frac{p}{\Omega}\sin\beta_w + \frac{q}{\Omega}\cos\beta_w)\} \\
&- \frac{\mu}{4}[6a_0\lambda(1-\epsilon) - \frac{a_1 b_1}{2}(1-\epsilon^2) - 3(1-\epsilon)^2 a_0\frac{\dot{a}_0}{\Omega} \\
&- \frac{7}{4}(1-\epsilon)^2 a_1(\frac{\dot{a}_1}{\Omega} + b_1) + 2b_1(1-\epsilon^2)(\frac{p}{\Omega}\cos\beta_w + \frac{q}{\Omega}\sin\beta_w) \\
&- 2a_1(1-\epsilon^2)(-\frac{p}{\Omega}\sin\beta_w + \frac{q}{\Omega}\cos\beta_w) - \frac{5}{4}(1-\epsilon)^2 b_1(\frac{\dot{b}_1}{\Omega} - a_1)] \\
&- \mu^2[a_0 a_1(1-\epsilon)]
\end{aligned}
\tag{2.56}
$$

Main rotor hub moments Rotor hub moments expressions are:

$$M_w = (M_H)_w \cos\beta_w + (L_H)_w \sin\beta_w \tag{2.57}$$

$$L_w = -(M_H)_w \sin\beta_w + (L_H)_w \cos\beta_w \tag{2.58}$$

where:

$$
\begin{aligned}
(M_H)_w =& \frac{N}{2}[K_\beta a_1 - \frac{eM_\beta}{g}(\ddot{a}_1 + 2\dot{b}_1\Omega - a_1\Omega^2)] - \frac{N}{2}I_\beta\Omega^2\gamma\epsilon\{-[\frac{1}{6} + \frac{\mu^2}{8}(1-\epsilon)](A_{1c} - K_1 a_1) \\
&- \frac{\mu}{4}(1-\epsilon^2)a_0 + \frac{\mu^2}{8}(1-\epsilon)b_1 + (\frac{1}{6} - \frac{\epsilon}{4})(\frac{\dot{a}_1}{\Omega} + b_1) \\
&+ \frac{1}{6}(-\frac{p}{\Omega}\sin\beta_w + \frac{q}{\Omega}\cos\beta_w)\}
\end{aligned}
\tag{2.59}
$$

and

$$
\begin{aligned}
(L_H)_w =& \frac{N}{2}[K_\beta b_1 - \frac{eM_\beta}{g}(\ddot{b}_1 - 2\dot{a}_1\Omega - b_1\Omega^2)] - \frac{N}{2}I_\beta\Omega^2\gamma\epsilon\{\frac{\mu}{2}(1-\epsilon^2)(\theta_0 - K_1 a_0) \\
&- [\frac{1}{6} + \frac{3}{8}\mu^2(1-\epsilon)](B_{1c} - K_1 b_1) + \frac{\mu}{3}\theta_t + \frac{\mu}{2}(1-\epsilon)\lambda + \frac{\mu^2}{8}(1-\epsilon)a_1 \\
&- \frac{\mu}{4}(1-\epsilon)^2\frac{\dot{a}_0}{\Omega} + (\frac{1}{6} - \frac{\epsilon}{4})(\frac{\dot{b}_1}{\Omega} - a_1) + \frac{1}{6}(\frac{p}{\Omega}\cos\beta_w + \frac{q}{\Omega}\sin\beta_w)\}
\end{aligned}
\tag{2.60}
$$

Main rotor torque Rotor torque is written as:

$$
Q_F = \frac{N}{2}\rho acR^2(\Omega R)^2\frac{2C_Q}{a\sigma} \tag{2.61}
$$

$$
\begin{aligned}
(\frac{2C_Q}{a\sigma}) =& \frac{\delta}{4a}[1+(1-\epsilon^2)\mu^2] - (\theta_0 - K_1 a_0)[\frac{\lambda}{3} + (\frac{\epsilon}{3} - \frac{1}{4})\frac{\dot{a}_0}{\Omega} + \frac{\mu}{6}(\frac{\dot{b}_1}{\Omega}) \\
& - \frac{\mu\epsilon}{4}(\frac{\dot{b}_1}{\Omega} - a_1) + \frac{\mu}{6}(\frac{p}{\Omega}\cos\beta_w + \frac{q}{\Omega}\sin\beta_w)] - (A_{1c} - K_1 a_1)[(\frac{1}{8} - \frac{\epsilon}{6})(\frac{\dot{a}_1}{\Omega} + b_1) \\
& - \frac{\mu}{6}a_0 + \frac{b_1}{16}(1-\epsilon^2)\mu^2 + \frac{1}{8}(-\frac{p}{\Omega}\sin\beta_w + \frac{q}{\Omega}\cos\beta_w)] \\
& - (B_{1c} - K_1 b_1)[(\frac{1}{8} - \frac{\epsilon}{6})(\frac{\dot{b}_1}{\Omega} - a_1) + (\frac{\epsilon}{4} - \frac{1}{6})\mu\frac{\dot{a}_0}{\Omega} + \frac{1}{2}(1-\epsilon^2)(\frac{\mu\lambda}{2} + \frac{a_1}{8}\mu^2) \\
& + \frac{1}{8}(\frac{p}{\Omega}\cos\beta_w + \frac{q}{\Omega}\sin\beta_w)] - \theta_t[\frac{\lambda}{4} + (\frac{\epsilon}{4} - \frac{1}{5})\frac{\dot{a}_0}{\Omega} + \frac{\mu}{8}(\frac{\dot{b}_1}{\Omega}) - \frac{\epsilon\mu}{6}(\frac{\dot{b}_1}{\Omega} - a_1)] \\
& - \frac{1}{2}(1-\epsilon^2)\{\lambda^2 + \lambda\mu a_1 + 2\lambda\epsilon\frac{\dot{a}_0}{\Omega} + \mu\epsilon[a_1\frac{\dot{a}_0}{\Omega} + a_0(\frac{\dot{a}_1}{\Omega} + b_1)] \\
& + \mu^2(\frac{{a_0}^2}{2} + \frac{3}{8}a_1^2 + \frac{1}{8}b_1^2)\} + \frac{\mu}{3}[a_1(\frac{\dot{a}_0}{\Omega}) + a_0(\frac{\dot{a}_1}{\Omega} + b_1)] + \frac{2}{3}\lambda(\frac{\dot{a}_0}{\Omega}) \\
& - [-\frac{\mu}{3}a_0 + (\frac{1}{4} - \frac{\epsilon}{3})(\frac{\dot{a}_1}{\Omega} + b_1)](-\frac{p}{\Omega}\sin\beta_w + \frac{q}{\Omega}\cos\beta_w) \\
& - (\frac{1}{4} - \frac{\epsilon}{3})(\frac{\dot{b}_1}{\Omega} - a_1)(\frac{p}{\Omega}\cos\beta_w + \frac{q}{\Omega}\sin\beta_w) - \frac{1}{8}(-\frac{p}{\Omega}\sin\beta_w + \frac{q}{\Omega}\cos\beta_w)^2 \\
& - \frac{1}{8}(\frac{p}{\Omega}\cos\beta_w + \frac{q}{\Omega}\sin\beta_w)^2 - (\frac{1}{4} - \frac{2}{3}\epsilon + \frac{\epsilon^2}{2})\{(\frac{\dot{a}_0}{\Omega})^2 \\
& + \frac{1}{2}[(\frac{\dot{a}_1}{\Omega} + b_1)^2 + (\frac{\dot{b}_1}{\Omega} - a_1)^2]\}
\end{aligned}
\tag{2.62}
$$

For the case of a two-bladed teetering rotor, the forces and moments may be obtained by setting $\epsilon = 0$, $\dot{a}_0 = \ddot{a}_0 = 0$ in the above equations.

For a teetering rotor without cyclic pitch, as in many tail rotor systems, the forces and moments may be obtained by setting $A_{1c} = B_{1c} = 0$. Since flapping frequency of tail rotors is much higher than that of the main rotor systems, the tip-path plane may be neglected.Thus, for tail rotor applications, it is set $\dot{a}_0 = \dot{a}_1 = \dot{b}_1 = 0$ and $\ddot{a}_0 = \ddot{a}_1 = \ddot{b}_1 = 0$ in the above equations.

These rotor forces and moments are the contribution to the total aerodynamic forces and moments in the body axes of the aircraft. The set of these equations are:

$$\begin{cases} X_F = T_F \sin i_F - H_F \cos i_F \\ Y_F = Y_F \\ Z_F = -T_F \cos i_F - H_F \sin i_F \\ L_F = L_H F \cos i_F - Q_F \sin i_F + Y_F h_F + (T_F \cos i_F + H_F \sin i_F) d_F \\ M_F = M_H F - (T_F \sin i_F - H_F \cos i_F) h_F + (T_F \cos i_F + H_F \sin i_F) l_F \\ N_F = Q_F \cos i_f + L_H F \sin i_F + Y_F l_F + (T_F \sin i_F - H_F \cos i_F) d_F \end{cases} \tag{2.63}$$

2.1.4 Tail rotor forces and moments

The tail rotor is modelled as in reference [72]. Flapping dynamics is ignored, as well as tip-path plane dynamics, since flapping frequency is much higher than that of the main rotor. The first and second derivatives of the blade-flapping non-rotating coordinates are set equal to zero and a steady-state solution is considered. This means that in the force equations $\dot{a_o} = \dot{a_1} = \dot{b_1} = 0$ and $\ddot{a_0} = \ddot{a_1} = \ddot{b_1} = 0$. The resultant expression of a_1 and b_1 are:

$$a_{1TR} = \frac{1}{\Delta_{TR}}[K_{1TR}(1 + \frac{3}{2}\mu_{TR}^2) f_{1TR} - (1 + \frac{\mu_{TR}^2}{2}) f_{2TR}] \tag{2.64}$$

$$b_{1TR} = \frac{1}{\Delta_{TR}}[(1 - \frac{\mu_{TR}^2}{2}) f_{1TR} + K_{1TR}(1 + \frac{\mu_{TR}^2}{2}) f_{2TR}] \tag{2.65}$$

where $\Delta_{TR} = 1 - \frac{\mu_{TR}^4}{4} + K_{1TR}^2(1 + \frac{\mu_{TR}^2}{2})(1 + \frac{3}{2}\mu_{TR}^2)$, $f_{1TR} = \frac{4}{3}\mu_{TR} a_{0TR} - \frac{16}{\gamma_{TR}\Omega_{TR}} p_{TR} - \frac{q_{TR}}{\Omega_{TR}}$ and $f_{2TR} = \frac{8}{3}K_{1TR}\mu_{TR} a_{0TR} + \frac{16 q_{TR}}{\gamma_{TR}\Omega_{TR}} - \mu_{TR}(\frac{8}{3}\theta_{0TR} + 2\theta_{tTR} + 2\lambda_{TR}) - \frac{p_{TR}}{\Omega_{TR}}$

Forces and moments expressions are detailed in Appendix D of reference [72].

The inflow ratio is static and uniform and it is a steady state solution of the Pitt-Peters model [69], whose expression is:

$$\lambda_{TR} = \frac{-v_{TR}}{\omega_{TR} R_{TR}} - \frac{C T_{TR}}{2\sqrt{\mu_{TR}^2 + \lambda_{TR}^2}} \tag{2.66}$$

that should be solved with the Newton-Ralphson iterative procedure.

2.1.5 Fuselage

The fuselage forces and moments are evaluated as function of the angle of attack and of the sideslip angle, as presented in reference [73]. Main equations involved are:

$$\boldsymbol{V}_{fus} = \boldsymbol{V}_b + \boldsymbol{\omega}_b \times \boldsymbol{r}_{fus} \tag{2.67}$$

$$\alpha_{fus} = \arctan \frac{w_{fus}}{u_{fus}} \tag{2.68}$$

$$\beta_{fus} = \arcsin \frac{v_{fus}}{|\boldsymbol{V}_{fus}|} \tag{2.69}$$

$$D_{fus} = \frac{1}{2}\rho|\boldsymbol{V}_{fus}|^2 S_{ref} C_D(\alpha, \beta) \tag{2.70}$$

$$Y_{fus} = \frac{1}{2}\rho|\boldsymbol{V}_{fus}|^2 S_{ref} C_Y(\alpha, \beta) \tag{2.71}$$

$$L_{fus} = \frac{1}{2}\rho|\boldsymbol{V}_{fus}|^2 S_{ref} C_L(\alpha, \beta) \tag{2.72}$$

where D_{fus}, Y_{fus} and L_{fus} are respectively the fuselage drag, lateral and vertical forces in the wind system of axes about the fuselage reference point. Forces and moments in the body-fixed reference frame are:

$$\boldsymbol{F}^b_{fus} = \begin{bmatrix} -\cos\alpha_{fus}\cos\beta_{fus} & -\sin\alpha_{fus}\sin\beta_{fus} & \sin\alpha_{fus} \\ -\sin\beta_{fus} & \cos\beta_{fus} & 0 \\ -\sin\alpha_{fus}\cos\beta_{fus} & -\sin\alpha_{fus}\sin\beta_{fus} & \cos\alpha_{fus} \end{bmatrix} \tag{2.73}$$

$$\boldsymbol{M}^b_{fus} = \boldsymbol{r}_{fus} \times \boldsymbol{F}^b_{fus} \tag{2.74}$$

$\boldsymbol{r}_{fus}$ is the position of the fuselage pressure center with respect to the gravity center of the rotorcraft. Aerodynamic coefficients are obtained from estimated look-up tables.

2.2 Synch-rotor model

The mathematical model of the intermeshing rotors configuration is here presented. As for the helicopter model, the mathematical model comprises the complete non-linear equations of motion and the modelling of forces and moments acting on the vehicle. The interference between the two rotors is considered. To begin with, all the equation are reported. Subsequently the linearization procedure is applied and the stability derivatives are presented. Finally, stability analysis is performed, resulting in root loci poles.

2.2.1 Synch-rotor non-linear model

The considered components are the two counter-rotating tilted main rotors, the fuselage, the horizontal plane and the vertical fin. The basic assumptions and the reference frames

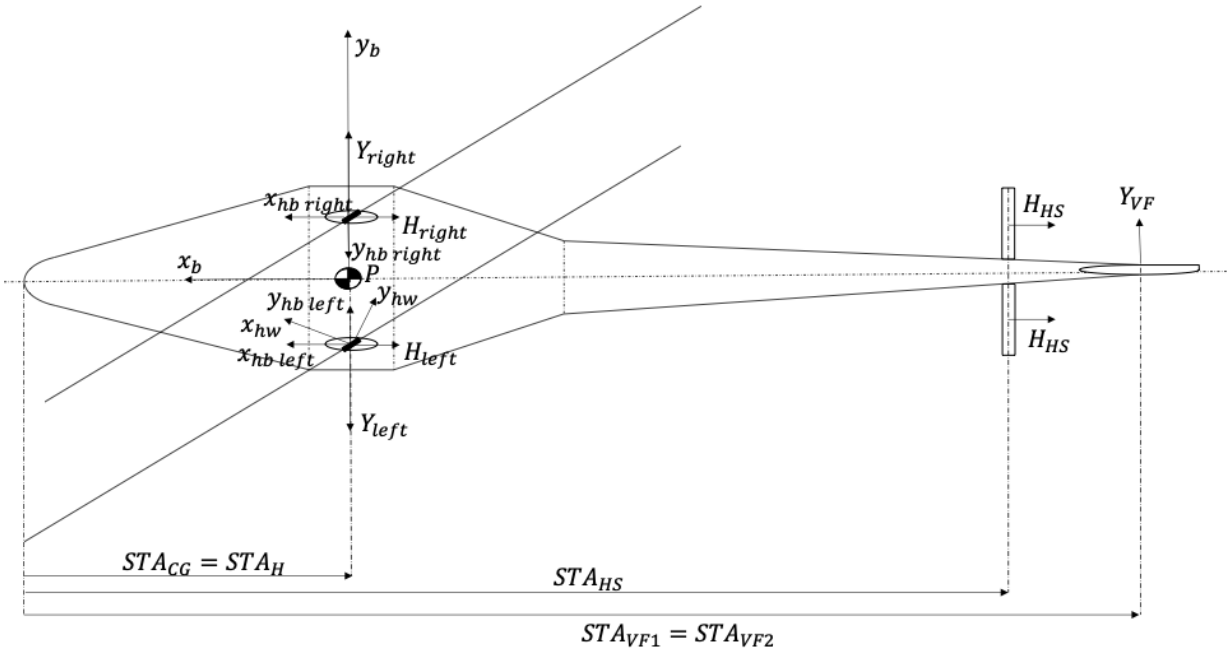

Figure 2.5: Synch-rotor XY view

are those stated at the beginning of section 2.1. Figures 2.5, 2.6 and 2.7 show the reference frames for the synch-rotor.

Before proceeding with the model equations, the rotational matrix from hub-body to wind-hub coordinate system is given:

$$\Pi_{hb} = \begin{bmatrix} 1 & 0 & 0 \\ 0 & \cos\frac{\Gamma}{2} & -\sin\frac{\Gamma}{2} \\ 0 & \sin\frac{\Gamma}{2} & \cos\frac{\Gamma}{2} \end{bmatrix} \tag{2.75}$$

where Γ is the tilt angle between the rotors masts. To implement the calculated Hub-Body component into the equations of motion, these are rotated in the Wind-Hub system:

$$\begin{bmatrix} (\quad)_x \\ (\quad)_y \\ (\quad)_z \end{bmatrix}_{wh} = \begin{bmatrix} \cos\beta_w & \sin\beta_w & 0 \\ -\sin\beta_w & \cos\beta_w & 0 \\ 0 & 0 & 1 \end{bmatrix} \begin{bmatrix} (\quad)_x \\ (\quad)_y \\ (\quad)_z \end{bmatrix}_{hb} \tag{2.76}$$

where β_w is the sideslip angle of equation (2.10).

Equations of motion are the same for the helicopter 6 DoF model, that are equations (2.1), (2.2), (2.3) and (2.4).

As in the case of the helicopter model, the external forces are the sum of aerodynamic and gravity contributions, whereas total moments are the aerodynamic ones. Gravity

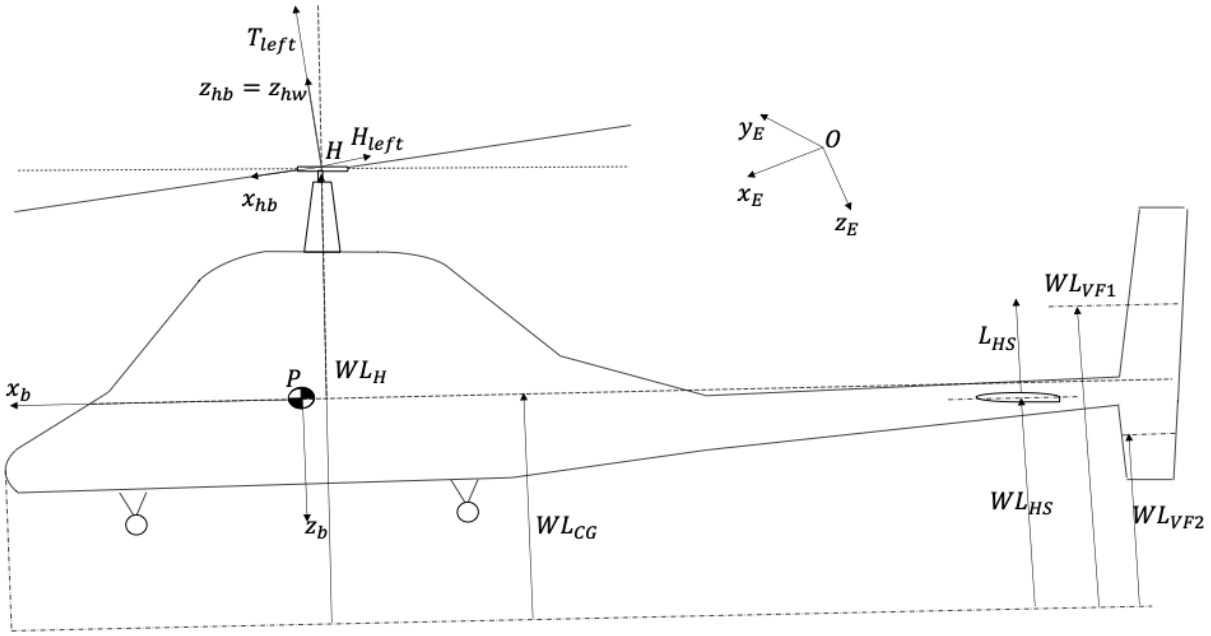

Figure 2.6: Synch-rotor XZ view

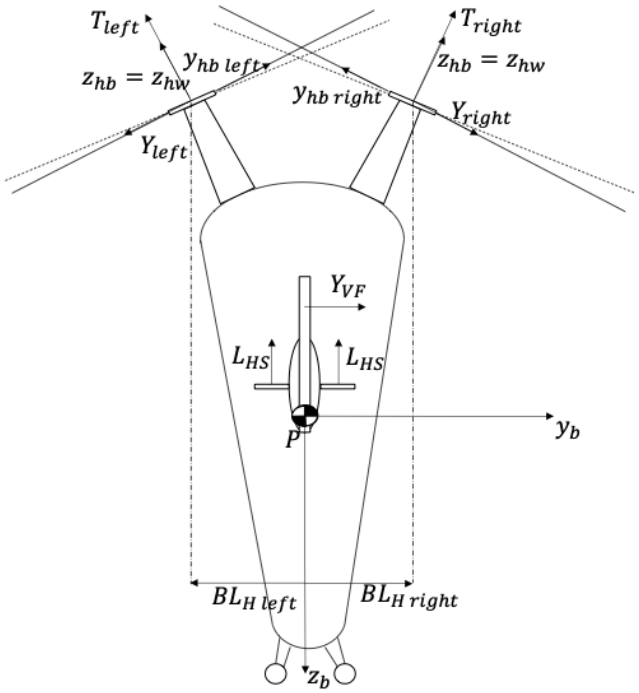

Figure 2.7: Synch-rotor YZ view

forces are expressed in equation (2.6).

Aerodynamic forces and moments are the sum of the components contribution:

$$\boldsymbol{F}^{(a)} = \boldsymbol{F}^{(\text{left mr})} + \boldsymbol{F}^{(\text{right mr})} + \boldsymbol{F}^{(\text{fus})} + \boldsymbol{F}^{(\text{hr})} + \boldsymbol{F}^{(\text{vs})} \tag{2.77}$$

$$\boldsymbol{M}^{(a)} = \boldsymbol{M}^{(\text{left mr})} + \boldsymbol{M}^{(\text{right mr})} + \boldsymbol{M}^{(\text{fus})} + \boldsymbol{M}^{(\text{hr})} + \boldsymbol{M}^{(\text{vs})} \tag{2.78}$$

Main rotors model

The intermeshing rotors system is made of two counter-rotating tilted main rotors. For the mathematical modelling purposes, equations for a single counter clockwise rotor are first derived in the same way presented in section 2.1 for the helicopter model. Then, by means of symmetrical coordinate systems [74], equations for the clockwise rotor are obtained. Interference effects related to the overlapping disc area are then included. Blades are assumed rigid. forces and moments are radially integrated and summed about the azimuth. Rotor is assumed as a teetering one. The equations presented in section 2.1 are employed for the counter-clockwise rotor. These equations are now applied to clockwise rotor by using the left-hand coordinate system and using a direction indicator χ in lateral equations, which value is equal to 1 when rotor is counter-clockwise; -1 otherwise. Resulting equations for clockwise rotor are given as follows:

$$\begin{aligned}
\boldsymbol{V}_{cl} &= \Pi_1 \boldsymbol{V}_{ccl} \\
\boldsymbol{\Omega}_{cl} &= \Pi_2 \boldsymbol{\Omega}_{ccl} \\
\boldsymbol{F}_{cl} &= \Pi_1 \boldsymbol{F}_{ccl} \\
\boldsymbol{M}_{cl} &= \Pi_2 \boldsymbol{M}_{ccl} \\
\boldsymbol{U}_{cl} &= \Pi_1 \boldsymbol{U}_{ccl}
\end{aligned} \tag{2.79}$$

provided

$$\Pi_1 = \begin{bmatrix} 1 & 0 & 0 \\ 0 & \chi & 0 \\ 0 & 0 & 1 \end{bmatrix} \tag{2.80}$$

$$\Pi_2 = \begin{bmatrix} \chi & 0 & 0 \\ 0 & 1 & 0 \\ 0 & 0 & \chi \end{bmatrix} \tag{2.81}$$

and $\boldsymbol{U} = [\theta_0 \quad A_{1s} \quad B_{1s}]$.

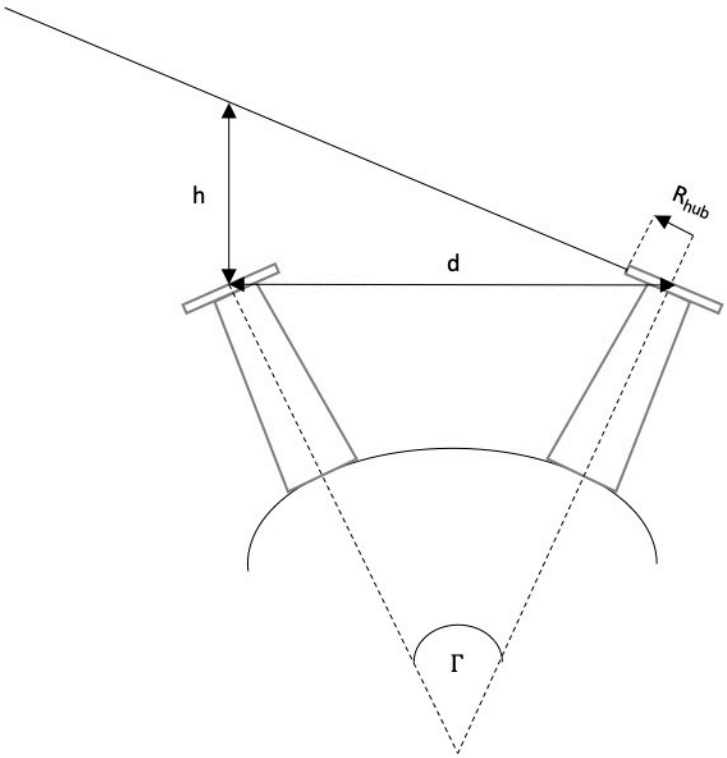

Figure 2.8: Synch-rotor geometry

Rotors geometry and interference

A generalized geometrical framework for addressing preliminary design of the two rotors is given. Let d be the distance between the two main rotors hub on the rotorcraft buttline; h be the height over the rotor hub between the hub itself and the plane normal to shaft axis of the other rotor. Let R be the rotor radius and R_{hub} be the hub length. Considering Γ the angle between the rotors, referring to Figure 2.8.

If the distance between the rotors allows them not to collide, that is $d > R + R_{hub}$, Γ can be zero and the rotors masts can stay parallel. If $d \leq R + R_{hub}$, the masts should be tilted in order to avoid the collision, so the angle Γ should be different from zero. h states how much the rotors have to be tilted, it is a design parameter. Equation (2.82) links d and Γ:

$$d = h \cot(\frac{\Gamma}{2}) \tag{2.82}$$

Figure 2.9 shows the trend of Γ in function of the normalized distance d/R for three

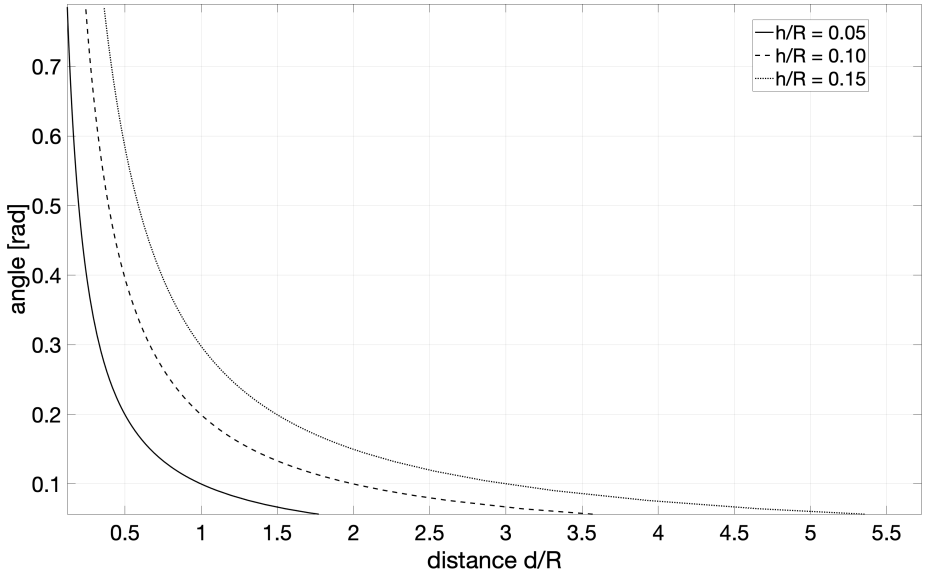

Figure 2.9: Trend of d vs Γ

different normalized values of h/R. For low angles the distance is higher and for high angles the distance tends to zero.

Interference effects are included considering the overlapping between the two main rotors. These effects are consistent with those presented by Leishman in ref. [75]. Since rotors are not coaxial, the rotor interference induced power factor k is adequately scaled in thrust computation, in order to account for the actual overlapping fraction of the disk area. Factor k is obtained multiplying the Leishman induced power factor for coaxial rotors by a scaling factor, that is the ratio between the overlapping area A_{OV} and the rotor area. Overlapping area between the rotors is calculated projecting the radius of a single tilted rotor from XY Hub-Body plane to the un-tilted XZ Body plane and considering the length of overlapping distance. The area is geometrically estimated, whereas seen from the top it appears as an intersection of two circular sectors. Then equivalent radius is estimated and the ratio between the areas is found. See Figure 2.10. Equations for overlapping area are as follows:

$$A_{OV} = 2A_{CS} - A_R \tag{2.83}$$

where $A_{CS} = \frac{R_{PRO}^2 \alpha}{2}$ is the area of the circular sector with projected radius $R_{PRO} = R\cos(\frac{\Gamma}{2})$ and angular opening $\alpha = 2\cos^{-1}(\frac{d}{R_{PRO}})$; $A_R = dR_{PRO}\sin(\frac{\alpha}{2})$ is the area of the rhombus with diagonals d and $2R_{PRO}\sin(\frac{\alpha}{2})$.

Figure 2.11 shows the trend of factor k for Γ varyig from 5 deg to 45 deg. As the tilt angle increases, the interference factor value decreases, being function of the overlapping

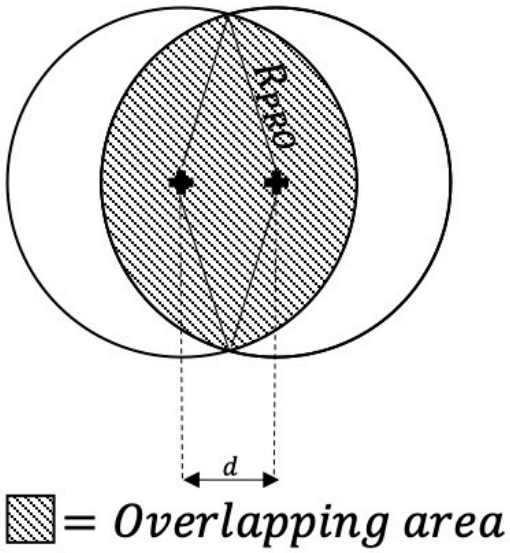

Figure 2.10: Overlapping area geometry

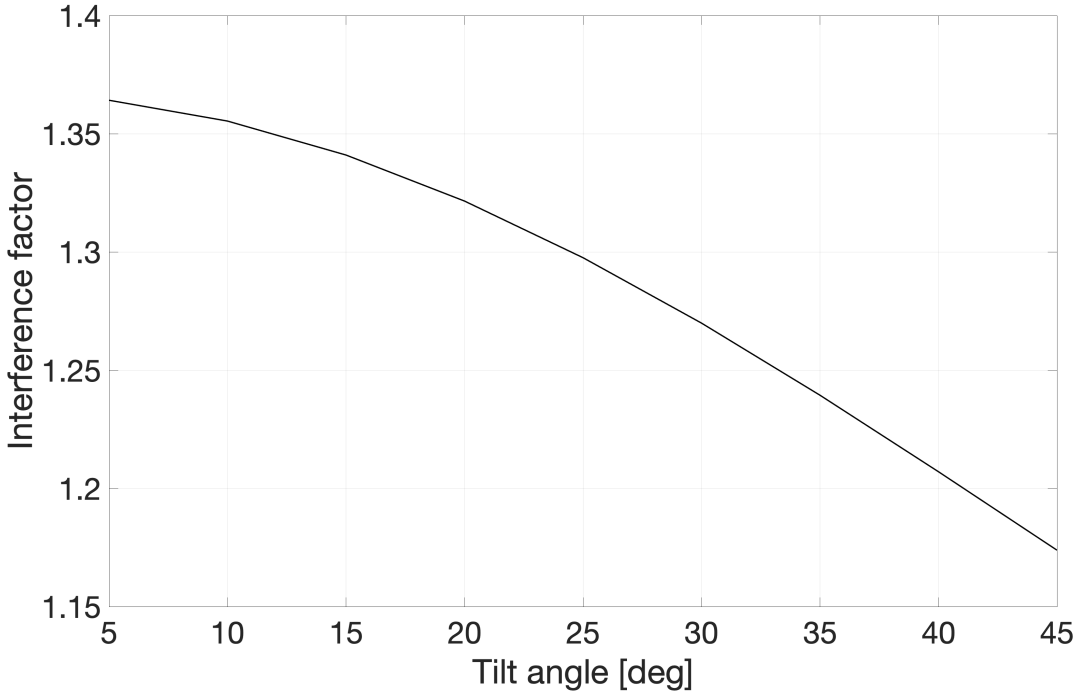

Figure 2.11: Interference actor k vs tilt angle

area.

Fuselage and empennages model

Fuselage and tail surfaces are modelled as follows. The fuselage aerodynamic model provides forces and moments as a function of angle of attack and sideslip angle along the flight envelope. Effects are accounted into performance and stability analysis for forward speeds. Continuity in numerical estimation is mandatory in order to prevent unrealistic linear or angular accelerations in response to small changes in attitude. In this model, continuity is provided by a linear interpolation for forces and moments on angles range not covered. Details on the procedure and forces and moments equations are available in [72]. Vertical fin and horizontal tail are considered as lift and drag producers and are approximated for all angles of attack and sideslip. Principal assumptions include:

1. Surfaces are modelled with symmetrical profiles;
2. An elliptical distribution with uniform downwash is considered;
3. Forces are applied at the quarter chord of each surface;
4. Maximum lift coefficient is specified;
5. Profile drag coefficient varies with angle of attack;
6. The induced drag coefficient at the square of the calculated lift coefficient.

Equations are given in detail in [72].

2.2.2 Linearized synch-rotor equations of motion

In this section linearization procedure is described and linearized equations of motion are given. Throughout this part, a synch-rotor configuration has been chosen to carry on the linearization procedure and to analyze the dynamic issues. Relevant data for the aircraft are reported in table C.1 in Appendix C of chapter C.

Let $f(\dot{\boldsymbol{X}}, \boldsymbol{X}, \boldsymbol{U}, t) = 0$ represent the non-linear model described by the equations (2.1), (2.2), (2.3), (2.4), where $\boldsymbol{X} = \{u, w, q, \theta, v, p, \phi, r, \psi\}$ is the state vector and $\boldsymbol{U} = \{A_{1s}, \theta_0, B_1, \theta_{ped}\}$ is the control vector. With small perturbation theory [86], it can be assumed that during disturbed motion, the vehicle behaviour can be described as a perturbation from the equilibrium condition, written in the form:

$$\boldsymbol{X} = \boldsymbol{X}_e + \delta\boldsymbol{X} \tag{2.84}$$

where $\delta \boldsymbol{X}$ represents the perturbed state.

Taylor's theorem states that it is possible to estimate the behavior of an analytic function in its range if the function and all its derivatives are known at any one point (the so called trim condition). The function is expanded in a series about this known point. Fundamental assumptions of linearization are that external forces and moments can be expressed as analytic functions of the disturbed motion variables and their derivatives and that disturbances are assumed small. In this way, higher order terms of Taylor's expansion are neglected because the dominant effect in the expansion results to be the linear one. Thus, aerodynamic forces and moments can be written in the form:

$$\Delta \boldsymbol{F}^{(a)} = \begin{bmatrix} \sum_{n=1}^{N} X_{\lambda_i} \lambda_i & \sum_{n=1}^{N} Y_{\lambda_i} \lambda_i & \sum_{n=1}^{N} Z_{\lambda_i} \lambda_i \end{bmatrix}^T \tag{2.85}$$

$$\Delta \boldsymbol{M}^{(a)} = \begin{bmatrix} \sum_{n=1}^{N} L_{\lambda_i} \lambda_i & \sum_{n=1}^{N} M_{\lambda_i} \lambda_i & \sum_{n=1}^{N} N_{\lambda_i} \lambda_i \end{bmatrix}^T \tag{2.86}$$

where $\lambda = \boldsymbol{\Lambda} - \boldsymbol{\Lambda_0}$, with $\boldsymbol{\Lambda}$ the vector of all variables affecting aerodynamic forces and moments, whose stability derivatives are written in a semi-normalized form with the notation:

$$X_{\lambda_i} = \frac{1}{m} \frac{\partial X^{(a)}}{\partial \Lambda_i} \tag{2.87}$$

for all forces; and

$$M_{\lambda_i} = \frac{1}{I_{yy}} \frac{\partial M^{(a)}}{\partial \Lambda_i} \tag{2.88}$$

for M moment stability derivatives, and, as examples,

$$L'_p = \frac{I_{zz}}{I_{xx} I_{zz} - I_{xz}^2} L_p + \frac{I_{xz}}{I_{xx} I_{zz} - I_{xz}^2} N_p \tag{2.89a}$$

$$N'_r = \frac{I_{xz}}{I_{xx} I_{zz} - I_{xz}^2} L_r + \frac{I_{xx}}{I_{xx} I_{zz} - I_{xz}^2} N_r \tag{2.89b}$$

for L and N ones.

Linearized equations in the state-space form are:

$$\dot{\boldsymbol{X}} = \boldsymbol{A}\boldsymbol{X} + \boldsymbol{B}\boldsymbol{U} \tag{2.90}$$

where the state and control matrices are obtained as:

$$\boldsymbol{A} = \left(\frac{\partial \boldsymbol{f}}{\partial \boldsymbol{x}}\right)_{\boldsymbol{x}=\boldsymbol{x}_e}$$
$$\boldsymbol{B} = \left(\frac{\partial \boldsymbol{f}}{\partial \boldsymbol{u}}\right)_{\boldsymbol{x}=\boldsymbol{x}_e} \tag{2.91}$$

2.2.3 Synch-rotor stability derivatives

Aircraft stability derivatives are obtained both analytically, by using closed-form approximate models, and numerically, by applying central finite different method directly on simulation software [86]. On one hand, numerical linearization allows for a complete and accurate modelling of system dynamics. On the other hand, there may be a lack of physical understanding since relationship between aircraft design and dynamic behaviour is straightforward. In this respect, analytical approximations may help in addressing the dynamics analysis in a deeper detail. In what follows, according to Padfield approach [86], a selection of relevant stability derivatives of the synch-rotor configuration (see table C.1) are examined.

Translational velocity derivatives

Rotor flapping, changes in rotor lift and drag and the incidence and sideslip angles of the flow around fuselage and empennage are influenced by translational velocity perturbations. This gives rise to a complex behavior, also considering that the orientation of the Body axes and the Hub ones are affected by the shaft tilt, rotor flapping and the sideslip angle. So, a u perturbation in Body axes causes μ_x, μ_y and μ_z perturbations in Hub axes.

Z_w The aerodynamic force acting along $\boldsymbol{z}_B$ for a conventional helicopter configuration is [87]: $Z = -T_{MR}$, where $T_{MR} = \rho A(\Omega R)^2 C_T$. For the synch-rotor configuration, Z force results to be: $Z = -2T_{MR}\Pi_{hb}(3,3) = -2T_{MR}\cos\frac{\Gamma}{2}$. By differentiating with respect to z: $\frac{\partial Z}{\partial w} = -\frac{\partial(2\rho A(\Omega R)^2 C_T \cos\frac{\Gamma}{2})}{\partial w} = -2\rho A(\Omega R)^2 \cos\frac{\Gamma}{2}\frac{\partial C_T}{\partial w}$. Applying the chain rule for multivariable functions the coefficient derivative is computed [88]:

$$\frac{\partial C_T}{\partial w} = \frac{\partial C_T}{\partial w_H}\frac{\partial w_H}{\partial w} = \frac{1}{\Omega R}\left[\frac{\partial C_T}{\partial \mu_z}\Pi_{hb}(3,3)\right] = \frac{1}{\Omega R}\left[\frac{\partial C_T}{\partial \mu_z}\cos\frac{\Gamma}{2}\right] \tag{2.92}$$

where the derivative $\frac{\partial C_T}{\partial \mu_z}$ is provided by [86], that is for the hovering case:

$$\frac{\partial C_T}{\partial \mu_z} = \frac{2a_0 s\lambda_0}{16\lambda_0 + a_0 s} \tag{2.93}$$

Z_w, known in literature as the heave damping derivative, is the initial acceleration following an abrupt vertical gust. It is highly influenced by the inverse of rotor blade

loading $\frac{M_a}{A_b}$, which appears in equation (2.92) if it is normalized by M_a. This gives rise to a lower gust sensitivity with respect to fixed-wing aircrafts. In Table 2.1 values for Z_w, calculated with the proposed analytical expression and numerically evaluated, are reported with the percentage error in hovering. The semi-normalized form is used.

Table 2.1: Analytical vs numerical values for Z_w

Γ	$Z_w analytical$	$Z_w numerical$	$\%error$
Hovering			
0°	-0.2535	-0.2424	4.5701 %
5°	-0.2531	-0.2421	4.5212 %
15°	-0.2494	-0.2396	4.0747 %
25°	-0.2422	0.2349	3.1077 %
35°	-0.2314	-0.2278	1.5637 %
45°	-0.2171	-0.2183	0.5477 %

Figure 2.12 shows Z_w and Z_u stability derivatives for $\Gamma = [0°, 5°, 15°, 25°, 35°, 45°]$ along the flight envelope, considering straight-and-level flight at different airspeed at an altitude of 113 m. The dihedral angle does not have a strong influence on these stability derivatives and the trend is similar to that of a conventional single main rotor helicopter, as stated in reference [86].

X_u, X_v, Y_u, Y_v The direct force damping X_u at high forward speed tend to be linear with velocity, like for conventional single main rotor helicopters [86], reflecting the drag and the sideforce. Discs tilts in response to u and v perturbations are the main reason of these direct derivatives. The coupling derivatives tends to zero. As for Z_w and Z_u, the dihedral angle does not influence strongly the derivatives trends, as in Figure 2.13 and Figure 2.14.

M_u, M_w, M_v These stability derivatives are known as speed and static stability derivatives and have influence on handling qualities. Main rotor moments due to speed changes are almost constant, but aerodynamic moments from fuselage and horizontal and vertical tails notably vary with forward velocity. Especially for the horizontal stabilizer, whose normal load gives a pitching moment at the center of mass, affecting M_u. As for single main rotor helicopters, the static speed stability arises from the increase in forward speed that induced the disc to flap back and from an increment of the download on the horizontal stabilizer, bringing to a nose-up pitching moment that contributes to reduce the speed. As known from the literature [86], the incidence stability derivative M_w, as M_u, is given by

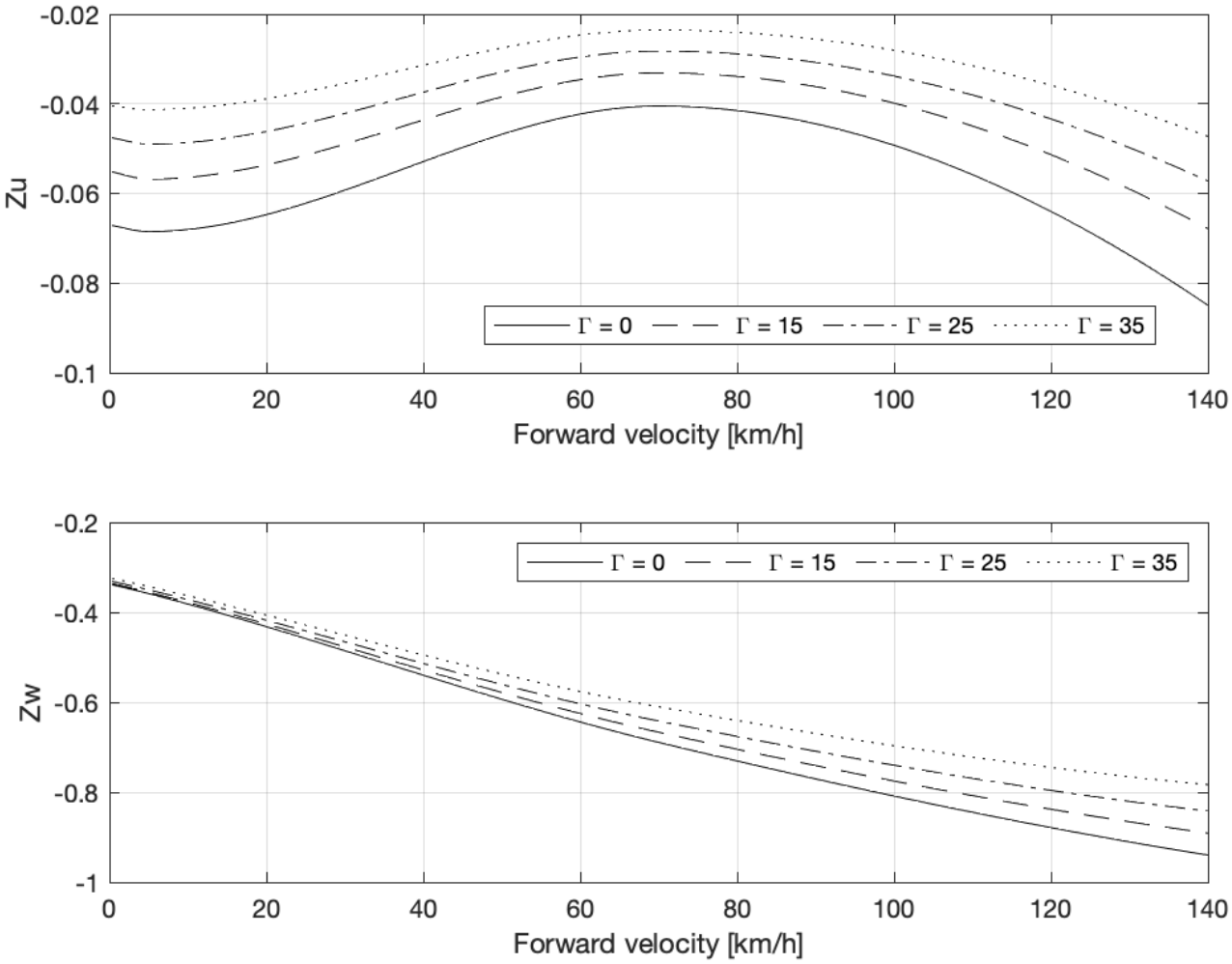

Figure 2.12: Stability derivatives - $Z_w Z_u$

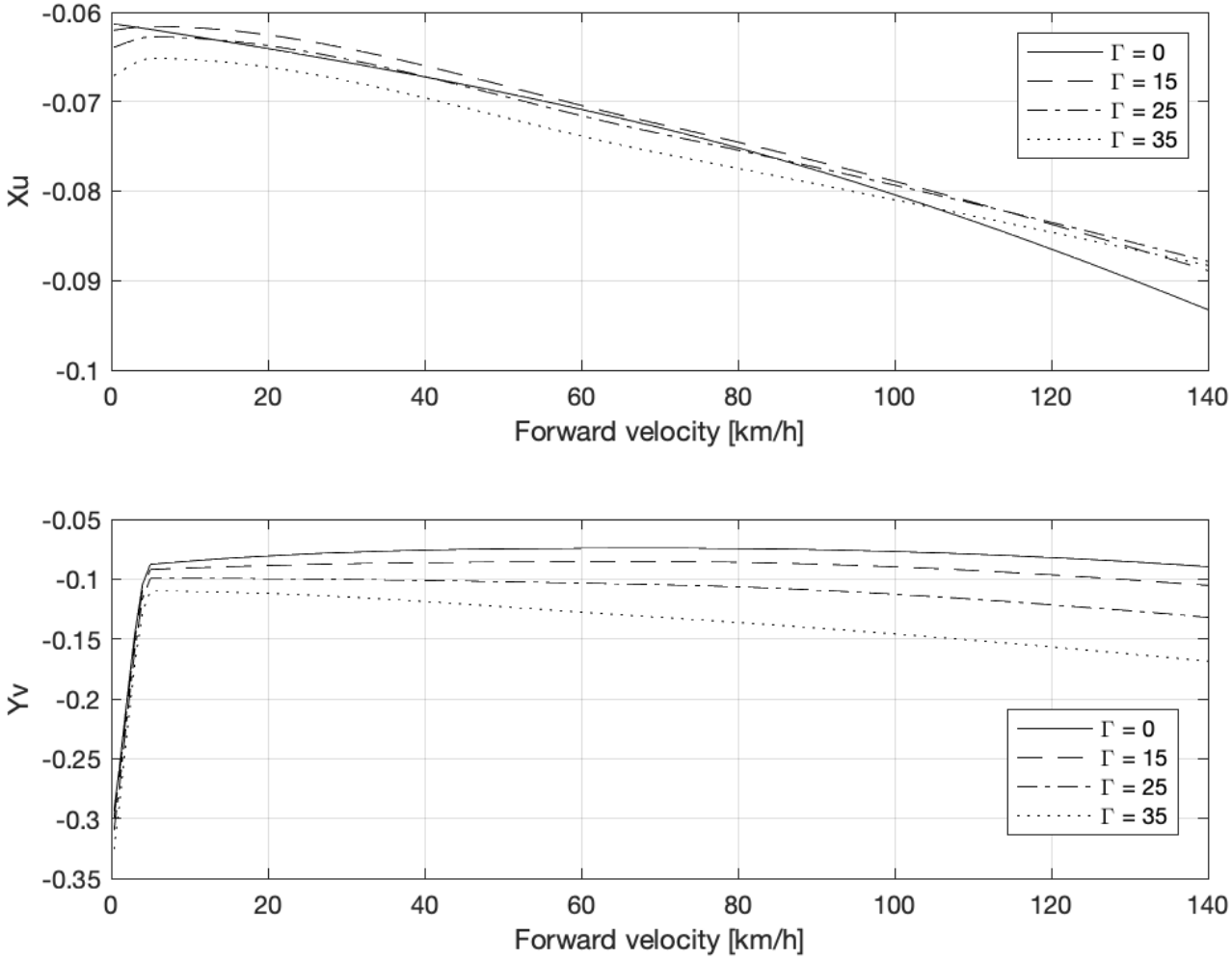

Figure 2.13: Stability derivatives - $X_u Y_v$

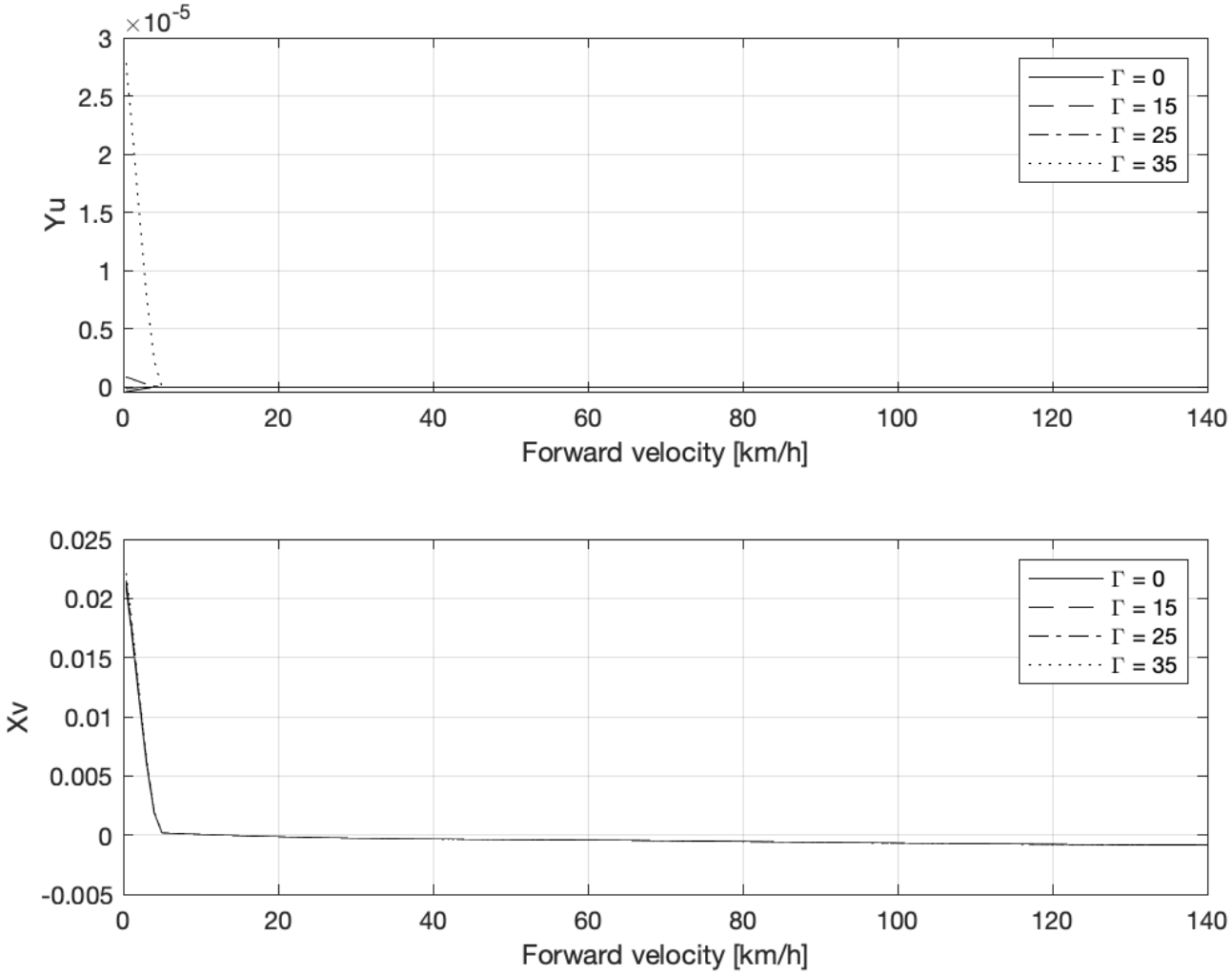

Figure 2.14: Stability derivatives - $X_v Y_u$

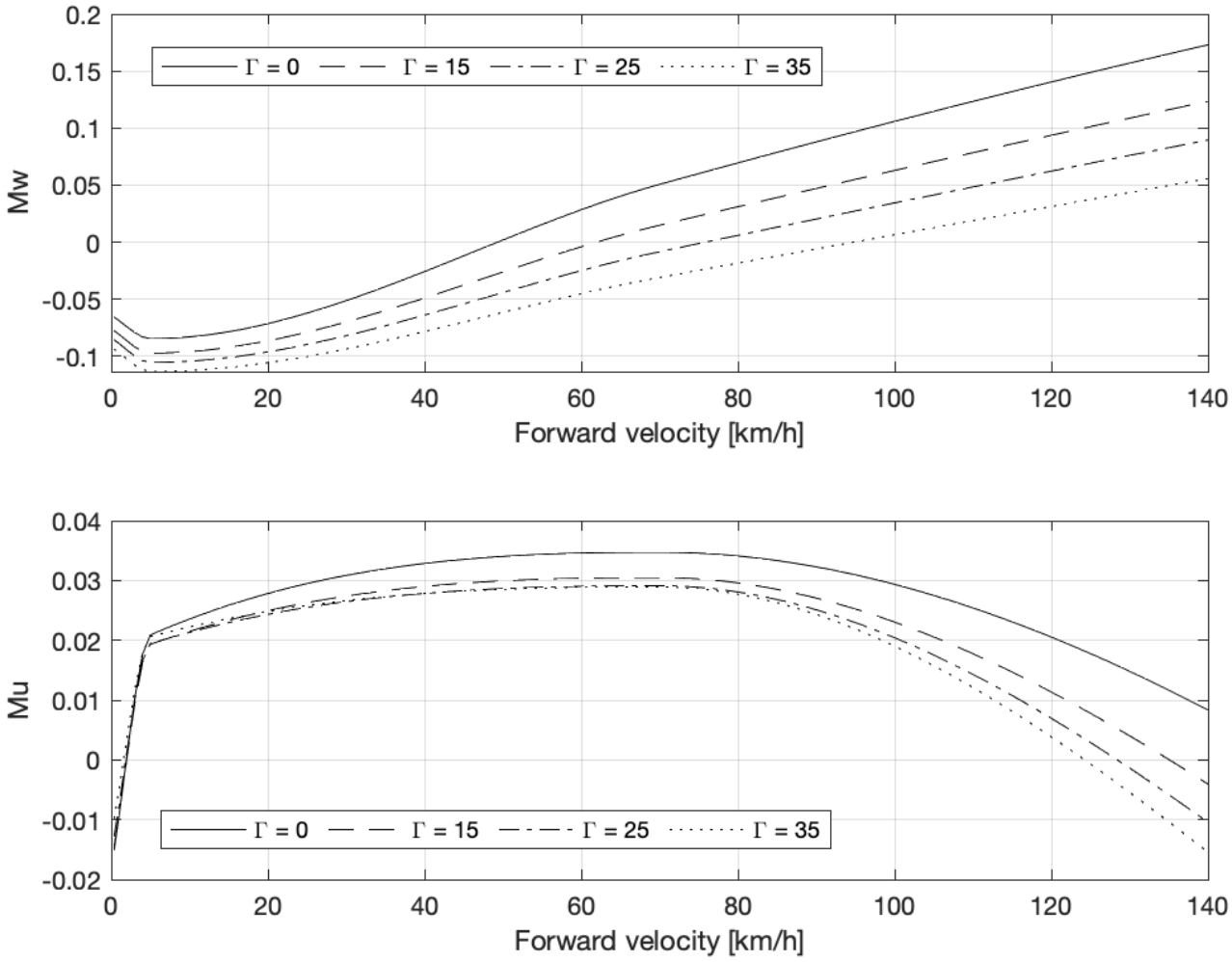

Figure 2.15: Stability derivatives - $M_u M_w$

the three contributions from main rotor, fuselage and horizontal stabilizer. In the case of a synchrotor helicopter, the contribution of the main rotor includes both the rotors, the left and the right one. The horizontal stabilizer always contributes positively to M_w, in fact, to a positive change in w follows an increment in tailplane lift, resulting in a nose-down pitch moment. The contribution of a single main rotor is a combination of a moment proportional to the disc tilt and one to the thrust. It may be stabilizing or destabilizing, it depends on the position of the center of mass with respect to the thrust. If the center of mass is forward it is stabilizing. M_w results to be statically stable if it is negative. For both the derivatives, the dihedral angle does not give a strong contribution, as depicted in Figure 2.15.

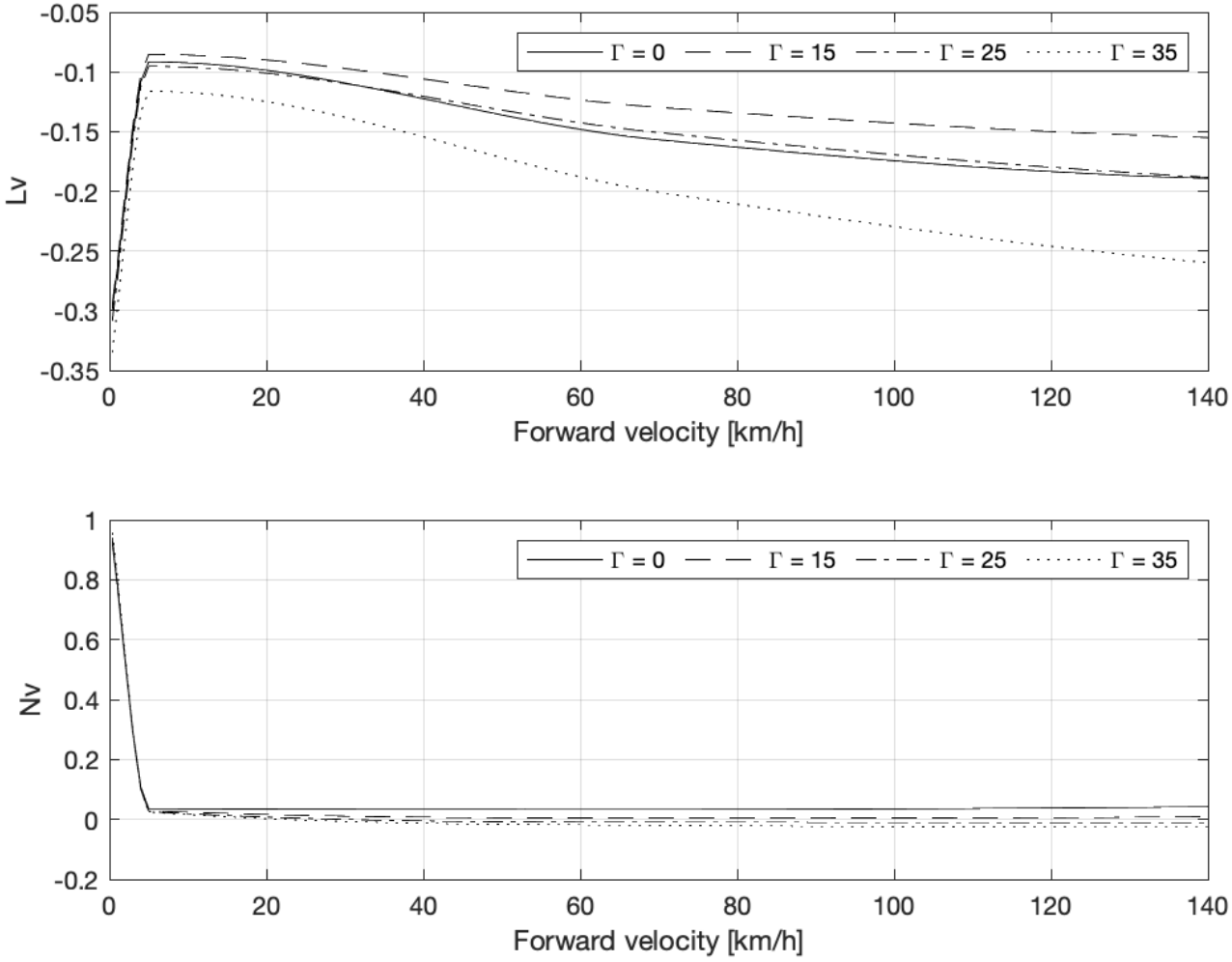

Figure 2.16: Stability derivatives - $L_v N_v$

L_u, L_v, L_w The rolling moment derivatives are strongly related to the yawing ones, belonging to the lateral/directional stability derivatives. The so called dihedral effect L_v is stabilizing if it is negative. As shown in Figure 2.16, L_v has a negative value, indicating a stabilizing effect of the dihedral. L_v is generated similarly to M_u. If a positive lateral velocity perturbation is applied to the synchrotor configuration, both rotors experiences a rolling moment to port, even if the effect is greater for one and less for the other, due to the lateral shaft tilt. The rotor stiffness, the Lock number and the lift on the blades affect the amount of flap response.

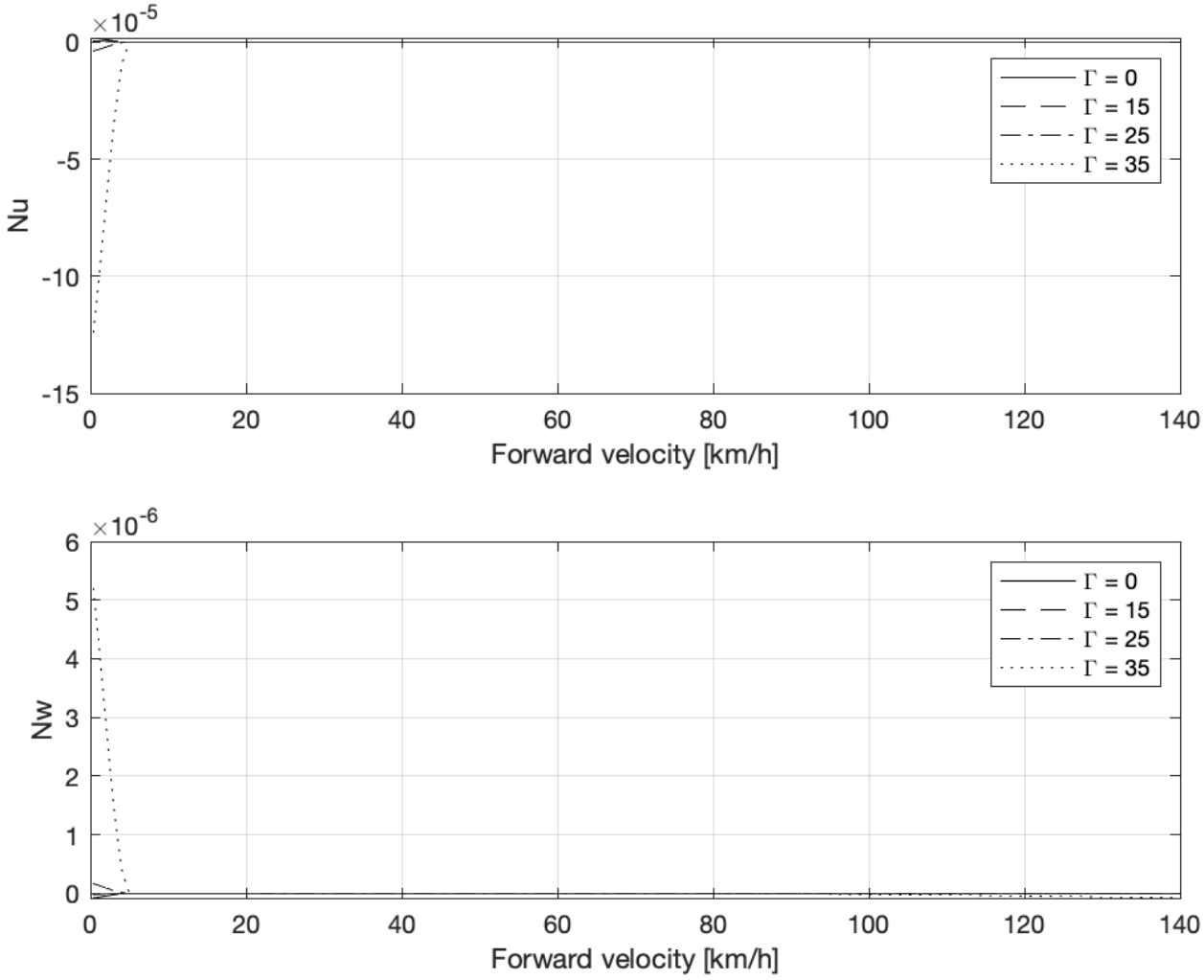

Figure 2.17: Stability derivatives - $N_u N_w$

N_u, N_v, N_w The weathercock stability derivative N_v for a single main rotor helicopter is given by the tail rotor, the fuselage and the vertical fin. In the case of synchrotor, only the fuselage and the vertical fin gives contribution to N_v. It is stabilizing with a positive value. The vertical fin contributes with a positive value; the fuselage is destabilizing if the pressure center is behind the center of mass. N_u and N_w arise from changes in rotors torque due to velocity perturbation, with the vertical fin giving its contribution to N_u similarly to horizontal stabilizer to M_u.

Angular velocity derivatives

The angular velocity force derivatives are often associated with the trim inertial velocity component, that, in some cases, have a primary effect and so the associated derivatives are negligible, like for example Z_q and Y_r.

X_q, Y_p X_q and Y_p are dominated by main rotors. The changes in X and Y forces bring a primary contribution to pitch and roll moments. If small drag forces are ignored, the rotor X force of the main rotor results to be $X = T \cos \frac{\Gamma}{2} a_1$. Accordingly, X_q depends by the flapping derivatives $\frac{\partial a_1}{\partial q}$, that is [87]:

$$\frac{\partial a_1}{\partial q} = -\frac{16}{\gamma \Omega (1 - \frac{e}{R})^2} \tag{2.94}$$

The equation (2.94) represents the disc lag following a pitch rate, that produces a pitch damping moment opposite to q. The Lock number γ, that is the ratio between aerodynamical and inertial forces, plays a crucial role. Y_p analysis agree with that resented above for X_q, with the only differences in sign and flapping angle. With respect to a conventional helicopter, the trend is opposite, due to the presence of two lateral tilted rotors.

M_q, L_p, M_p, L_q This set of stability derivatives has a fundamental role for dynamic analysis. M_q and L_p primary damping derivatives are related to handling characteristics and short-term, while the cross-coupling derivatives M_p and L_q are involved in the pitch-roll and roll-pitch couplings. These are mainly influenced by the main rotors. The moment due to in-plane rotor loads, the moment of the thrust vector tilt from the center of mass and the moment derived from the effective rotor stiffness are the principal components for both the rotor pitching and rolling moments. M_q stability derivative has a strong influence at high speed by the horizontal tailplane.

N_r, L_r These derivatives are involved in in lateral/directional stability and control characteristics of the aircraft. All the yaw derivatives are mostly influenced by the tail rotor and the vertical fin for a conventional single main rotor helicopter, especially the yaw damping derivative N_r. Considering the synchrotor configuration, the absence of the tail rotor contributes to lower the value of the yaw damping derivative. The rolling moment due to yaw rate is mainly influenced by the vertical fin, since the tail rotor contribution is not present. The vertical tail sideforce increases to starboard as the aircraft nose goes to starboard, being L_r positive. It is affected by the product of inertia I_{xz}, that couples the roll into the yaw.

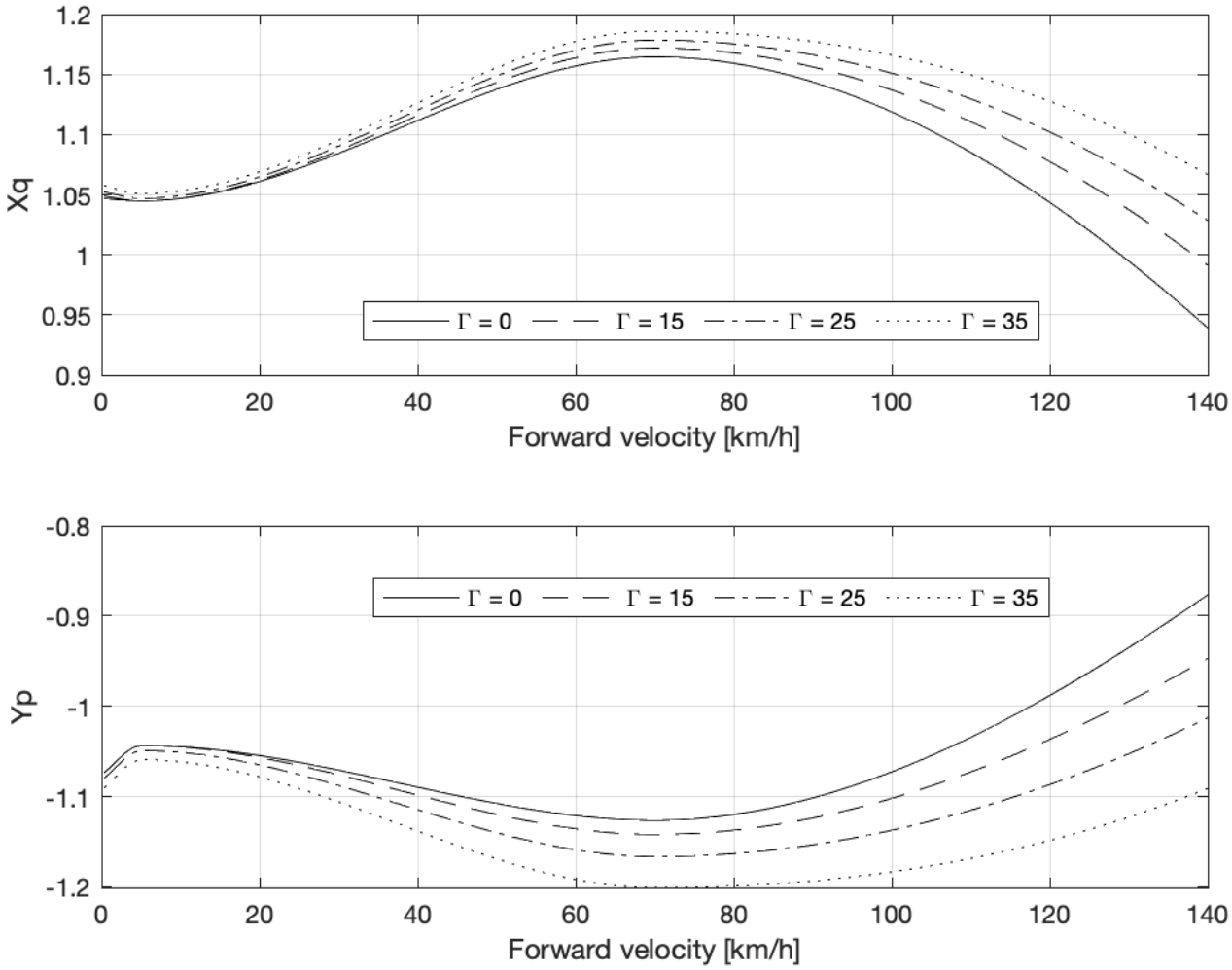

Figure 2.18: Stability derivatives - $X_q Y_p$

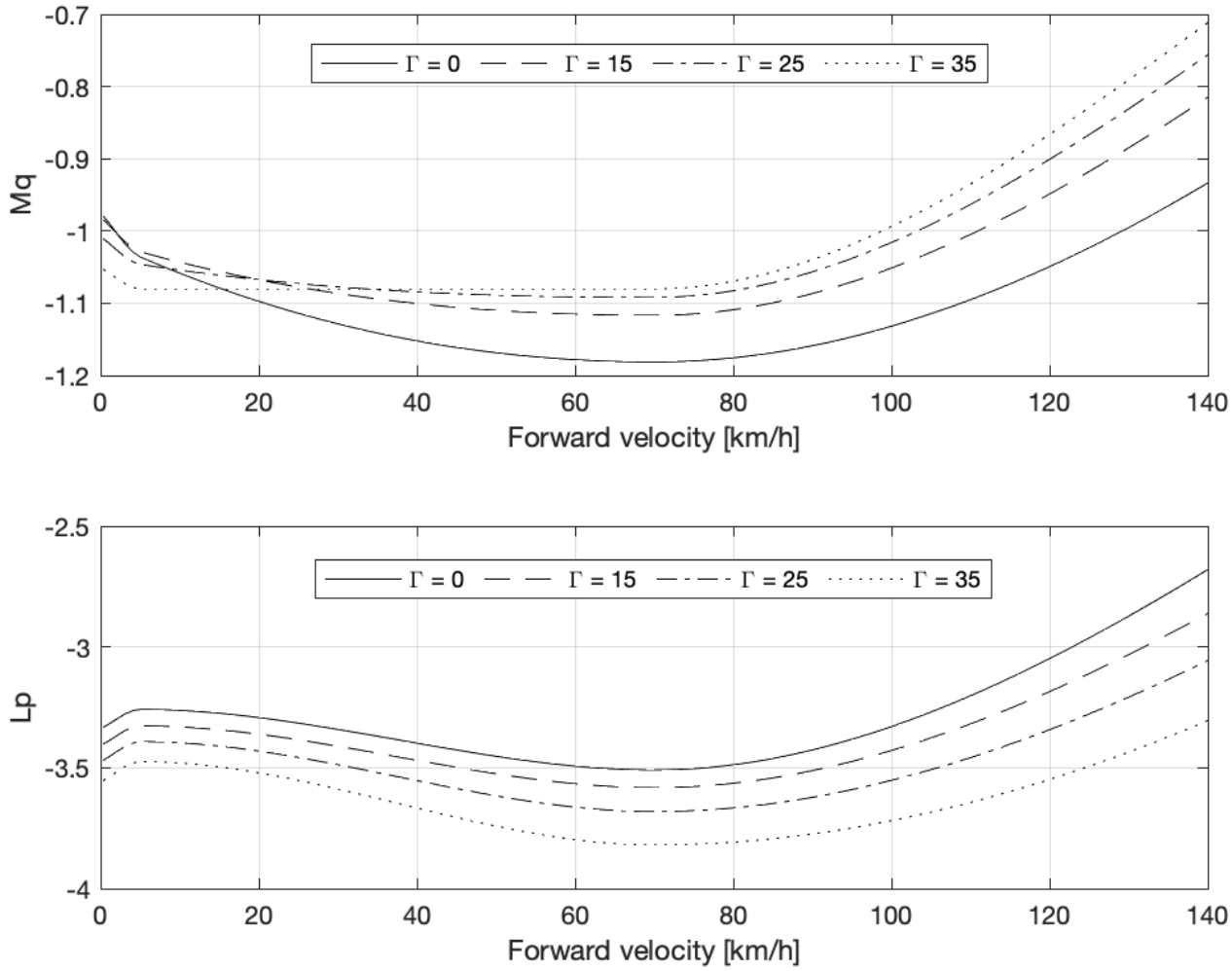

Figure 2.19: Stability derivatives - $M_q L_p$

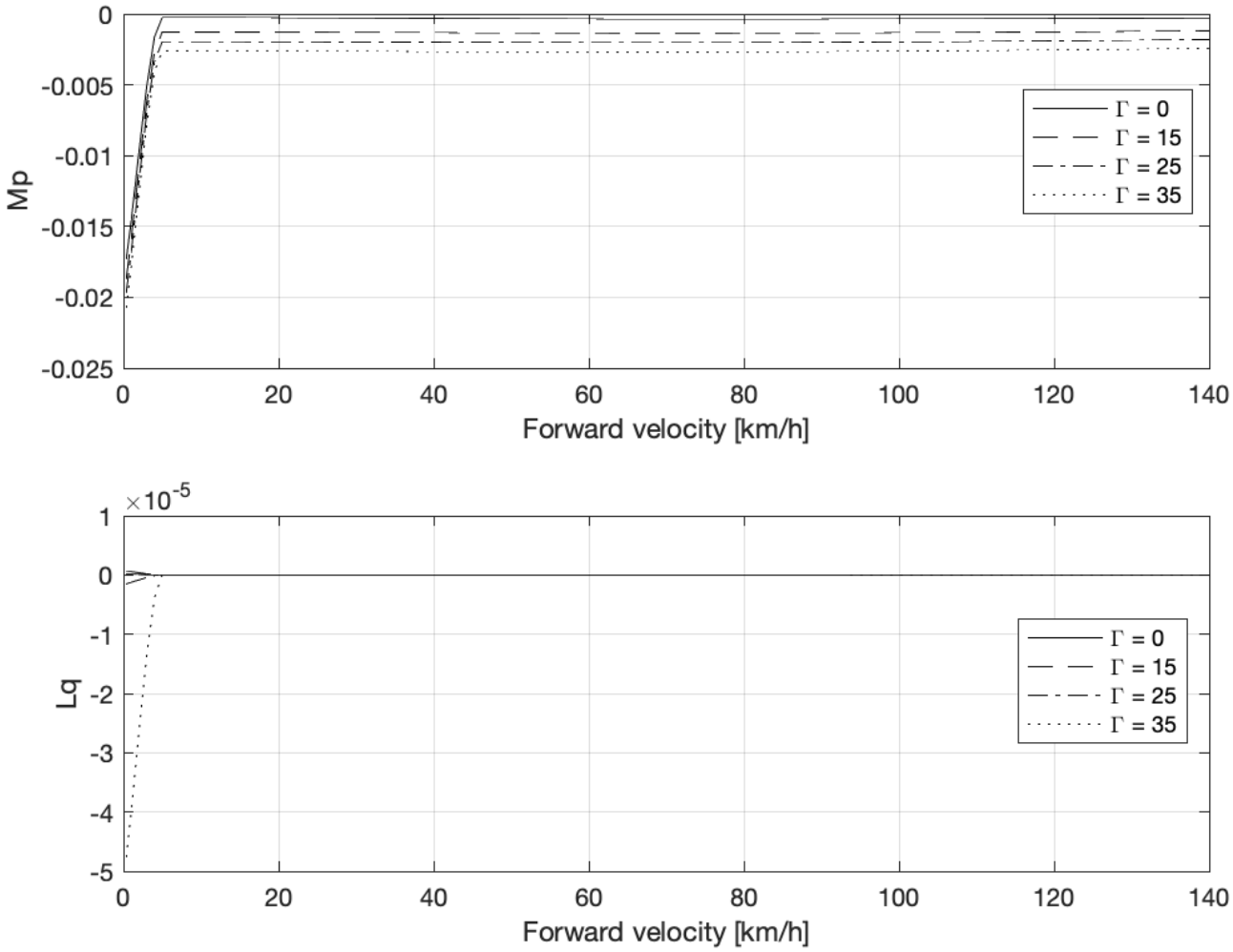

Figure 2.20: Stability derivatives - $M_p L_q$

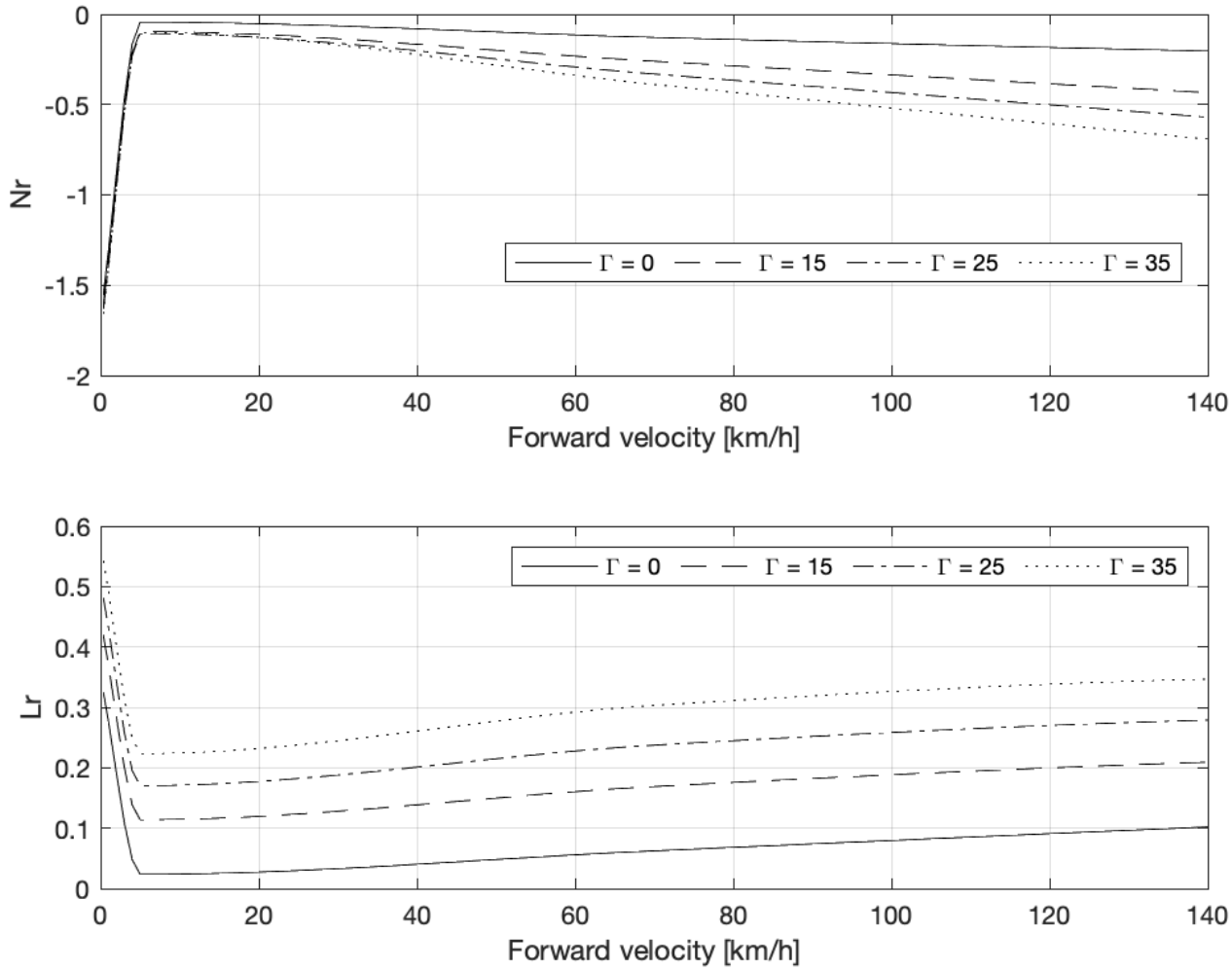

Figure 2.21: Stability derivatives - $L_r N_r$

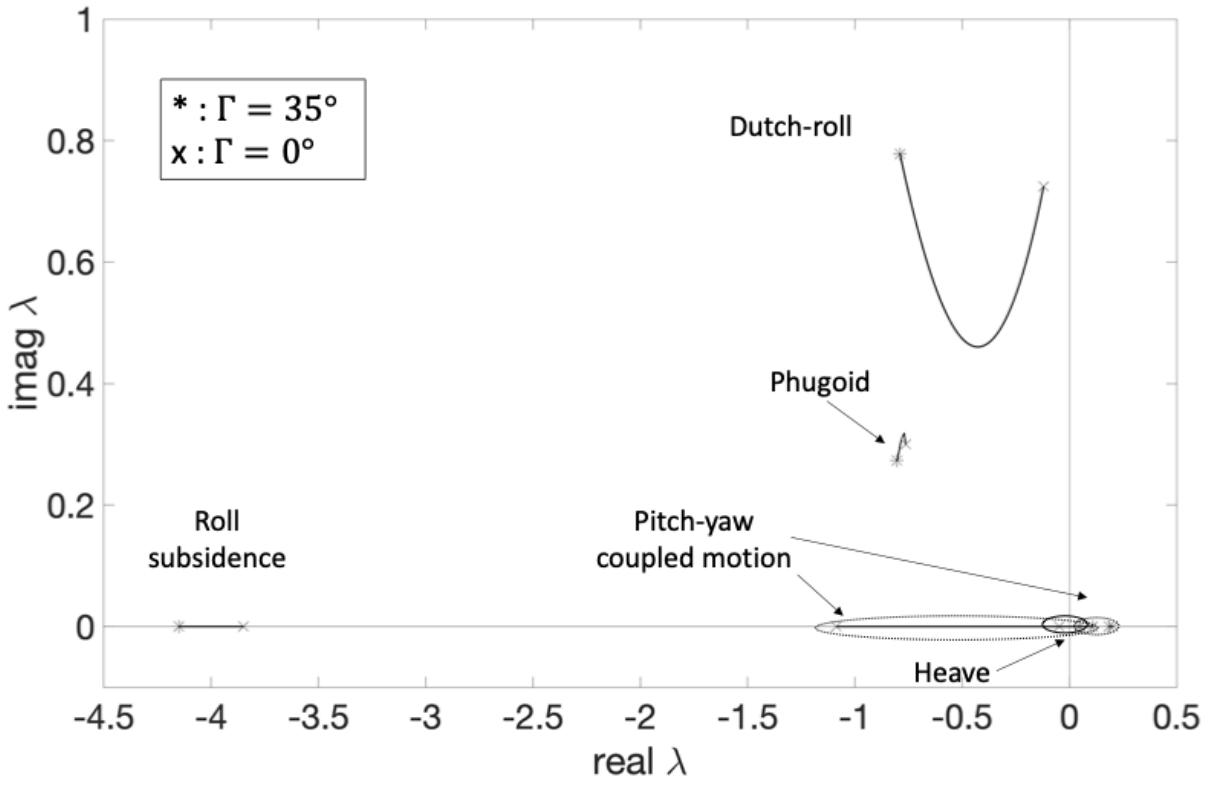

Figure 2.22: Loci of synch coupled eigenvalues as a function of different dihedral angle Γ in hovering

2.2.4 Synch-rotor stability analysis

The linear model obtained in section 2.2.2 is used for the stability analysis in both coupled and decoupled form. The decoupled form consists in longitudinal and lateral sets, in the same way presented by Padfield [86]. Longitudinal state vector consists of $x_{long} = [u \quad w_0 \quad w \quad q]^T$, where $w_0 = w - U_e\Theta$, while lateral state vector is $x_{lat} = [v_0 \quad v \quad \dot{v} \quad p]^T$ with $v_0 = v + U_e\psi$. Coupled and decoupled state and control matrices are reported in Appendix D of chapter D. The approximation done to decouple the system is that the eigenvalues fall into two separated sets on the complex plane. For stability analysis purpose, the equation associated to the heading angle state variable ψ is omitted, that is the kinematic equation relating the change of ψ euler angle to the rate p, q, r.

Figure 2.22 illustrates the eigenvalues for the synch-rotor of the coupled system in hovering condition for Γ varying from 0 deg to 35 deg. Looking first to the phugoid mode, it is a stable oscillation for all the dihedral angles considered, as the Dutch-roll oscillation. The other modes are the roll subsidence and heave and the pitch-yaw coupled motion.

In Figure 2.23 and Figure 2.24 are reported the decoupled motions.

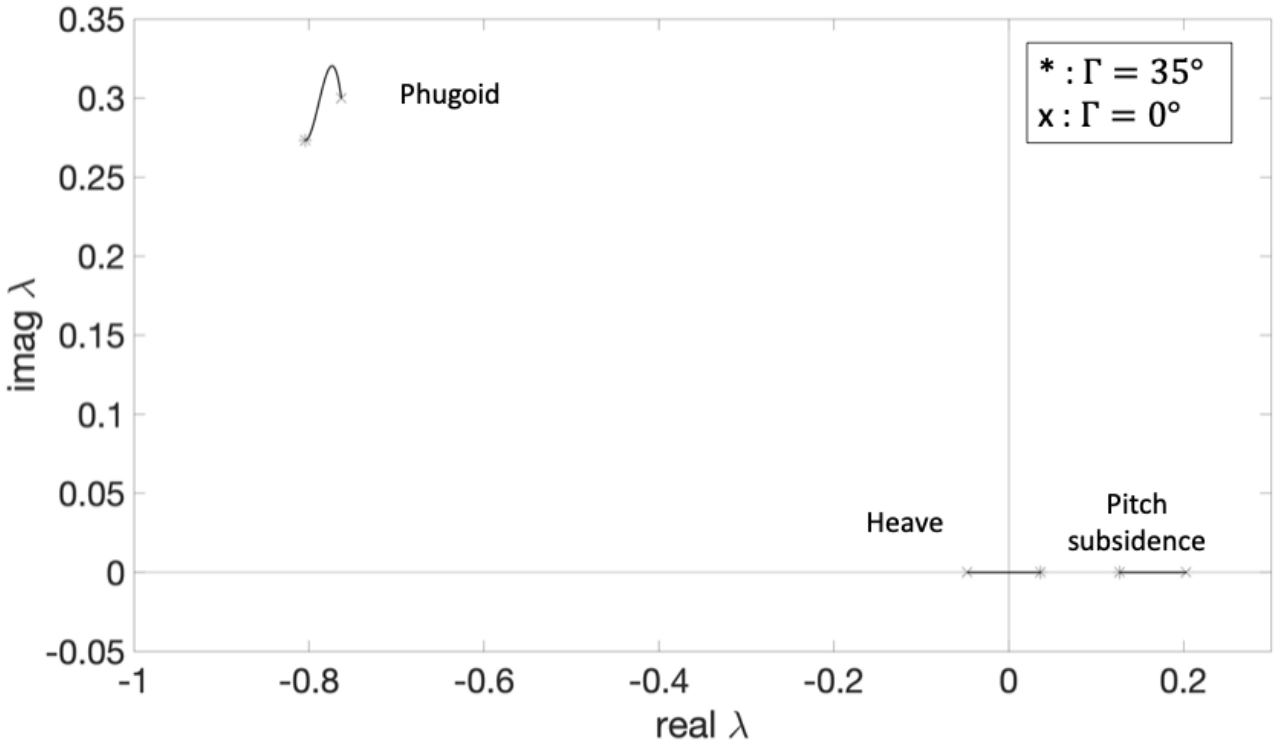

Figure 2.23: Loci of synch longitudinal eigenvalues as a function of different dihedral angle Γ in hovering

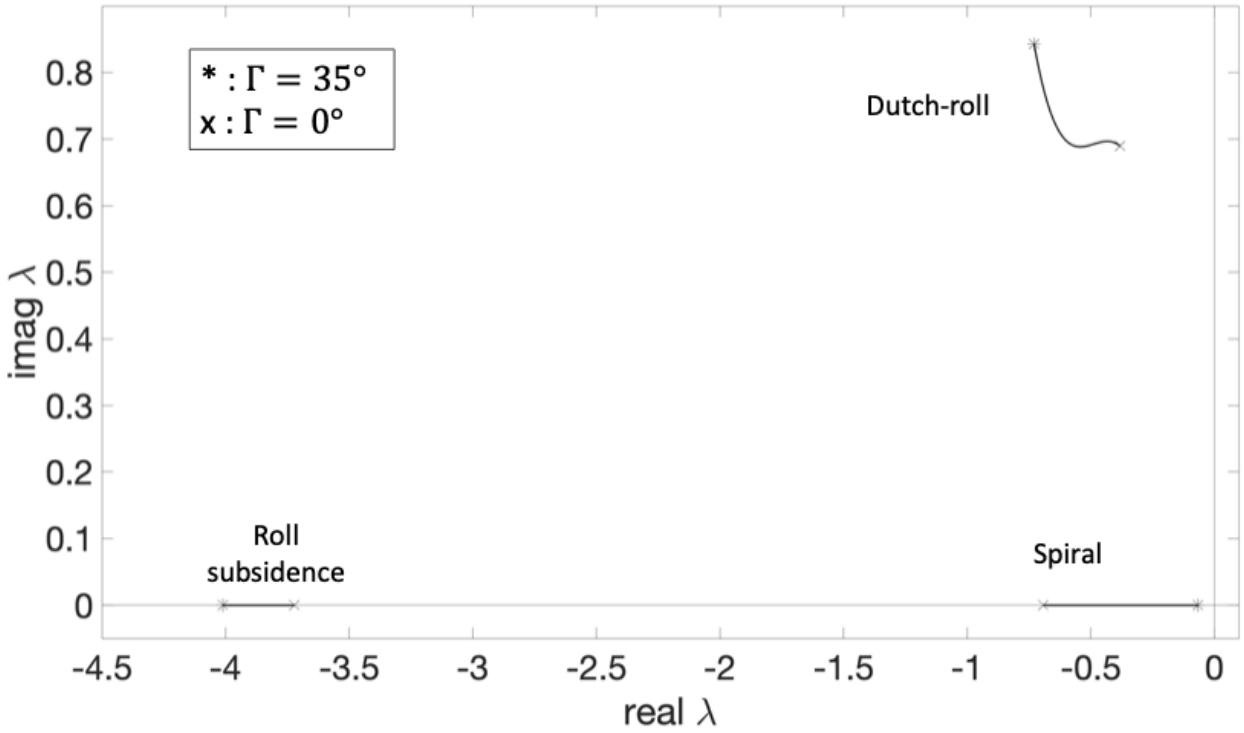

Figure 2.24: Loci of synch lateral eigenvalues as a function of different dihedral angle Γ in hovering

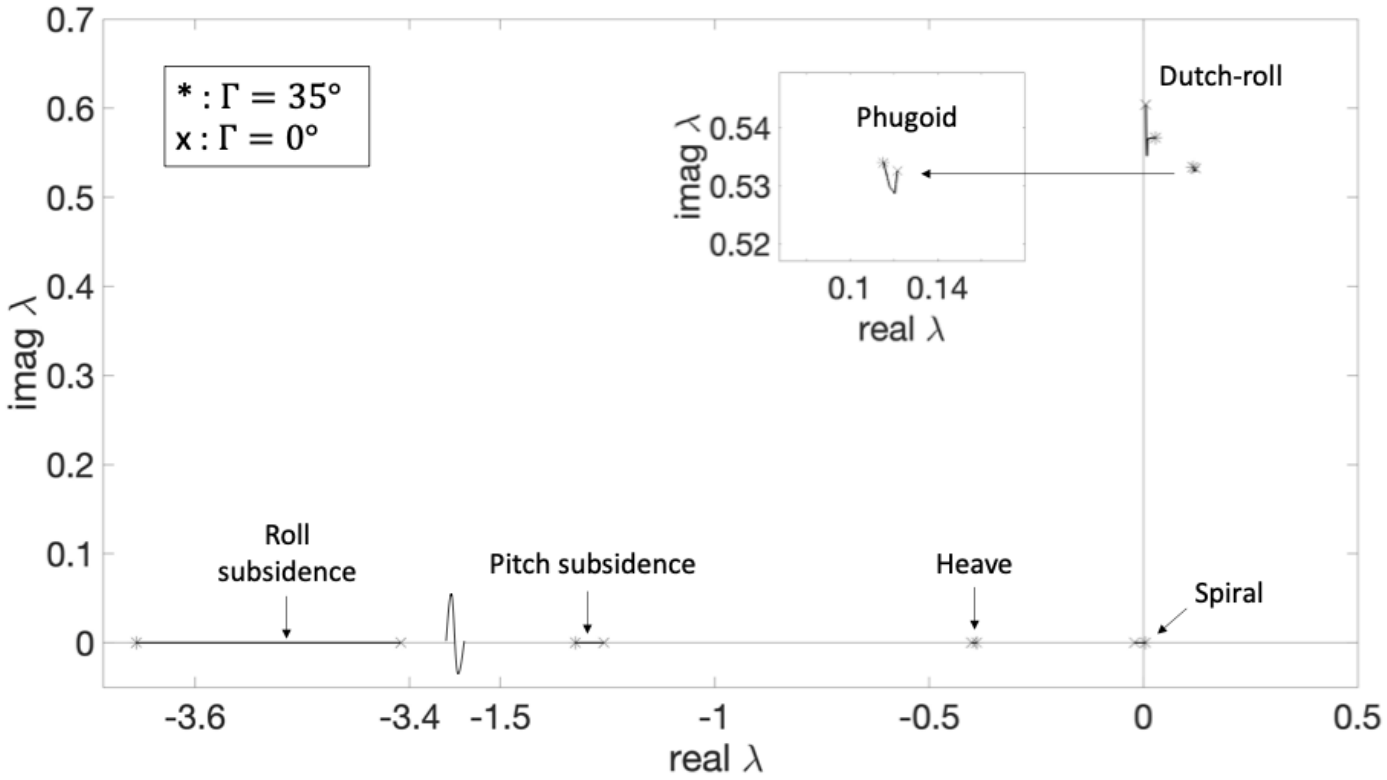

Figure 2.25: Loci of synch coupled eigenvalues as a function of different dihedral angle Γ in hovering without the horizontal stabilizer

The phugoid behaviour for a conventional single main rotor helicopter is usually unstable [86]. With the aim to deepen this aspect, the eigenvalues of the synch-rotor configuration obtained only considering the two counter-rotating intermeshing rotors and the fuselage are reported in hovering for the same set of dihedral angles. As shown in Figures 2.25, 2.26 and 2.27, without the horizontal stabilizer, the vehicle results in an unstable phugoid mode.

Figure 2.28, Figure 2.29 and Figure 2.30 show the poles of the synch-rotor for both coupled and decoupled systems at a straight and level flight condition with a forward speed of 140 km/h for different values of Γ. At high speed, the phugoid mode for the complete aircraft is still a stable oscillation. On the contrary, the Dutch-roll mode presents an unstable behaviour.

Longitudinal dynamics

The longitudinal model involves the u, q, w and θ variables, as explained at the beginning of this section. At the hovering condition, the approximation of the phugoid frequency and

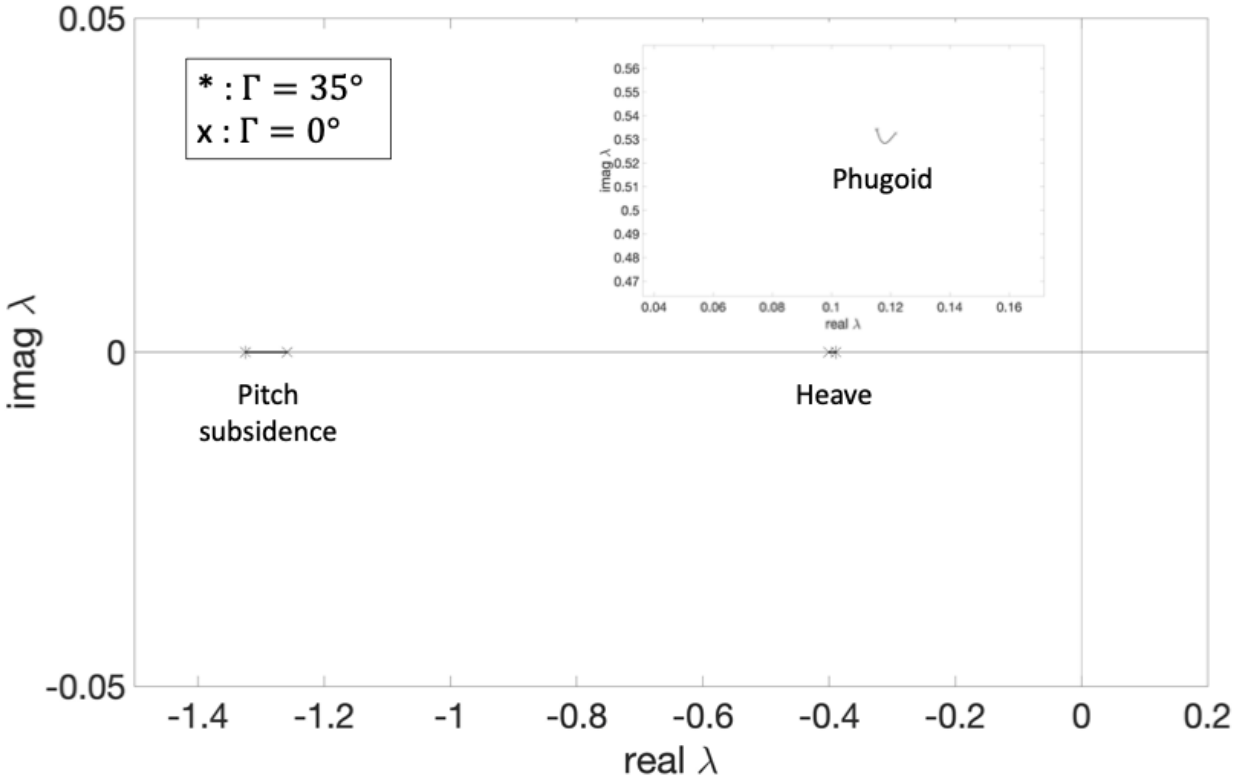

Figure 2.26: Loci of synch longitudinal eigenvalues as a function of different dihedral angle Γ in hovering without the horizontal stabilizer

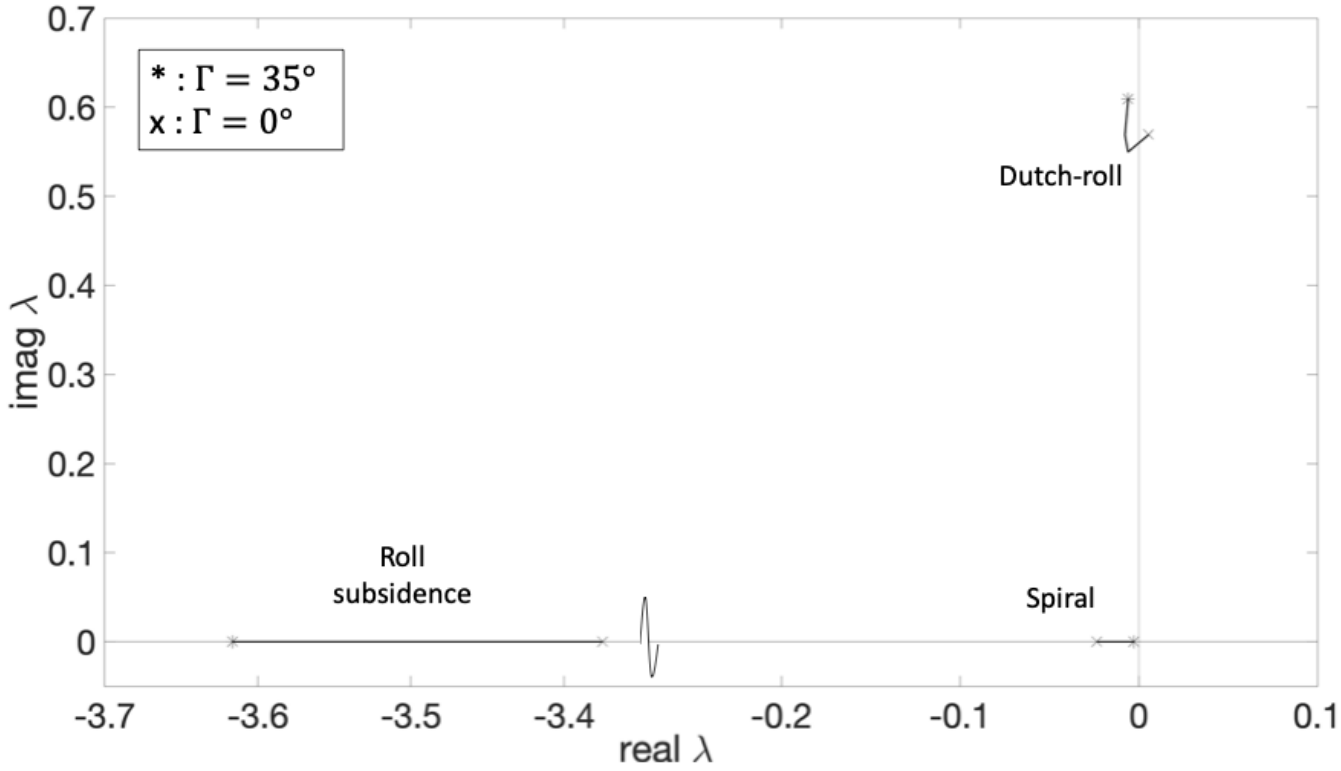

Figure 2.27: Loci of synch lateral eigenvalues as a function of different dihedral angle Γ in hovering without the horizontal stabilizer

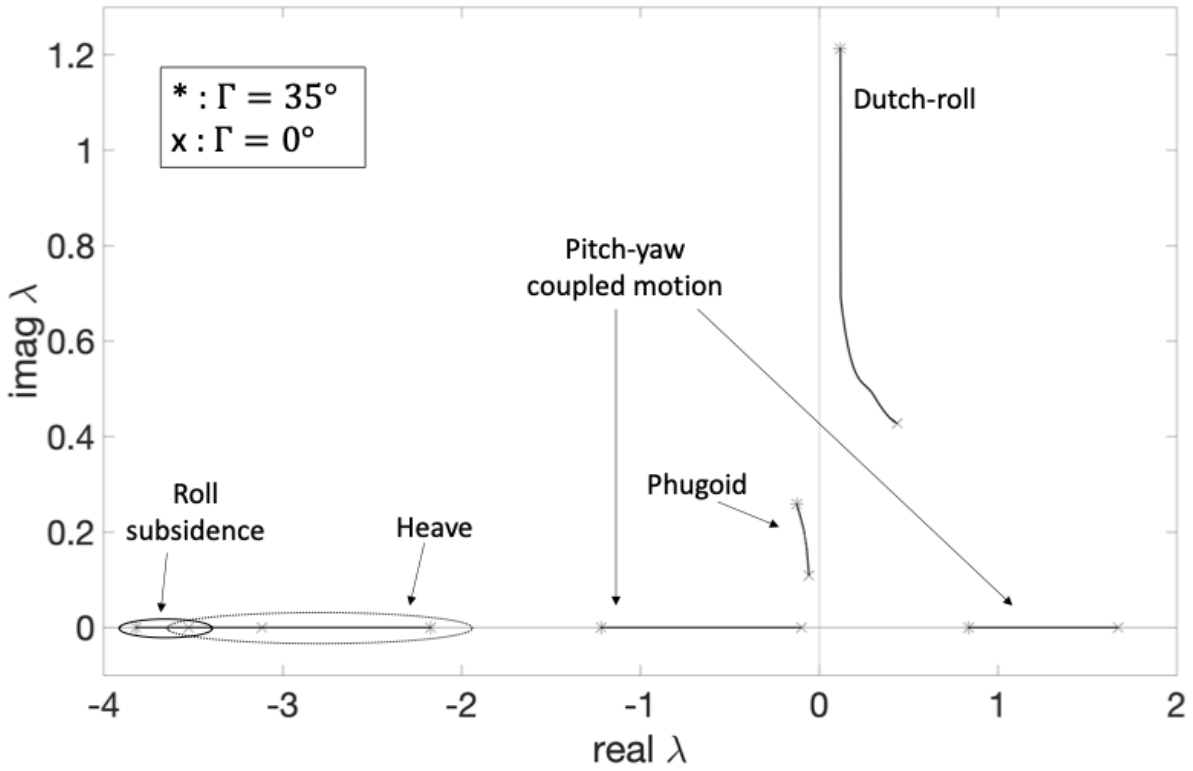

Figure 2.28: Loci of synch coupled eigenvalues as a function of different dihedral angle Γ at 140 km/h

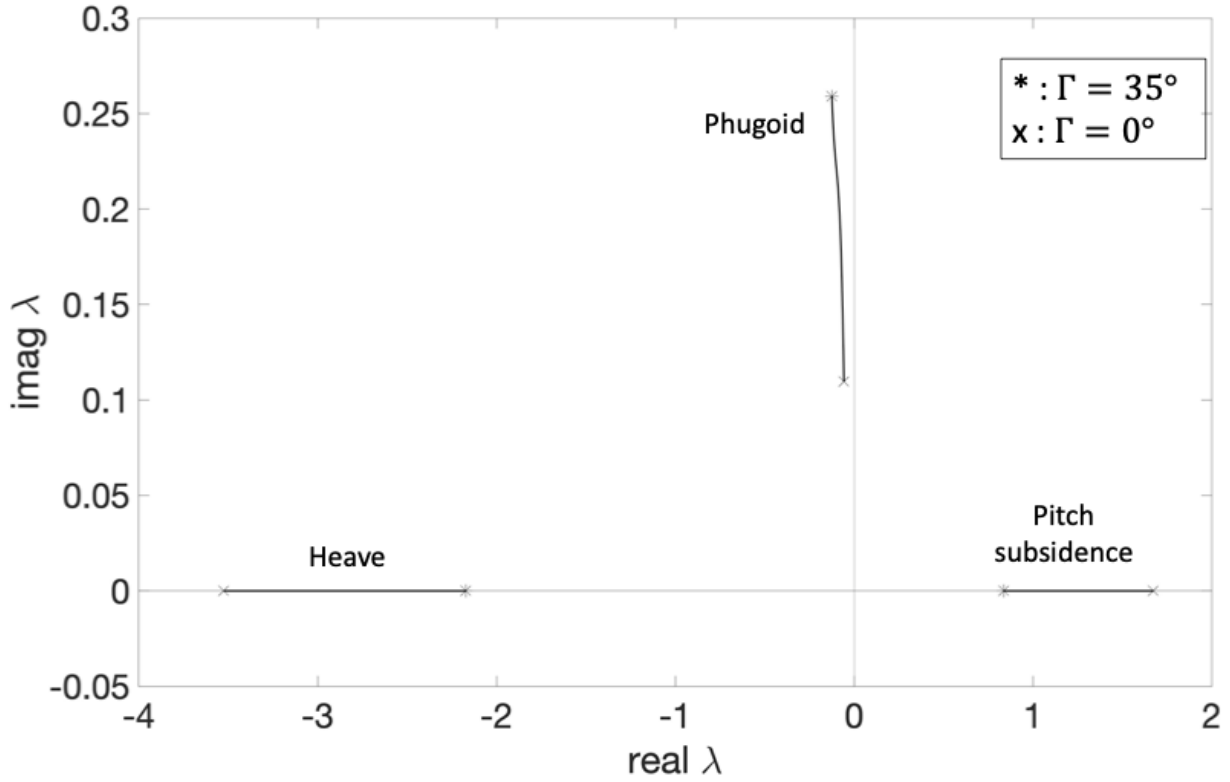

Figure 2.29: Loci of synch longitudinal eigenvalues as a function of different dihedral angle Γ at 140 km/h

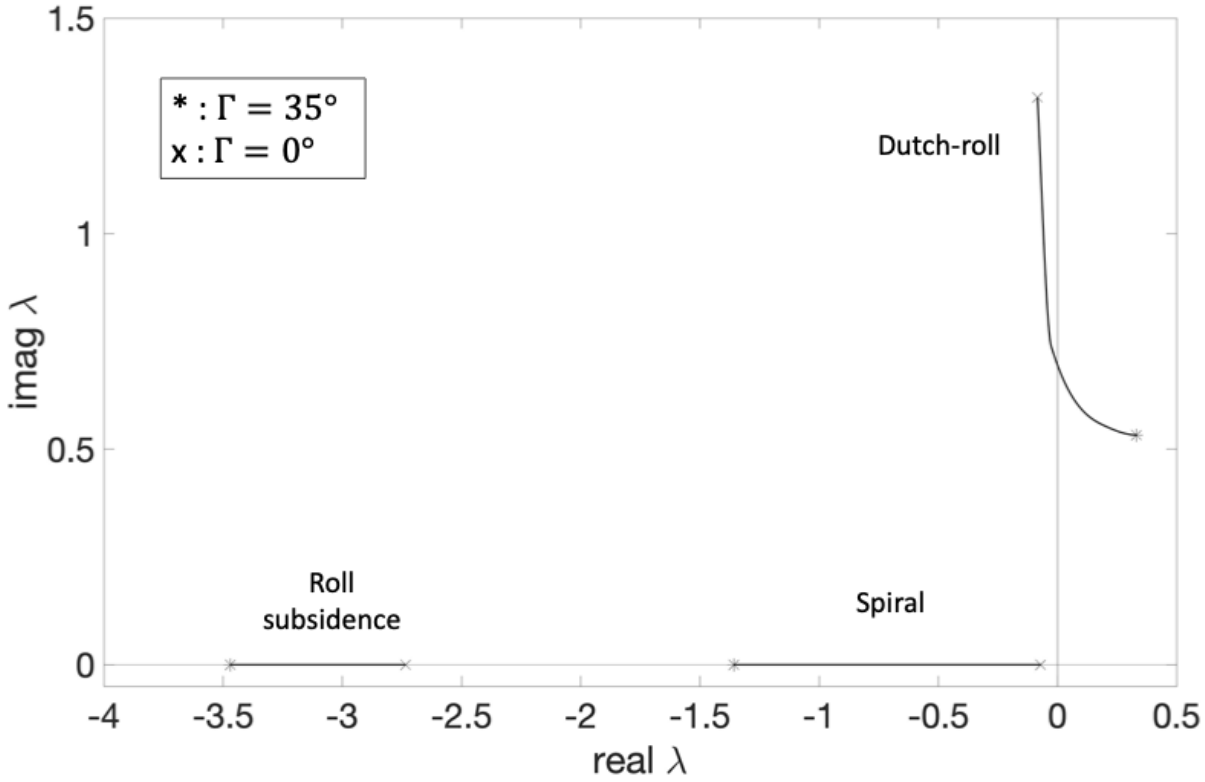

Figure 2.30: Loci of synch lateral eigenvalues as a function of different dihedral angle Γ at 140 km/h

damping presented by Padfield [86], that are:

$$\omega_p^2 = -g\frac{M_u}{M_q} \tag{2.95}$$

$$2\omega_p\zeta_p = -(X_u + g\frac{M_u}{M_q^2}) \tag{2.96}$$

are not valid for the synchrotor, for all the investigated Γ angles. At low forward speed of 5 km/h, the approximation gives better results, as for some conditions at higher velocities, whose approximation is again that reported in [86]. Frequency and damping values for phugoid are given in Table 2.2 for the synch-rotor configuration with the dihedral angle varying from 0° to 35° in hovering and at 5, 70 and 140 km/h :

Table 2.2: Comparison of exact and approximated values of phugoid frequency and damping

Hovering	ω_{app}	ζ_{app}	ω_{ex}	ζ_{ex}
$\Gamma = 0°$	0.3895	0.2776	0.8199	0.9307
$\Gamma = 15°$	0.3814	0.2750	0.8340	0.9240
$\Gamma = 25°$	0.3532	0.2652	0.8422	0.9310
$\Gamma = 35°$	0.3026	0.2545	0.8492	0.9467
$5\ km/h$	ω_{app}	ζ_{app}	ω_{ex}	ζ_{ex}
$\Gamma = 0°$	0.4447	-0.1922	0.4634	-0.1805
$\Gamma = 15°$	0.4292	-0.1370	0.4401	-0.1770
$\Gamma = 25°$	0.4270	-0.1306	0.4261	-0.1712
$\Gamma = 35°$	0.4326	-0.1250	0.4145	-0.1625
$70\ km/h$	ω_{app}	ζ_{app}	ω_{ex}	ζ_{ex}
$\Gamma = 0°$	11.197	-0.1593	0.5250	-0.4556
$\Gamma = 15°$	0.6538	-0.1615	0.4940	-0.2446
$\Gamma = 25°$	0.4638	-0.1622	0.4626	-0.0748
$\Gamma = 35°$	0.3783	-0.1632	0.4128	0.0949
$140\ km/h$	ω_{app}	ζ_{app}	ω_{ex}	ζ_{ex}
$\Gamma = 0°$	0.1073	0.8195	0.1236	0.4620
$\Gamma = 15°$	0.1700	0.3367	0.1786	0.3863
$\Gamma = 25°$	0.2190	0.3626	0.2225	0.3857
$\Gamma = 35°$	0.2994	0.4198	0.2874	0.4331

Lateral/directional dynamics

The lateral/directional model concerns the p, v, r and ϕ variables, in the same way exposed at the beginning of this section. As for a conventional helicopter configuration, the involved modes are the Dutch-roll oscillation and the roll and spiral aperiodic subsidences. The roll subsidence mode is well characterized by the L_p stability derivative. For the synch-rotor, the roll damping stability derivative outlines the roll mode throughout the speed envelope. With regards to the spiral mode, the expression reported by Padfield is valid also for the synch-rotor for almost the flight conditions. Furthermore, the approximation for the oscillatory Dutch-roll is still suitable for the intermeshing configuration, even if there are some discrepancies, especially for the damping estimation in hovering condition. Table 2.3 reports the exact and approximated values for the lateral/directional modes for the synch-rotor configuration with a dihedral angle varying from 0° to 35° at four different forward velocities.

Table 2.3: Comparison of exact and approximated values of lateral/directional modes

Hovering	ω_d	ζ_d	λ_r	λ_s
$\Gamma = 0° - App.$	0.7219	-4.1388	-3.332	-0.4957
$\Gamma = 0° - Ex.$	0.7881	0.4840	-4.0104	-0.6922
$\Gamma = 15° - App.$	0.6091	-4.43	-3.4019	-0.2641
$\Gamma = 15° - Ex.$	0.9413	0.6597	-3.8162	-0.2500
$\Gamma = 25° - App.$	0.5756	-4.5555	-3.4686	-0.1546
$\Gamma = 25° - Ex.$	1.048	0.6651	-3.9032	-0.1217
$\Gamma = 35° - App.$	0.5626	-4.6199	-3.553	-0.0908
$\Gamma = 35° - Ex.$	1.1146	0.6545	-4.0104	-0.0657
$5\ km/h$	ω_d	ζ_d	λ_r	λ_s
$\Gamma = 0° - App.$	0.5647	0.0896	-3.2586	-0.0305
$\Gamma = 0° - Ex.$	0.5537	0.0180	-3.3398	-0.0305
$\Gamma = 15° - App.$	0.5503	0.3394	-3.3266	-0.0514
$\Gamma = 15° - Ex.$	0.5251	0.0528	-3.4079	-0.0512
$\Gamma = 25° - App.$	0.5784	0.4501	-3.3918	-0.0550
$\Gamma = 25° - Ex.$	0.5423	0.0555	-3.483	-0.0548
$\Gamma = 35° - App.$	0.6320	0.5026	-3.4743	-0.0495
$\Gamma = 35° - Ex.$	0.5833	0.0463	-3.5815	-0.0493
$70\ km/h$	ω_d	ζ_d	λ_r	λ_s
$\Gamma = 0° - App.$	0.9047	0.0864	-3.509	-0.0616
$\Gamma = 0° - Ex.$	0.8920	0.0504	-3.559	-0.0625

$\Gamma = 15° - App.$	0.4995	0.3133	-3.5825	-0.3636
$\Gamma = 15° - Ex.$	0.5091	-0.0508	-3.6365	-0.3438
$\Gamma = 25° - App.$	0.0556	3.6101	-3.6815	-4.52
$\Gamma = 25° - Ex.$	0.4503	-0.3361	-3.7459	-0.6739
$\Gamma = 35° - App.$	0.3782	0.6323	-3.8192	1.52
$\Gamma = 35° - Ex.$	0.4900	-0.4478	-3.8987	-0.8800
$140km/h$	ω_d	ζ_d	λ_r	λ_s
$\Gamma = 0° - App.$	1.3476	0.0827	-2.68	-0.0690
$\Gamma = 0° - Ex.$	1.3186	0.0638	-2.7344	-0.0706
$\Gamma = 15° - App.$	0.7862	0.2880	-2.8615	-0.3643
$\Gamma = 15° - Ex.$	0.7390	0.0360	-2.9491	-0.3986
$\Gamma = 25° - App.$	0.1056	2.8092	-3.0567	3.18
$\Gamma = 25° - Ex.$	0.5886	-0.3402	-3.1777	-0.9809
$\Gamma = 35° - App.$	0.6975	0.5159	-3.3045	1.16
$\Gamma = 35° - Ex.$	0.6273	-0.5274	-3.469	-1.36

The approximated expression for the spiral, roll and Dutch-roll mode employed are:

$$\lambda_s \approx \frac{g}{L_p}\frac{(L_v N_r - N_v L_r)}{(U_e N_v + \sigma_s L_v)} \tag{2.97}$$

$$\lambda_r \approx L_p \tag{2.98}$$

$$2\omega_d\zeta_d \approx -(N_r + Y_v + \sigma_s\{\frac{L_r}{U_e} - \frac{L_v}{L_p}\})/(1 - \frac{\sigma_s L_r}{L_p U_e}) \tag{2.99}$$

$$\omega_d^2 \approx (U_e N_v + \sigma_s L_v)/(1 - \frac{\sigma_s L_r}{L_p U_e}) \tag{2.100}$$

where $\sigma_s = \frac{g - N_p U_e}{L_p}$.

2.3 Rover model

The mathematical modelling of the rover used for simulations is detailed in this section. A rover with four wheels is considered. The steering system enables a terrestrial vehicle to move. Depending on the required precision, the steering system is chosen. Briefly, the different steer configurations depend upon the Instantaneous Center of Rotation (ICR) definition. This point is the intersection of the four wheel axes if there is no wheels slip. On the contrary, it is not possible to define a unique ICR. Among the steering systems, the common ones are:

1. Independent steering
2. Ackermann steering
3. Articulated frame
4. Skid steering
5. Articulated axle

In this work an independent steering model is presented and used for subsequent simulations.

Rover independent steering model In the independent steering model rover the left and the right wheels may spin independently. The model presented relies on reference [77]. The state vector is $x = [x_N \ y_E \ \chi]$, where x_N and y_E are the north and the east vehicle position in meters and χ is the heading angle in radians. The kinematics equations are written depending on which input vector is chosen. If the input vector contains the wheels speed, equations are:

$$\begin{bmatrix} \dot{x_N} \\ \dot{y_E} \\ \dot{\chi} \end{bmatrix} = \begin{bmatrix} \frac{r}{2}\cos\chi & \frac{r}{2}\cos\chi \\ \frac{r}{2}\sin\chi & \frac{r}{2}\sin\chi \\ -\frac{r}{2d} & -\frac{r}{2d} \end{bmatrix} \begin{bmatrix} \dot{\phi_L} \\ \dot{\phi_R} \end{bmatrix} \tag{2.101}$$

where r is the wheel radius in meters, d is the track width in meters, $\dot{\phi_L}$ and $\dot{\phi_R}$ are the left and right wheel speed in m/s.

If the inputs are the speed and the heading angular rate, equations are:

$$\begin{bmatrix} \dot{x_N} \\ \dot{y_E} \\ \dot{\chi} \end{bmatrix} = \begin{bmatrix} \cos\chi & 0 \\ \sin\chi & 0 \\ 0 & 1 \end{bmatrix} \begin{bmatrix} v \\ \omega \end{bmatrix} \tag{2.102}$$

where $v = \frac{r}{2}(\dot{\phi_L} + \dot{\phi_R})$ is the rover speed in m/s and $\omega = \frac{r}{2d}(\dot{\phi_R} - \dot{\phi_L})$ is the vehicle angular velocity in rad/s.

Figure 2.31 shows the principal parameters.

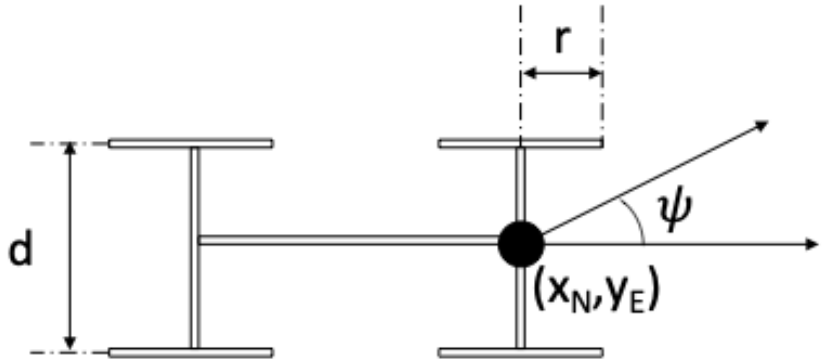

Figure 2.31: Rover independent steering model

CHAPTER 3

Control systems algorithms

Helicopters are intrinsically unstable aircraft and operations require adequate piloting skills for both manned and unmanned configurations. The development of suitable control systems is thus a mandatory task. The architectural overview of the flight control system for the helicopters is reported in figure 3.1. Basically, classical approach has been implemented to stabilize the attitude and to control the speed of the vehicles. These controllers are used both as baseline controllers for developing the adaptive ones, both to be used also in the cooperative scenario. The well-known mathematics of these control systems allowed the author to safely test the algorithms during the flight campaign. After the classical controllers, modern control approaches have been investigated and the $\mathcal{L}_1$ adaptive technique has been applied to improve baseline performances. As for the case of classical ones, the control systems are designed to stabilize the attitude of the vehicle and to control the speed. Both the approaches are finally integrated to be used by the vehicles in the cooperative scenario. Formation control strategies are presented. In particular, the author discusses an architecture that allows the pilot that control the formation to switch among different strategies without difficulties. This means that it is possible to to modify the formation configuration throughout the flight. In addition, the proposed framework make the vehicles autopilot independent from the cooperative one. In this way, it is easier to implement and test many different agents control systems in the cooperative framework, without changing the cooperative control algorithm and make it simple to be implemented for the experimental campaign.

At the beginning of this chapter the classical strategies are described in the first section.

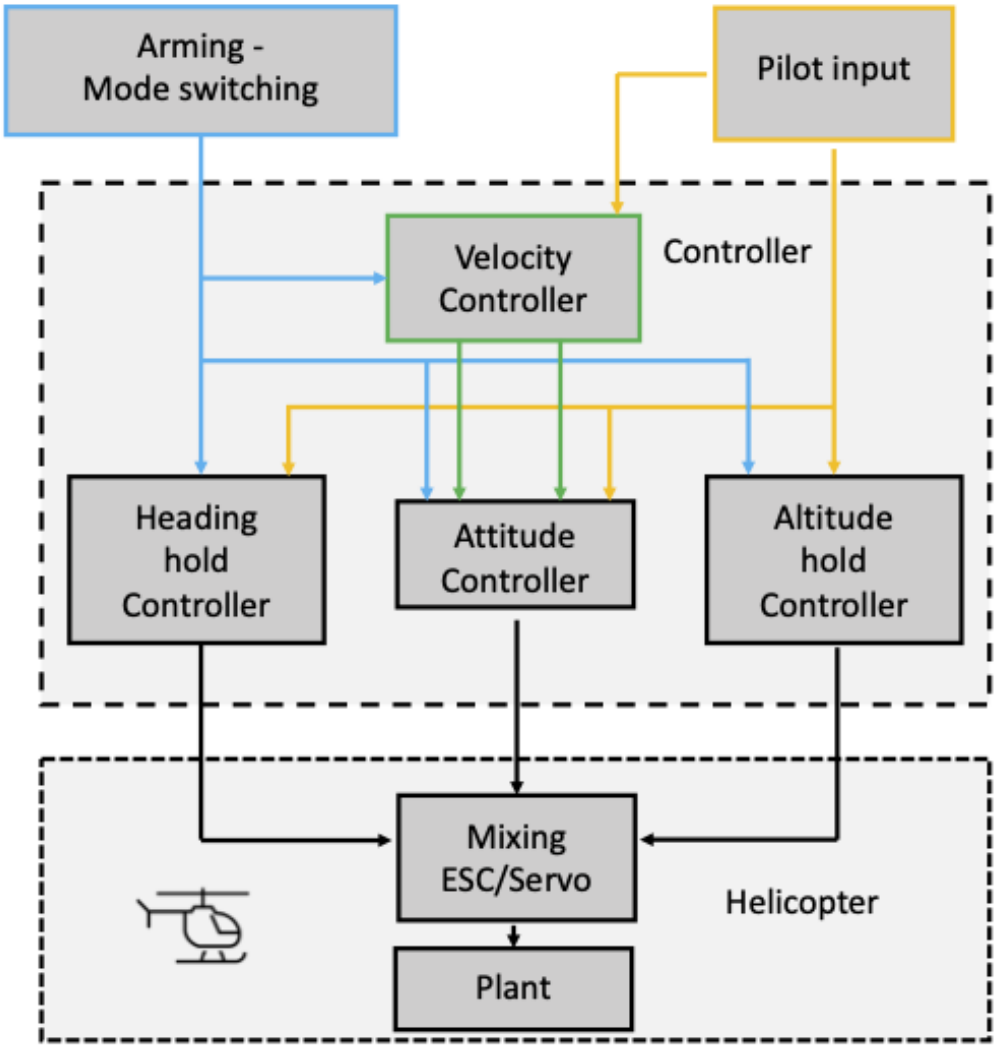

Figure 3.1: Flight control software overview

Then the adaptive controllers are illustrated. Finally, the cooperative control strategies are reported.

3.1 Classical flight controllers

This section provides the description of the classical controllers for a remotely-piloted small-scale helicopter and for a synchrotor. Essentially, PIDs based control systems are developed for the attitude stabilization and for the speed controller. The attitude controller is first described and subsequently the speed controller.

Proportional-Integral-Derivative (PID) control technique dominates in many practical control problems and offers simple and effective solutions [78], [79]. Despite the availability of an advanced class of control schemes, PID controllers are still used to solve many industrial problems. So far, numerous design methods and techniques for tuning have been developed. PID gains may be set based on the system parameters if these can be estimated precisely. Differently, the system may be considered like a black-box and PID gains can be calculated just based on the system tracking error if the system parameters are unknown. For these reasons, PID control technique has been chosen as baseline controller. It is organized as a cascade control system [80], in which a primary controller and a primary dynamics are components of the outer loop. This outer loop incorporates a secondary control loop and it calculates the inner loop's set-points. Moreover, in order to achieve good results, the inner loop should have much faster dynamics than the outer loop. This assumption helps them to limit potential interactions and improve stability characteristics. Thus, a higher gain in the inner loop can be set. Angular rates and attitudes are used as measured feedback signals. Thanks to the application of a cascade control structure, the PID control strategy can be adapted to control the helicopter complex dynamics. In the sections below, each flight controller is explained.

3.1.1 Attitude controller

Figures 3.2 and 3.3 show the controller architecture for attitude control on roll and pitch axes.

The outer loop deals with the Euler angles ϕ and θ, respectively, the roll and the pitch angles. It utilizes attitude estimations calculated into the helicopter model during the simulations or during flight the attitude estimations calculated by the extended Kalman filter of the Pixhawk®, whose characteristics are presented in chapter 5. Here a proportional gain is used. The inner loop concerns with the angular velocities in a PI scheme. Let's

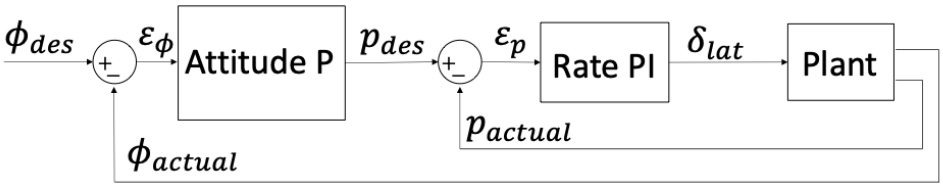

Figure 3.2: Helicopter roll controller architecture

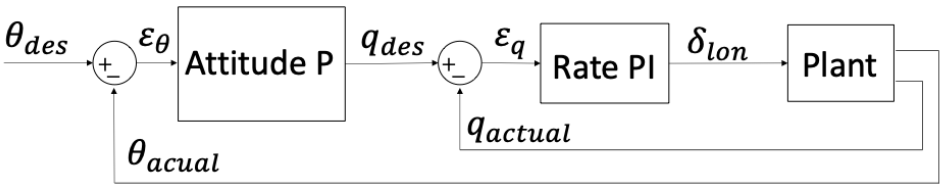

Figure 3.3: Helicopter pitch controller architecture

define the following error signals:

$$\begin{cases} \epsilon_\phi = \phi_{des} - \phi \\ \epsilon_\theta = \theta_{des} - \theta \\ \epsilon_p = p_{des} - p \\ \epsilon_q = q_{des} - q \end{cases} \tag{3.1}$$

The cascade P-PI control output can be written as follows:

$$\begin{cases} p_{des} = K_{P\phi}\epsilon_\phi \\ q_{des} = K_{P\theta}\epsilon_\theta \\ \delta_{lat} = K_{Pp}\epsilon_p + K_{Ip}\int_0^t \epsilon_p dt \\ \delta_{lon} = K_{Pq}\epsilon_q + K_{Iq}\int_0^t \epsilon_q dt \end{cases} \tag{3.2}$$

where K_P are the proportional gains and K_I the integral gains, referred to the proper variables.

3.1.2 Heading hold controller

Figure 3.4 shows the design of the heading hold controller.

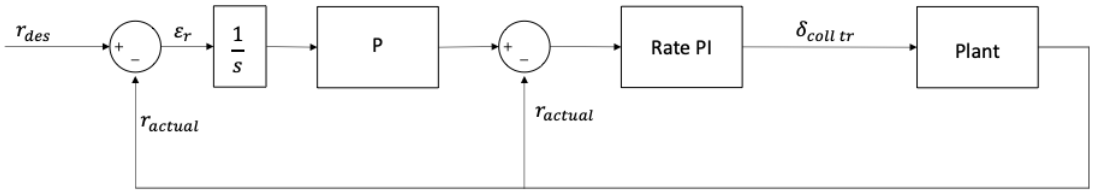

Figure 3.4: Helicopter yaw rate controller architecture

This architecture is similar to that presented for attitude controller, the only difference appears in dealing with the user's input signal. As a matter of fact, it provides direct control on the yaw rate r instead of on the real heading angle ψ. The ψ_{des} reference for the outer loop is obtained integrating the ϵ_r signal, starting from an appropriate initial value. By defining the error signals as follows:

$$\begin{cases} \epsilon_\psi = \int_0^t \epsilon_r dt \\ \epsilon_r = r_{des} - r \end{cases} \tag{3.3}$$

The cascade P-PI control output results to be:

$$\begin{cases} r_{des} = K_{P\psi}\epsilon_{\psi} \\ \delta_{coll\ tr} = K_{Pr}\epsilon_r + K_{Ir}\int_0^t \epsilon_r dt \end{cases} \tag{3.4}$$

3.1.3 Altitude hold controller

Altitude hold controller allows to control vertical speed and acceleration acting on the main rotor collective. In this flight mode the pilot input act as a reference vertical velocity. With the aim to ensure good performance, the input signal is integrated to have a reference altitude that prevents oscillations, in same manner presented for the heading hold controller. Let's define the following error signals as:

$$\begin{cases} \epsilon_z = \int_0^t v_z dt \\ \epsilon_{v_z} = v_{zdes} - v_{zact} \end{cases} \tag{3.5}$$

The control output results to be:

$$\begin{cases} v_{zdes} = K_{Pz}\epsilon_z \\ \delta_{coll\ mr} = K_{Pv_z}\epsilon_{v_z} + K_{Iv_z}\int_0^t \epsilon_{\dot{z}} dt + K_{Da_z}a_z \end{cases} \tag{3.6}$$

Figure 3.5 shows the altitude hold control scheme.

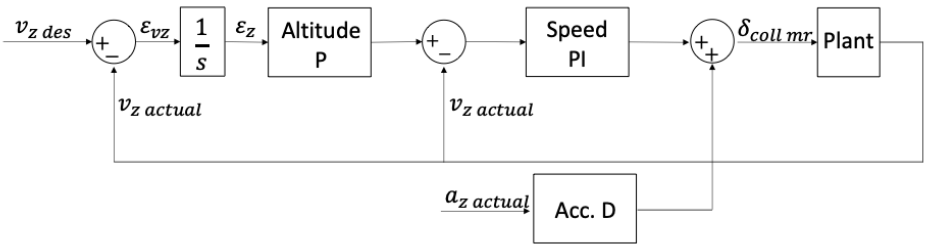

Figure 3.5: Helicopter altitude hold controller scheme

3.1.4 Velocity controller

The velocity controller for the helicopter is now presented. Figures 3.6a and 3.6b show the architecture.

The controller belongs to the main cascade control scheme. It is designed as a feedback proportional controller that has forward and right velocities v_{fdes} and v_{rdes} as reference

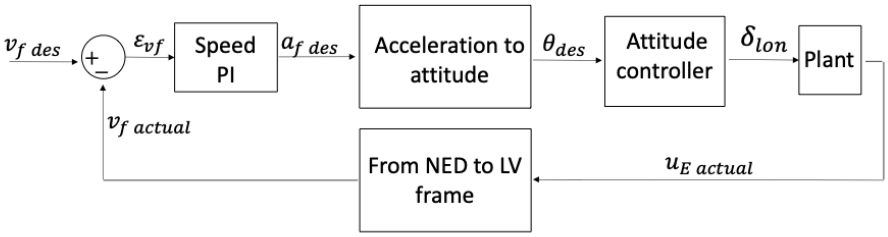

(a) Forward velocity controller architecture

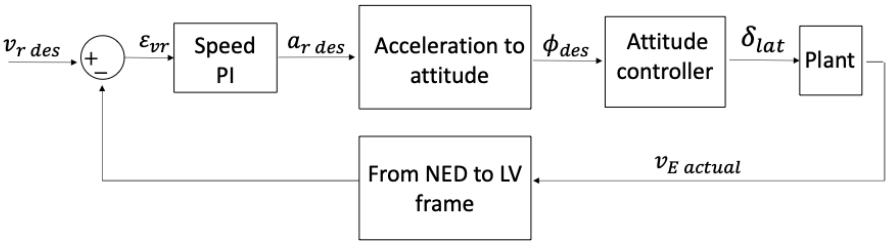

(b) Lateral velocity controller architecture

Figure 3.6: Helicopter speed hold controllers

inputs and gives desired roll and pitch angles as inputs to the inner control loop. The reference frame considered to evaluate the forward and the right velocities is the local vertical frame $\mathbb{F}_{LV}$, presented in chapter 2.1, that is equivalent to the NED frame $\mathbb{F}_E$ rotated by the euler heading angle ψ. Let the speed errors be:

$$\begin{bmatrix} e_{vf} \\ e_{vr} \end{bmatrix} = \begin{bmatrix} \cos\psi & \sin\psi \\ -\sin\psi & \cos\psi \end{bmatrix} \begin{bmatrix} u_{des} - u \\ v_{des} - v \end{bmatrix}_E = \begin{bmatrix} v_{fdes} - v_f \\ v_{rdes} - v_r \end{bmatrix}_{LV} \tag{3.7}$$

A proportional integral controller is implemented with the following form:

$$\begin{cases} a_{fdes} = K_{Pvf}\epsilon_{vf} + K_{Ivf}\int_0^t \epsilon_{vf}dt \\ a_{rdes} = K_{Pvr}\epsilon_{vr} + K_{Ivr}\int_0^t \epsilon_{vr}dt \end{cases} \tag{3.8}$$

Desired accelerations have to be expressed as function of the desired roll and pitch angles needed with airspeed increasing.

Simplifying equations (2.1), (2.2), the forward, right and down accelerations are:

$$\begin{cases} a_{fdes} = -f\cos\phi\sin\theta \\ a_{rdes} = f\sin\phi \\ a_{ddes} = -f\cos\phi\cos\theta + g \end{cases} \tag{3.9}$$

By setting $a_{ddes} = 0$, the expressions for ϕ_{des} and θ_{des} are:

$$\begin{cases} \phi_{des} = \arctan\frac{a_{rdes}\cos\theta_{des}}{g} \\ \theta_{des} = -\arctan\frac{a_{fdes}}{g} \end{cases} \tag{3.10}$$

3.2 $\mathcal{L}_1$ adaptive controller

In this section $\mathcal{L}_1$ adaptive controller is presented, as given in reference [81] and showed in figure 3.7. It is based on the structure given by Hovakimyan and Cao in reference [67] in chapter 2.4. It is the $\mathcal{L}_1$ controller for nonlinear systems under the hypothesis of matched uncertainties. The main issue is related to the reference dynamics. These are obtained by identification of the helicopter behaviour with baseline controllers tuned for the hovering flight condition. In this way the adaptive controller has to maintain the same desired behaviour for all the flight envelope.

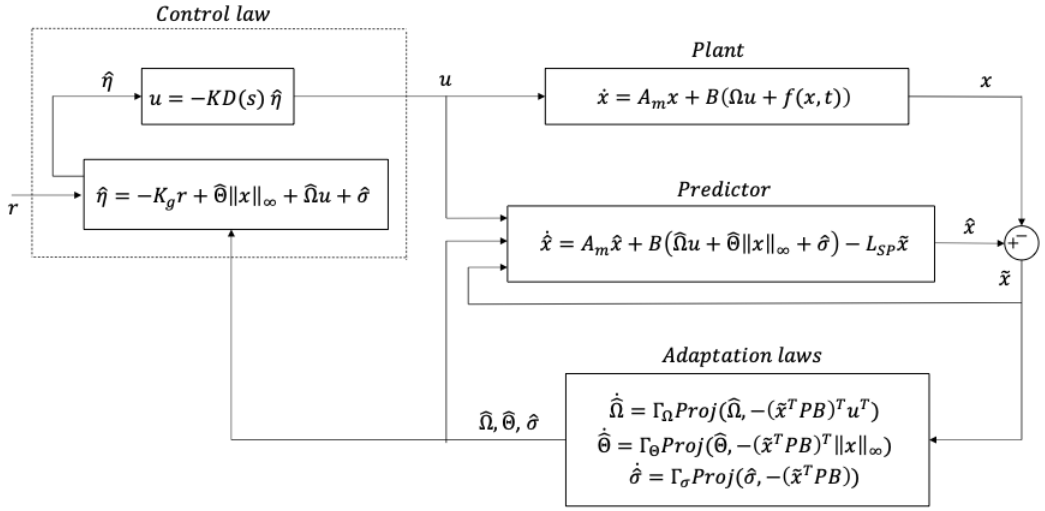

Figure 3.7: $\mathcal{L}_1$ adaptive control scheme

As for the case of classical controllers, both the attitude control loop both the speed

control loop have been designed with the adaptive technique. The first scheme is given in figure 3.8. It illustrates the architecture of the augmented adaptive controller for the attitude loop stabilization on both pitch and roll angles and the yaw-rate. The augmented signal is the sum of the adaptive contribution and that one of the baseline.

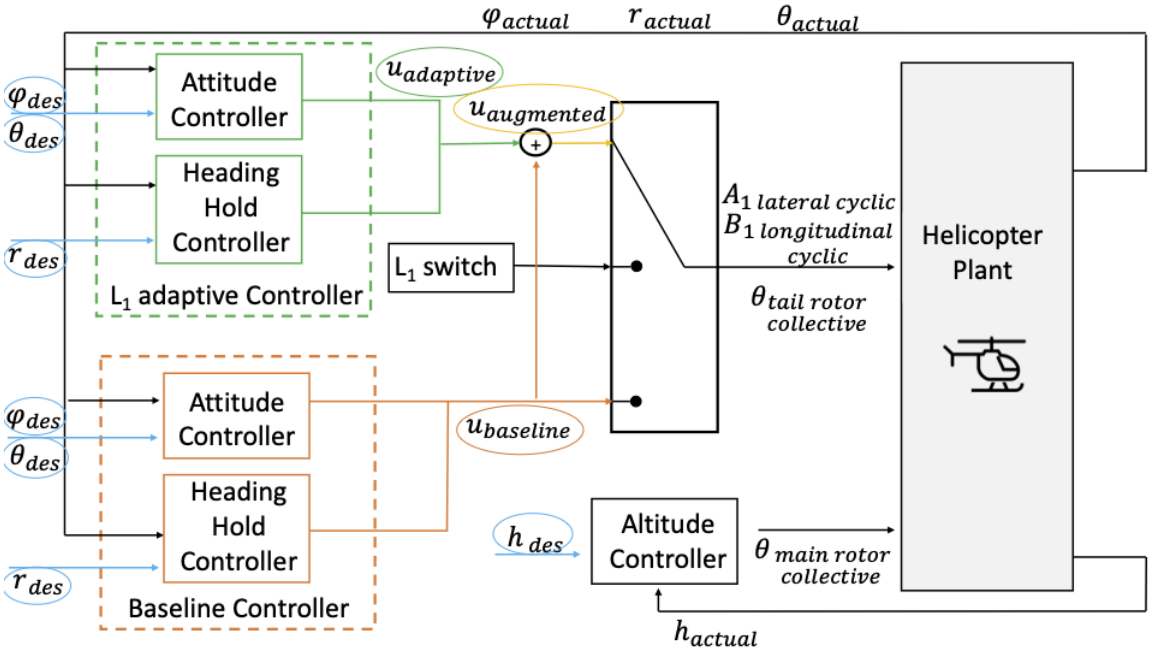

Figure 3.8: $\mathcal{L}_1$ adaptive control scheme for attitude stabilization

Figure 3.9 shows the speed hold controller realized with the adaptive laws. Desired north and east speed in navigation reference frame are given as inputs to the outer loop with $\mathcal{L}_1$ adaptive controller. The outputs of this outer loop are the desired roll and pitch attitude angles. For this case the helicopter inner loop attitude is stabilized through the PIDs control system which gives to the helicopter the longitudinal and lateral cyclic inputs B_1 and A_1. Altitude and heading are controlled by the altitude hold and the heading hold respectively, based on PIDs control laws, as illustrated in section 3.1. Differently from the adaptive attitude controller, the adaptive speed controllers are not the sum of the contributions of the baseline plus the adaptive one. In this case, the outer loop that controls the velocities is made only by the $\mathcal{L}_1$ input.

In what follows the mathematical model for $\mathcal{L}_1$ controller for nonlinear systems is described.

Consider the class of systems

$$\begin{aligned} \dot{x}(t) &= A_m x(t) + B_m(\Omega u(t) + f(x(t), t)), \quad x(0) = x_0 \\ y(t) &= Cx(t) \end{aligned} \tag{3.11}$$

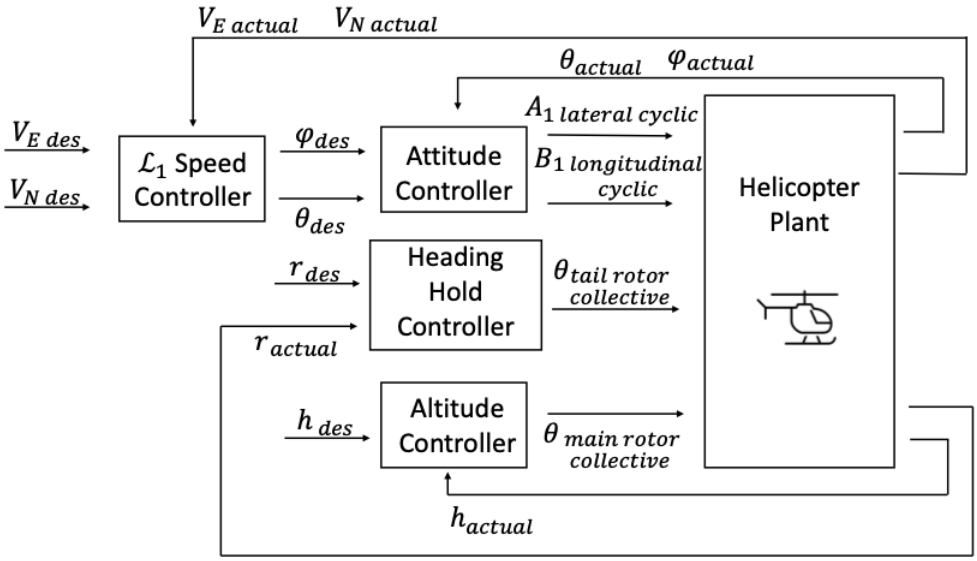

Figure 3.9: $\mathcal{L}_1$ adaptive control scheme for velocity

where $x(t) \in \mathbb{R}^n$ is the system state (measured), $u(t) \in \mathbb{R}^m$ is the control signal, $A_m \in \mathbb{R}^{n\times n}$ is a known Hurwitz matrix specifying the desired closed loop dynamics; $B \in \mathbb{R}^{n\times m}$ and $C \in \mathbb{R}^{r\times n}$ are known constant matrix, ; $\Omega \in \mathbb{R}^{m\times m}$ is an unknown constant matrix with diagonal terms of known signs, representing the uncertainty in the system input gain; $f(t,x) : \mathbb{R} \times \mathbb{R}^n \to \mathbb{R}^m$ is an unknown nonlinear map continuous in its arguments which represents system nonlinear uncertainties; $y(t) \in \mathbb{R}^n$ is the regulated output. The initial condition x_0 is assumed to be inside an arbitrarily large known set $||x_0||_\infty \leq \rho_0$. It is assumed that the nonlinear uncertainties map satisfies the semi-global lipschiz condition for all $\|x\|_\infty \leq \delta$ and $\|\overline{x}\|_\infty \leq \delta$, such that

$$|f(x,t) - f(\overline{x},t)| \leq L\|x - \overline{x}\|_\infty \tag{3.12a}$$

$$|f(0,t)| \leq B \tag{3.12b}$$

The control objective is to design a state feedback adaptive controller to ensure that $y(t)$ tracks a given reference signal $r(t)$.

The $\mathcal{L}_1$ adaptive controller is comprised of the state predictor, the adaptive laws and the control law, as detailed below.

State predictor

The state predictor is defined similarly to the plant equations, but the unknown variables are replaced by their estimates. Equations are given:

$$\begin{aligned} &\dot{\hat{x}}(t) = A_m\hat{x}(t) + B_m(\hat{\Omega}u(t) + \hat{\Theta}(t)\|x(t)\|_\infty + \hat{\sigma}(t)) - L_{sp}\tilde{x}(t), \hat{x}(0) = \hat{x}_0, \\ &\hat{y}(t) = C\hat{x}(t), \end{aligned} \tag{3.13}$$

where $\hat{\Omega} \in \mathbb{R}^{m\times m}$, $\hat{\Theta} \in \mathbb{R}^m$, $\hat{\sigma} \in \mathbb{R}^m$ are adaptive estimates obtained as results of $\mathcal{L}_1$ controller adaptation laws. L_{sp} is a positive definite diagonal matrix used to assign faster poles to the prediction error dynamics and $\tilde{x}(t) = \hat{x}(t) - x(t)$ i the error dynamics. It is assumed that system uncertainties $f(x,t)$ could be parameterized as $\hat{f}(x,t) = \hat{\Theta}(t)\|x(t)\|_\infty + \hat{\sigma}(t)$.

Adaptation Laws

The adaptation laws for $\hat{\Omega}$, $\hat{\Theta}$ and $\hat{\sigma}$ are defined as:

$$\begin{aligned} \dot{\hat{\Omega}}(t) &= \Gamma_\Omega Proj(\hat{\Omega}(t), -(\tilde{x}^T(t)PB)^T u^T(t)), \hat{\Omega}(0) = \hat{\Omega}_0, \\ \dot{\hat{\Theta}}(t) &= \Gamma_\Theta Proj(\hat{\Theta}(t),\ -(\tilde{x}^T(t)PB)^T\|x(t)\|_\infty), \hat{\Theta}(0) = \hat{\Theta}_0, \\ \dot{\hat{\sigma}}(t) &= \Gamma_\sigma Proj(\hat{\sigma}(t),\ -\tilde{x}^T(t)PB), \hat{\sigma}(0) = \hat{\sigma}_0 \end{aligned} \tag{3.14}$$

where $\tilde{x}(t) = \hat{x}(t) - x(t)$ is the prediction error, $\Gamma_\Omega, \Gamma_\Theta, \Gamma_\sigma \in \mathbb{R}^{n\times n}$ are the adaptation gains, $P = P^T > 0$ is the solution to the Lyapunov equation ${A_m}^T P + A_m P = -Q$ for arbitrary $Q = Q^T > 0$ and the $Proj(.,.)$ denotes the projection operator as defined in [82]. The projection operator ensures that $\hat{\Omega}(t) \in \Omega_s$, $\|\hat{\Theta}_i(t)\|_\infty \leq \Theta_b$ and $\|\hat{\sigma}_i(t)\|_\infty \leq \sigma_b$, where Ω_s is a compact convex set which includes estimated input gain matrix and Θ_b, σ_b are adaptation terms bounds.

Control law

The control signal is generated as the output of the following feedback system:

$$u(s) = -KD(s)\hat{\eta}(s), \tag{3.15}$$

where $K \in \mathbb{R}^{m\times m}$ is a diagonal feedback gain matrix, $D(s)$ is a strictly proper transfer function and $\hat{\eta}(t)$ is the Laplace transform of:

$$\hat{\eta}(t) = \hat{\Omega}u(t) + \hat{\Theta}(t)\|x(t)\|_\infty + \hat{\sigma}(t) - K_g r(t) \tag{3.16}$$

where $K_g = -(C^T {A_m}^{-1} B)^{-1}$ and $r(t)$ is the reference signal. Let's choose $D(s) = \frac{1}{s}\mathbb{I}_m$, where $\mathbb{I}_m$ is the identity matrix of size m. Assuming that the adaptive estimation of the uncertainty input gain $\hat{\Omega}$ converges to Ω after a transient time, the input $u(s)$ to the system in equations (3.11) and the predictor in equations (3.13) is filtered trough

$$C(s) = \Omega K(s\mathbb{I}_m + \Omega K)^{-1} \tag{3.17}$$

where $C(s)$ is a strictly proper filter with DC gain $C(0) = \mathbb{I}_m$. K and $D(s)$ need to ensure that exists a positive ρ_r such that:

$$\|G(s)\|_{\mathcal{L}_1} < \frac{\rho_r - \|K_g C(s) H(s)\|_{\mathcal{L}_1} \|r\|_\infty - \|\rho_0\|_{\mathcal{L}_1}}{L_\rho \rho_r + B} \tag{3.18}$$

where

$$H(s) = (s\mathbb{I}_n - A_m)^{-1} B, \tag{3.19a}$$
$$G(s) = H(s)\left(\mathbb{I}_m - C(s)\right), \tag{3.19b}$$
$$\rho_0 = (s\mathbb{I}_n - A_m)^{-1} x_0 \tag{3.19c}$$

and $L_\rho = \Theta_b$, $B = \sigma_b$. As stated in [83], the upper bound in equation (3.18) is a consequence of equation (3.12). If $f(x,t)$ is globally Lipschitz with uniform Lipschitz constant L, then $\rho_r \to \infty$ and the upper bound in equation (3.18) degenerates into

$$\|G(s)\|_{\mathcal{L}_1} < \frac{1}{L_\rho} \tag{3.20}$$

Reference dynamics

The reference dynamics adopted in the predictor, that $\mathcal{L}_1$ controller has to track, are identified directly in the hovering condition sing the helicopter linearized model with the baseline controllers.

For the attitude control loop the reference dynamics are the following:

$$\phi(s) = \frac{6}{s+6}\delta_{lat}(s) \tag{3.21a}$$
$$\theta(s) = \frac{6}{s+6}\delta_{lon}(s) \tag{3.21b}$$
$$r(s) = \frac{4}{s+4}\delta_{coll\ tr}(s) \tag{3.21c}$$

where ϕ, θ and r are roll angle, pitch angle and yaw rate respectively. δ_{lat}, δ_{lon} and $\delta_{coll\ tr}$ are the lateral cyclic, longitudinal cyclic and tail rotor collective control inputs.

Reference dynamics are stable and uncoupled, letting the adaptive system to adapt and reduce coupling effects. Given closed loop desired model as in equations (3.21), reference matrices are $A_m = -diag(6, 6, 4)$, $B = diag(6, 6, 4)$ and $C = \mathbb{I}_m$.

Concerning the velocity control loop, reference dynamics are also identified around hovering conditions considering the attitude PIDs together with the helicopter dynamics in the linearized model. In this way the identified system inputs are roll and pitch attitude references $u(t) = [\theta_{ref}, \phi_{ref}]$ and the outputs are $y(t) = [V_N, V_E]$. The identified system outputs coincides with the system states, so matrix C is equal to the identity matrix. The identified dynamics are stable due to the presence of the attitude controller. The speed loop desired dynamics are then shaped trough a full state feedback using pole placement technique. Reference matrices are: $A_m = (-5\ 0; 0\ \ -10)$, $B = (-5.3735\ 0.0106; 0.0109\ 5.3584)$ and $C = \mathbb{I}_m$.

Low pass filter shaping

Assuming that $f(x, t)$ is globally Lipschitz, $C(s)$ is shaped such that condition in equation (3.20) is always satisfied. This is achieved by choosing the right feedback gain matrix K and the set Ω_s. Selected K results as follows

$$K = \begin{bmatrix} 30 & 0 & 0 \\ 0 & 30 & 0 \\ 0 & 0 & 1 \end{bmatrix} \tag{3.22}$$

Since Ω has to be strictly diagonally dominant, one possible Ω_s that satisfy also this condition is

$$\Omega_s = \begin{bmatrix} [0.75, 1.25] & [-0.35, 0.35] & [-0.35, 0.35] \\ [-0.35, 0.35] & [0.75, 1.25] & [-0.35, 0.35] \\ [-0.35, 0.35] & [-0.35, 0.35] & [0.75, 1.25] \end{bmatrix} \tag{3.23}$$

Using this Ω_s and the K matrix of equation (3.22), considering that adaptation estimates limits are $|\Theta_b| = 1$, $|\sigma_b| = 1$, and so $L_\rho = 1$, $B = 1$, condition given in equation (3.20) is always satisfied.

Estimation laws and predictor shaping

$\mathcal{L}_1$ adaptive control decouples estimation from control. The adaptation laws gains $\Gamma_\Omega, \Gamma_\Theta, \Gamma_\sigma$ should have the greater possible values in order to achieve the fastest possible estimation. However there are limitations that come from the hardware on which the $\mathcal{L}_1$ adaptive control runs on. Satisfactory adaptation gains values are selected by a trial

and error procedure during simulations. Control systems sample time is set $T_s = 0.004$. Final chosen values are $\Gamma_\Omega = \Gamma_\Theta = \Gamma_\sigma = \Gamma = diag\,(5000, 5000, 3000)$. $Q = \mathbb{I}_n$ is chosen in order to solve the Lyapunov equation needed to compute P matrix in equations (3.14). Error dynamics is shaped trough L_{sp} matrix. Satisfactory results are obtained by the following values $L_{sp} = diag(60, 60, 240)$.

Baseline augmentation

$\mathcal{L}_1$ adaptive control is designed to work in parallel with the baseline PID controllers in case of attitude stabilization. Figure 3.10 shows the selected architecture highlighting the $\mathcal{L}_1$ activation switch. Inputs computed by baseline and $\mathcal{L}_1$ controllers are summed together, but the switch may be used to cut off adaptive control contribution. This design choice has two main reasons. On one hand, before a fly there could be the necessity to test the helicopter actuators on ground. In this condition, a lack of response of the helicopter to a pilot command could bring to a wrong estimation of the $\mathcal{L}_1$ adaptive terms. This could contribute to force the saturation of the actuators before flying. On the other hand, it is possible to perform safe flight tests through the use of a secure $\mathcal{L}_1$ switch in case of malfunctioning.

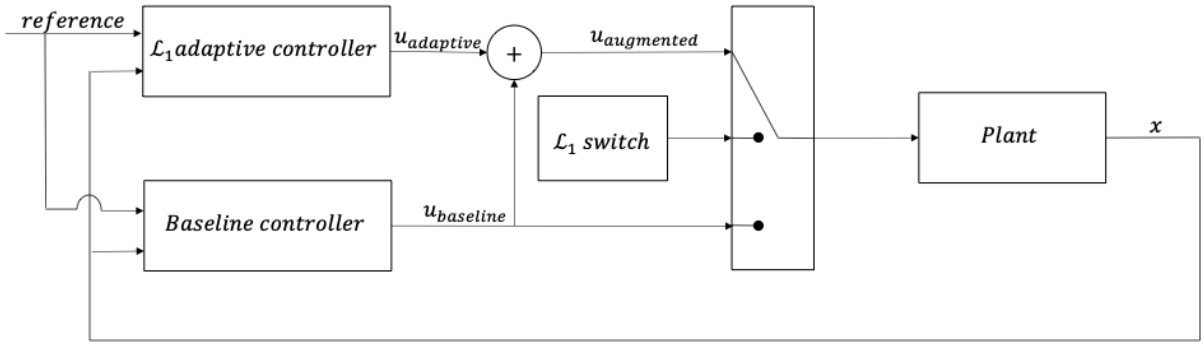

Figure 3.10: $\mathcal{L}_1$ augmentation of baseline PID

3.3 Cooperative control

The cooperative use of unmanned vehicles is an attractive topic for researchers due to the potentiality to increase their operational capabilities. In future civil aerospace scenarios, it is supposed that cooperative control will have a key role for many operation, e. g. in aerial monitoring, with an higher robustness and reliability with respect to the use of a single aircraft [89]. In this section the cooperative strategies implemented are given. The scenario combines the use of a terrestrial vehicle with a small-scale unmanned helicopter, whose models and control systems have been already introduced in the previous sections. As already stated, the original contribution is in the implementation of the algorithm. In particular, the possibility to switch among the different formation schemes without difficulties and the independence of the control system of each agent from the cooperative algorithm. This last one gives the chance to change the vehicles autopilot regardless of the choice of the formation scheme and cooperative controller. Hence it is possible to test many different agents control systems in the cooperative framework, without changing the cooperative control algorithm and make it simple to be implemented for the experimental campaign.

3.3.1 Cooperative control scenario and strategies problem definition

The agents involved in the cooperative scenario are a rover and a small-scale helicopter in a conventional single main rotor configuration. Due to the peculiarity of the implemented algorithm, it is possible to widen the functionality of the algorithm to more and/or different vehicles. The purpose is to build a scenario in which the agents interact to compute a predefined mission and to complete tasks for which a terrestrial vehicle plus an helicopter are the best choice. For instance, in a rescue mission the UAV can fly above the prescribed area with the aim to detect the target. Once the target location has been identified, the position is sent to the rover that can reach it for different reasons, from objects supply (an emergency kit for example) to pointing out the optimal path to reach the desired location. Another strategy may be represented by the two agents interacting in order to fulfill a surveillance mission. Otherwise, the required task may be that the flying vehicle has to reach the rover for disparate reasons, from the need to pick up and moving something quickly from a desired point to another, to the possibility to set up the terrestrial vehicle as fast recharge moving station.

There are many formation control architectures, depending on the sensing capability and on the interaction topology of agents. Both software and hardware design are influenced

by this choice. In reference [25] three main structures are discussed and reported in figures 3.11a, 3.11b and 3.11c. In the leader-wingman structure one vehicle is identified as leader, that follows its own prescribed trajectory. The others are called wingmen and refer their positions to another aircraft, keeping a fixed relative distance from it. This structure is widely employed for its simplicity despite the fact that errors propagate between the wingmen. In the virtual-leader structure all the vehicles receive the same information, that usually is the virtual leader trajectory. this latter may be a real aircraft or simply an ideal point. In this case there is no error propagation and each agent exhibits the same transient response. However, there may be collisions due to the absence of an explicit feedback to the formation since only the behaviour of the virtual leader is given. Lastly, in the behavioural approach the control action for each vehicle is a weighted average. In particular, each aircraft has to maintain a prescribed distance from the Formation Geometry Centre (FGC), whose position is determined by the relative positions between all the agents of the formation. Indeed collision is avoided, since each agent is capable to sense the others and to adjust the position to re-establish the geometry. Giulietti and Mengali [25] proved the superiority of this structure, whose main disadvantages are the greater complexity and the need to exchange more information.

This thesis presents two main formation control scenarios: the leader-wingman and the behavioural approach. These may be adapted to fulfil the demanded tasks. In both cases, the helicopter is required to stay at a certain altitude and the problem simplifies from a three-dimensional to a plane one. The proposed strategy applies under two hypotheses:

1. Position data are available for both the agents.

2. Each agent is provided with its own speed hold controller.

The overall architecture of the cooperative algorithm is given in figure 3.12. The scheme clearly shows the possibility to switch among the different formation flight strategies: helicopter as leader and rover as wingman; rover as leader and helicopter as wingman; behavioural approach with the two vehicles following the FGC. In all the considered situations the pilot or the ground station commands, in case of completely autonomous mission, are sent to the leader or to the flight geometry center in terms of desired velocity along the north and east axes. The commanded velocity is passed to the leader vehicle in case of leader-wingman situation or directly to determine the FGC speed. Under any circumstance each vehicle control system receives is demanded to follow the desired speed. The vehicle actual position is used to calculate the actual distance from the leader or from the FGC and it is compared with the desired one $\bar{d}$. In such a way the distance error feeds the vehicle cooperative control to generate the desired velocity that each vehicle has to follow

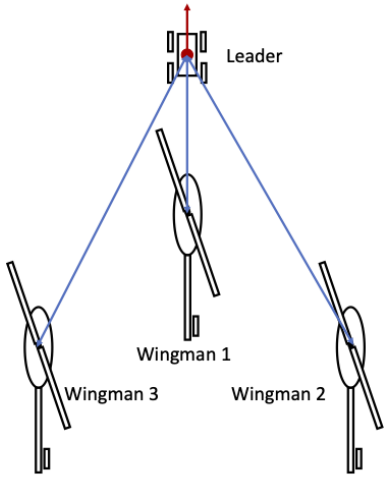

(a) Leader-wingman configuration

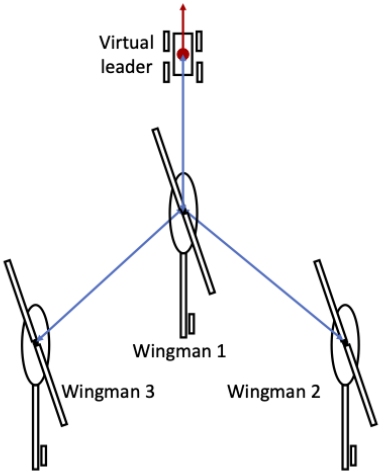

(b) Virtual-leader configuration

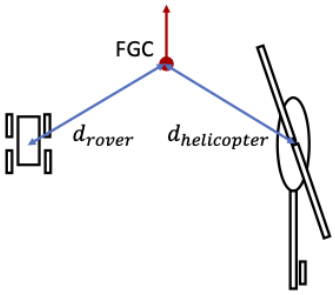

(c) Behavioural approach configuration

Figure 3.11: Wind velocity components

in order to maintain the required formation during the mission. The situation illustrated in figure 3.12 is the leader-wingman case with the rover as leader and the helicopter that has to follow it at a prescribed distance $\bar{d}_H$. In fact the commanded velocity from the pilot/ground station works only as reference for the rover, while the helicopter desired speed $\bar{V}_H$ is set by the helicopter cooperative control algorithm.

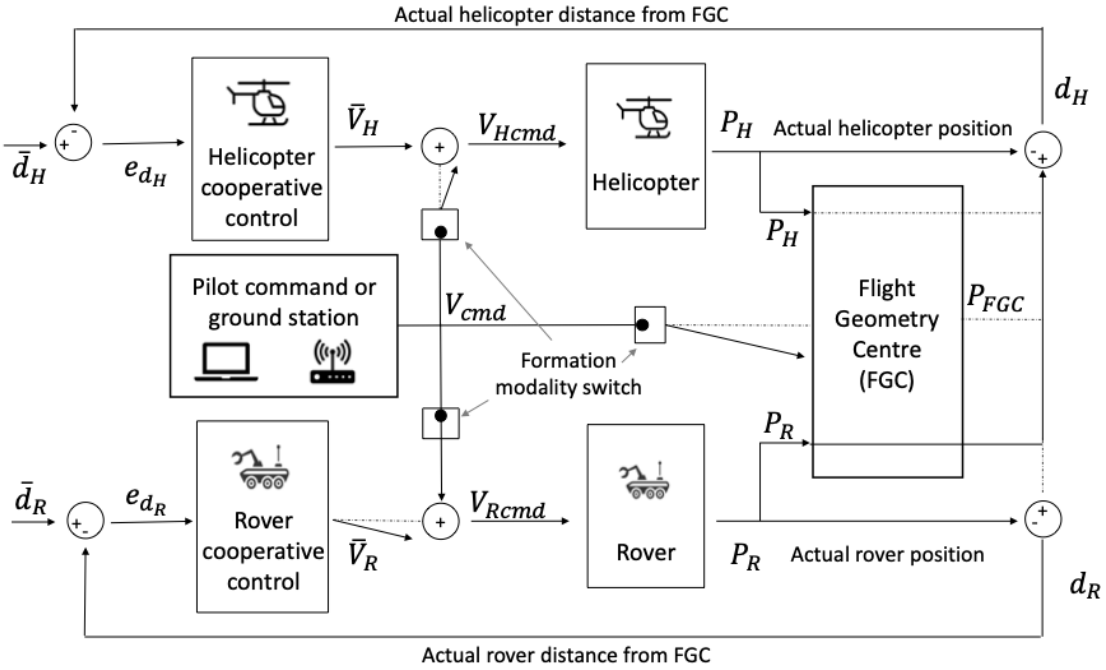

Figure 3.12: Cooperative control strategy global architecture

In either scenarios one of the most important aspects is ensuring that each agent can maintain a predetermined distance from a reference point, whatever it may be, from another vehicle to the geometry formation center. The knowledge of the distance dynamic is thus required. A suitable mathematical model to evaluate this dynamic is here presented, based on equations from reference [25]. Assume the i-th vehicle has to stay at a specified distance $\bar{d}_i$ from a reference point, moving with velocity $\bar{V}$. Let r_i and r_r be the distance from the origin of the inertial frame and the i-th agent and the reference point respectively. d_i is the actual distance between the i-th vehicle and the reference point, as depicted in Figure 3.13. The following relations are obtained:

$$r_r + d_i = r_i \tag{3.24}$$

and

$$r_r + \bar{d}_i = \bar{r}_i \tag{3.25}$$

from which

$$\bar{d}_i - d_i = \bar{r}_i - r_i \tag{3.26}$$

Provided $\dot{r}_i = V_i$ and $\dot{\bar{r}}_i = \bar{V}_i$ and taking the derivative of equation (3.26):

$$\dot{d}_i - \dot{\bar{d}}_i + \omega_i \times (d_i - \bar{d}_i) = V_i - \bar{V}_i \tag{3.27}$$

where ω_i is the velocity of the axis-frame.

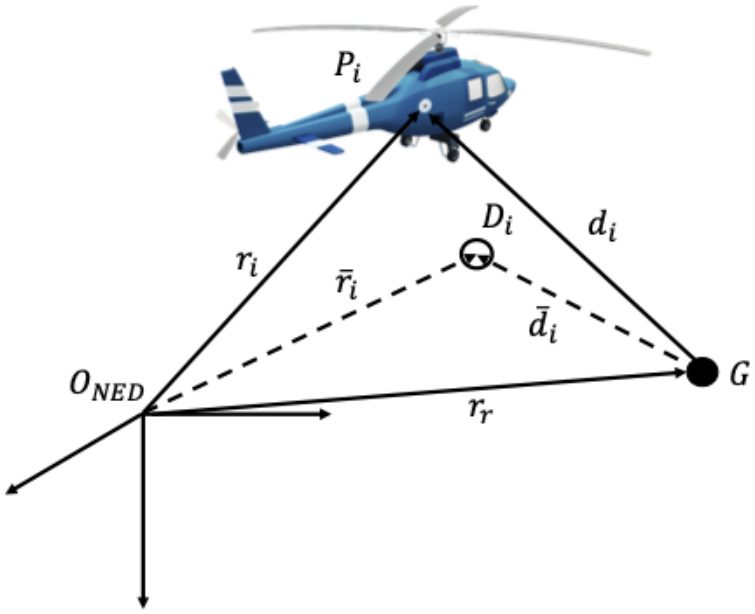

Figure 3.13: Cooperative control problem definition

Since the helicopter has to keep a desired altitude, the problem simplify to the plane one and figure 3.14 illustrates the plane problem definition.

Let D be the desired point in the North-East plane with N_D and E_D the relative position coordinates, R the rover and H the helicopter with the associated coordinates. In order to find the desired point coordinates N_D and E_D, the following equations are given:

$$d^2 = (E_D - E_R)^2 + (N_D - N_R)^2 \tag{3.28a}$$

$$\tan\alpha = \frac{E_D - E_R}{N_D - N_R} = \frac{E_H - E_R}{N_H - N_R} \tag{3.28b}$$

Two ways to determine the desired heading angle have been implemented and tested in this work. The first one is based on pure geometrical considerations, whose equations are reported subsequently:

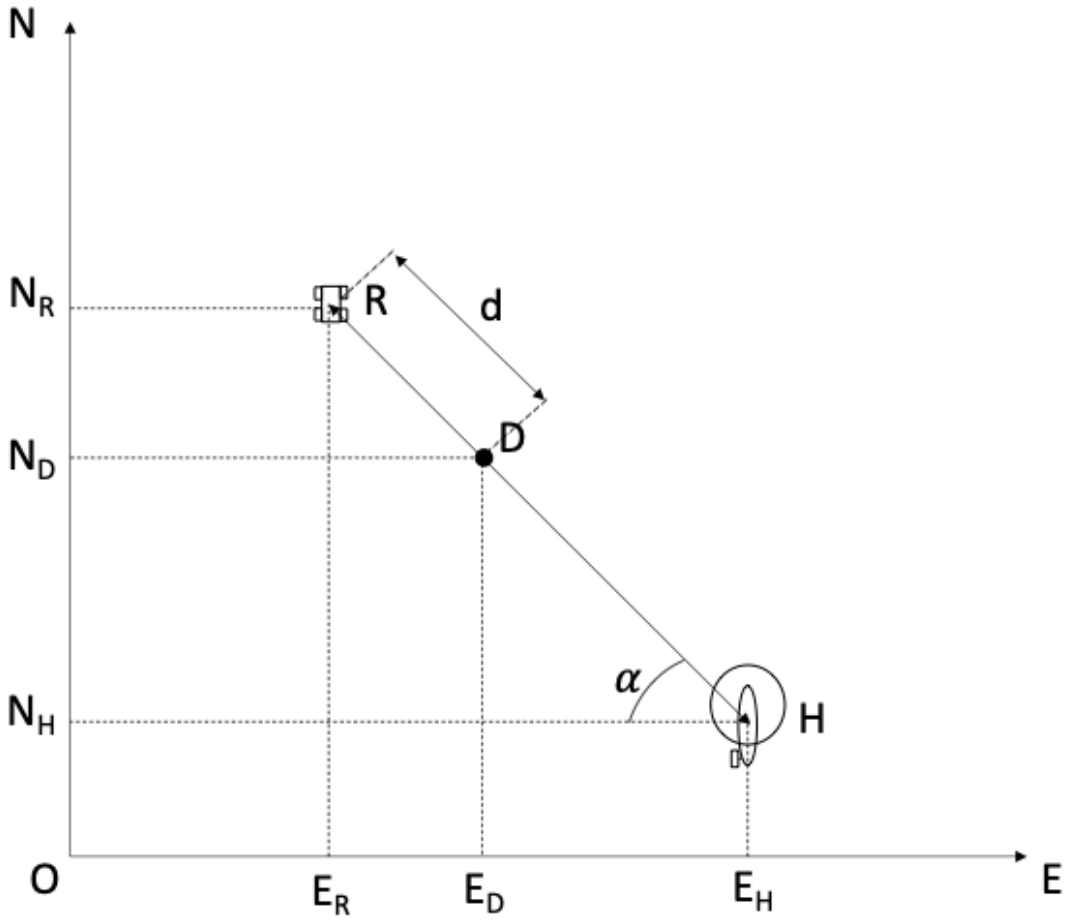

Figure 3.14: Cooperative control plane problem definition

$$\begin{cases} \alpha = \arctan(\frac{E_R - E_H}{N_R - N_H}) & & & \\ case1 : \psi_{des} = \alpha \quad for \quad E_R > E_H & & N_R > N_H \\ case2 : \psi_{des} = \alpha \quad for \quad E_R < E_H & & N_R > N_H \\ case3 : \psi_{des} = \pi + \alpha \quad for \quad E_R > E_H & & N_R < N_H \\ case4 : \psi_{des} = -\pi + \alpha \quad for \quad E_R < E_H & & N_R < N_H \end{cases} \tag{3.29}$$

The other one is based on the nonlinear guidance logic presented in reference [90]. This logic generates a lateral acceleration command to track a reference point on the desired trajectory. With reference to figure 3.15, L_1 is the distance between the vehicle center of gravity and the reference point and η is the angle between the vehicle velocity and the L_1 vector. The lateral acceleration command results to be:

$$a_{cmd} = 2\frac{V^2}{L_1}\sin\eta \tag{3.30}$$

This guidance law has two important properties:

1. The direction of the acceleration depends on η sign. In this way the vehicle will tend to align its velocity to the L_1 direction.

2. At each time point is possible to define a circular path by the position of the reference point, the vehicle position and by the vehicle velocity vector tangent. For this reason, a_{cmd} is equal to the centripetal acceleration and results to be $a_{cmd} = \frac{V^2}{R}$.

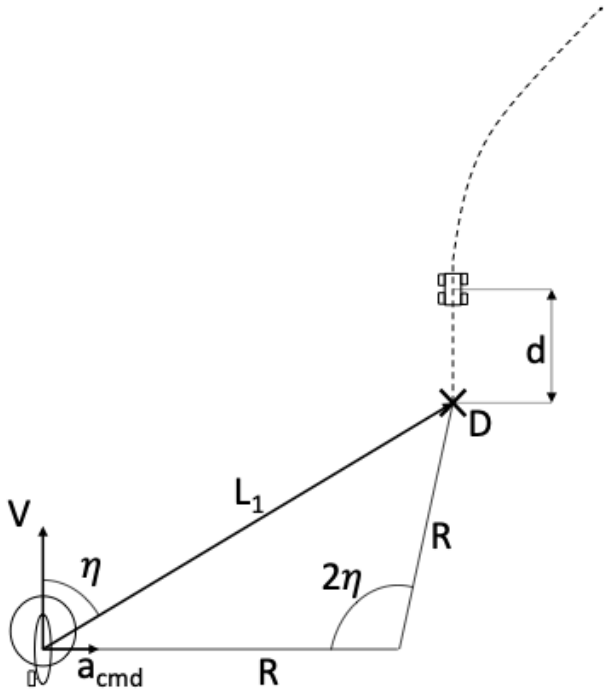

Figure 3.15: Cooperative control guidance logic diagram

As mentioned previously, in this thesis two main scenarios have been investigated. In both cases, the helicopter autopilot may be either based on the classical approach, with PIDs controlling attitude and velocity, or on the adaptive laws. In the first scenario the rover is identified as the leader of the formation and the helicopter, a wingman, has to follow at a prescribed distance $\bar{d}$ the rover. Actually, the rover may track a prescribed trajectory automatically through its own autopilot or may be remotely piloted.

The second scenario is based on the behavioural approach as described in [25]. The vehicles in formation are required to keep a specified distance $\bar{d}$ from the FGC. The position of this point depends on the relative distances between the vehicles in the formation. In this way each vehicle is capable to detect if the other one moves from the nominal position. The equations for the FGC dynamics on the $x-y$ plane are:

$$\begin{bmatrix} \dot{x} \\ \dot{y} \end{bmatrix} = \frac{1}{n_v} \sum_{i=1}^{n_v} \begin{bmatrix} V_i \cos\psi_i \\ V_i \sin\psi_i \end{bmatrix} \tag{3.31}$$

where n_v is the n-th vehicle. The position along north and east axes of the FGC point is obtained integrating equation (3.31). The coordinates of the desired positions of each vehicles with respect to the FGC point are calculated by the algorithm as illustrated in equations (3.27), (3.28). Equations (3.28) are adapted for this second case for the rover (3.32) and for the helicopter (3.33):

$$\bar{d_R}^2 = (E_D - E_{FGC})^2 + (N_D - N_{FGC})^2 \tag{3.32a}$$

$$\tan\alpha_R = \frac{E_D - E_{FGC}}{N_D - N_{FGC}} = \frac{E_R - E_{FGC}}{N_R - N_{FGC}} \tag{3.32b}$$

$$\bar{d_H}^2 = (E_D - E_{FGC})^2 + (N_D - N_{FGC})^2 \tag{3.33a}$$

$$\tan\alpha_H = \frac{E_D - E_{FGC}}{N_D - N_{FGC}} = \frac{E_H - E_{FGC}}{N_H - N_{FGC}} \tag{3.33b}$$

The difference between the first and the second scenario is that in the first one the rover moves independently from the helicopter (the dual scenario is easy to be implemented). On the contrary, in the second one both the vehicles have to keep a desired distance from the FGC. This allows each vehicle to be informed about the other one position, avoiding collisions, and to comply with formation variations.

3.3.2 Cooperative control navigation architecture

The control architecture is based on PID controllers. A general control scheme is given in figure 3.16, that may be adapted to different cooperative control scenario, from the helicopter following the rover, the rover following the helicopter, both the vehicles that follow a virtual leader or the FGC. Assumptions made in the strategies description are still valid. Despite the simplicity of the PID control laws, the algorithm architecture allows a fast choice of the formation flight strategy, that can also be changed during the execution of the assigned tasks. The controllers deal with the helicopter and the rover velocities and

positions and the desired point North-East coordinates as presented in equation (3.28) and with dynamic distance of equation (3.27). The output to the vehicle is a vector of reference velocities in NED frame and heading angle in order to track properly the desired point. Depending on the considered case, the cooperative algorithm gives instructions to both vehicles or only to one, leaving the other one piloted manually or by an automatic control system. Let's define the following error signals:

$$\begin{cases} \epsilon_N = N_D - N_{H/R} \\ \epsilon_E = E_D - E_{H/R} \\ \epsilon_{v_N} = v_{N_D} - v_{N_{H/R}} \\ \epsilon_{v_E} = v_{E_D} - v_{E_{H/R}} \\ \epsilon_\psi = \psi_{des} - \psi_{actual} \end{cases} \tag{3.34}$$

So the control output can be written as:

$$\begin{cases} V_{Ncmd} = K_{PvN}\epsilon_N + K_{DvN}\epsilon_{vN} + K_{IvN}\int_0^t \epsilon_N dt \\ V_{Ecmd} = K_{PvE}\epsilon_E + K_{DvE}\epsilon_{vE} + K_{IvE}\int_0^t \epsilon_E dt \\ V_{\psi cmd} = K_{P\psi}\epsilon_\psi + K_{I\psi}\int_0^t \epsilon_\psi dt \end{cases} \tag{3.35}$$

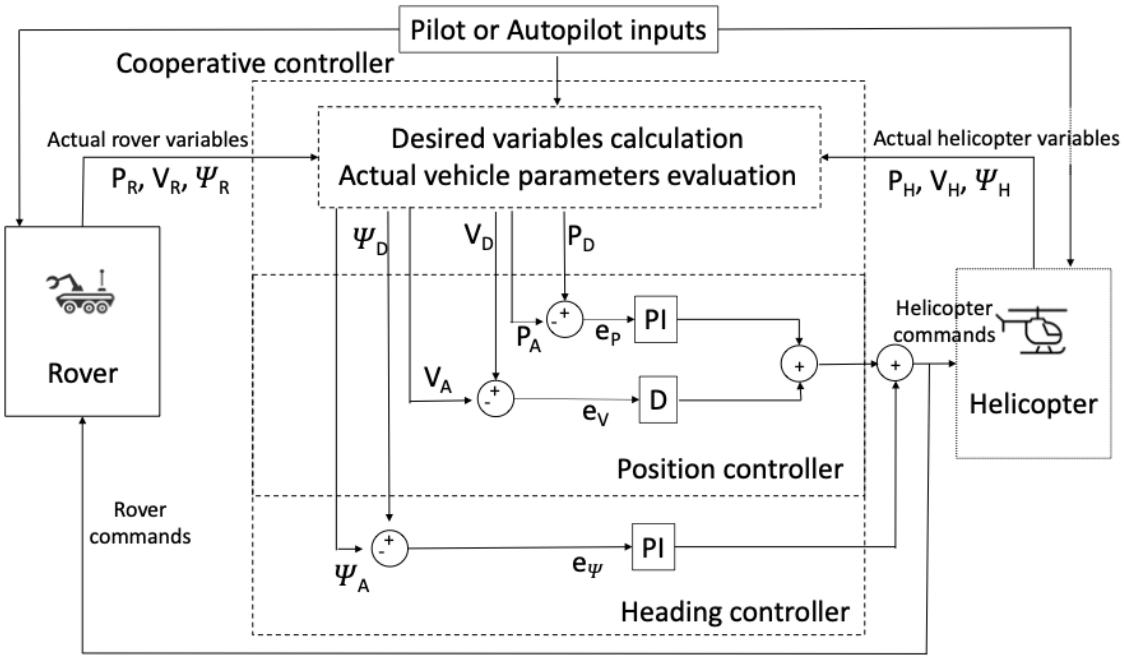

Figure 3.16: Cooperative control architecture

CHAPTER 4

Simulation

In this chapter simulations results are presented. First, simulations results from classical controllers presented in section 3.1 are given for the conventional single main rotor helicopter and for the synchrotor. Then the author presents results from the adaptive control system for the helicopter, whose architecture is described in section 3.2. Ultimately, simulations are carried out in the multi-agent scenario to test the cooperative control algorithms introduced in section 3.3. Simulations are ran in Matlab/Simulink® environment.

For all the cases, the mathematical models presented in chapter 2 are used. The full nonlinear dynamic model presented in section 2.1 for the conventional single main rotor helicopter is employed parameterized for the remotely-piloted SAB® Goblin700 Thunder helicopter, whose main parameters are reported in table B.1 in Appendix B of chapter B. Figure 4.1 shows the SAB® Goblin700 Thunder helicopter. Data for the intermeshing rotors configuration are given in table C.1 in Appendix C. In some cases, a joystick Logitech Saitek X52 Pro interfaced with Simulink® and with the open source FlightGear® flight simulator is used mainly for visualization purposes, as in figure 4.2.

4.1 Classical flight controllers simulation results

This section presents the results of the simulation carried out with the classical PIDs controllers described in section 3.1. First, results for conventional helicopter configuration are showed both for attitude and speed controllers. Then results for synchrotor are discussed.

Figure 4.1: SAB® Goblin700 Thunder helicopter

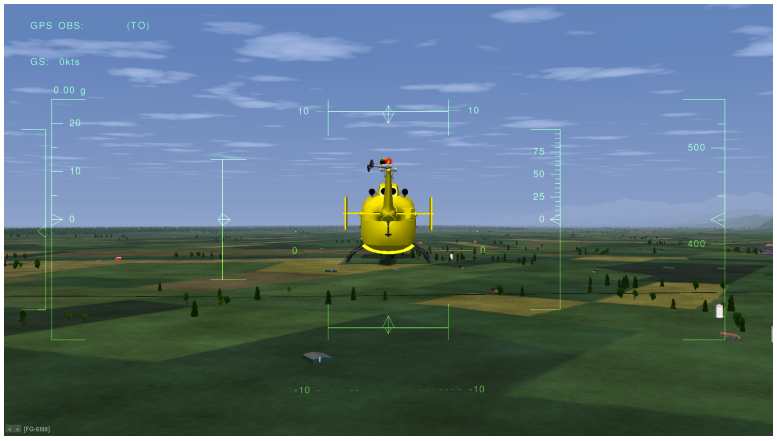

Figure 4.2: FlightGear flight simulator

4.1.1 Helicopter PID controllers simulation results

Utilizing the helicopter model presented in section 2.1 parameterized for the remotely-piloted SAB® Goblin700 Thunder helicopter, simulations with the PID controllers are carried out and outcomes are discussed. Many flight conditions are examined. Initially velocity profiles on each axis are given as reference inputs to the controllers. Then the helicopter has to track a way-points trajectory. Subsequently the helicopter is directly piloted by a human pilot through the joystick to simulate as much as possible a real flight. This last test is simulated also with the use of three wind disturbance mathematical representations. The first type is the wind shear model, whose implementation is based on the mathematical theory in the Military Specification MIL-F-8785C [84]. Wind speed

at 6 m of altitude is set to 15 m/s with a direction of 0 deg clockwise from north. The second wind disturbance is a discrete wind gust on all the three axes, that starts at 5 s with a gust amplitude of $[u_g v_g w_g] = [3.5\ 3.5\ 3.0]$ m/s, where u_g, v_g and w_g are the gust components. The third disturbance is the discrete Dryden wind turbulence model, that uses the Dryden spectral representation to add the turbulence as in reference [85]. Wind speed at 6 m is set to 15 m/s with a direction of 0 deg clockwise from north. All these model are combined and used for the human pilot simulated flight. In all the simulated flight situations, the helicopter started from the hovering trim condition at a fixed altitude of 100 meters above sea level.

Velocity profiles tracking

Figures 4.3 and 4.4 show, respectively, actual and reference north, east and down velocities, pitch angle, roll angle and yawrate response to track the north velocity profile. It is 0 m/s at the beginning of the simulation; it goes linearly to 10 m/s after 100 s and it comes back to 0 m/s after 100 more seconds. The other reference velocities and the reference yawrate are set to zero. Simulations show that PID controllers are able to track precisely the reference signal on all the axis, even if there is coupling, especially on roll and pitch axes. This is illustrated in figure 4.3b, where the actual east velocity varies slightly while north velocity is increasing. The maximum deviation from the reference value on east axis is 0.016 m/s, that is considered acceptable.

Similar tests have been computed on the other axes. East and down velocities have been asked to track reference values changing from 0 m/s to 5 m/s in 50 s and coming back to 0 m/s on east axis and from 0 m/s to 2 m/s at 20 s and again 0 m/s at 40 s on down axis. The heading hold controller is tested giving it a yaw-rate velocity profile to track. Plot of these simulations are not reported here for the sake of compactness since results are comparable to those just presented.

Trajectory tracking

In what follows results of the trajectory tracking are reported in figures 4.5, 4.6. The helicopter has to move along a square path of side 50 m formed by four way-points at the fixed assigned altitude of 100 m above the sea level.

On east and north axes the speed controller is capable to track the reference signal despite small overshoots where the velocity suddenly changes, as seen at second 30 in figures 4.5a, 4.5b. The altitude hold controller keeps the desired down velocity near to zero, with an error of 0.001 m/s and so the altitude does not change. The attitude controllers do not show errors in tracking the reference signal. The heading hold controller has the

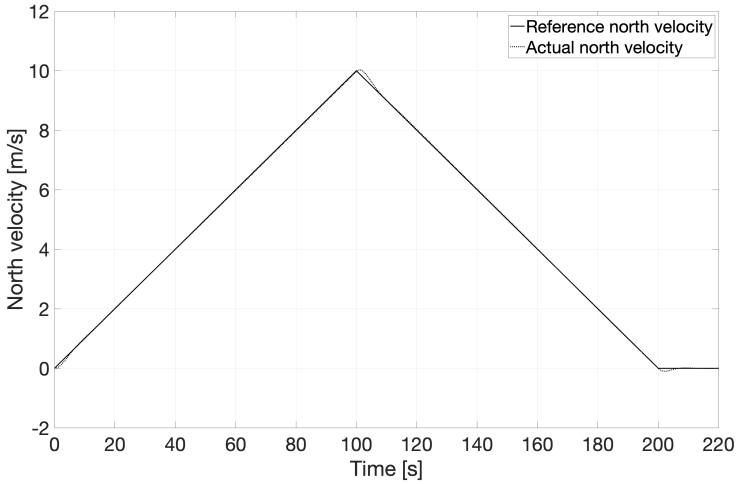

(a) Reference vs actual north velocity - helicopter PID controller

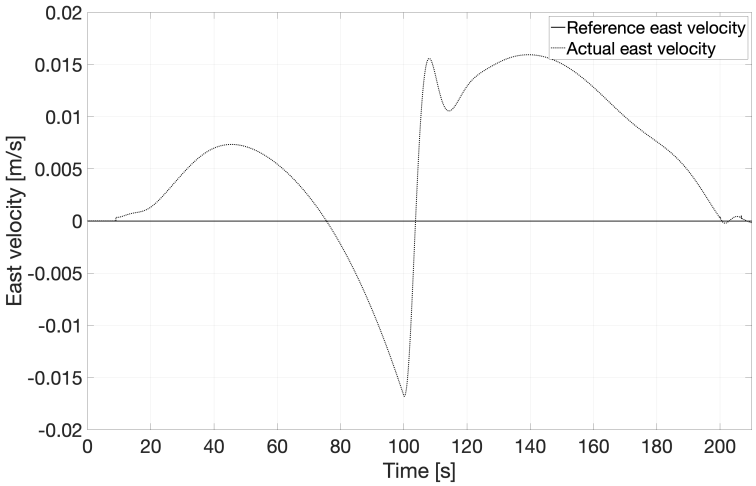

(b) Reference vs actual east velocity - helicopter PID controller

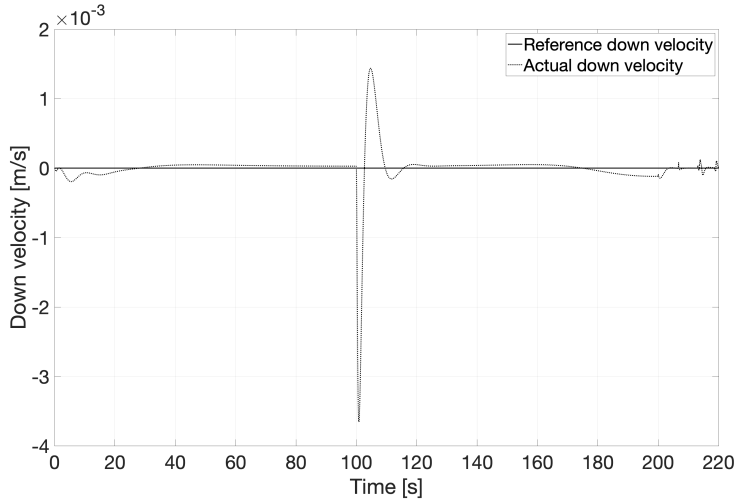

(c) Reference vs actual down velocity - helicopter PID controller

Figure 4.3: North velocity profile tracking - NED velocities

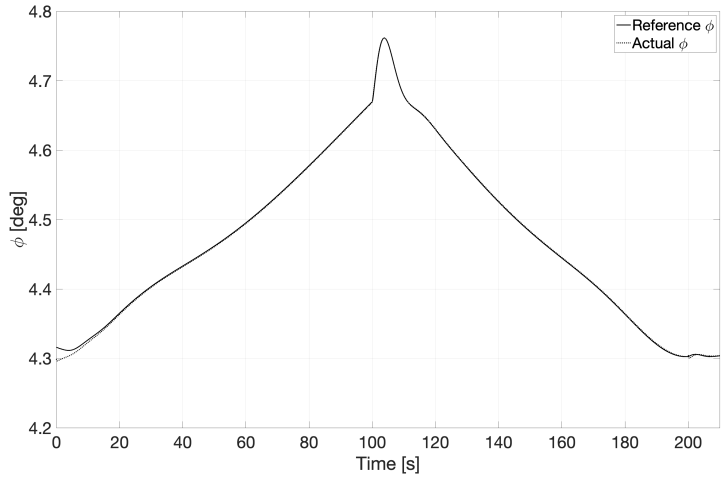

(a) Reference vs actual roll angle - helicopter PID controller

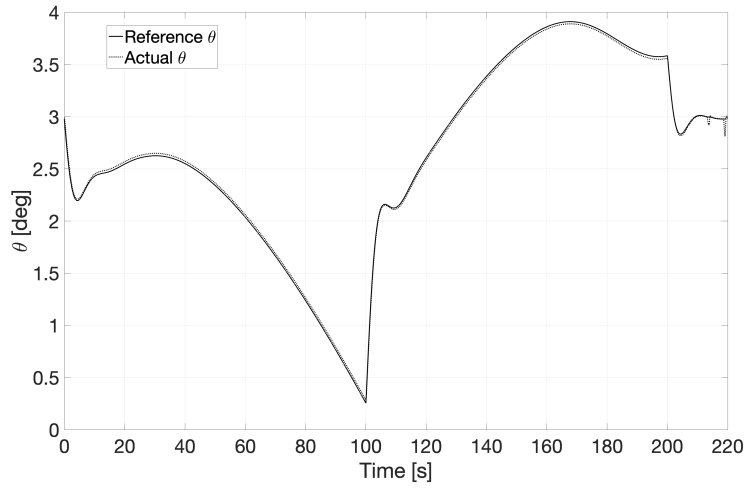

(b) Reference vs actual pitch angle - helicopter PID controller

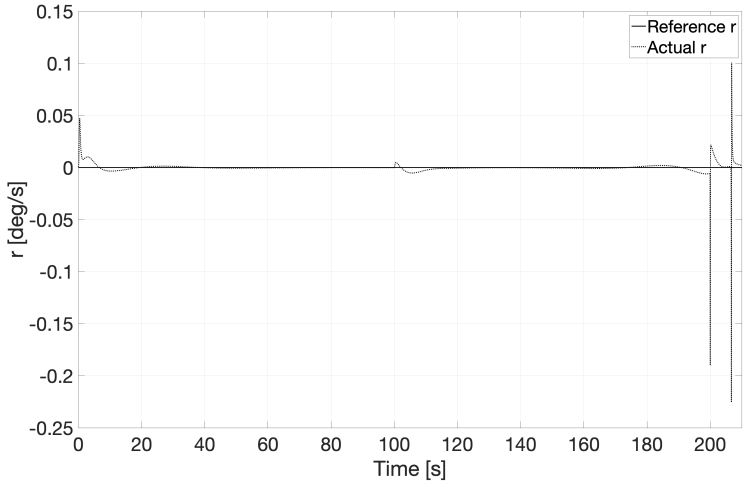

(c) Reference vs actual yawrate - helicopter PID controller

Figure 4.4: North velocity profile tracking - roll, pitch angles and yawrate

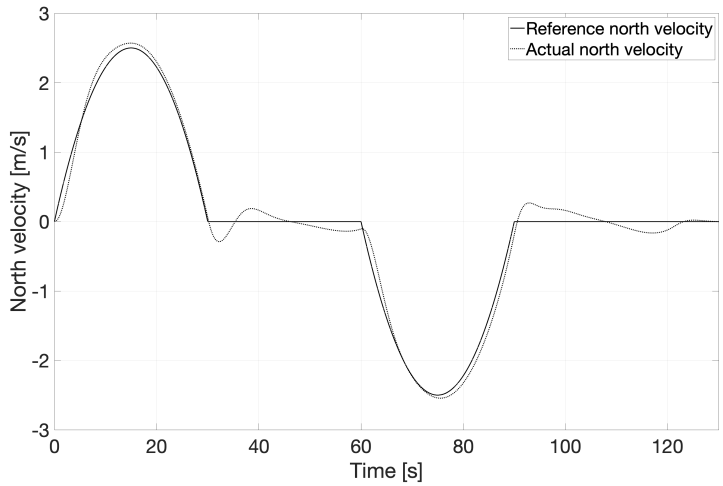

(a) Reference vs actual north velocity - helicopter PID controller

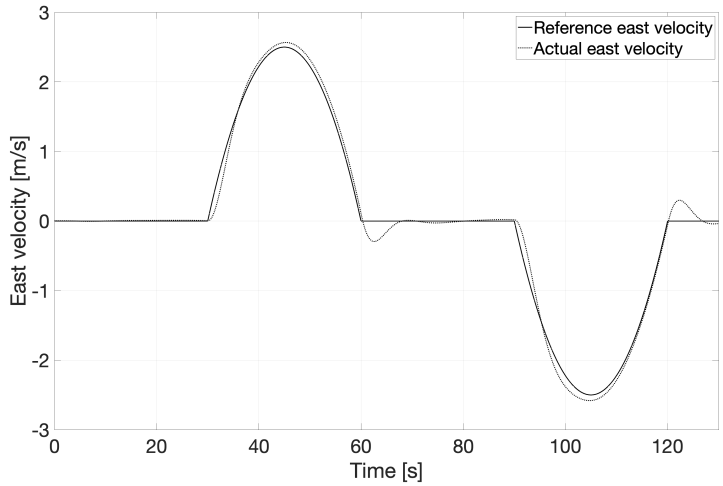

(b) Reference vs actual east velocity - helicopter PID controller

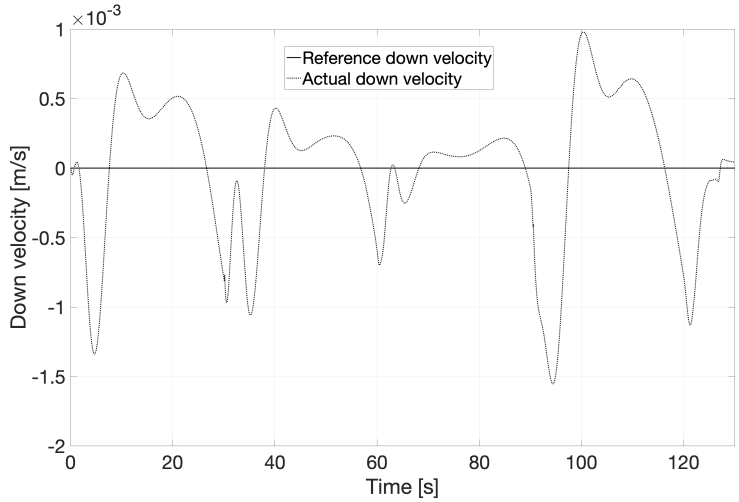

(c) Reference vs actual down velocity - helicopter PID controller

Figure 4.5: Trajectory tracking - NED velocities

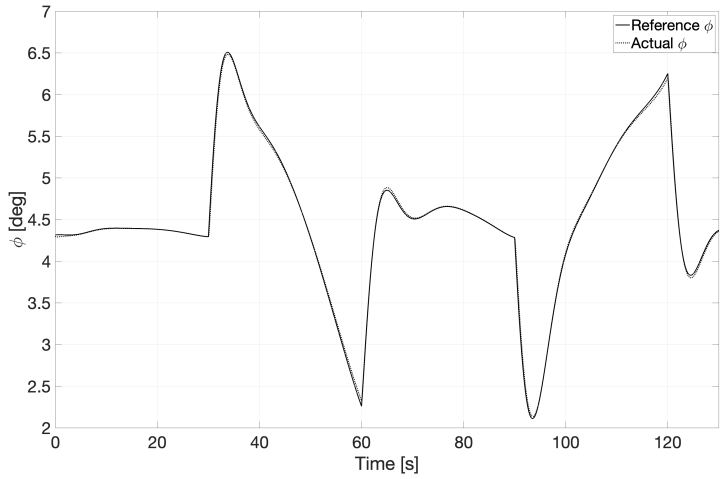

(a) Reference vs actual roll angle - helicopter PID controller

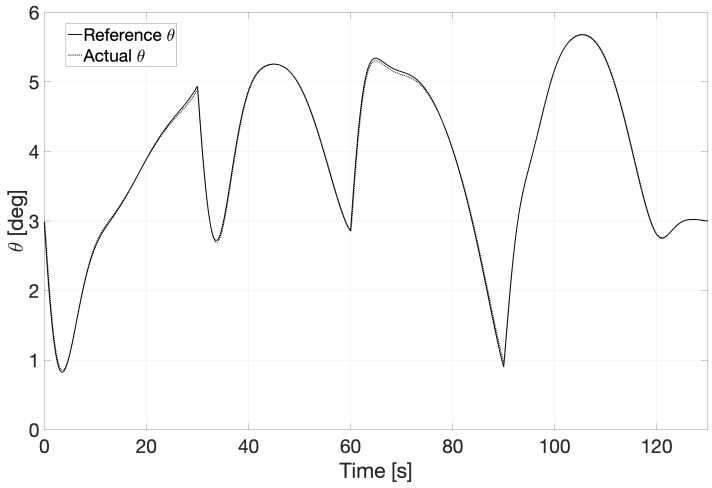

(b) Reference vs actual pitch angle - helicopter PID controller

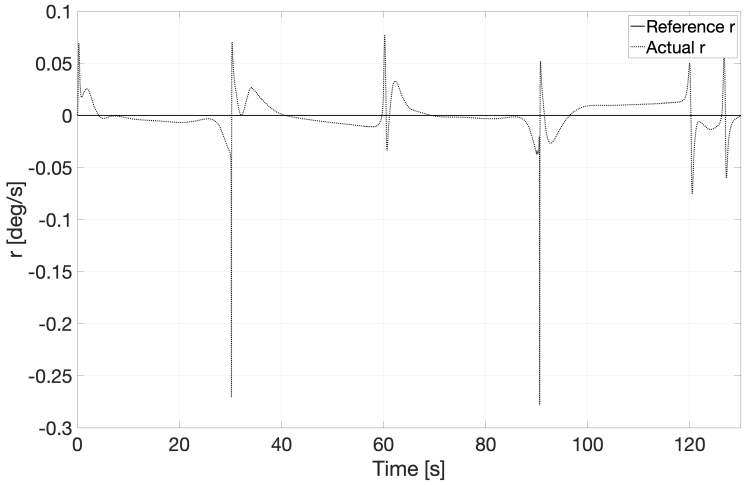

(c) Reference vs actual yawrate - helicopter PID controller

Figure 4.6: Trajectory tracking - roll, pitch angles and yawrate

same behaviour of the speed controllers, displaying a small deviation when north and east velocities change.

Human pilot inputs tracking

With the aim of being as realistic as possible, this last subsection provides the outcomes of a simulated flight in which inputs are given with a joystick by a human pilot. The comparison between reference and actual values of NED velocities is showed in figure 4.7. Figure 4.8 illustrates the same flight but with the addition of the wind models to test the controller performances.

Previous results show the capability of the PID controllers to track the reference inputs in either situations. Figures 4.7a and 4.7b illustrate that the speed controllers are capable of following the reference signal even if there are some over-shootings in correspondence of abrupt and fast speed changes on both the axes simultaneously. In case of no wind disturbances, the altitude hold controller stays on the reference signal with a very small error and a delay of few seconds, see figure 4.7c. When the wind disturbances are applied, all the controllers show in figure 4.8 a loss in performance that is proper of the PIDs which are proving not to be enough robust. This is one of the main reason why adaptive controllers have been implemented.

4.1.2 Synchrotor PID controllers simulation results

Results of the classical control approach with the same architecture illustrated in section 3.1 are given for the intermeshing rotors configuration. Data for the simulated aircraft are reported in table C.1. For this configuration, a full scale model has been used.

Figure 4.9 illustrates the actual and the desired attitude angles ϕ, θ and ψ. The system is asked to track the reference value of -0.1 rad $= -5.72$ deg starting from zero initial condition for roll and pitch angles and to track 0.1 rad $= 5.72$ deg for yaw angle. Figure 4.10 shows the reference and the actual values of the north velocity in km/h. The desired values is set to 50 km/h. The vehicle starts from the hovering condition and has to achieve the desired velocity. Results indicates that both controllers are capable to properly accomplish the requested task, even if there are some small overshoots in all the cases. Simulations to test response on the other axes and to different inputs have been computed but results are similar to those already presented.

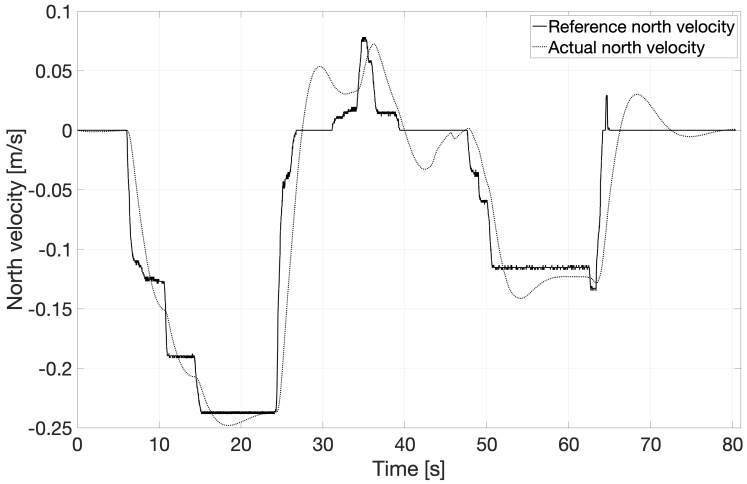

(a) Reference vs actual north velocity - helicopter PID controller

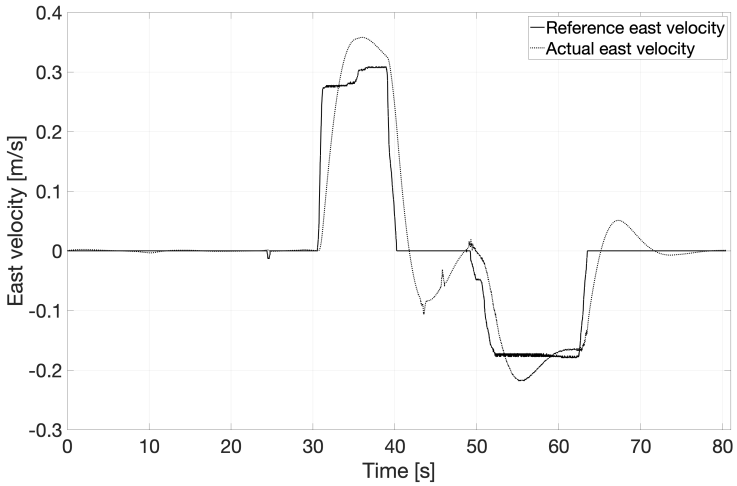

(b) Reference vs actual east velocity - helicopter PID controller

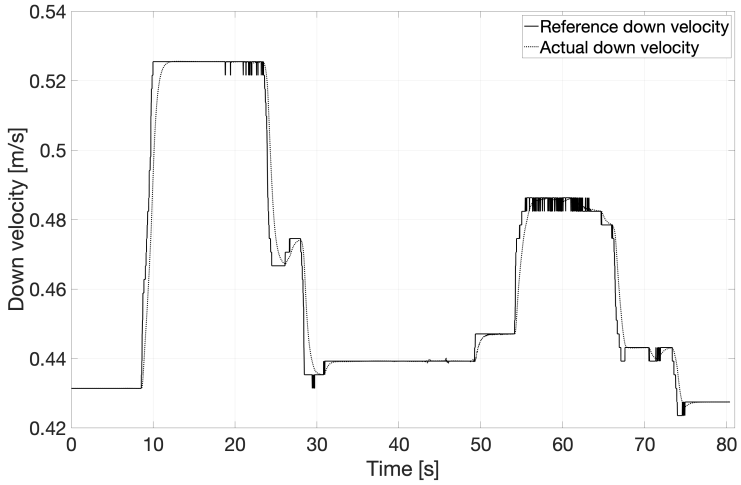

(c) Reference vs actual down velocity - helicopter PID controller

Figure 4.7: Simulation with human pilot - NED velocities

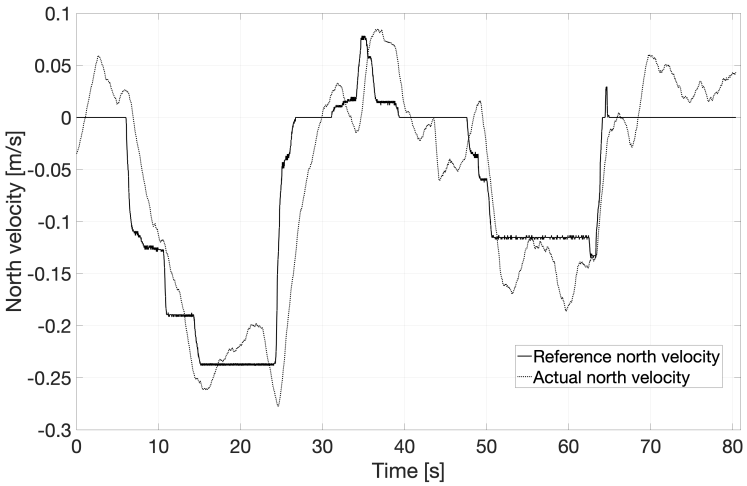

(a) Reference vs actual north velocity - helicopter PID controller

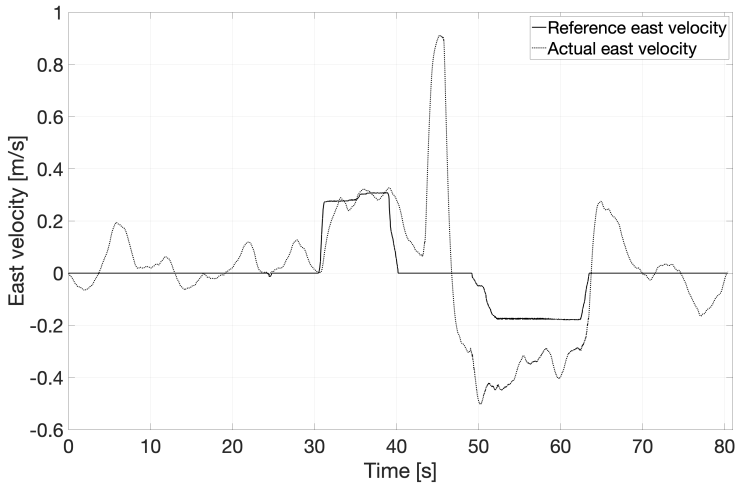

(b) Reference vs actual east velocity - helicopter PID controller

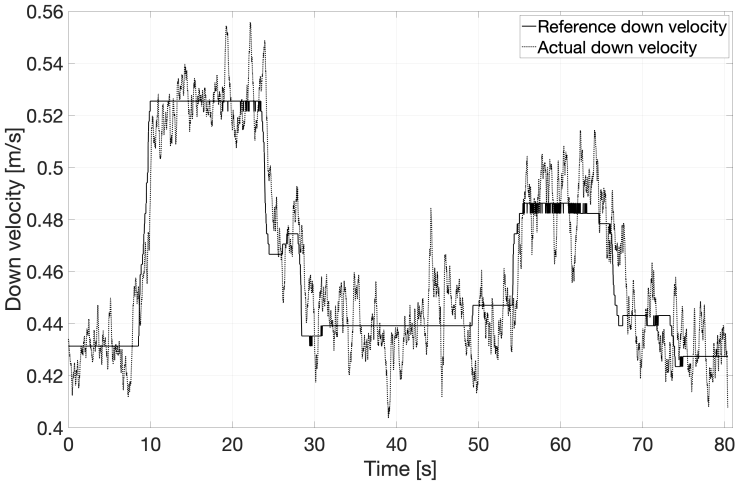

(c) Reference vs actual down velocity - helicopter PID controller

Figure 4.8: Simulation with human pilot and wind - NED velocities

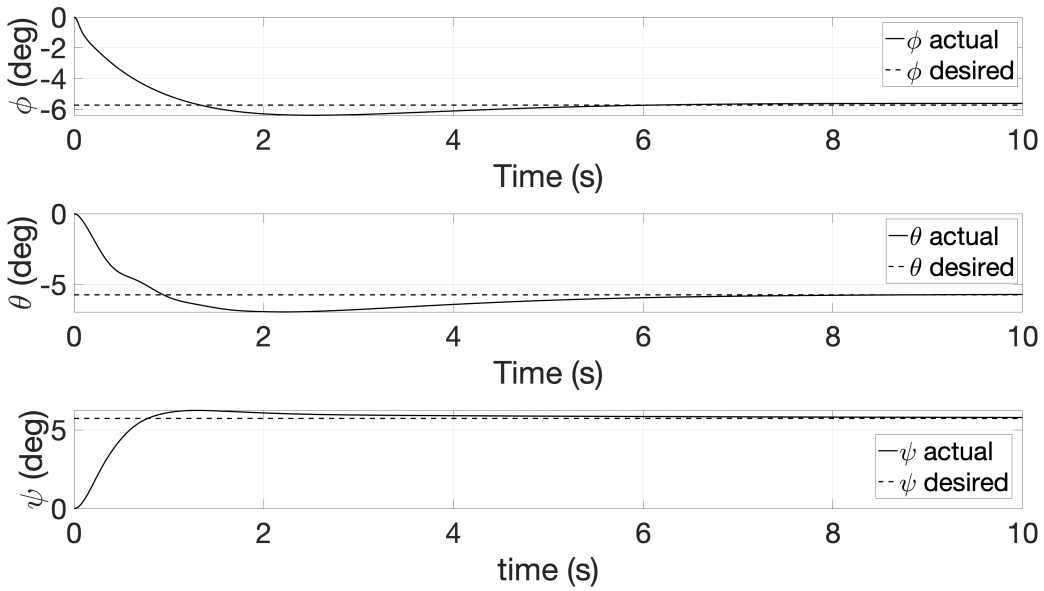

Figure 4.9: Reference vs actual attitude angles - synchrotor PID controller

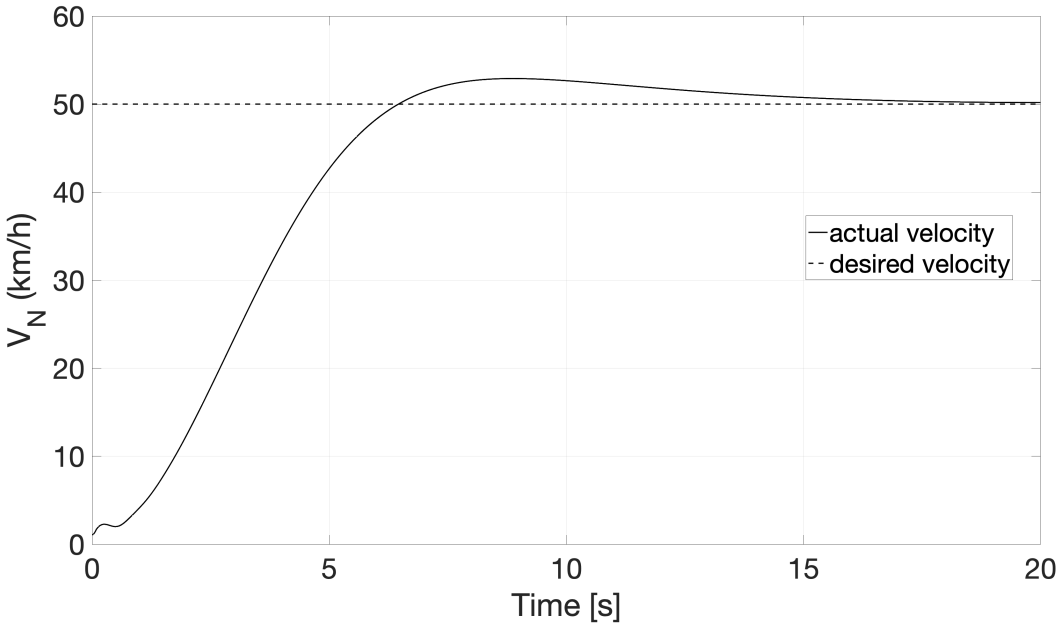

Figure 4.10: Reference vs actual north velocity - synchrotor PID controller

4.2 $\mathcal{L}_1$ adaptive controllers simulation results

The outcomes of the simulations with the adaptive controllers as designed in 3.2 are given in this section. At first, the author discuss the attitude stabilization through the use

of $\mathcal{L}_1$ control system. Then the adaptive speed controller simulation is examined.

4.2.1 $\mathcal{L}_1$ adaptive controller for attitude stabilization

This section presents the results of the simulations with the augmented controller for the attitude stabilization. To begin with, a comparison between the baseline and the augmented controllers is presented, showing how $\mathcal{L}_1$ architecture improves the baseline performances. Then the switching procedure effects are illustrated. Finally, robustness of the system to wind disturbances is tested.

Baseline vs Augmented controls

The first simulation result presented is a comparison between the baseline and the augmented controllers. The helicopter has to follow a simple sequence of two steps as reference signal starting from the hovering trim condition. In figure 4.11a pitch response to a first step input of 2.5 deg at 20 s of simulation and to a second step of -10 deg at 70 s is reported. Compared to the augmented system, the baseline controller has a slower response to step inputs. This is also confirmed by figure 4.11b, where the system is asked to track a first step input of 5 deg at 20 s and a second step of -5 deg at 70 s on the roll axis. Finally, yawrate response to a first step input of 5 deg/s at time 20 s and to a second step of -5 deg/s at time 70 s is showed in figure 4.11c. For all the axes, the augmented controller is able to improve the system performances, especially in operational regions far from the baseline design point. Similar results are presented in figures 4.12a, 4.12b 4.12c. Herein, pitch angle, roll angle and yawrate responses to different single step inputs are reported starting from the hovering initial equilibrium condition.

In figure 4.13 a simulated test flight is illustrated. In this test the helicopter is piloted trough a joystick by an human operator through the use of the FlightGear® interface. Pilot control commands are recorded and used both to test baseline performances and augmented control performances. As expected, augmented control systems performances lead to smaller errors achieving desired helicopter response and couplings effects are also mitigated. In figure 4.14 the three axis normalized inputs are showed. $\mathcal{L}_1$ adaptive control contributes only for a part of the total control signal, as it appears by comparing baseline and augmented control inputs. Figures 4.15a, 4.15b, 4.15c and 4.15d show adaptation parameters during the same simulated flight test.

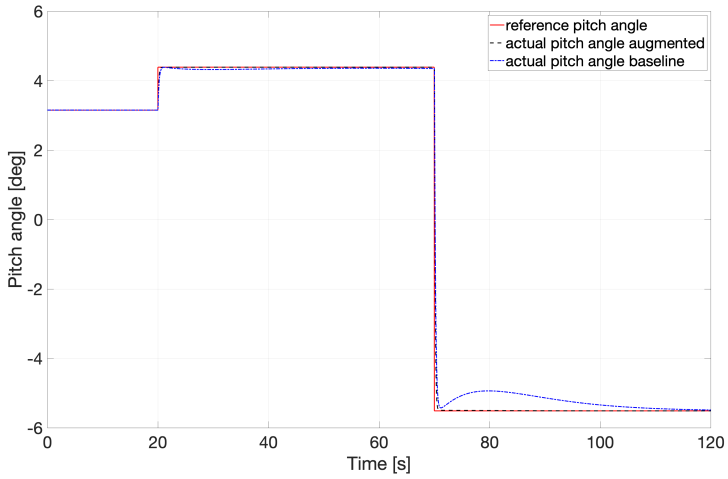

(a) Pitch reference tracking, baseline PID vs augmented PID

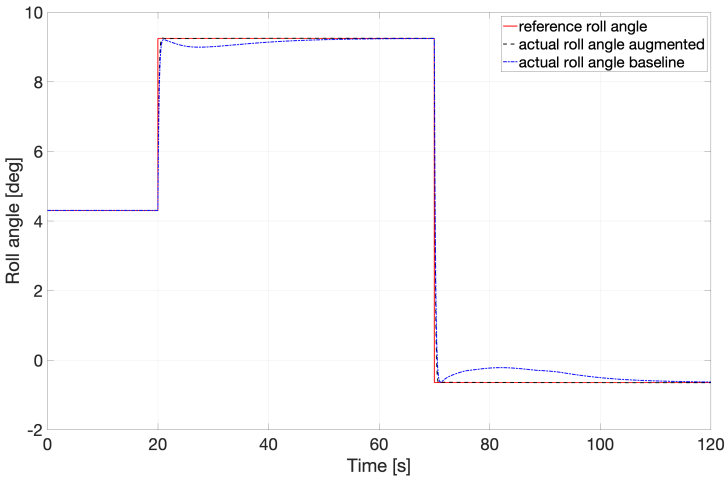

(b) Roll reference tracking, baseline PID vs augmented PID

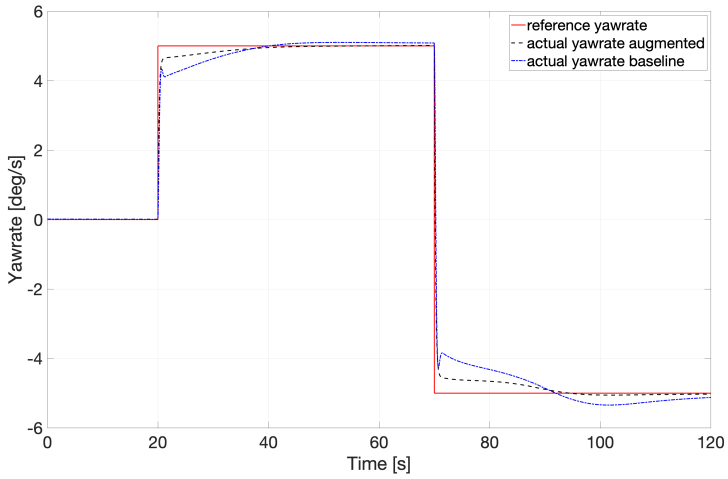

(c) Yawrate reference tracking baseline PID vs augmented PID

Figure 4.11: Reference tracking baseline PID vs augmented PID

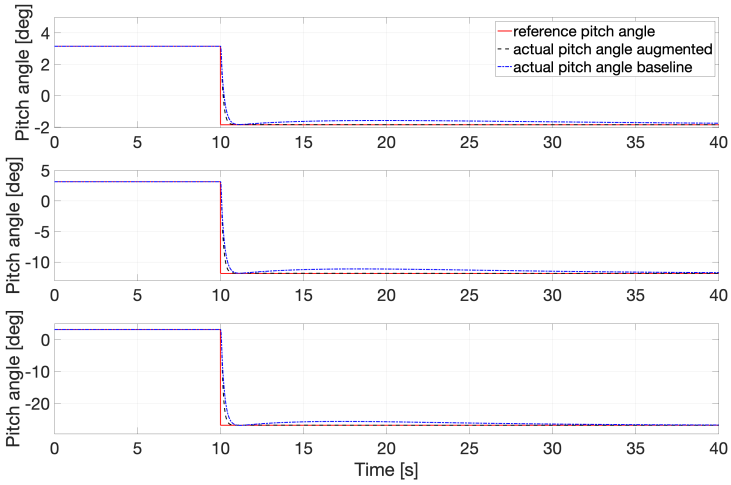

(a) Multiple pitch reference tracking, baseline PID vs augmented PID.

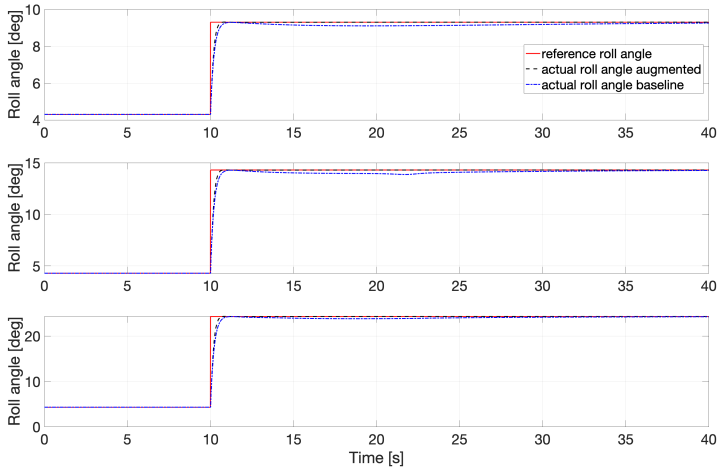

(b) Multiple roll reference tracking, baseline PID vs augmented PID.

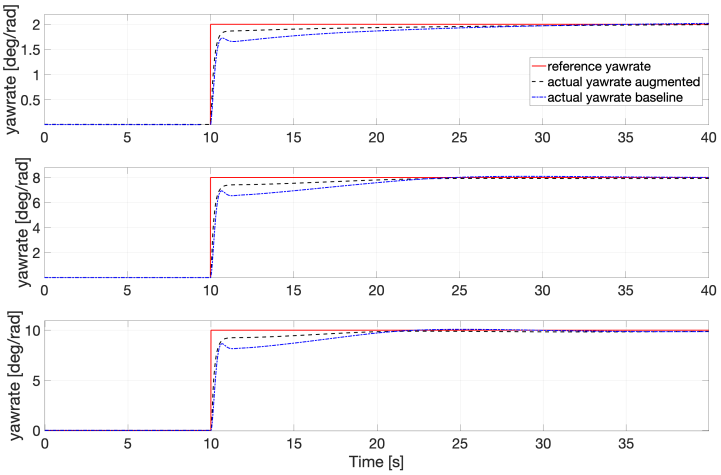

(c) Multiple yawrate reference tracking, baseline PID vs augmented PID.

Figure 4.12: Multiple Reference tracking baseline PID vs augmented PID.

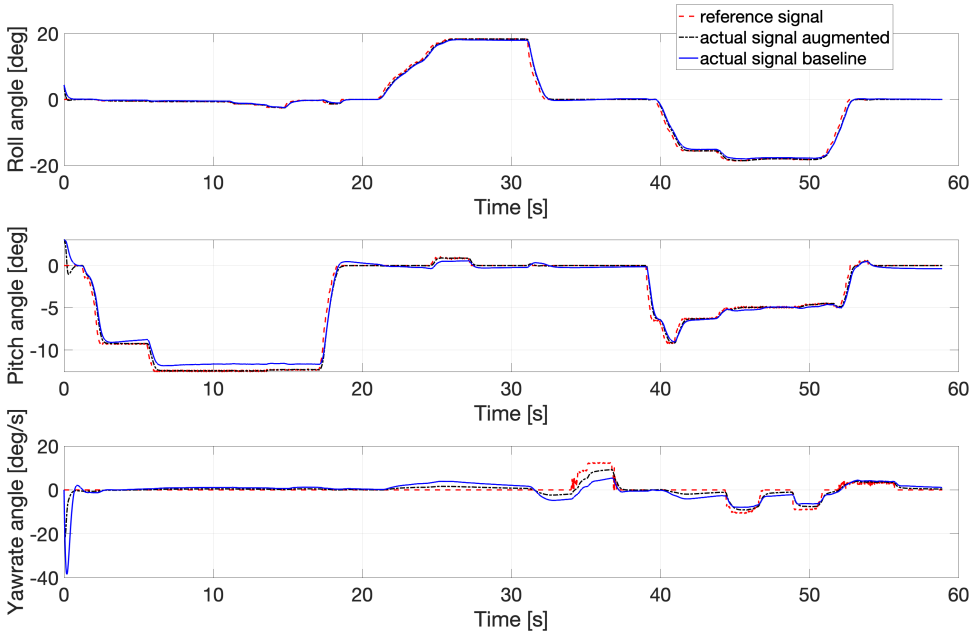

Figure 4.13: Attitude and yawrate in simulation

$\mathcal{L}_1$ switch

The effects of the procedure to switch on/off the $\mathcal{L}_1$ contribution are illustrated in figures 4.16a, 4.16b, 4.16c. The value of the switch signal is set to zero when the $\mathcal{L}_1$ contribution is off, while it is equal to 1 when the adaptive contribution is on. The switching procedure is performed in simulation while the helicopter is in hovering, that is a trim condition. As soon as the $\mathcal{L}_1$ controller is switched on, pitch angle, roll angle and yawrate set to reference values after a small spike. The switching off procedure is less critical, unless on the yaw axis, for which the procedure induces a spike that in any case does not affect the flight.

Wind disturbance rejection

Wind disturbance rejection towards the three mathematical representations of wind is tested also with the augmented controller. Wind characteristics are illustrated at the beginning of this section. Results are showed in figure 4.17, in which all the presented wind models are combined together. The simulated flight is the same presented in figure 4.13, aside from the inclusion of the wind velocity. The augmented controller presents better reference tracking capabilities even in presence of wind disturbance with respect to the baseline controller.

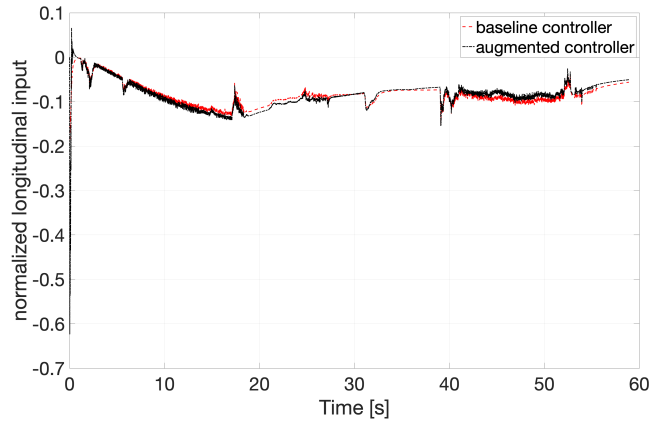

(a) Normalized longitudinal input

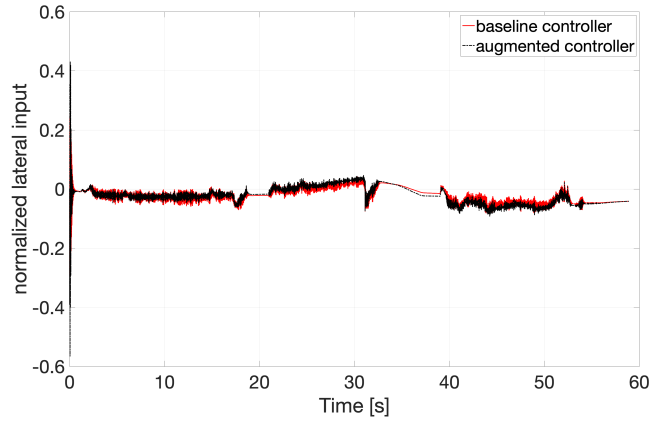

(b) Normalized lateral input

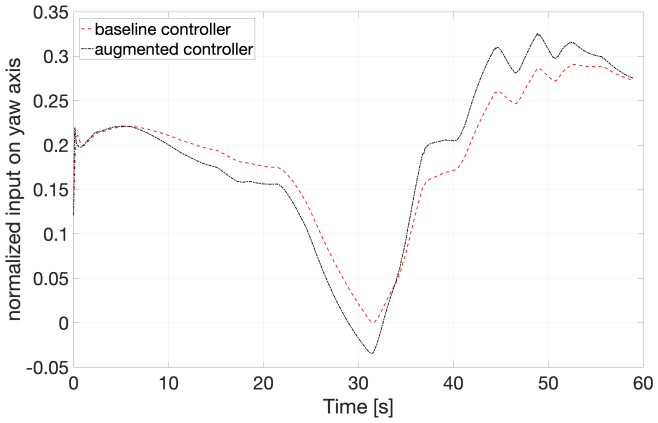

(c) Normalized yaw input

Figure 4.14: Helicopter normalized inputs

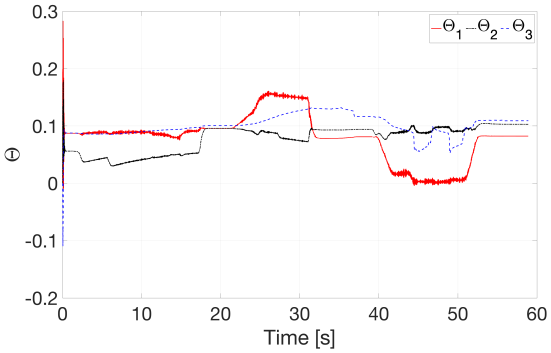

(a) Theta

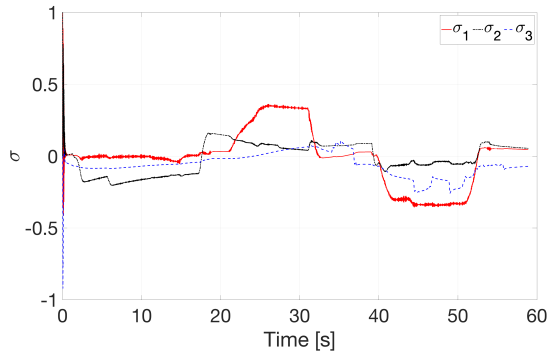

(b) Sigma

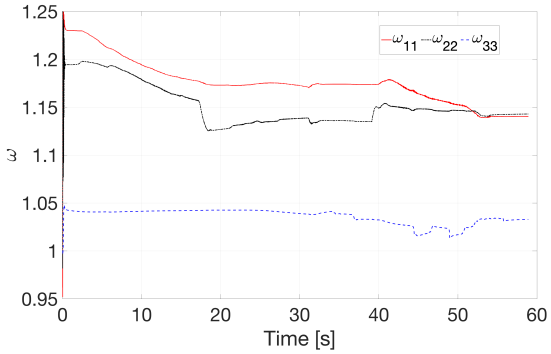

(c) Omega diagonal terms

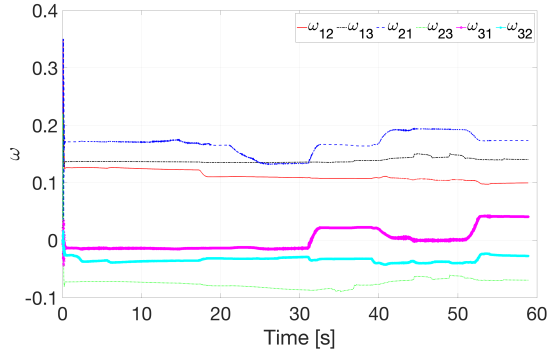

(d) Omega extra-diagonal terms

Figure 4.15: Adaptation terms over time

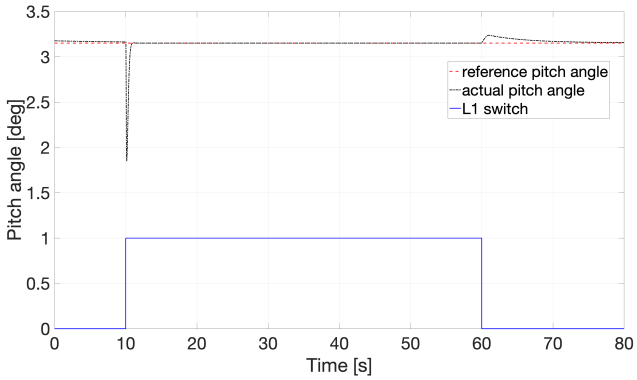

(a) Switch effect on pitch

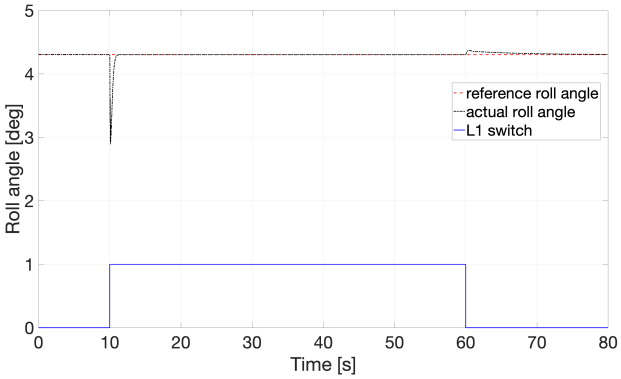

(b) Switch effect on roll

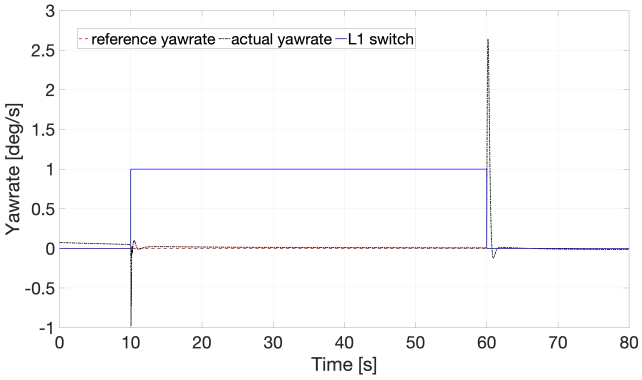

(c) Switch effect on yawrate

Figure 4.16: Switch effect on attitude and yawrate

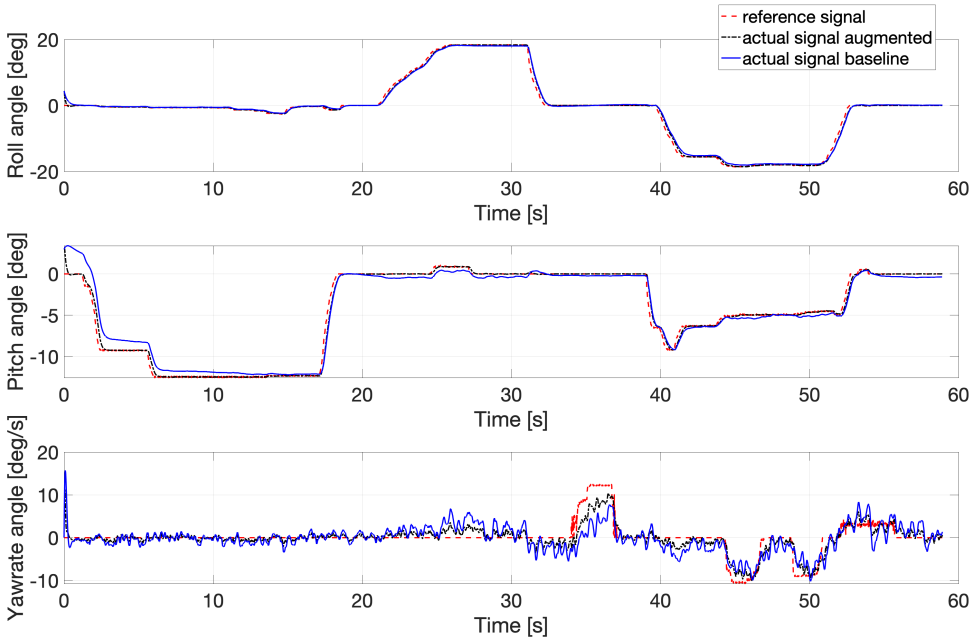

Figure 4.17: Combined model wind rejection

4.2.2 $\mathcal{L}_1$ adaptive controller for speed hold

Results of simulations carried out to test the adaptive speed hold are here discussed. In this case, the results illustrated are the comparison between the PIDs controller and the adaptive one in terms of capability to track the desired velocities on north and east axes. Tests are computed with and without the wind disturbances.

A series of North speed references are given to the helicopter. V_N goes from 0 m/s up to 30 m/s with an increment of 5 m/s every 10 s. The helicopter starts from the equilibrium condition in hovering. The east velocity is asked to stay at 0 m/s. Figures 4.18 and 4.19 show respectively how the two controllers track the reference signals on the two axes. Both PIDs and $\mathcal{L}_1$ controllers maintain the helicopter at the desired speed, but the $\mathcal{L}_1$ adaptive control system is able to follow the desired dynamics, guaranteeing proper control system performance. This is clearly depicted on the north axis in figure 4.18. On the east axis in figure 4.19 it seems that for low north velocities $\mathcal{L}_1$ adaptive controller displays an higher overshoot if compared to the PID behaviour while tracking the zero east velocity reference. On the other hand, PIDs based control system performs a sign reversal for low north velocities, that increases its overshoot as V_N grows. This behaviour may be due to the fact that while the north speed increases, $\mathcal{L}_1$ adaptive controller tries to keep the desired dynamics. The PID controllers do not perform this task.

To test disturbance rejection the same inputs are passed to the controllers in presence

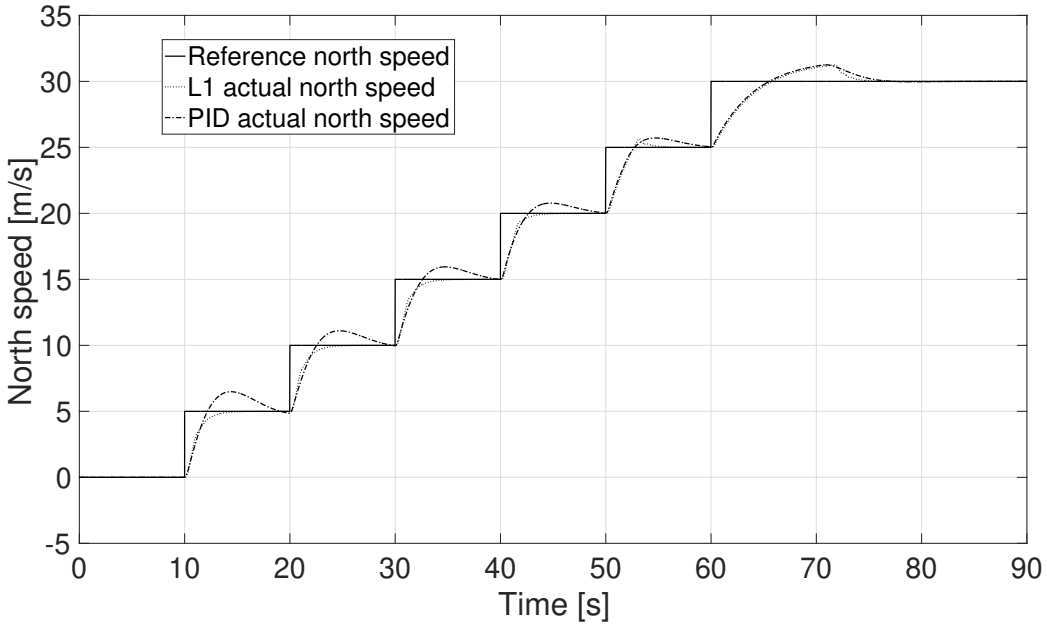

Figure 4.18: V_N reference tracking, adaptive vs PID

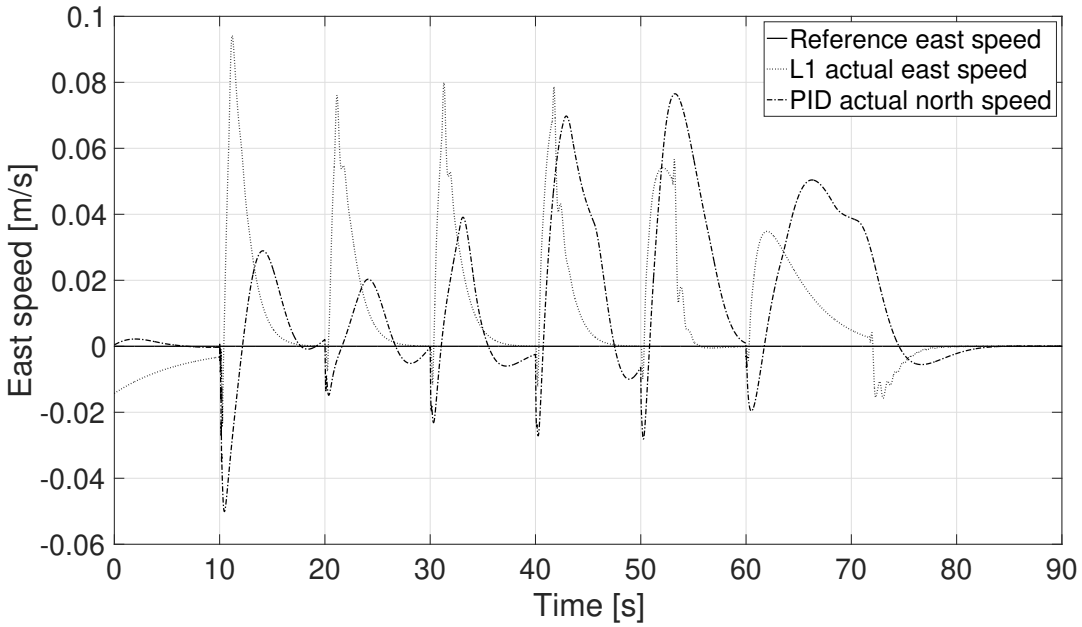

Figure 4.19: V_E reference tracking, adaptive vs PID

of the three wind disturbances described at the beginning of section 4.1.1. As for the case of attitude stabilization, the adaptive controller can overcome wind disturbances better than the PIDs. It is clearly reported in figures 4.20 and 4.21, which show the comparison

between the classical and the adaptive controllers in following the desired velocities in case of wind disturbances. Again, V_N varies from 0 m/s up to 30 m/s with an increment of 5 m/s every 10 s, while V_E has to be zero. Especially on the lateral axis, the adaptive control system perform much better than the PID one, which displays higher V_E oscillations.

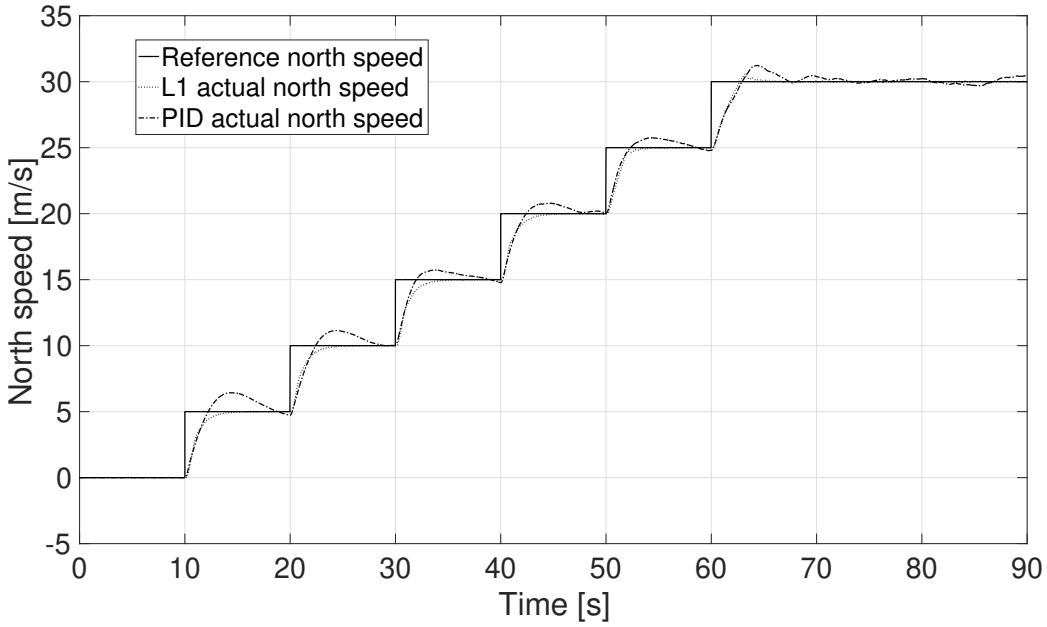

Figure 4.20: V_N reference tracking, adaptive vs PID in case of wind disturbances

4.3 Cooperative control

The capabilities of the developed cooperative control algorithm have been tested in simulation and results are here presented. The involved vehicles are the rover and the helicopter, whose mathematical models are in sections 2.3 and 2.1 respectively. Each vehicle control system is described in the corresponding sections of chapter 3.

Three situations are simulated to test the algorithms. The first one is a simple case in which the rover stays in a fixed position at a certain distance from the helicopter, that has to reach a specified distance $\bar{d}$ from it, as explained in section 3.3 of the previous chapter. In the second case the rover does not stand in a fixed position and the helicopter has to follow it and reach the desired distance $\bar{d}$ from the rover. The third case presents the simulations related to the behavioural strategy. Accordingly, both vehicles must keep the desired distance $\bar{d}$ from the formation geometry center. The helicopter has to maintain the desired starting altitude. With regards to the helicopter control system, both classical both adaptive controllers have been used during the simulations.

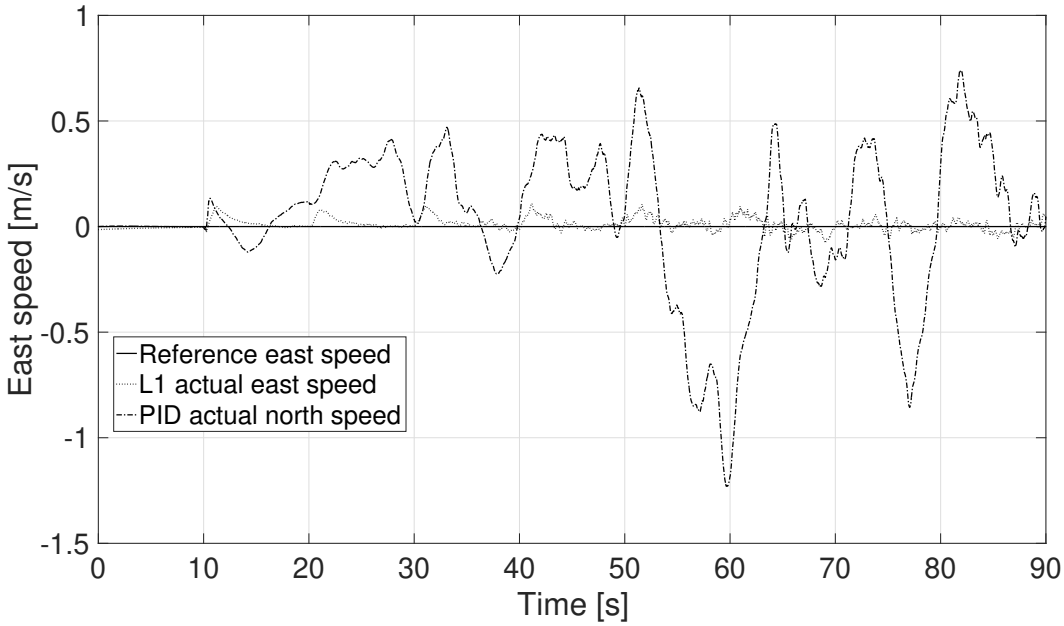

Figure 4.21: V_E reference tracking, adaptive vs PID in case of wind disturbances

4.3.1 Simulations for leader-wingman scenario

In the leader-wingman scenario many simulations have been carried out to test the control laws. Either possible cases have been investigated: first the rover as leader and then the helicopter. In any case two step simulations have been conducted. Firstly, the leader stands in a fixed position and the wingman has to move to the desired position and to keep it. Secondly, the leader moves with prescribed velocity and direction and the follower should move consequently to reach and preserve the required position. For the sake of compactness, in this section only the results of test with the rover as leader and the helicopter as wingman are given.

Simulation test 1: rover stays in a fixed position

For this first test, the leader is located at 25 m both on north both on east directions and it has to stay fixed in this position. The helicopter starts from zero position on both axes in hovering flight condition and has to reach a distance of 5 m from the rover. Figures 4.22a and 4.22b show the reference and the actual values for position respectively on north (4.22a) and east (4.22b) axes. The cooperative control algorithm is able to execute the required task in few seconds with high precision, since at the end of simulation the helicopter actual position coincide with the desired one. In figure 4.23 the helicopter trajectory is given in North-East plane to confirm the ability of the control system in moving to the desired

position.

Simulation test 2: rover moves with a constant velocity

In the second simulation, the leader starts moving along the north direction with a velocity of approximate 3 m/s. The rover initial position is set at 300 m on the north and at 2 m on the east axis. As in the previous case, the helicopter starts from the origin of the NED axes. The distance that the wingman has to keep in following the leader is of 5 m along the two north and east axes. An equivalent test have been performed using both the classical and the adaptive approaches in the helicopter speed hold control system, as reported in chapter 3 and whose performances are discussed in sections 4.1.1 and 4.2.

Figures 4.24a, 4.24b, 4.24c illustrates the reference and the actual values for positions and heading angle of the helicopter while following the rover. The helicopter speed hold control system tested in this case is based on PIDs. As proved by the plots, the control system fulfills the demanded task being the final actual values coincident with the desired ones. For this test case it is also reported the behaviour of the helicopter heading angle controller in figure 4.24c that validates the cooperative control system.

As stated before, an equivalent test has been carried out with the adaptive helicopter speed hold. This time the rover initial position is set at 10 m on the north and at 0 m on the east axis and it moves with a speed of 2 m/s along north axis. The helicopter should track the leader with a desired distance of 5 m on both axes at an altitude of 10 m starting from the origin of NED axes. Figures 4.25a and 4.25b illustrate the distance error along the north and east axes. These plots demonstrate that also with an adaptive helicopter speed hold controller, the cooperative algorithm is able to perform properly. In addition, this test validates the capability of entire cooperative control implementation to preserve the independence of each vehicle control system from the cooperative one.

4.3.2 Simulations for behavioural approach scenario

As for the leader-wingman scenario, numerical tests have been performed. Vehicles are required to keep a specified distance $\bar{d}$ from the FGC, as defined in section 3.3. $\bar{d}$ is set to a value of 5 m. Rover initial position is $N_R = 100$ m, $E_R = 100$ m. Helicopter initial position is $N_H = 0$ m, $E_H = 0$ m. Both heading angles are set equal to zero at the beginning.

Figure 4.26 shows the reference and the actual values of rover positions. The same variables for the helicopter are given in figure 4.27. Simulations prove that also for the behavioural approach the control algorithm is able to perform the required task. Both vehicles employ few seconds to reach the desired position without appreciable errors. In particular the cooperative control law for the rover does not even show overshoots while

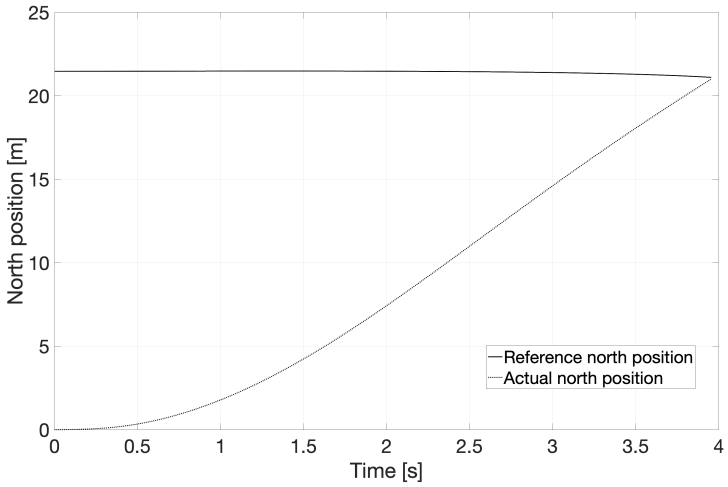

(a) Reference vs actual position along north axis

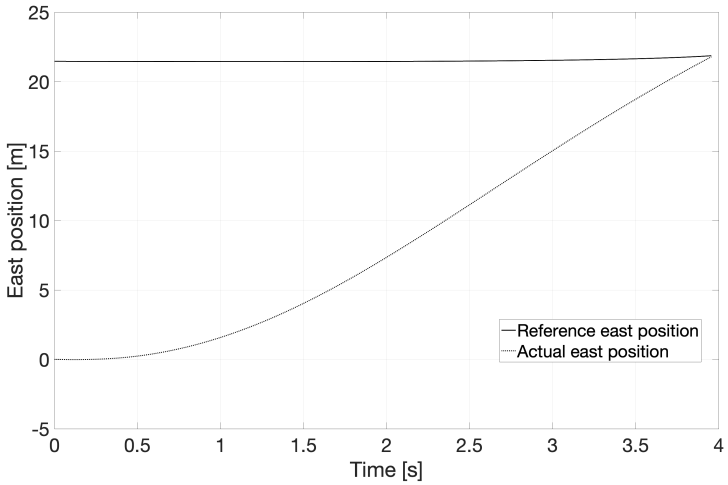

(b) Reference vs actual position along east axis

Figure 4.22: Cooperative control simulation - First test

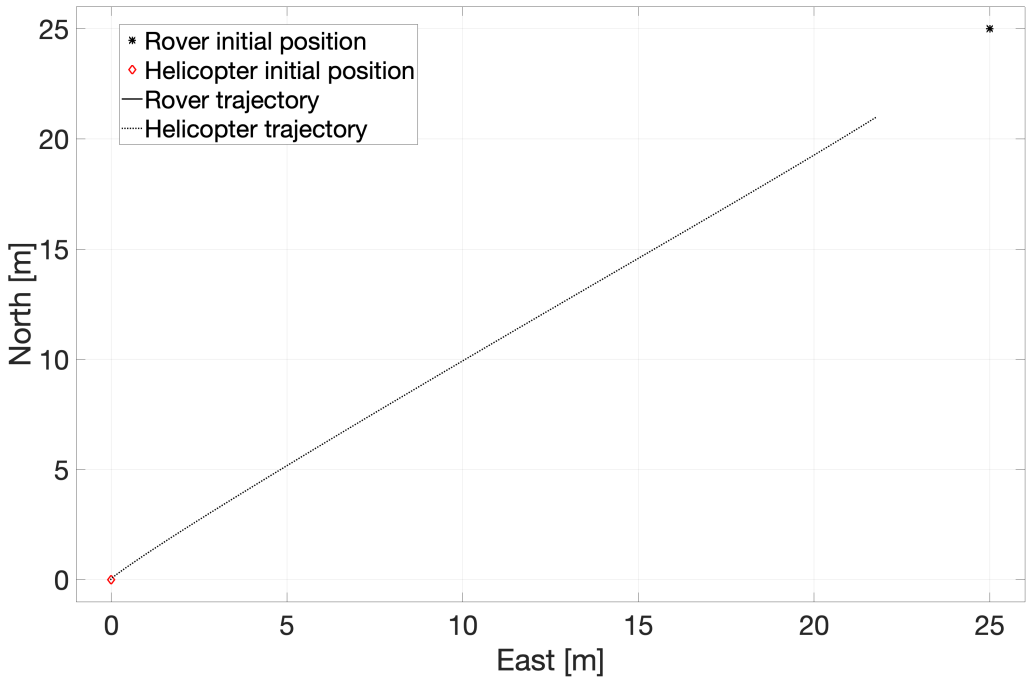

Figure 4.23: Rover and helicopter trajectories - First test

approaching the desired point, whereas the helicopter cooperative controller is proven to be little less precise. Many other simulations have been computed, but results are not here showed for conciseness.

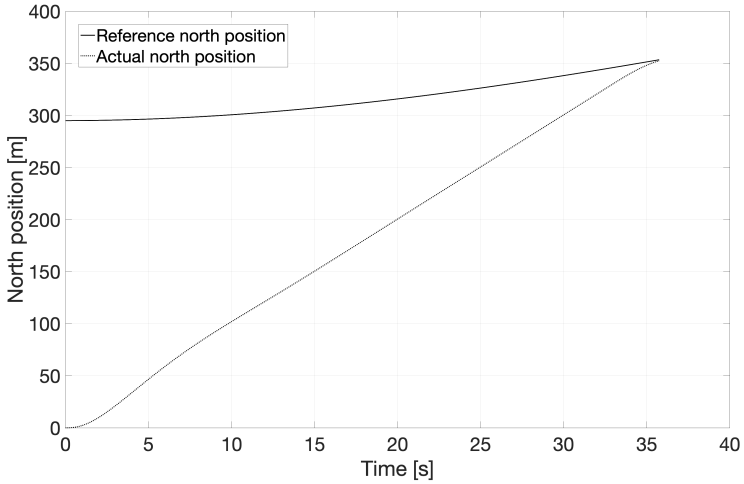

(a) Reference vs actual position along north axis

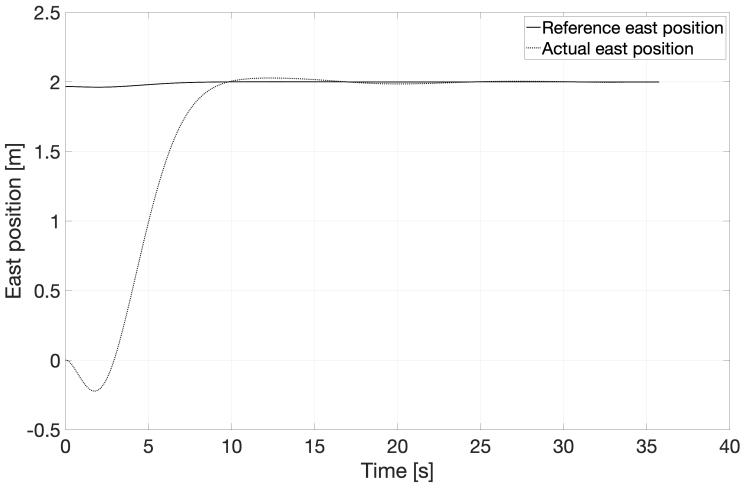

(b) Reference vs actual position along east axis

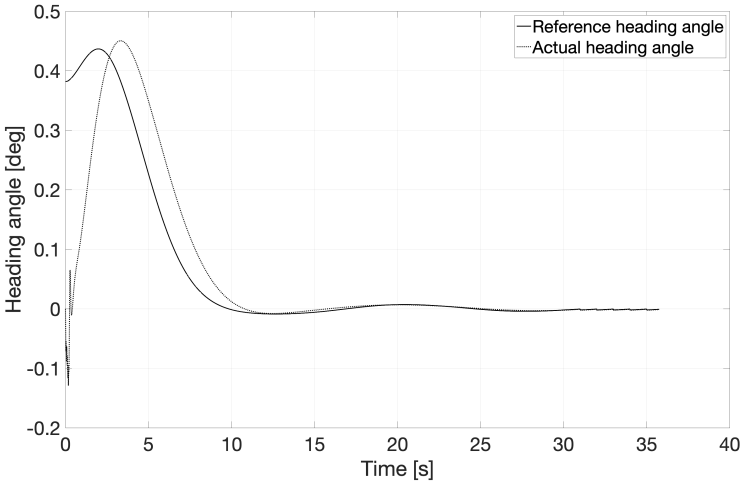

(c) Reference vs actual heading angle

Figure 4.24: Cooperative control simulation - Second test

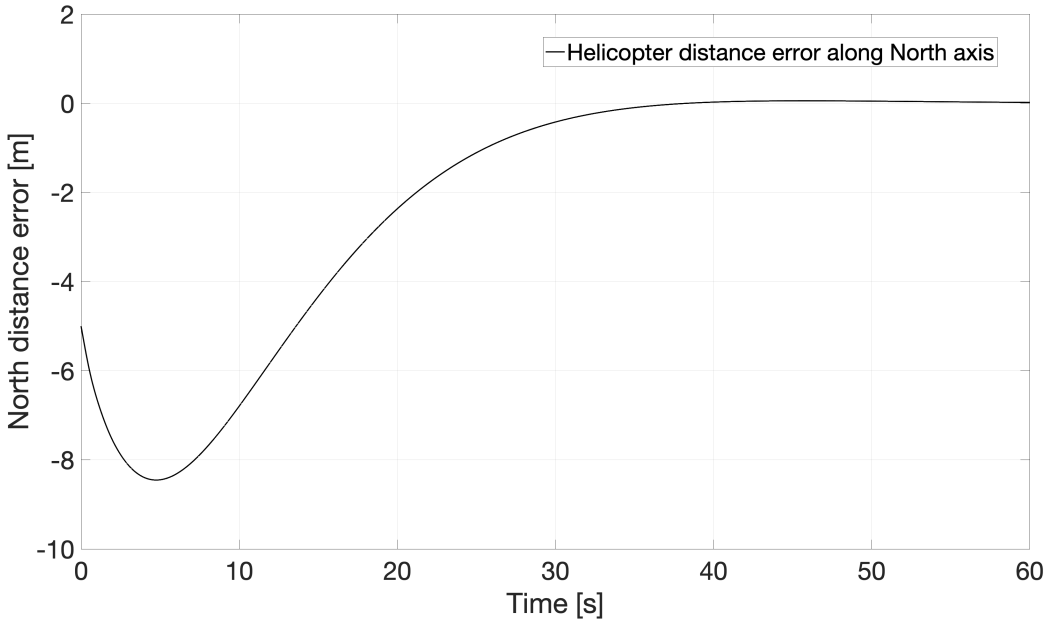

(a) North distance error in case of helicopter adaptive speed hold controller

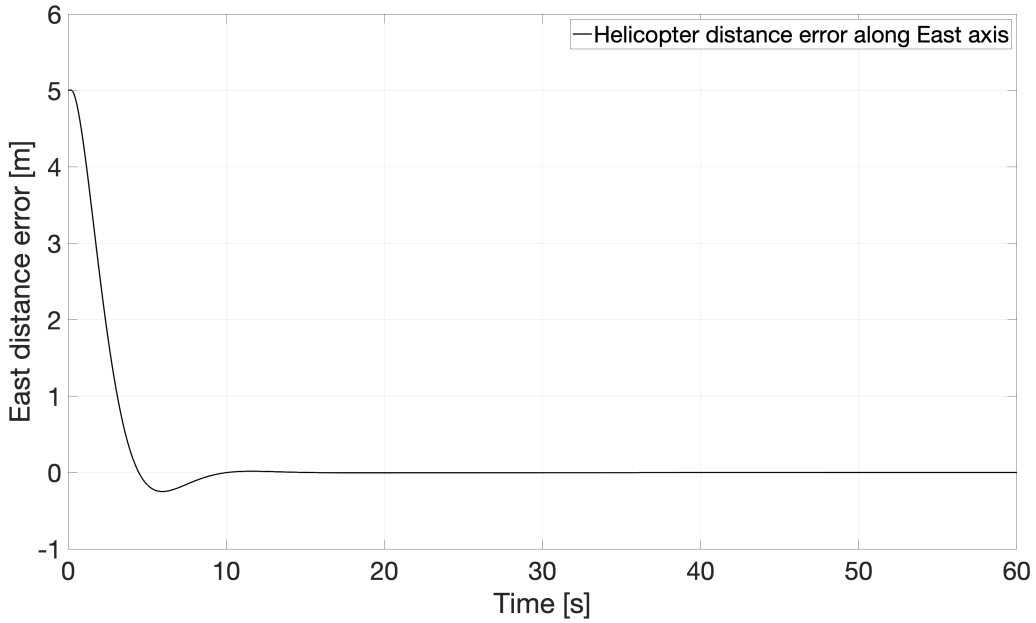

(b) East distance error in case of helicopter adaptive speed hold controller

Figure 4.25: Distance errors in case of helicopter adaptive speed hold controller

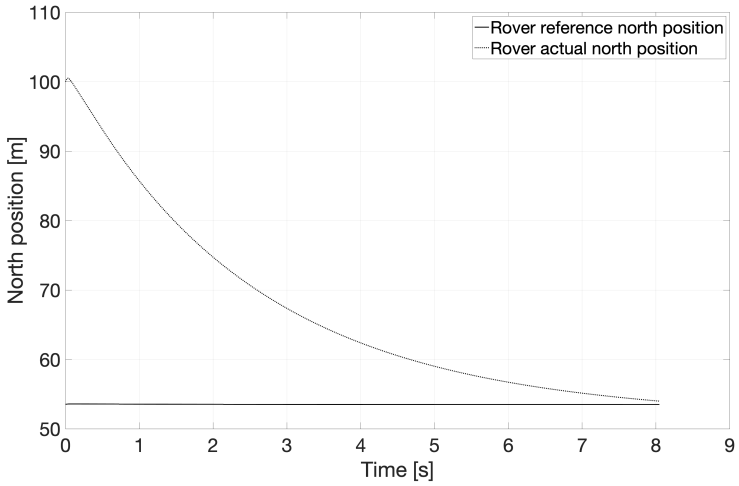

(a) Reference vs actual position along north axis for rover

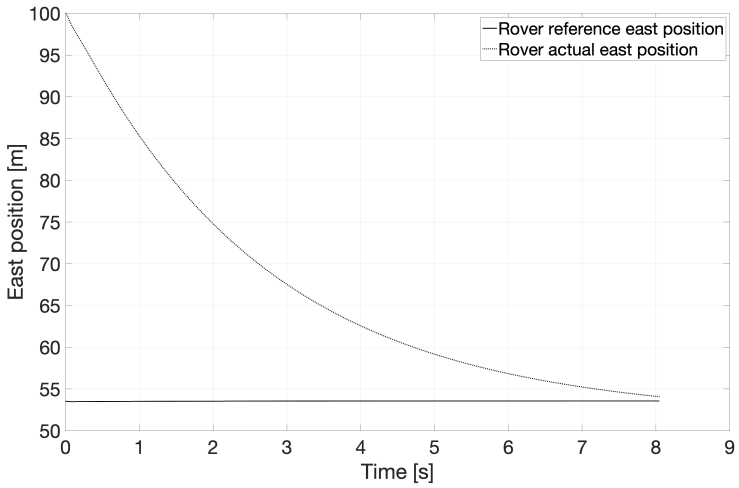

(b) Reference vs actual position along east axis for rover

Figure 4.26: Reference vs actual values for rover in cooperative control - behavioural approach

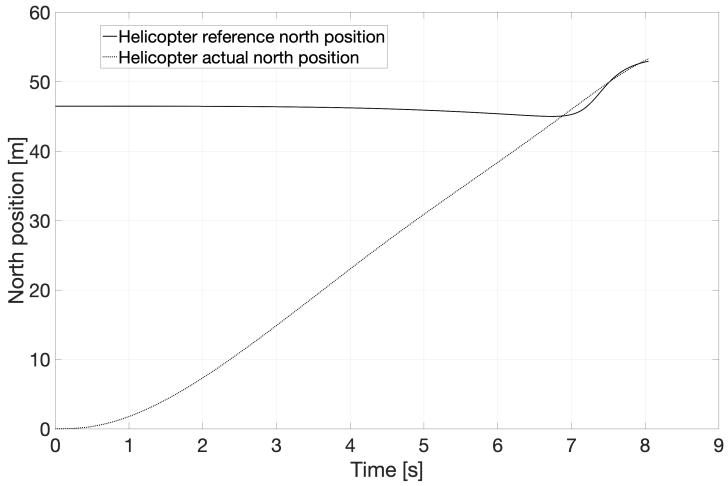

(a) Reference vs actual position along north axis for helicopter

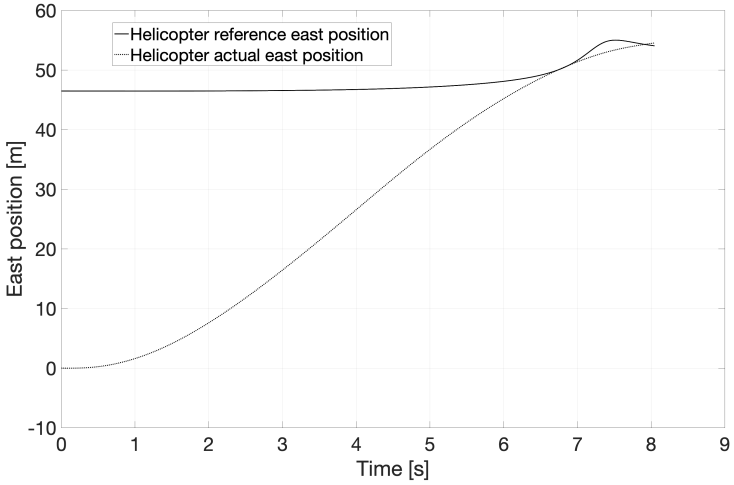

(b) Reference vs actual position along east axis for helicopter

Figure 4.27: Reference vs actual values for helicopter in cooperative control - behavioural approach

CHAPTER 5

Experimental validation

In this chapter results of the experimental campaign are given. Primarily the experimental setup is entirely introduced with an overview of all its components. Then flight tests outcomes are discussed. The experimental campaign has been operated for the validation of topics with the use of the conventional single main rotor helicopter, since it has not been possible to develop a prototype for the synchrotor in these years of Ph.D.

5.1 Experimental setup

An experimental helicopter UAV platform consists of the airframe, the avionics hardware, the ground station and the relevant software.

5.1.1 Helicopter airframe

The SAB® Goblin Thunder 700 helicopter has been used, whose data are reported in Table B.1. This Radio Commanded (RC) helicopter has been equipped with the electronic showed in the scheme of figure 5.1.

The engine mounted on the UAV is the XNOVA lightning motor 4025-1120KV Shaft A, that is a brushless high performance motor proper for this type of small-scale helicopters. The power is provided by a a Lipo battery with 6 cells, 6300 mAh. As illustrated in the scheme of figure 5.1, there is a Safety Power Switch (SPS). It is an electronic primary switch designed for switching off/on the main power supply. It adds an element of safety when

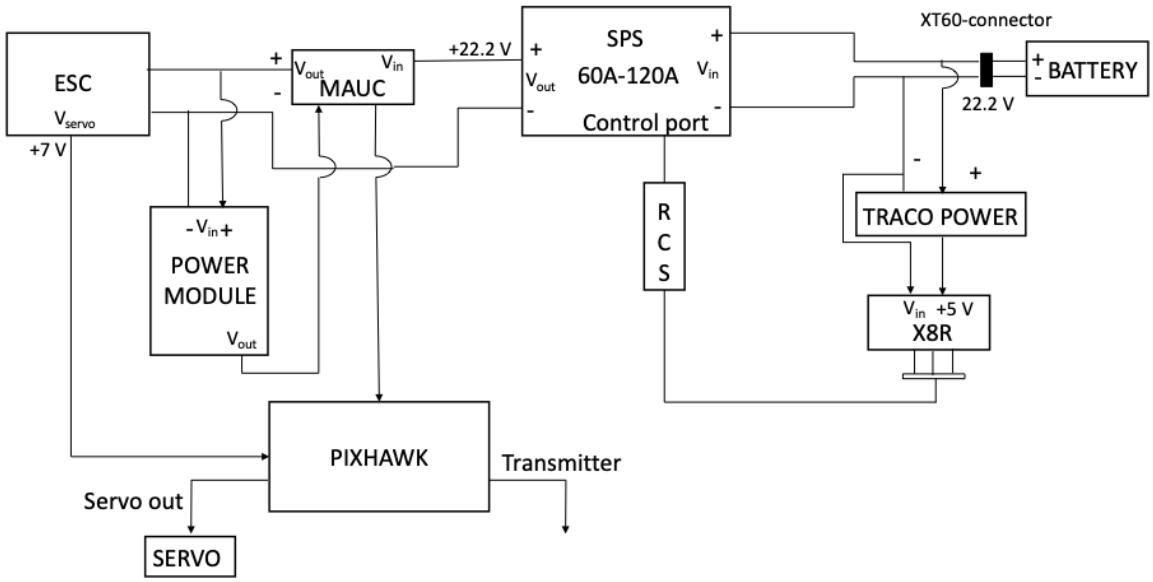

Figure 5.1: Goblin 700 helicopter electronic scheme

handling the vehicle, without the need to physically disconnection of the main battery pack. It is linked to the Radio Command (RC) through the related telemetry system. In order to govern the electric motor, an Electronic Speed Control (ESC) is employed. It is directly connected to the power module and to the autopilot hardware, that is described below. Since the helicopter has four control inputs, there are four servo controls: three for the main rotor control (collective, roll and pitch) and one for tail rotor (yaw axis).

5.1.2 Hardware

The avionics hardware of the helicopter is a Pixhawk® autopilot. It may be indicated as "Pixhawk Flight Management Unit (FMU)". It is an open hardware management unit suitable for a large variety oh vehicles, from aerial to terrestrial ones. It incorporates an high-performance microcontroller, based on Cortex-M4F processor, an inertial measurements unit (IMU), which integrates three-axis gyroscopes and accelerometers, a barometer and a set of external sensors including Global Navigation satellite System (GNSS) and magnetometers. All the important specifications, including data sensors, are reported in the Pixhawk® websites [92]. This hardware has been selected for its open-source features and for the possibility of the direct interaction with the Matlab/Simulink® suite through the toolbox Pixhawk® Pilot Support Package (PSP). By using the PSP, the user can

work with Simulink® and directly can generate code for the FMU. As a matter of fact, this toolbox automatically translates the Simulink® code into Pixhawk® compatible code languages.

5.1.3 Flight software

In this section the flight control software is described. In figure 5.2 the proposed software architecture is shown, as it has been designed in Simulink®. The software is uploaded on the FMU through the PSP.

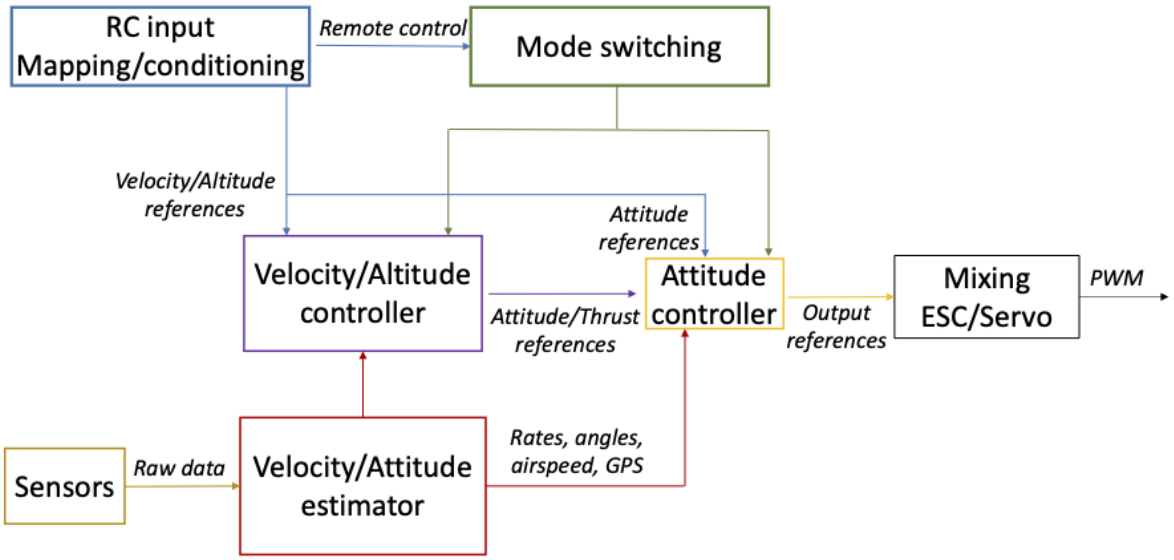

Figure 5.2: Goblin 700 Flight control architecture

The flight control software should have the capacity to be easily adapted to the various demands according to the automation level required. For this reason, different flight modes have been designed and implemented on the FMU. These modes are how the autopilot responds to inputs, controlling the vehicle and providing many levels of autopilot assisted flight. The pilot has the possibility to select the right flight mode for the mission and can also change it during the flight. Usually, it is done by using a switching on the RC or on a ground control station. The number and the types of flight modes may be different. In reference to the required level of automation, these can be typically arranged into manual, assisted and auto modes [93].

In the so-called manual mode, the pilot has direct control of the vehicle actuators and the automation is absent or minimum. In the assisted modes, pilot has still vehicle control, but autopilots offer a certain level of assistance. The autopilot triggers different feedback control chains to regulate the actuators. Common assisted modes are:

- Attitude rate flight mode: pilot controls roll, pitch and yaw rates, while the throttle/collective is purely manual. It it also called Acro mode.
- Attitude flight mode: pilot controls roll and pitch angles and yaw rate, throttle/collective is manual. It is also known as Stabilize mode. The attitude and the heading hold controller presented in chapter 3 belong to this mode.
- Altitude flight mode: it is the same of Attitude mode with the autopilot controlling also the altitude. Thus, the user controls the roll and pitch angles, the yaw rate and the vertical speed. The control scheme is presented in chapter 3 under the paragraph altitude hold controller.
- Speed flight mode: pilot controls lateral and forward ground speed, yawrate and vertical speed. It is also known as Speed Hold and its architecture for the helicopter is presented in chapter 3 as Velocity controller.

Finally, auto flight modes have the higher level of automation. The vehicle may compute autonomously tasks as trajectory tracking or pre-programmed missions.

5.1.4 Ground station

The ground station employed for flight tests is the open source program Mission Planner®. It is a full-featured ground station application for the ArduPilot open source autopilot project [94]. It supports the application layer message protocol called MAVlink.

5.2 Flight test

This section presents the results from flight test performed with the setup illustrated above. The first results presented are those related to the validation of the helicopter trim curve. Afterwards those related to the validation of the PID controller architecture. Finally, outcomes of the $\mathcal{L}_1$ experimental validation.

5.2.1 ArduCopter flight test

Results of flight test performed with the ArduCopter firmware are given. The scope of these tests is to provide accurate trim data to validate the conventional single-main rotor helicopter mathematical model presented in chapter 2. This is the reason that led to the choice of ArduPilot. It is an open source firmware that enables the creation and use of trusted, autonomous, unmanned vehicle systems. It provides a comprehensive suite of

tools suitable for almost any vehicle and application [95]. Through the use of this autopilot it is possible to acquire adequate precise data. In what follows results of a flight test to find trim data in hovering condition are reported. The test was carried out with three available flight mode: stabilize, altitude hold and loiter. This last one allows the pilot to control position on roll and pitch axes, yawrate and the vertical speed as in the altitude hold mode and it has been used. The pilot had to simply take off and bring the helicopter to the desired altitude and then let the autopilot acting to stabilize the vehicle in hovering without moving the sticks. Subsequent table 5.1 reports a comparison between experimental and simulated trim values for attitude angles in degrees during the hovering. By taking the average value from the experimental data, the attitude trim angles in hovering are given at an altitude of 6. There is a discrepancy on the trim pitch angle due to the estimation of the vehicle longitudinal center of gravity position. In fact, moving the center of gravity along the longitudinal axis, the trim angle changes consequently.

Table 5.1: Comparison of simulated and experimental values of trim attitude angles in hovering

Trim data	Simulated	Experimental
ϕ	4.32°	4.8°
θ	2.98°	0.77°

5.2.2 Helicopter PIDs flight test

Experimental validation of the PID baseline control architecture is realized by means of a set of flight tests. As described above, the rotorcraft is equipped with the Pixhawk® FMU in which the proposed software is directly deployed with PSP toolbox. The proposed PID based controller architecture is described in chapter 3. The firmware architecture is showed in figure 5.2. Control tasks and estimation are carried out in real-time directly by the autopilot unit with a frequency set to 250 Hz and the data are captured with a sampling rate of approximately 8 Hz for the actual state variables and 3 Hz for the command inputs. PID gains are settled in empirical way starting from simulations values around a trim flight condition. In what follows data from flight test performed with the PID based Speed Hold autopilot are given. Hovering condition and maneuver are both operated by the pilot and results are discussed in the subsequent plots.

Data for hovering are reported in a time window of approx 10 s. NED velocities are presented in figure 5.3 to verify the effective flight condition. Values for the three velocities are in a range between -0.3 m/s to 0.1 m/s, that can be considered an hovering.

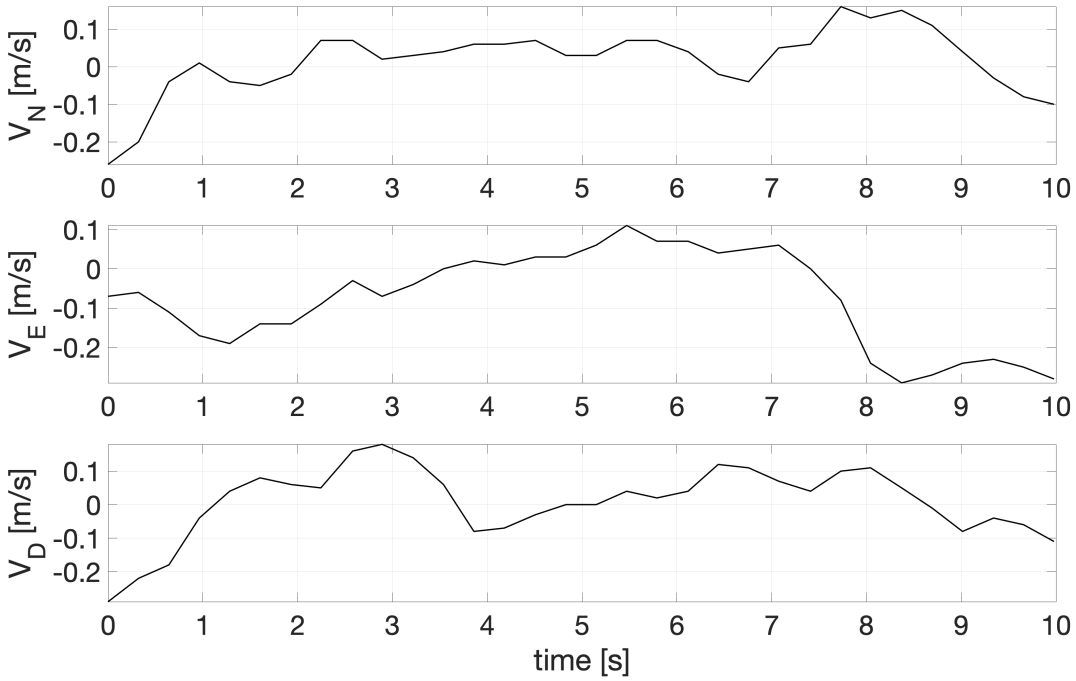

Figure 5.3: Helicopter actual velocities in hovering

Figures 5.4, 5.5 and 5.6 illustrate the percentage error computed respectively on roll and pitch angles and on yaw-rate. The error is calculated as in equation (5.1):

$$e_{\%} = \frac{X_{reference} - X_{measured}}{X_{reference}} * 100 \tag{5.1}$$

where the reference values are those required by the controller and the measured are the actual values of the variables. The two plots 5.4, 5.5 validate the capability of the attitude hold control system to track the desired values for ϕ and θ angles, since percentage error is manly under 10%. On the other hand, the heading hold control system in figure 5.6 exhibits to be less precise with percentage errors spikes up to 33%. Actually, one of the most challenging tasks for a helicopter is stabilizing the tail. The presence of external disturbances deteriorates the controller performances. However, the overall behaviour is considered acceptable to maintain the helicopter heading stable. Due to time reasons it was not possible to refine the tuning since it has been done empirically during flight tests.

With the aim to show the control system behaviour in a flight condition different from the hovering, figures 5.7, 5.8 and 5.9 show the controller response to a pilot maneuver in terms of percentage error, whose formula is given in (5.1). This maneuver is reported in terms of NED velocities in figure 5.10. It covers a time interval of approx 20 s. Data prove the capability of both the attitude hold and heading hold controllers to stabilize the

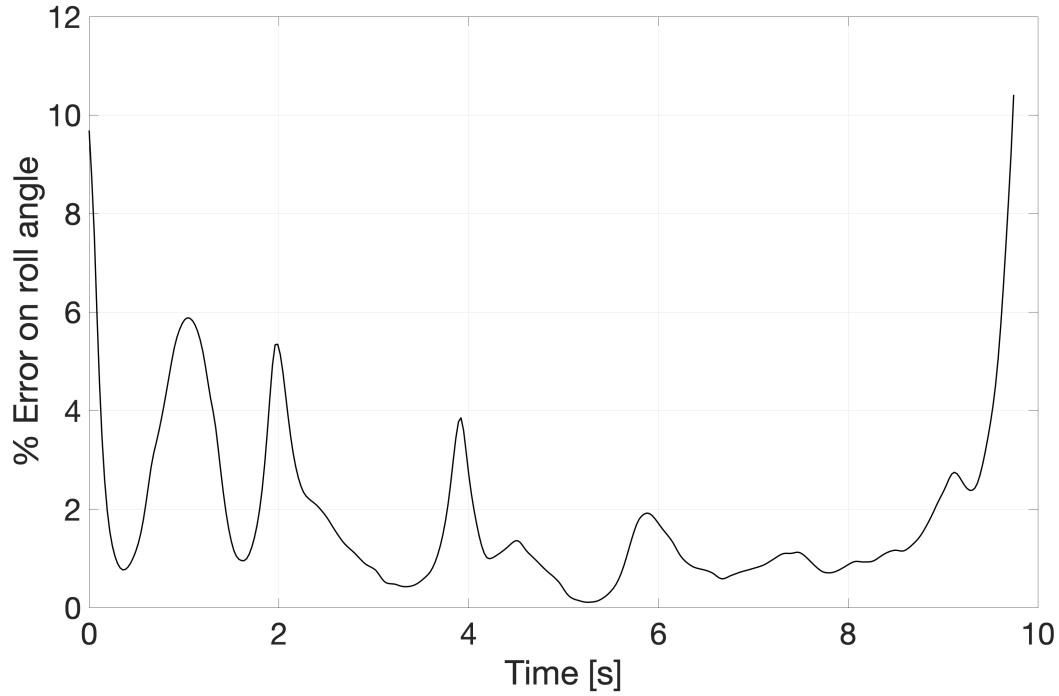

Figure 5.4: Helicopter percentage error on roll angle in hovering

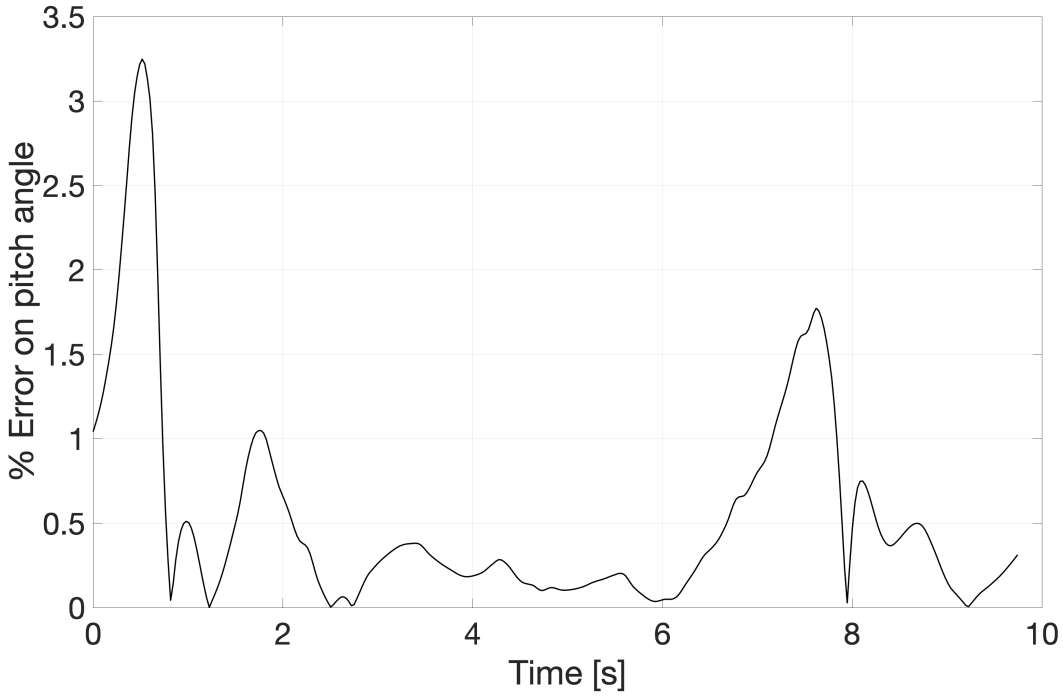

Figure 5.5: Helicopter percentage error on pitch angle in hovering

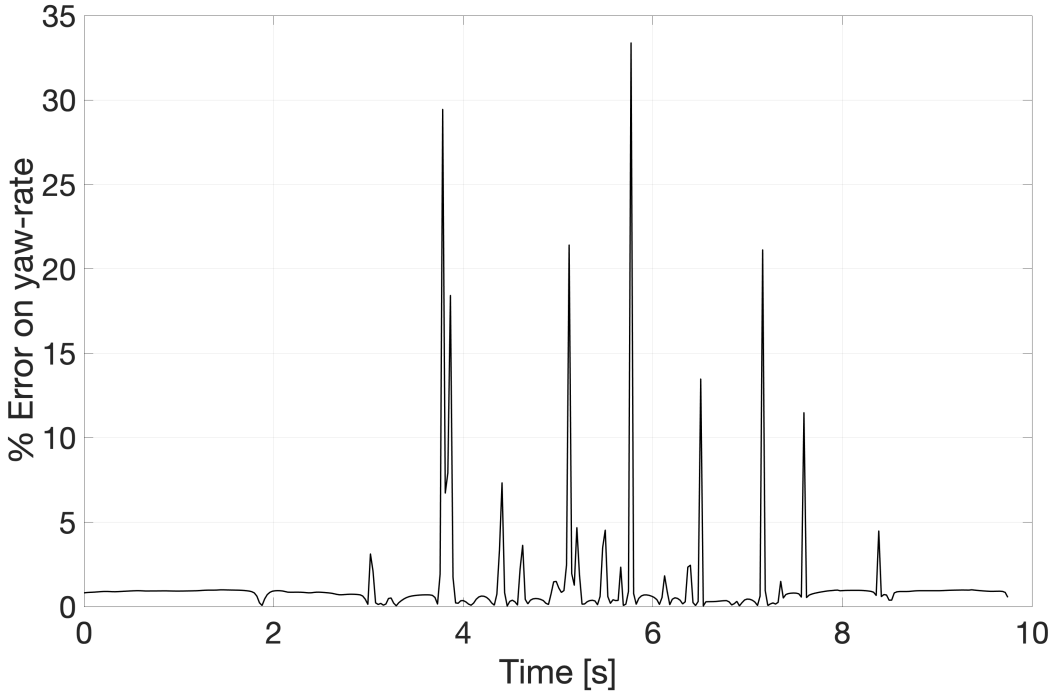

Figure 5.6: Helicopter percentage error on yaw-rate in hovering

helicopter, even if there are some significant spikes. Especially on the first 2 s of the test, roll axis show errors whose values are up to 70%. This undesired behaviour is linked to the fact that both north and east velocities were experiencing a a remarkable and quick change, as illustrated in figure 5.10. As a matter of fact, whenever the velocities go through abrupt variations, errors occur in attitude stabilization. Indeed the demand for attitude autopilots is considerable because of this significant fluctuation and the reported errors on the actual attitude are considered tolerable.

Results prove that the classical PID controllers are capable to maintain the required flight condition, but there still need the necessity to improve the gains tuning. At the same time, PID gains are tuned for a prescribed flight condition empirically with pilot help, so it should be necessary to add some techniques as gain scheduling to guarantee robustness for all the flight envelope. However the candidate decided to implement the $\mathcal{L}_1$ adaptive control technique to face the problem.

5.2.3 $\mathcal{L}_1$ flight test

Concerning the experimental validation of $\mathcal{L}_1$ adaptive controller, tests have been carried out with the help of an experienced helicopter pilot. The $\mathcal{L}_1$ safe switch mechanism has been implemented as described in chapter 3. In this way, it was possible to safely take off

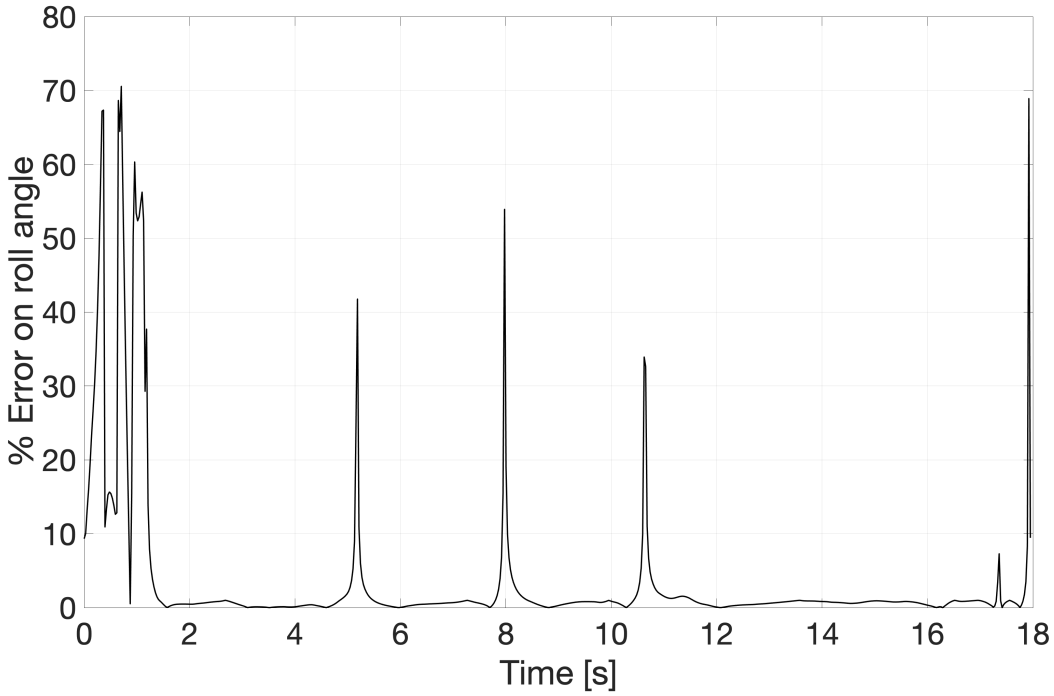

Figure 5.7: Helicopter percentage error on roll angle

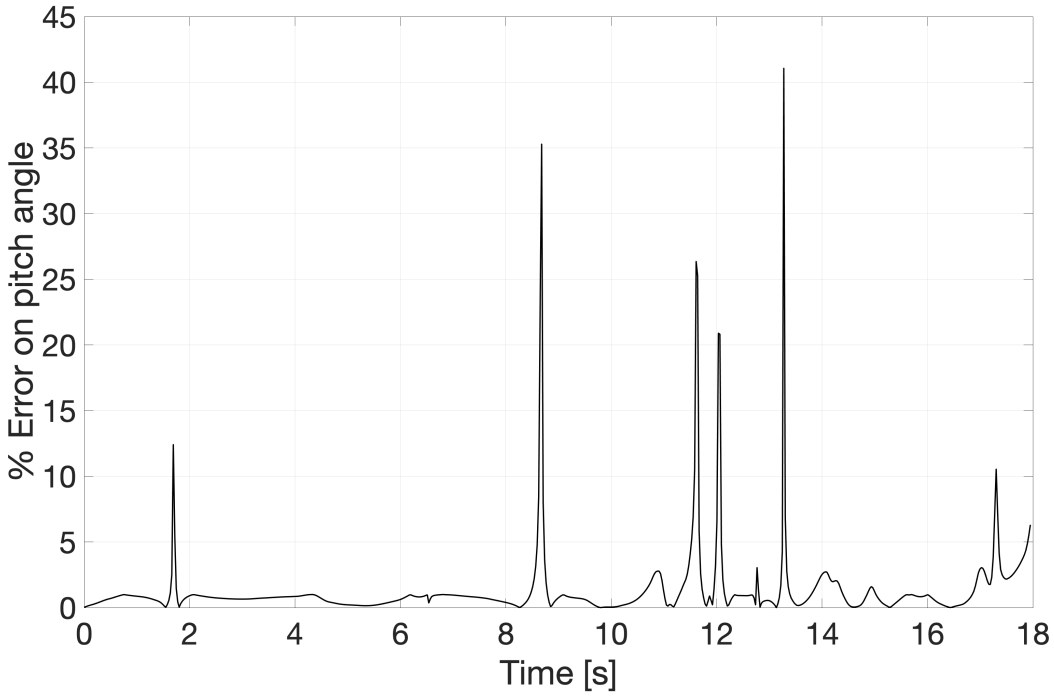

Figure 5.8: Helicopter percentage error on pitch angle

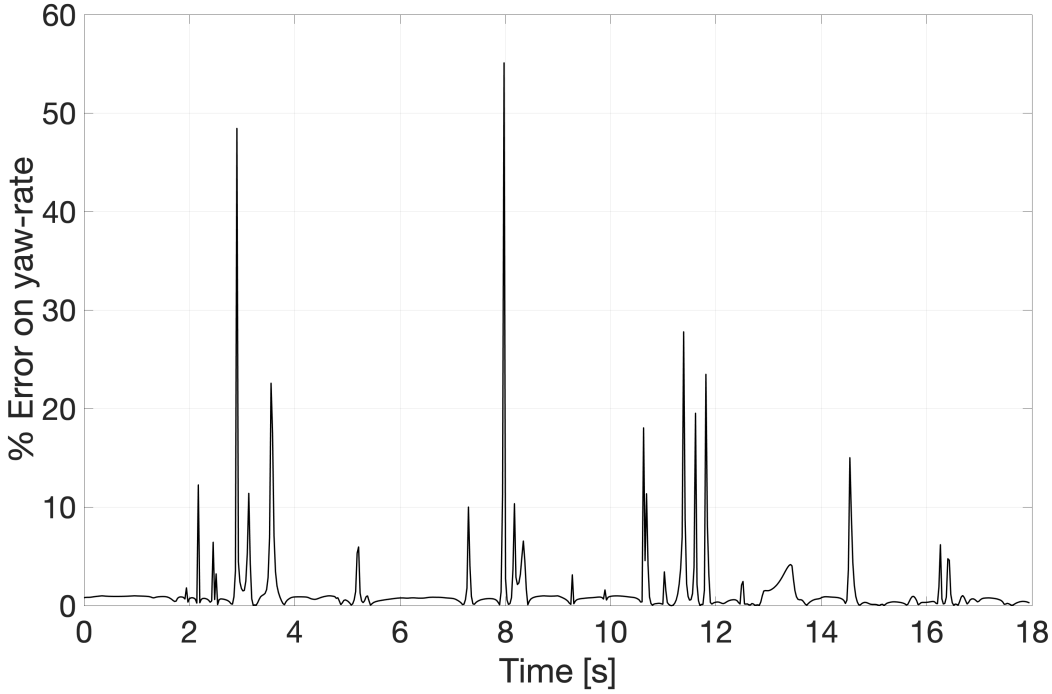

Figure 5.9: Helicopter percentage error on yaw-rate

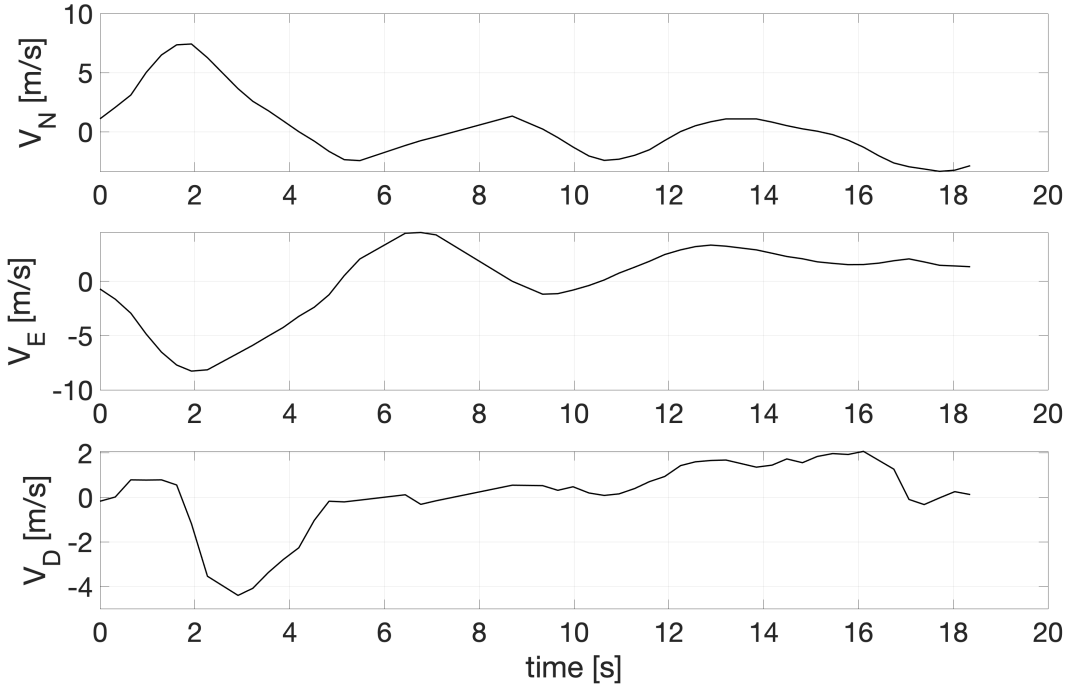

Figure 5.10: Helicopter actual velocities

without the adaptive contribution and to activate it directly in flight. As a matter of fact, being the first flight tests, the main goal was to assess the functionality and the safety of the augmented controller. For this reason, the performed maneuvers with the adaptive contribution activated are short. Furthermore, it was not possible at this stage of the experimental campaign to perform the same maneuvers with the only baseline controller and with the augmented one separately. Also for these tests the autopilot frequency is set to 250 Hz and the data are captured with a sampling rate of approximately 8 Hz for the actual state variables and 3 Hz for the command inputs. The adaptive terms, the reference dynamics and gains have been set in empirical way starting from values utilized in simulations. The Acro flight mode was set by the pilot to take off and then it was switched initially to Stabilize and then the $\mathcal{L}_1$ contribution was enabled. Subsequent plots are extracted in different moments from the same flight test, with and without the adaptive contribution. Time axis is scaled from zero to the end of the selected time window. This is the reason why the time period is different for the two situations. The $\mathcal{L}_1$ contribution is reported on all the three axes.

Figure 5.11a and 5.11b show the controller action on the roll axis and reference vs actual values in degrees are reported. Since the inputs given by the pilot are not the same, it is not easy to clearly recognize the benefits in the use of the augmented controller if compared to simulations results illustrated in chapter 4. PID baseline controller reported in plot 5.11a follows the reference signal with a delay of approximately 1.3 s and an error of 22% approx. Differently, figure 5.11b shows that the augmented controller tracks the reference input with a lower error (approx 14%) in fewer time (less than 1 s). Errors for both controller are reported in figures 5.12a and 5.12b. This proves that the adaptive contribution increases the controller performance. It should be noted that the time window of $\mathcal{L}_1$ activation does not guarantee to the controller adaptation terms to reach their steady values. In addition, differently from simulations, wherein inputs to controllers were given starting from trim conditions, the pilot was continuously adjusting all the command inputs, especially the main rotor collective, varying the thrust contribution and forcing the adaptive terms to vary.

Figures 5.13a and 5.13b present the pitch controller with and without the adaptive contribution, displaying the reference and actual pitch angle in degrees. Errors of the controllers are given in figures 5.14a, 5.14b. In figures 5.15a and 5.15b the reference and the actual yawrate in degrees/seconds are shown, respectively for the baseline and the augmented controllers.

A time delay of 0.71 s is reported by the baseline controller in figure 5.13a with an error of 17%. $\mathcal{L}_1$ helps the baseline controller to track better and faster the reference. In fact figure 5.13b provides that with the augmented control system the time delay is 0.62 s with

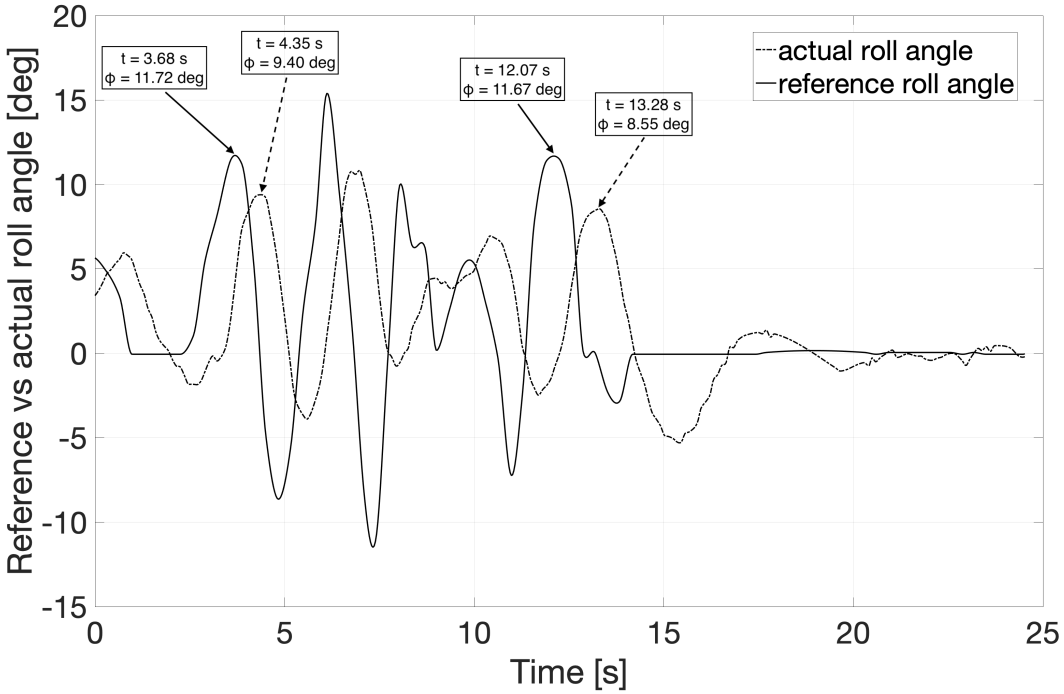

(a) Helicopter flight test results: reference and actual roll angle, baseline controller

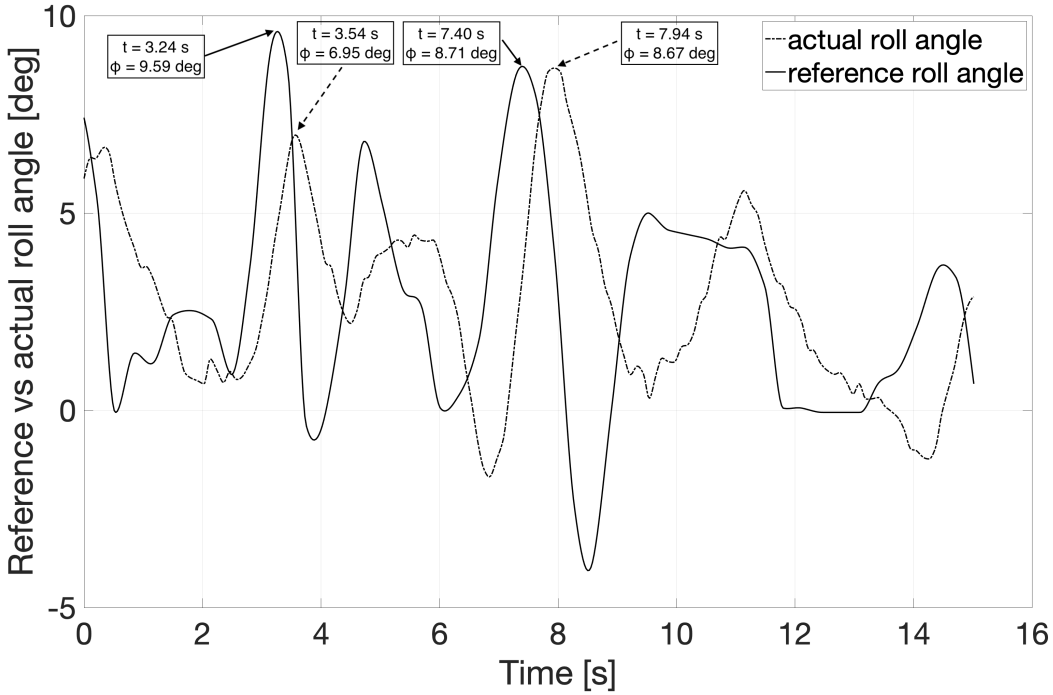

(b) Helicopter flight test results: reference and actual roll angle, augmented controller

Figure 5.11: Helicopter flight test results: reference and actual roll angle, baseline vs augmented controller

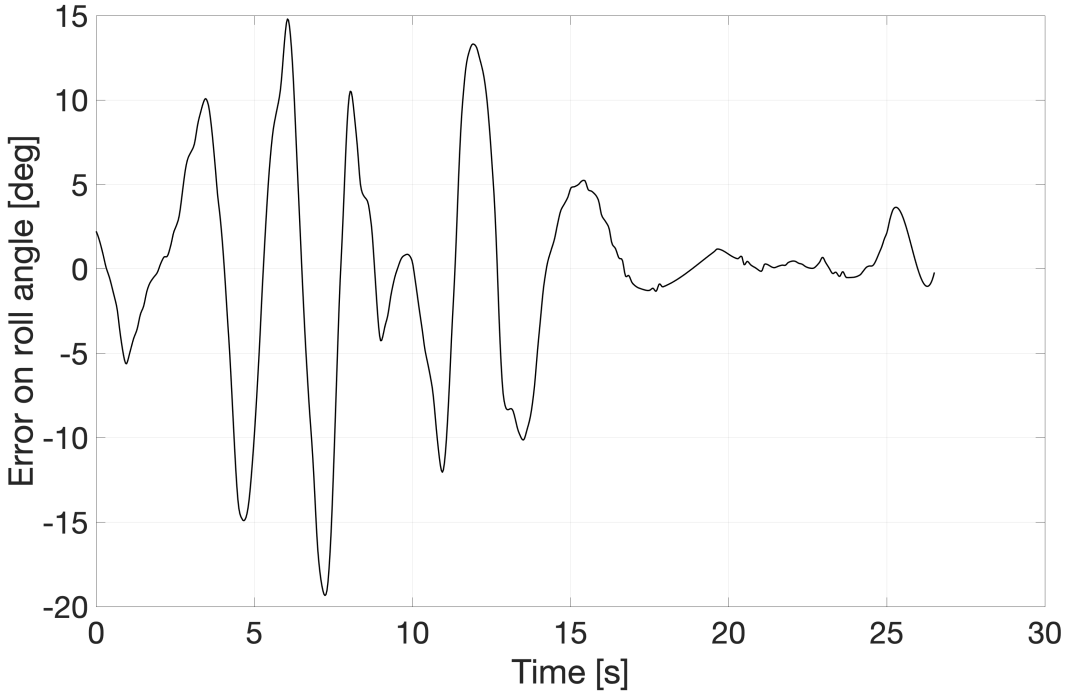

(a) Helicopter flight test results: error of roll angle, baseline controller

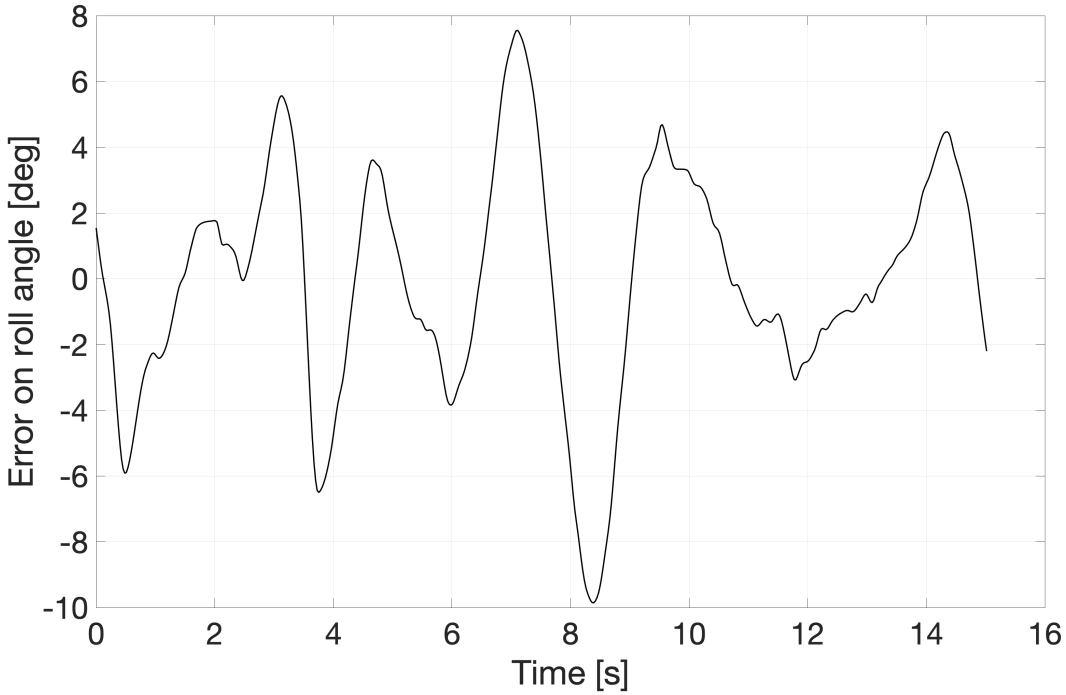

(b) Helicopter flight test results: error of roll angle, augmented controller

Figure 5.12: Helicopter flight test results: error of roll angle, baseline vs augmented controller

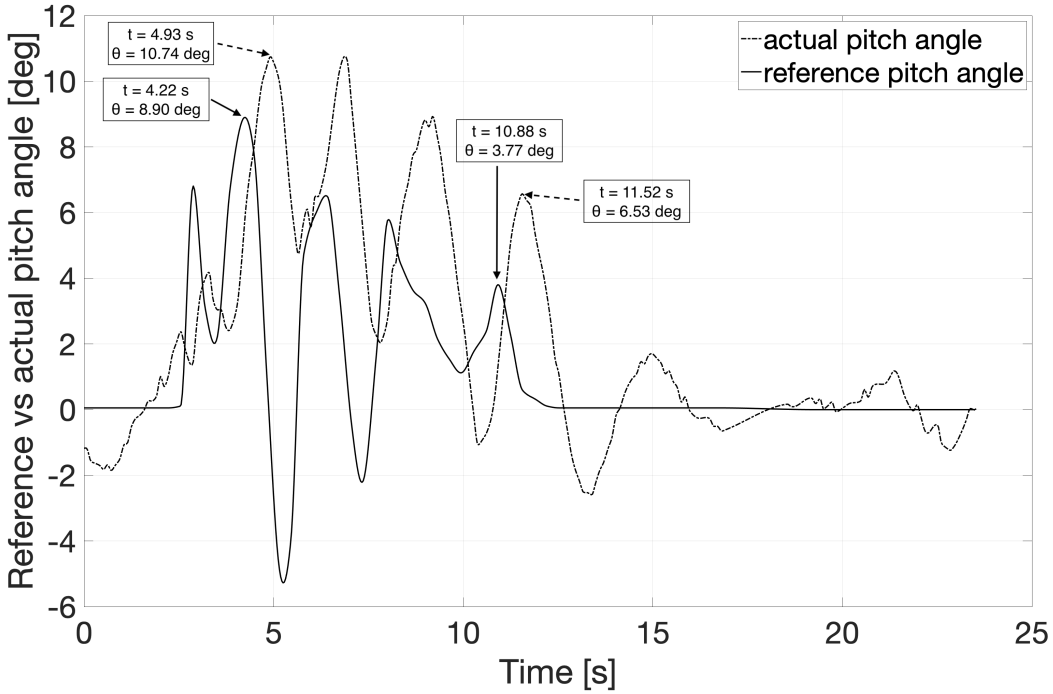

(a) Helicopter flight test results: reference and actual pitch angle, baseline controller

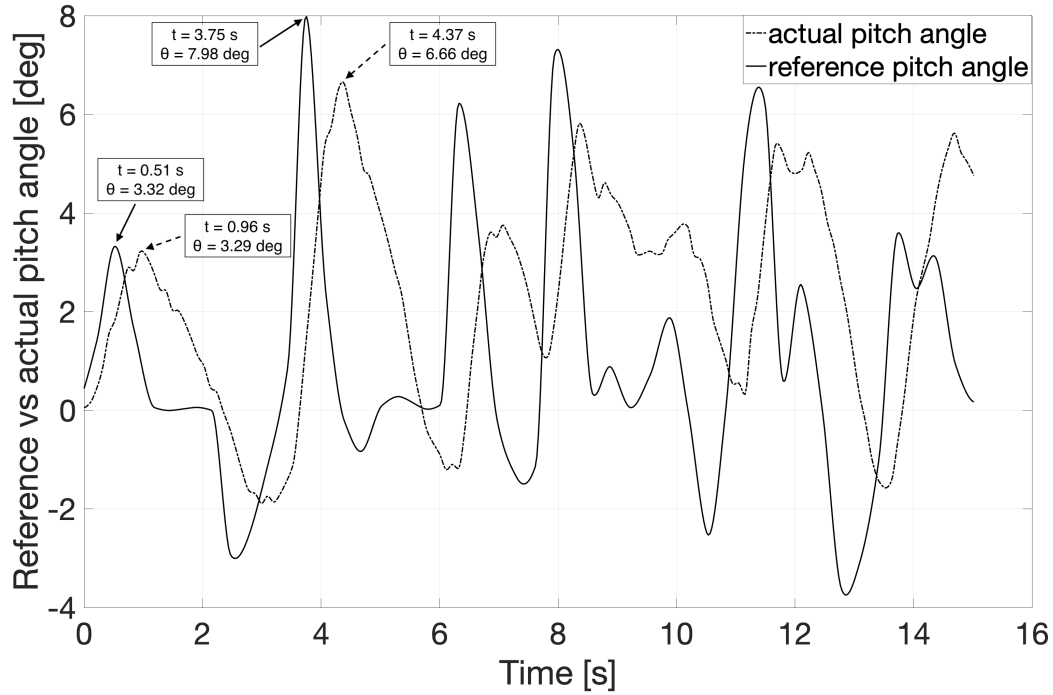

(b) Helicopter flight test results: reference and actual pitch angle, augmented controller

Figure 5.13: Helicopter flight test results: reference and actual pitch angle, baseline vs augmented controller

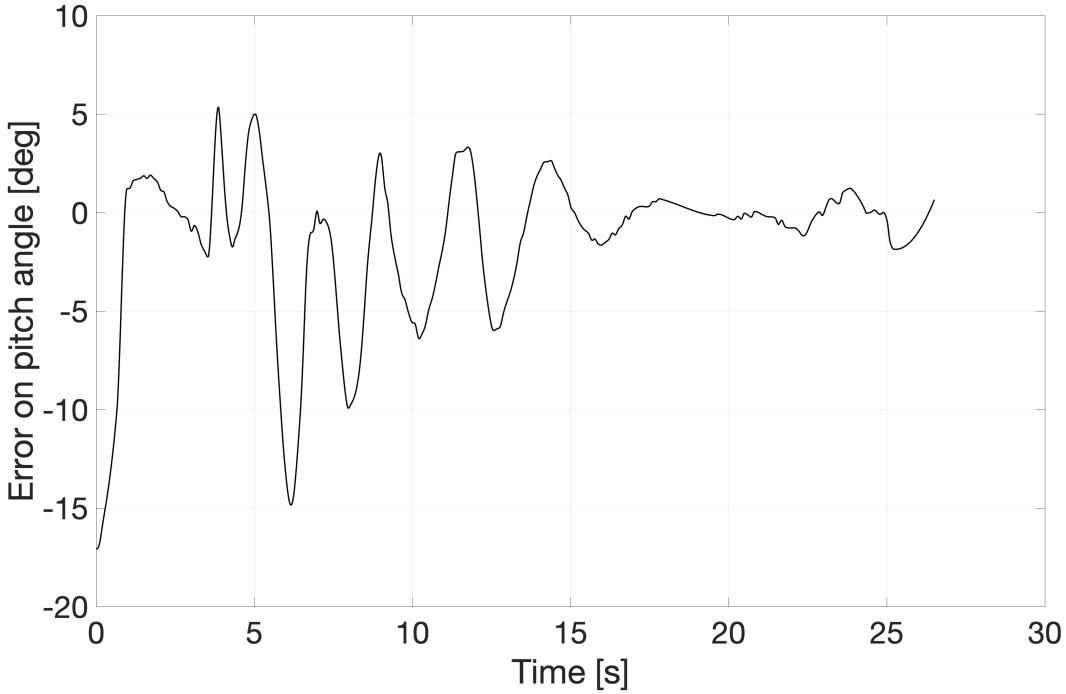

(a) Helicopter flight test results: error of pitch angle, baseline controller

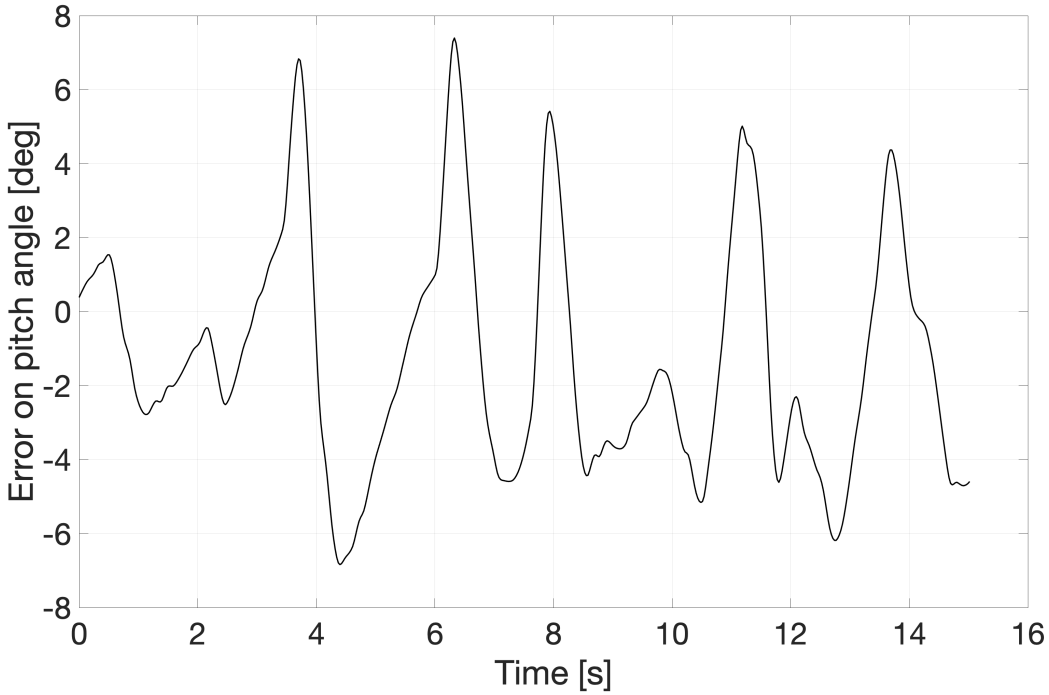

(b) Helicopter flight test results: error of pitch angle, augmented controller

Figure 5.14: Helicopter flight test results: error of pitch angle, baseline vs augmented controller

an error of 16%. On pitch axis the adaptive contribution has less impact with respect to the roll axis. This is to be expected if analyzing the baseline tests reported in section 5.2.2. According to the experimental results, the attitude hold controller on the pitch axis performs better than the one on the roll axis. This is also highlighted in figures 5.12a and 5.14a in which errors on ϕ and θ angles are showed for the baseline controllers.

Concerning the yaw axis, the adaptive contribution distinctly improve the PID controller despite the fact that it is still noisy. The augmented control system on yaw axis is capable to track better the reference signal as clearly demonstrated by data of figure 5.15b. The noisy aspect of the yawrate controller is highlighted also in the simulation results, for instance in figure 4.17.

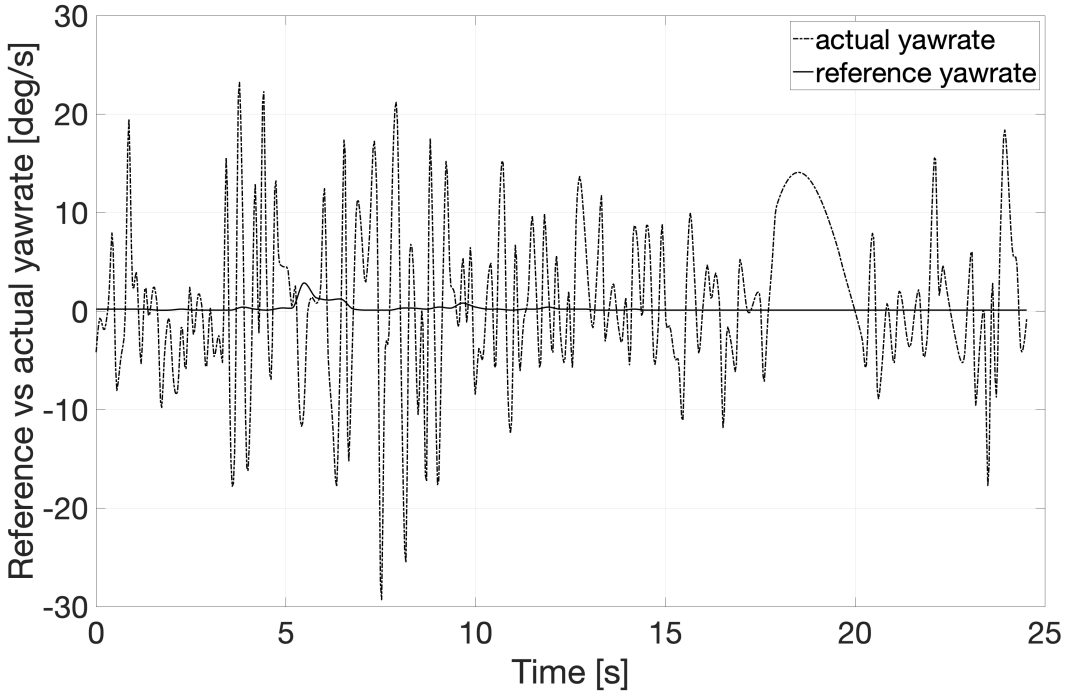

(a) Helicopter flight test results: reference and actual yawrate, baseline controller

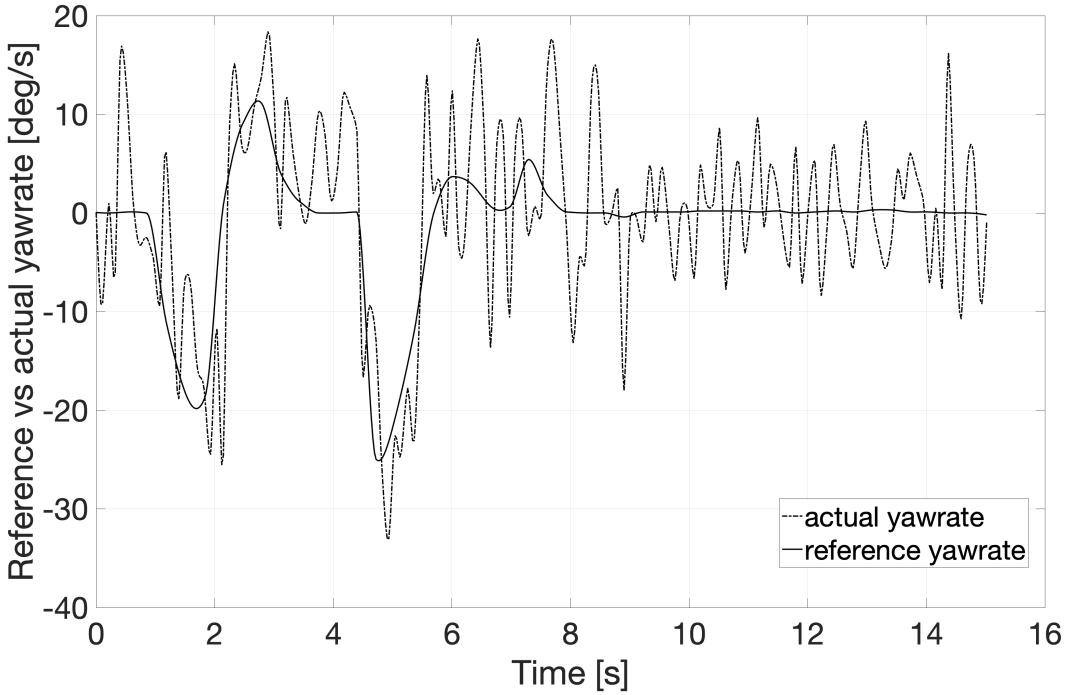

(b) Helicopter flight test results: reference and actual yawrate, augmented controller

Figure 5.15: Helicopter flight test results: reference and actual yawrate, baseline vs augmented controller

CHAPTER 6

Conclusions

In this thesis topics related to modelling and control of rotorcrafts in multi-agent scenario have been studied.

The model of a conventional single main rotor helicopter has been presented and a proper control system has been designed based on this model. It has been implemented in Matlab/Simulink® environment. Two different controllers have been proven to be suitable for an unmanned helicopter: a simple PID baseline controller and an augmented one with adaptive techniques. The use of the $\mathcal{L}_1$ adaptive contribution to the PID baseline controller is shown to improve the control system performance of the unmanned small-scale helicopter. The entire software addresses attitude stabilization and velocity control. Embedded codes have been generated by Simulink® and have been validated by simulations and by experimental tests. The numerical and experimental investigation carried out in this thesis demonstrates that $\mathcal{L}_1$ adaptive controller is a promising technique for helicopters control system design even in presence of uncertainties of the model.

In the present work the problem of cooperative control of different agents has been faced. The helicopter and the rover model have been implemented in scenarios that represent a preliminary stage of research and rescue or surveillance missions. Two man scenarios of formation flight have been implemented and tested: the leader-wingman and the behavioural approach. The innovative aspect stays in the implementation of the algorithm itself, that keeps the architecture open. In this way it is easy to switch from a scenario to another and to add/remove agents. Another crucial key is the independence of each involved vehicle autopilot from the cooperative control system so that many control design may be tested.

By means of a test campaign, cooperative control algorithms have been proven to be useful to achieve the required tasks and their application may be extended to complete complex missions.

As a further contribution, the analysis of the dynamic modes and the stability issues of the synch-rotor has been given. This unconventional helicopter configuration has been studied and its analytical framework has been developed. Interference between the two intermeshing rotors have been included in the complete mathematical model. The performance and stability results have been addressed working with the linearized model. The analysis takes into account the peculiar parameters of the configuration geometry. Several properties of the synch-rotor have been showed, most important the dynamic behaviour in relation to the variation of its distinctive parameters. Promising results confirm the revived interest for the use of this configuration as unmanned aircraft in future applications such as air mobility.

APPENDIX A

Tip path plane equations

$$\tilde{D} = \begin{bmatrix} \frac{\gamma}{2}(\frac{1}{4} - \frac{2}{3} + \frac{\epsilon^2}{2}) & 0 & -\frac{\gamma\mu}{4}(\frac{1}{3} - \epsilon + \epsilon^2) \\ 0 & \frac{\gamma}{2}(\frac{1}{4} - \frac{2\epsilon}{3} + \frac{\epsilon^2}{2}) & 2 \\ -\frac{\gamma\mu}{2}(\frac{1}{3} - \epsilon + \epsilon^2) & -2 & \frac{\gamma}{2}(\frac{1}{4} - \frac{2}{3} + \frac{\epsilon^2}{2}) \end{bmatrix}$$

$$\tilde{K} = \Omega^2 \begin{bmatrix} P^2 + \frac{\gamma K_1 \mu^2}{4}(\frac{1}{2} - \epsilon + \frac{\epsilon^2}{2}) & -\frac{\gamma\mu}{4}(\frac{\epsilon}{2} - \epsilon^2) & -\frac{\gamma K_1 \mu}{4}(\frac{2}{3} - \epsilon) \\ \frac{\gamma\mu}{2}(\frac{1}{3} - \frac{\epsilon}{2}) & P^2 - 1 + \frac{\gamma K_1 \mu^2}{8}(\frac{1}{2} - \epsilon + \frac{\epsilon^2}{2}) & \frac{\gamma}{2}(\frac{1}{4} - \frac{2}{3}\epsilon + \frac{\epsilon^2}{2}) + \\ & & \frac{\gamma\mu^2}{8}(\frac{1}{2} - \epsilon + \frac{\epsilon^2}{2}) \\ -\frac{\gamma K_1 \mu}{2}(\frac{2}{3} - \epsilon) & -\frac{\gamma}{2}(\frac{1}{4} - \frac{2}{3}\epsilon + \frac{\epsilon^2}{2}) + & \\ & \frac{\gamma\mu^2}{8}(\frac{1}{2} - \epsilon + \frac{\epsilon^2}{2}) & P^2 - 1 + \frac{3\gamma K_1 \mu^2}{8}(\frac{1}{2} - \epsilon + \frac{\epsilon^2}{2}) \end{bmatrix}$$

$$\tilde{f} = \Omega^2 \begin{bmatrix} \frac{\gamma}{2}[(\frac{1}{4} - \frac{\epsilon}{3}) + & & & \\ \frac{\mu^2}{2}(\frac{1}{2} - \epsilon + \frac{\epsilon^2}{2})] & \frac{\gamma}{2}[(\frac{1}{5} - \frac{\epsilon}{4}) + \frac{\mu^2}{2}(\frac{1}{3} - \frac{\epsilon}{2})] & 0 & -\frac{\gamma\mu}{2}(\frac{1}{3} - \frac{\epsilon}{2}) \\ 0 & 0 & \frac{\gamma}{2}[(\frac{1}{4} - \frac{\epsilon}{3}) + \frac{\mu^2}{4}(\frac{1}{2} - \epsilon + \frac{\epsilon^2}{2})] & 0 \\ -\frac{\gamma\mu}{2}(\frac{2}{3} - \epsilon) & -\frac{\gamma\mu}{2}(\frac{1}{2} - \frac{2\epsilon}{3}) & 0 & \frac{\gamma}{2}[(\frac{1}{4} - \frac{\epsilon}{3}) + \\ & & & \frac{3\mu^2}{4}(\frac{1}{2} - \epsilon + \frac{\epsilon^2}{2})] \end{bmatrix} \begin{bmatrix} \theta_0 \\ \theta_t \\ A_{1c} \\ B_{1c} \end{bmatrix}$$

$$+ \Omega^2 \begin{bmatrix} \frac{\gamma\mu}{8\Omega}(\frac{2}{3} - \epsilon) & 0 & 0 & 0 \\ -\frac{2}{\Omega}(1 + \frac{eM_\beta}{I_\beta}) & -\frac{\gamma}{2\Omega}(\frac{1}{4} - \frac{\epsilon}{3}) & 0 & -\frac{1}{\Omega^2} \\ -\frac{\gamma}{2\Omega}(\frac{1}{4} - \frac{\epsilon}{3}) & \frac{2}{\Omega}(1 + \frac{eM_\beta}{I_\beta}) & -\frac{1}{\Omega^2} & 0 \end{bmatrix} \begin{bmatrix} p_w \\ q_w \\ \dot{p_w} \\ \dot{q_w} \end{bmatrix} +$$

$$\Omega^2 \begin{bmatrix} \frac{\gamma}{2}(\frac{1}{3} - \frac{\epsilon}{2}) \\ 0 \\ -\frac{\gamma\mu}{2}(\frac{1}{2} - \epsilon + \frac{\epsilon^2}{2}) \end{bmatrix} \lambda + \begin{bmatrix} \frac{M_\beta}{I_\beta}[(\dot{w} - uq + pv) - g] \\ 0 \\ 0 \end{bmatrix}$$

Table A.1: Tip path plane equation

APPENDIX B

Relevant helicopter data

Table B.1: Relevant helicopter data

Parameter	Symbol	Value	Units
Vehicle data			
Mass	m	4.8	kg
Principal moments of inertia	$I_x,\ I_y,\ I_z$	0.0465, 0.2971, 0.2567	kg m^2
Inertia products	$I_{xy},\ I_{yz},\ I_{xz}$	0.0079, 0.0033, 0.0006	kg m^2
Stationline position of CG	STA_{CG}	0.34	m
Buttline position of CG.	BL_{CG}	0	m
Waterline position of CG.	WL_{CG}	0.174	m
Main rotor data			
Stationline position of hub	STA_H	0.3305	m
Buttline position of hub	BL_H	0	m
Waterline position of hub	WL_H	0.35	m
Number of rotor blades	N_{blades}	2	
Nominal angular velocity	Ω_{nom}	1995.3	RPM
Radius	R	0.79	m
Mean blade chord	$\bar{c}$	0.06	m
Flapping spring constant	K_β	162.69	Nm/rad
Pitch-flap coupling tangent of δ_3	K_1	0	
Virtual hinge offset	ϵ	0.0314	m

Table B.1 – continued from previous page

Parameter	Symbol	Value	Units
Blade Inertia moment	I_β	0.0344	kg m^2
Blade profile lift curve slope	C_{l_α}	2π	rad^{-1}
Blade twist angle	θ_{tw}	0	rad
Precone angle (required for teetering rotor)	a_0	0	rad
Solidity	σ	0.0479	
Shaft tilt	$\frac{\Gamma}{2}$	0.0524	rad
Tail rotor data			
Stationline position of hub	STA_H	1.385	m
Buttline position of hub	BL_H	0.052	m
Waterline position of hub	WL_H	0.205	m
Number of rotor blades	N_{blades}	2	
Nominal angular velocity	Ω_{nom}	9976	RPM
Radius	R	0.115	m
Mean blade chord	$\bar{c}$	0.031	m
Solidity	σ	0.1716	
Pitch-flap coupling tangent of δ_3	K_1	0	
Blade Inertia moment	I_β	0.00002665	kg m^2
Blade profile lift curve slope	C_{l_α}	2π	rad^{-1}
Blade twist angle	θ_{tw}	0	rad
Fuselage			
Stationline position of fuselage	STA_H	0	m
Buttline position of fuselage	BL_H	0	m
Waterline position of fuselage	WL_H	0	m
Frontal area	S_{front}	0.02042	m^2
Lateral area	S_{front}	0.0633	m^2
Top area	S_{front}	0.09739	m^2

APPENDIX C

Relevant synch-rotor data

Table C.1: Relevant synch-rotor data

Parameter	**Symbol**	**Value**	**Units**
Vehicle data			
Mass	m	794.4	kg
Principal moments of inertia	I_x,	260.8476,	kg m^2
Inertia products	I_{xy},	0.4146,	kg m^2
Stationline position of CG	STA_{CG}	2	m
Buttline position of CG.	BL_{CG}	0	m
Waterline position of CG.	WL_{CG}	1.2848	m
Rotor data			
Stationline position of hub	STA_H	2	m
Buttline position of left hub	BL_H	0.25	m
Buttline position of right hub	BL_H	-0.25	m
Waterline position of hub	WL_H	2.4	m
Number of rotor blades	N_{blades}	2	
Nominal angular velocity	Ω_{nom}	396.3	RPM
Radius	R	2.8	m
Mean blade chord	$\bar{c}$	0.195	m
Flapping spring constant	K_β	0	Nm/rad
Pitch-flap coupling tangent of δ_3	K_1	0	

Table C.1 – continued from previous page

Parameter	Symbol	Value	Units
Hinge offset	ϵ	0	m
Blade Inertia moment	I_β	27.3651	kg m^2
Blade profile lift curve slope	$C_{l\alpha}$	5.8101	rad^{-1}
Blade twist angle	θ_{tw}	-0.0742	rad
Tip loss factor	B	0.96	
Precone angle	a_0	0.0262	rad
Solidity	σ	0.0443	
Lateral shaft tilt	$\frac{\Gamma}{2}$	12.5	deg
Fuselage (Fus.)			
Fus. drag, $\alpha = \beta = 0$	D_1	0.2803	m^2
Fus. drag, variation with α	D_2	-0.1377	m^2/rad
Fus. drag, variation with α^2	D_3	1.307	m^2/rad^2
Fus. drag, variation with β^2	D_4	5.306	m^2/rad^2
Fus. drag, $\alpha = 90°$	D_5	2.074	m^2
Fus.drag, $\beta = 90°$	D_6	3.310	m^2
Fus. lift, $\alpha = \beta = 0$	XL_0	-0.08014	m^2
Fus. lift, variation with α	XL_1	0.8635	m^2/rad
Fus. lift, variation with α^2	XL_2	-1.256	m^2/rad^2
Fus. lift, variation with β^2	XL_3	-4.812	m^2/rad^2
Fus. lift, $\alpha = 90°$	XL_4	1.3590	m^2
Fus. lift, $\beta = 90°$	XL_5	0.0136	m^2
Fus. side force, variation with β	Y1	-2.062	m^2/rad
Fus. rolling moment, variation with β	YL1	-1.956	m^3/rad
Fus. rolling moment,$\beta = 90°$	YL2	1.832	m^3
Fus. pitch moment, $\alpha = \beta = 0$	XM1	-0.3069	m^3
Fus. pitch moment, variation with α	XM2	0.03538	m^3/rad
Fus. pitch moment, $\alpha = 90°$	XM3	-5.621	m^3
Fus. pitch moment, variation with α^2	XM4	4.038	m^3/rad^2
Fus. pitch moment, variation with β	XM5	-0.1521	m^3/rad
Fus. pitch moment, variation with β^2	XM6	18.57	m^3/rad^2
Fus. pitch moment, $\beta = 90°$	XM7	3.819	m^3
Fus. yawing moment, variation with β	XN1	3.268	m^3/rad
Fus. yawing moment, $\beta = 90°$	XN2	7.790	m^3
Fus. yawing moment, $\alpha = 90°$	XN3	0.1527	m^3

Table C.1 – continued from previous page

Parameter	Symbol	Value	Units
Horizontal Stabilizer (HS)			
Stationline position of HS	STA_{HS}	6.199	m
Buttline position of HS	BL_{HS}	0	m
Waterline position of HS	WL_{HS}	1.394	m
HS incidence angle	i_{HS}	-2	deg
HS area	s_{HS}	0.2145	m^2
HS aspect ratio	AR_{HS}	4.71	
HS dynamic pressure ratio	η_{HS}	0.633	
HS lift curve slope	$CL_{max_{HS}}$	1.1	
Upper Vertical fin (Vf)			
Stationline position of Vf	STA_{VF1}	6.1	m
Buttline position of Vf	BL_{VF1}	0	m
Waterline position of Vf	WL_{VF1}	1.683	m
Vf incidence angle	i_{VF1}	-4	deg
Vf area	s_{VF1}	0.1544	m^2
Vf aspect ratio	AR_{VF1}	4.304	
Vf sweep angle	λ_{VF1}	33.16	rad
Vf dynamic pressure ratio	η_{VF1}	0.41	
Vf lift curve slope	$CL_{max_{VF1}}$	1.16	
Lower Vertical fin (Vf)			
Stationline position of Vf	STA_{VF2}	6.069	m
Buttline position of Vf	BL_{VF2}	0	m
Waterline position of Vf	WL_{VF2}	0.996	m
Vf incidence angle	i_{VF2}	-2	deg
Vf area	s_{VF2}	0.1268	m^2
Vf aspect ratio	AR_{VF2}	3.358	
Vf sweep angle	λ_{VF2}	33.15	deg
Vf dynamic pressure ratio	η_{VF2}	0.54	
Vf lift curve slope	$CL_{max_{VF2}}$	1.21	

APPENDIX D

State and Control matrices

$$A = \begin{bmatrix} X_u & X_w - Q_e & X_q - W_e & A_{14} & X_v + R_e & X_p & 0 & X_r + V_e \\ Z_u + Q_e & Z_w & Z_q + U_e & A_{24} & Z_v + P_e & Z_p - V_e & A_{27} & Z_r \\ M_u & M_w & M_q & 0 & M_v & A_{36} & 0 & A_{38} \\ 0 & 0 & \cos\Theta_e & 0 & 0 & 0 & A_{47} & \sin\Theta_e \\ Y_u - R_e & Y_w + P_e & Y_q & A_{54} & Y_v & Y_p + W_e & A_{57} & Y_r - U_e \\ L'_u & L'_w & A_{63} & 0 & L'_v & A_{66} & 0 & A_{68} \\ 0 & 0 & \sin\phi_e \tan\Theta_e & A_{74} & 0 & 1 & 0 & \cos\phi_e \tan\Theta_e \\ N'_u & N'_w & A_{83} & 0 & N'_v & A_{86} & 0 & A_{88} \end{bmatrix}$$

where:

$A_{14} = -g\cos\Theta_e,$

$A_{24} = -g\cos\phi_e\sin\Theta_e,$

$A_{27} = -g\sin\phi_e\cos\Theta_e,$

$A_{36} = M_p - 2P_eI_{xz}I_{yy} - R_e(I_{xx} - I_{zz})I_{yy},$

$A_{38} = M_r + 2R_eI_{xz}I_{yy} - P_e(I_{xx} - I_{zz})I_{yy},$

$A_{47} = -\Omega_a\cos\Theta_e,$

$A_{54} = -g\sin\phi_e\sin\Theta_e,$

$A_{57} = g\cos\phi_e\cos\Theta_e,$

$A_{63} = L'_q + k_1P_e - k_2R_e,$

$A_{66} = L'_p + k_1Q_e,$

$A_{68} = L'_r - k_2Q_e,$

$A_{74} = \Omega_a \sec \Theta_e$,
$A_{83} = N'_q - k_1 R_e - k_3 P_e$,
$A_{86} = N'_p - k_3 Q_e$,
$A_{88} = N'_r - k_1 Q_e$.
A is the state matrix. B, the control matrix, is:

$$B = \begin{bmatrix} X_{\Theta_0} & X_{A_1} & X_{B_1} & X_{\Theta_{0T}} \\ Z_{\Theta_0} & Z_{A_1} & Z_{B_1} & Z_{\Theta_{0T}} \\ M_{\Theta_0} & M_{A_1} & M_{B_1} & M_{\Theta_{0T}} \\ 0 & 0 & 0 & 0 \\ Y_{\Theta_0} & Y_{A_1} & Y_{B_1} & Y_{\Theta_{0T}} \\ L'_{\Theta_0} & L'_{A_1} & L'_{B_1} & L'_{\Theta_{0T}} \\ 0 & 0 & 0 & 0 \\ N'_{\Theta_0} & N'_{A_1} & N'_{B_1} & N'_{\Theta_{0T}} \end{bmatrix}$$

The longitudinal and lateral state matrices are:

$$A_{LON} = \begin{bmatrix} X_u & g\cos\Theta_e/U_e & X_w - g\cos\Theta_e/U_e & X_q - W_e \\ Z_u & g\sin\Theta_e/U_e & Z_w - g\sin\Theta_e/U_e & Z_q \\ Z_u & g\sin\Theta_e/U_e & Z_w - g\sin\Theta_e/U_e & Z_q + U_e \\ M_u & 0 & M_w & M_q \end{bmatrix}$$

$$A_{LAT} = \begin{bmatrix} 0 & 0 & Y_v & g \\ 0 & 0 & 1 & 0 \\ -N'_r & -U_e N'_v & N'_r + Y_v & g - N'_p U_e \\ L'_r/U_e & L'_v & -L'_r/U_e & L'_p \end{bmatrix}$$

Bibliography

[1] Austin, R., "Unmanned aircraft systems, UAVs design, development and deployment", Princeton University Press, 2012

[2] Beard, R. W., McLain, T. W., "Small unmanned aircraft, Theory and practice", Wiley, 2010

[3] Hartmann, K., Giles, K., "UAV exploitation: a new domain for cyber power". *Cyber Conflict (CyCon), 8th International Conference on IEEE*, pp .205-221, 2016.

[4] Skjervold, E., Hoelsaeter, O. T., "Autonomous, Cooperative UAV Operations using COTS Consumer Drones and Custom Ground Control Station" *MILCOM 2018 - 2018 IEEE Military Communications Conference (MILCOM)*, pp .1-6, 2018. doi: 10.1109/MILCOM.2018.8599684

[5] Sargolzaei, A., Abbaspour, A., Crane, C. D., "Control of cooperative unmanned aerial vehicles: review of applications, challenges and algorithms", *Amini M. (eds) Optimization, Learning, and Control for Interdependent Complex Networks. Advances in Intelligent Systems and Computing*, Springer International Publishing, vol. 1123, pp. 229-255, 23th February 2020. https://doi.org/10.1007/978-3-030-34094-0

[6] Ren, W., Beard, R. W., Atkins, E. M., "Information consensus in multivehicle cooperative control", *IEEE Control Systems*, vol. 27, no. 2, pp. 71-82, 2007.

[7] Wang, Q., Gao, H., Alsaadi, F., Hayat, T., "An overview of consensus problems in constrained multi-agent coordination," *Systems Science and Control Engineering: An Open Access Journal*, vol. 2, no. 1, pp. 275-284, 2014.

[8] Anderson, B. D., Yu, C., Hendrickx, J. M., "Rigid graph control architectures for autonomous formations," *IEEE Control Systems*, vol. 28, no. 6, 2008.

[9] Oh, K. K., Park, M. C., Ahn, H. S., "A survey of multi-agent formation control," *Auto-matica*, vol. 53, pp. 424-440, 2015.

[10] Zhu, B., Xie, L., Han, D., Meng, X., Teo, R., "A survey on recent progress in control of swarm systems," *Science China Information Sciences*, vol. 60, no. 7, p. 070201, 2017.

[11] Senanayake, M., Senthooran, I., Barca, J. C., Chung, H., Kamruzzaman, J., Murshed, M., "Search and tracking algorithms for swarms of robots: A survey," *Robotics and Autonomous Systems*, vol. 75, pp. 422-434, 2016.

[12] Asl, A.N., Menhaj, M.B., Sajedin, A., "Control of leader-follower formation and path planning of mobile robots using asexual reproduction optimization (aro)" *Applied Soft Computing*, vol. 14, pp. 563-576, 2014. https://doi.org/10.1016/j.asoc.2013.07.030

[13] Balch, T., Arkin, R., "Behaviour-based formation control for multi-robot systems" *IEEE Transactions on Robotic and Automation*, vol. 14, no. 6, pp. 926-939, 1998. doi 10.1109/70.736776

[14] Do, K.D., "Output-feedback formation tracking control of unicycle-type mobile robots with limited sensing ranges" *Robotics and Autonomous systems*, vol. 57, no. 1, pp. 34-47, 2009. https://doi.org/10.1016/j.robot.2008.03.006

[15] Egerstedt, M., HU, X., "Formation constrained multi-agent control" *IEEE Transactions on Robotic and Automation*, vol. 17, no. 6, pp. 947-951, 2001. doi 10.1109/70.976029

[16] Rezaee, H., Abdollahi, F., "Motion synchronization in unmanned aircrafts formation control with communication delays" *Communications in Nonlinear Science and Numerical Simulation*, vol. 1, no. 3, pp. 744-756, 2013. https://doi.org/10.1016/j.cnsns.2012.08.015

[17] Rahimi, R., Abdollahi, F., Naqshi, K., "Time-varying formation control of a collaborative heterogeneous multi agent system" *Robotics and Autonomous systems*, vol. 62, no. 12, pp. 1799-1805, 2014. doi.org/10.1016/j.robot.2014.07.005

[18] Aghaeeyan, A., Abdollahi, F., Talebi, H.A., "Uav-ugvs cooperation: with a moving center based trajectory" *Robotics and Autonomous systems*, vol. 63, pp. 1-9, 2015. https://doi.org/10.1016/j.robot.2014.10.005

[19] Das, A.K., Fierro, R., Kumar, V., Ostrowski, J.P., Spletzer, J., Taylor, C.J., "A vision- based formation control framework" *IEEE Transactions on Robotic and Automation*, vol. 18, no. 5, pp. 813-825, 2002. doi 10.1109/TRA.2002.803463

[20] Peng, Z., Wen, G., Rahmani, A., Yu, Y., "Leader-follower formation control of nonholonomic mobile robots based on a bioinspired neurodynamic based approach" *Robotics and Autonomous systems*, vol. 61, no. 9, pp. 988-996, 2013. https://doi.org/10.1016/j.robot.2013.05.004

[21] Mohammadi, A., Menhaj, M.B., "Formation control and obstacle avoidance for nonholonomic robots using decentralized mpc" *Proceedings of the IEEE International Conference on Networking, Sensing and Control, ICNSC,*, Evry, pp. 112-117, 2013. DOI: 10.1109/ICNSC.2013.6548721

[22] Panagou, D., Kumar, V., "Cooperative visibility maintenance for leader-follower formations in obstacle environments" *IEEE Transactions on Robotic and Automation*, vol. 30, no. 4, pp. 831-844, 2014. DOI 10.1109/TRO.2014.2304774

[23] Rezaee, H., Abdollahi, F., Menhaj, M.B., "Model-free fuzzy leader-follower formation control of fixed wing uavs" *Proceedings of the Iranian Fuzzy Systems Conference, IFSC*, Qazvin, Iran pp. 1-5, 2013. DOI: 10.1109/IFSC.2013.6675677

[24] Dehghani, M.A., Menhaj, M.B., "Communication free leader follower formation control of unmanned aircraft systems" *Robotics and Autonomous systems*, vol. 80, pp. 69-75, 2016. https://doi.org/10.1016/j.robot.2016.03.008

[25] Giulietti, F., Mengali, G., "Dynamics and control of different aircraft formation structures" *The Aeronautical Journal*, vol. 108, pp. 117-124, 2004. DOI:10.1017/S0001924000000026

[26] Valavanis, K.P., "Advances in unmanned aerial vehicles: State of the art and the road to autonomy", *Micro-processor-Based and Intelligent Systems Engineering Series*, July 2007, pp. 15-46.

[27] Kumar, V., Michael, N., "Opportunities and challenges with autonomous micro aerial vehicles". *The International Journal of Robotics Research*, Vol.31, No. 11, pp .1279-1291, 2012. https://doi.org/10.1177/0278364912455954

[28] Cai, G., Dias, J., Seneviratne, L., "A survey of small-scale unmanned aerial vehicles: recent advances and future development trends". *Unmanned Systems*, Vol. 2, No. 2, pp .175-199, 2014. DOI:10.1142/S2301385014300017

[29] M.B.Tischler, M.B., Remple, R.K., " Aircraft and Rotorcraft System Identification", *AIAA Education Series* AIAA, Washington, 2006 https://doi.org/10.2514/4.868207

[30] Leishman, J. G., "Principles of helicopter aerodynamics", Cambridge University Press, 2000

[31] Wei, F.S.J., Moore, E. and Gates, A., "An intermeshing rotor helicopter design and test", *AIAA SciTech 2015*, Kissmmee, Florida, January 5-9, 2015

[32] Wei, F.S.J., Gallagher,F., "K-MAX Rotor Blade Flight Loads Survey for Out-of-envelope Flight Test", *The 64th American Helicopter Annual Forum*, Montreal, Canada, April 29-May 1, 2008

[33] Gallagher,F., Wei, F.S.J., Gates, A., "Kaman K-MAX K-1200 High Altitude Performance", *The 58th American Helicopter Annual Forum*, Montreal, Canada, June 11-13, 2002

[34] Mansur, M.H., Tischler, M.B., Bielefield, M.D., Bacon, J.W., Cheung, K.K., Berrios, M.G. and Rothman,K.E., "Full Flight envelope inner-loop control law development for the unmanned K-MAX", 67^{th} *American Helicopter Society Annual Forum*, Virginia Beach, VA, May 3-5, 2011

[35] Frost, C.R., Tischler, M.B., Bielefield, M.D., LaMontagne, T., "Design and test of flight control laws for the Kaman Burro unmanned aerial vehicle", *AIAA, Atmospheric Flight Mechanics Conference*, Denver, CO, U.S.A., August 14-17, 2000

[36] Colbourne, J.D., Tischler, M.B., Tomashofski, C.A., LaMontagne, T., "System identification and control system design for the Burro autonomous UAV", *Proceedings for the American Helicopter Society* 56^{th} *annual forum*, Virginia Beach, VA, May, 2000

[37] McGonagle, J., "The design, test and development challenges of converting the K-MAX® helicopter to a heavy lift rotary wing UAV", Proceedings of the American Helicopter Society Annual Forum 57^{th}, Washington, DC, May 9-11, 2001

[38] Barth, A., Spieb, C., Kondak, K. and Hajek, M., "Design, Analysis and Flight Testing of a High Altitude Synchropter UAV", textitAHS International 74^{th} Annual Forum&Technology Display, Phoenix, Arizona, USA, May 14-17, 2018

[39] Mettler, B., "Identification Modeling and Characteristics of Miniature Rotorcraft", Springer, Boston, MA, 2003. https://doi.org/10.1007/978-1-4757-3785-1

[40] Raptis, I., Valavanis, K., "Linear and Nonlinear Control of Small-Scale Unmanned Helicopters", *Intelligent system 45*, 2011. DOI: 10.1007/978-94-007-0023-9

[41] Hu, J., Gu, H., "Survey on flight control technology for large-scale helicopter", *International journal of aerospace engineering*, vol. 17, Article ID 5309403, 14 pages, 2017. https://doi.org/10.1155/2017/5309403

[42] Shim, D. H., Kim, H. J., Sastry, S., "Control system design for rotorcraft-based unmanned aerial vehicles using time-domain system identification," *Proceedings of the 2000. IEEE International Conference on Control Applications. Conference Proceedings (Cat. No.00CH37162)*,pp. 808-813, 2000. doi: 10.1109/CCA.2000.897539.

[43] Jiang, T. Y., Prasad, J. V. R., Calise, A. J., "Adaptive fuzzy logic flight controller for rotorcraft," *Proceedings of the Guidance, Navigation, and Control Conference and Exhibit*, San Diego, Calif, USA, July 1996. https://doi.org/10.2514/6.1996-3850

[44] Prasad, J. V. R., Calise, A. J., Pei, Y., Corban, J. E., "Adaptive nonlinear controller synthesis and flight test evaluation on an unmanned helicopter," *Proceedings of the 1999 IEEE International Conference on Control Applications (Cat. No.99CH36328)*, vol. 1, pp. 137-142, 1999. doi: 10.1109/CCA.1999.806163.

[45] Hoffmann, F., Koo, T., Shakernia, O., "Evolutionary design of a helicopter autopilot", *3rd online world conference on soft computing (WSC3)*, 1998. DOI:10.1007/978-1-4471-0819-1-15

[46] Ghaoui, L. E., Arrier, A., Bryson, A. E., "Linear quadratic minimax controllers," *Journal of Guidance, Control, and Dynamics*, vol. 15, no. 4, pp. 953-961, 1992. https://doi.org/10.2514/3.20929

[47] Aslan, Y., Beauvois, D., Rossiter, J. A., "Eigenstructure approximations and their use for a commutative controller strategy: application to a helicopter," *Control Engineering Practice*, vol. 1, no. 2, pp. 357-363, 1993. https://doi.org/10.1016/0967-0661(93)91628-A

[48] McFarlane, D., Glover, K., "A loop-shaping design procedure using H_∞ synthesis," *IEEE Transactions on Automatic Control*, vol. 37, no. 6, pp. 759-769, 1992. DOI: 10.1109/9.256330

[49] Postlethwaite, I., Smerlas, A., Walker, D. J., et al., "H_∞ control of the NRC Bell 205 fly-by-wire helicopter," *Journal of the American Helicopter Society*, vol. 44, no. 4, pp. 276-284, 1999. https://doi.org/10.4050/JAHS.44.276

[50] La Civita, M., Papageorgiou, G., Messner, W. C., Kanade, T., "Design and flight testing of a high-bandwidth H_∞ loop shaping controller for a robotic helicopter", *Proceedings of the AIAA Guidance, Navigtion and Control Conference*, AIAA, Monterey, CA, 2002. https://doi.org/10.2514/6.2002-4836

[51] Weilenmann, M. F., Christen, U., Geering, H. P., "Robust helicopter position control at hover", *American Control Conference*, Baltimore, pp. 2491-2495, 1994. DOI:10.1109/ACC.1994.735007

[52] Shin, J., Y., Balas, G. J., Kaya, M., A., "Blending methodology of linear parameter varying control synthesis of F-16 aircraft system," *Journal of Guidance, Control, and Dynamics*, vol. 25, no. 6, pp. 1040-1048, 2002. https://doi.org/10.2514/2.5008

[53] Fujimori, A., Miura, K., "Autonomous flight control system for longitudinal motion of a helicopter," *Proceedings of the SICE(Society of Instrument and Control Engineers)Annual Conference (SICE '07)*, IEEE, Takamatsu, Japan, pp. 2258-2263, September 2007. DOI: 10.1109/SICE.2007.4421364

[54] Spurgeon, S. K., Edwards, C., Foster, N. P., "Robust model reference control using a sliding mode controller/observer scheme with application to a helicopter problem," *Proceedings of the IEEE International Workshop on Variable Structure Systems*, pp. 36-41, Tokyo, Japan, December 1996. DOI: 10.1109/VSS.1996.578542

[55] Raptis,I. A., Valavanis, K. P., Moreno, W. A., "A novel nonlinear backstepping controller design for helicopters using the rotation matrix," *IEEE Transactions on Control Systems Technology*, vol. 19, no. 2, pp. 465-473, 2011. DOI: 10.1109/TCST.2010.2042450

[56] Bogdanov, A. A., Wan, E. A., Carlsson, M., Zhang, Y., Kieburtz, R., Baptista, A., "Model predictive neural control of a high-fidelity helicopter model," *Proceedings of the AIAA Guidance, Navigation, and Control Conference and Exhibit*, QuÃ©bec, Canada, August 2001. https://doi.org/10.2514/6.2001-4164

[57] Anavatti S G, Santoso F, Garratt M A., "Progress in adaptive control systems: past, present, and future," *2015 International Conference on Advanced Mechatronics, Intelligent Manufacture, and Industrial Automation (ICAMIMIA)*, pp. 1-8, 2015. DOI: 10.1109/ICAMIMIA.2015.7537196

[58] Sahani, N. A., Horn, J. F., "Adaptive model inversion control of a helicopter with structural load limiting," *Journal of Guidance, Control, and Dynamics*, vol. 29, no. 2, pp. 411-420, 2006. https://doi.org/10.2514/1.13391

[59] Ertugrul, T., Adli, M. A., Salamci, M. U., "Model reference adaptive control design for helicopters using gain scheduled reference models," *Proceedings of the 17th IEEE International Carpathian Control Conference (ICCC '16)*, Tatranska Lomnica, Slovakia, pp. 182-187, May 2016. DOI: 10.1109/CarpathianCC.2016.7501090

[60] Rysdyk, R. T., Calise, A. J., "Adaptive model inversion flight control for tilt-rotor aircraft," *Journal of Guidance, Control, and Dynamics*, vol. 22, no. 3, pp. 402-407, 1999. https://doi.org/10.2514/2.4411

[61] Hovakimyan, N., Kim, N., Calise, A., Prasad, J. R. V., Corban, E., "Adaptive Output Feedback for High-Bandwidth Control of an Unmanned Helicopter", *Conference of Guidance, Navigation and Control*, AIAA, 2001. https://doi.org/10.2514/6.2001-4181

[62] Guerreiro, B. J., Silvestre, C., Cunha, R., Cao, C., Hovakimyan, N. "L1 adaptive control for autonomous rotorcraft", *American Control Conference*, pp. 3250-3255, 2009. DOI: 10.1109/ACC.2009.5159940

[63] Michini, B., How, J., "L1 adaptive control for indoor autonomous vehicles: design process and flight testing", *AIAA Guidance, Navigation, and Control Conference*, 10 - 13 August, Chicago, Illinois, 2009. DOI: 10.2514/6.2009-5754

[64] Bichlmeier, M., Holzapfel, F., Xargay, E., Hovakimyan, N., "L1 adaptive augmentation of a helicopter baseline controller", *AIAA Guidance, Navigation, and Control (GNC) Conference*, 2013. DOI: 10.1109/ACC.2009.5159940

[65] Gaoyuan, L., Mei, W., Ashraf, A., "L1 Adaptive Control for Tandem-Rotor Helicopter with Anti-Disturbance Capability," *2018 International Conference on Control, Automation and Information Sciences (ICCAIS)*, pp. 372-377, 2018. doi: 10.1109/ICCAIS.2018.8570578

[66] Tian, S., Wang, J., Lin, D., Pei, P., "L1 adaptive control design of a helicopter in vertical flight". *Proceedings of the Institution of Mechanical Engineers, Part G: Journal of Aerospace Engineering*, Vol. 234, No. 14, pp. 2089-99, 2020. https://doi.org/10.1177/0954410020926619

[67] Hovakimyan, N., Cao, C., "L1 adaptive control theory: guaranteed robustness with fast adaptation", *Society for Industrial and Applied Mathematics*, USA, 2010. DOI: 10.1109/MCS.2011.941837

[68] Seckel, E., Curtiss, H.C., "Aerodynamic characteristics of helicopter rotors", Department of Aerospace and Mechanical Engineering Report No. 659, Princeton University, New Jersey, December 1963.

[69] Peters, D.A., Haquang, N., "Dynamic inflow for practical applications", *Journal of the American Helicopter Society*, Vol. 33, No. 4, pp. 64-68, October 1988.

[70] Chen, R.T N., "Effects of primary rotor parameters on flapping dynamics", NASA Technical paper 1431, Ames reasearch center, Moffett Field, California, January 1980.

[71] Hohenemser, K.H., Yin, S.K., "On the use of first order rotor dynamics in multiblade coordinates", Paper presented at 30th Annual National Forum, May 7-9, 1974.

[72] Talbot, P.D., Tinling, B.E., Decker, W.A., Chen, R.T.N., "A mathematical model of a single main rotor helicopter for piloted simulation", NASA Technical memorandum, Ames reasearch center, Moffett Field, California, September 1982.

[73] Heffley, R.K., Mnich, M. A, "Minimum-complexity helicopter simulation math model", USAAVSCOM Technical report87-A-7, Ames reasearch center, Moffett Field, California, April 1988.

[74] Choi, H.S., Kim, E.T., You, D.I. and Shim, H., "Improvements in Small-scale Helicopter Rotor Modeling for the Real-time Simulation of Hovering Flight", *The Japan Society for Aeronautical and Space Science*, Vol. 54, No. 185/186, pp. 229-37, 2011.

[75] Leishman, J. G., Syal, M., "Figure of merit definition for coaxial rotors", *Journal of the American Helicopter Society*, vol. 53, no. 3, pp. 290-300, July 2008.

[76] Kozlowski, K., Pazderski, D., "Modeling and control of a 4-wheel skid-steering mobile robot", *International Journal of Applied Mathematics and Computer Science*, Vol. 14, No. 4, pp. 477-496, 2004. http://eudml.org/doc/207713

[77] https://it.mathworks.com/help/robotics/ug/mobile-robot-kinematics-equations.html

[78] Ang, K.H., Chong, G., Li, Y., "PID control system analysis, design, and technology", *IEEE transactions on control systems technology*, vol. 33, No. 4, pp. 559-576, 2005.

[79] Astrom, K.J., Hagglumd, T., "PID Control in The Control Handbook", W.S. Levine, Ed. Piscataway, NJ: IEEE Press, pp. 198-209, 1996.

[80] Szafranski, G., Roman C., "Different approaches of PID control UAV type quadrotor", The international micro air vehicles conference. pp. 70-75, 2011.

[81] Bertolani, G., Giulietti, F., Pollini, L., Ryals, A.D., "Adaptive attitude control of an unmanned helicopter", CEAS Aerospace Europe Conference 2021, Warsaw, November 23-25, 2021.

[82] Lavretsky E, Gibson T. Projection operator in adaptive systems. arXiv e-Prints, 2011.

[83] Cao C, Hovakimyan N. L1 adaptive controller for a class of systems with unknown nonlinearities. American Control Conference, pp. 4093-4098, 2008.

[84] U.S. Military Specification MIL-F-8785C, November 5, 1980.

[85] *U.S. military handbook MIL-HDBK-1797B*, April 9, 2012.

[86] Padfield, G. D., "Helicopter Flight Dynamics", Blackwell Publishing, 1996

[87] Prouty R. W., "Helicopter Performance, Stability and Control", Krieger Publishing Company, Inc., 1989

[88] De Angelis, E. L., "Stability analysis of a multirotor vehicle hovering condition", Aerospace Science and Technology, no. 72, pp. 248-255, 2018

[89] Kendoul, F., Nonami, K., Suzuki, S., Wang, W., Nakazawa, D., "Autonomous Flying Robots: Unmanned Aerial Vehicles and Micro Aerial Vehicles", 2010.

[90] Park, S., Deyst, J., How, J. P., " A new nonlinear guidance logic for trajectory tracking", *AIAA Guidance, Navigation, and Control Conference and Exhibit, Guidance, Navigation, and Control and Co-located Conferences, American Institute of Aeronautics and Astronautics*, August 2004. https://doi.org/10.2514/6.2004-4900

[91] Giulietti, F., Innocenti, M., Napolitano, M., Pollini, L., "Dynamic and control issues of formation flight", *Aerospace Science and Technology*, Vol. 9, No. ¡, pp. 65-71, January 2005. doi:10.1016/j.ast.2004.06.011

[92] URL https://pixhawk.org/.

[93] Rossetti, G., "Development of a flight control architecture for rotary wing UAVs with model based design approach", *Ph. D. Dissertation thesis*, 2017.

[94] URL https://ardupilot.org/planner/docs/mission-planner-overview.html

[95] URL: https://ardupilot.org/ardupilot/index.html